Cerium as a quantum state probe for rare-earth qubits in a crystal

Karlsson, Jenny

2015

Cerium as a quantum state probe for rare-earth qubits in a crystal

Jenny Karlsson

Doctoral Thesis
2015

Cerium as a quantum state probe for rare-earth qubits in a crystal

Printed in Sweden by Media-Tryck, Lund, 2015

Division of Atomic Physics
Department of Physics
Faculty of Engineering, LTH
Lund University
P.O. Box 118
SE–221 00 Lund
Sweden

http://www.atomic.physics.lu.se

ISSN: 0281-2762
Lund Reports on Atomic Physics, LRAP-509 (2015)

ISBN (print): 978-91-7623-532-4
ISBN (pdf): 978-91-7623-533-1

Abstract

Rare-earth ions doped into a transparent crystal can have optically excited states with coherence times of milliseconds and hyperfine levels with coherence times of hours when cooled down to liquid helium temperatures. This makes them attractive for developing quantum computing hardware.

A quantum transistor can be implemented in a rare-earth-ion-doped crystal by utilizing a dipole blockade effect, where one excited ion prevents nearby ions from being excited. By using single rare-earth ions as qubits, the quantum processor is believed to be scalable to several qubits.

In this thesis a readout mechanism for qubits represented by single ions (Eu or Pr) in a Y_2SiO_5 crystal is explored. A single cerium ion, in the same crystal as the qubits, could potentially be used as an indicator ion for non-demolition quantum state detection of the qubits. Cerium has a strong transition with high fluorescence yield which makes it possible to detect single ions. A cerium ion can be controlled by a qubit via the dipole blockade effect, and fluoresce if the qubit is in state $|1\rangle$ but stay dark if the qubit is in state $|0\rangle$.

Relevant spectroscopic properties of Ce:Y_2SiO_5 are studied, as well as interactions between cerium ions and qubit ions.

The inhomogeneous and homogeneous linewidth of the Ce:Y_2SiO_5 4f-5d transition is measured and fluorescence spectra for ions in site 1 and site 2 are characterized. The change in electric dipole moment as a cerium ion is brought to the excited state is measured. The static dipole interaction between a single cerium ion and a qubit ion is shown to be strong enough for efficient qubit readout.

Energy transfer from cerium to qubit ions is investigated. A lower bound on the cerium-qubit distance is found in order to avoid energy transfer.

Satellite lines belonging to cerium-qubit pairs are mapped out.

A microscope set-up is built to detect single ions in a crystal. Single ion detection is believed to be within reach.

En indikator-jon för en kvantdator

Ända sedan transistorn uppfanns 1948 har datorer blivit allt mer kraftfulla. Trots den enorma utveckling som skett finns det fortfarande problem som är för svåra för en dator att lösa. Ett exempel är simulering av stora molekyler, t.ex. proteiner, vilket skulle vara användbart inom medicin och biologi, bland annat för att förutsäga hur kroppen reagerar på en viss medicin. Molekyler är så små att kvantmekanikens lagar måste användas för att beräkna vad som händer med dem, men så stora att antalet parametrar som behöver beräknas är för stort för dagens datorer.

Simuleringar av stora kvantsystem är en uppgift en så kallad kvantdator skulle kunna göra mycket lättare än en vanlig dator. En kvantdator fungerar på liknande sätt som en vanlig dator, men dess minsta enheter är enkla kvantsystem, som t.ex. atomer. Två energitillstånd i en atom kan användas för att representera en 1:a respektive en 0:a. Atomens två tillstånd utgör den minsta informationsenheten i en kvantdator, en så kallad kvantbit. Eftersom själva kvantdatorn är uppbyggd av kvantbitar som följer kvantmekanikens lagar, blir simuleringar av andra kvantsystem mycket mindre krävande.

Många olika typer av hårdvara för kvantdatorer har testats världen över, men hittills har bara ett fåtal kvantbitar kunnat skapas och kopplas ihop, och de flesta kvantdatorerna kräver stora laboratorium fyllda med utrustning.

Den här avhandlingen handlar om en viss typ av hårdvara, bestående av joner av jordartsmetaller, som sitter inuti en kristall. Kristallen kyls ner till -270 grader i flytande helium för att få jonerna att sitta alldeles stilla och en laser används för att koda 1:or och 0:or i enskilda joners kvant-tillstånd.

För att kunna använda en kvantdator måste vi kunna läsa ut om kvantbitarna är kodade som en 1:a eller en 0:a. Eftersom en enda jon används för att koda varje kvantbit är det svårt att läsa ut vilket tillstånd kvantbiten är i. Därför vill vi koppla kvantbitarna till en annan typ av joner, av ämnet cerium. Då man lyser på

cerium-jonerna med en ultraviolett laser börjar de lysa i blått, som i Illustration 1. Cerium-jonerna kan lysa mycket starkare än de joner vi använder som kvantbitar, så starkt att man kan mäta ljuset som kommer från en enda jon. Cerium-jonen kan då användas som en indikator, som lyser om en viss kvantbit är kodad som en 1:a, men är släckt om den är kodad som en 0:a, vilket visas i Illustration 2.

Målet med projektet som ligger till grund för den här avhandlingen har varit att undersöka om det är möjligt att använda cerium som en tillstånds-indikator för en kvantdator. Resultaten visar att kopplingen mellan en cerium-jon och en kvantbit är stark nog för att cerium-jonen ska kunna tändas och släckas beroende på tillståndet hos kvantbiten. I avhandlingen visas också att det finns andra typer av kopplingar mellan cerium-jonerna och kvantbitarna som kan förstöra utläsningen av information. Det kan undvikas genom att använda kvantbitar som sitter på precis rätt avstånd från cerium-jonen.

För att kunna se ljus från en enda cerium-jon inuti en kristall har ett mikroskop utvecklats och testats. Än så länge har försöken att se ljus från en enda cerium-jon inte lyckats. Med vissa förbättringar av mikroskopet finns goda möjligheter att det lyckas inom en snar framtid.

Illustration 1: *En kristall som innehåller cerium-joner lyser starkt i blått när den träffas av en laser.*

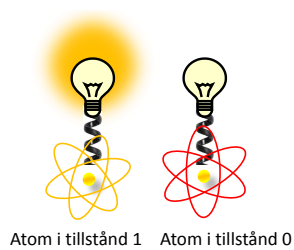

Illustration 2: *En cerium-jon kan ses som en indikator-lampa som lyser då en kvantbit är i tillstånd 1, men är släckt då en kvantbit är i tillstånd 0.*

List of Publications

This thesis is based on the following papers, which will be referred to in the text by their roman numerals.

I **Hole burning and frequency selective trapping in Ce:Y_2SiO_5 at liquid helium temperatures**
J. Karlsson, A. N. Nilsson, D. Serrano, A. Walther, L. Rippe and S. Kröll
A. Ferrier and P. Goldner.
Manuscript in preparation.

II **A confocal optical microscope for detection of single impurities in a bulk crystal at cryogenic temperatures**
J. Karlsson, L. Rippe, and S. Kröll.
(2015) *Submitted to Review of Scientific Instruments.*

III **Measurement of line-widths and permanent electric dipole moment change of the Ce 4f-5d transition in Y2SiO5 for a qubit readout scheme in rare-earth ion based quantum computing**
Y. Yan, J. Karlsson, L. Rippe, A. Walther, D. Serrano, S. Kröll, P. Goldner, D. Lindgren, M-E. Pistol, L. Zheng and J. Xu.
Phys. Rev. B **87**, 184205 (2013).

IV **Satellite line mapping in Eu^{3+}-Ce^{3+} and Pr^{3+}-Ce^{3+} codoped Y_2SiO_5**
D. Serrano, J. Karlsson, L. Zheng, Y. Dong, A. Ferrier, P. Goldner, A. Walther, L. Rippe, and S. Kröll.
Accepted for publication in J. of Lumin , (2015).

V **Impact of ion-ion energy transfer on quantum computing schemes in rare-earth doped solids**
D. Serrano, Y. Yan, J. Karlsson, L. Rippe, A. Walther, S. Kröll, A. Ferrier and P. Goldner.
J. of Lumin. **151**, 93-99 (2014).

VI **High-fidelity readout scheme for rare-earth solid-state quantum computing**
A. Walther, L. Rippe, Y. Yan, J. Karlsson, D. Serrano, A. N. Nilsson, S. Bengtsson and S. Kröll.
Phys. Rev. A **92**, 022319 (2015).

Abbreviations

REQC	Rare Earth Quantum Computing
IUPAC	International Union of Pure and Applied Chemistry
ZPL	Zero-Phonon Line
ECDL	External Cavity Diode Laser
EOM	Electro-Optic Modulator
AOM	Acousto-Optic Modulator
DDS	Direct Digital Synthesizer
DSP	Digital Signal Processing (card)
ULE	Ultra-Low Expansion (glass)
NA	Numerical Aperture
PSF	Point Spread Function
TA	Transverse Aberration
LA	Longitudal Aberration
CLC	Circle of Least Confusion
SIL	Solid Immersion Lens

Contents

Abstract iii

En indikator-jon för en kvantdator v

1 Introduction 1
- 1.1 Aim of the project . . . 2
- 1.2 A personal perspective . . . 2
- 1.3 Outline of the thesis . . . 3

2 Rare-earth-ion-doped crystals 5
- 2.1 Chemical properties of the Rare Earths . . . 5
  - 2.1.1 Lanthanide contraction and screening . . . 6
  - 2.1.2 Implications for quantum computing . . . 8
- 2.2 Spectroscopic properties of the Rare Earths . . . 8
  - 2.2.1 $4f^n$ energy levels . . . 8
  - 2.2.2 $4f^{n-1}5d$ energy levels . . . 11
  - 2.2.3 Hyperfine structure . . . 11
- 2.3 Influence of the crystal . . . 12
  - 2.3.1 Static dipole moment . . . 12
  - 2.3.2 Charge transfer processes . . . 12
  - 2.3.3 Phonons . . . 13
  - 2.3.4 Zero-phonon lines . . . 14
  - 2.3.5 Inhomogeneous linewidth . . . 14
- 2.4 Coherence and homogeneous linewidth . . . 15
  - 2.4.1 Homogeneous linewidth . . . 15
  - 2.4.2 Dephasing mechanisms . . . 16
- 2.5 Summary: Europium, Praseodymium and Cerium in Y_2SiO_5 16
  - 2.5.1 The Y_2SiO_5-crystal . . . 16
  - 2.5.2 Eu:Y_2SiO_5 and Pr:Y_2SiO_5 . . . 17
  - 2.5.3 Ce:Y_2SiO_5 . . . 19

3 Quantum Computing 21
- 3.1 Requirements for quantum computing . . . 22
- 3.2 Quantum computing implementations . . . 22
  - 3.2.1 Trapped ions . . . 23
  - 3.2.2 Superconducting circuits . . . 23
  - 3.2.3 NV-centres in diamond . . . 24
  - 3.2.4 Photons . . . 24
  - 3.2.5 Combining different systems . . . 25
- 3.3 Rare-earth quantum computing . . . 25
  - 3.3.1 Creation and characterization of one ensemble qubit 26
  - 3.3.2 Two-qubit gates . . . 26
  - 3.3.3 Scalability . . . 28
  - 3.3.4 Stochiometric crystals - The Canberra scheme . . . 28
  - 3.3.5 Single instance quantum computing - The Lund scheme 29

3.3.6 The aim of this thesis . . . 30

4 Dye laser system for qubit manipulation 31
4.1 Pound-Drever-Hall laser stabilization . . . 31
4.1.1 Transmission and reflection from a Fabry-Perot cavity 32
4.1.2 Cavity response to laser noise . . . 33
4.1.3 Generating the error signal . . . 33
4.2 Dye laser system . . . 35
4.2.1 Dye laser . . . 35
4.2.2 Stabilization system optics . . . 36
4.2.3 Low noise photo detectors . . . 38
4.2.4 Feedback actuators . . . 40
4.2.5 Feedback electronics . . . 41
4.2.6 Pulse shaping system . . . 44

5 Diode laser system for readout 45
5.1 Laser diode . . . 45
5.2 Littrow cavity design . . . 46
5.3 Collimation lens . . . 48
5.4 Tuning characteristics . . . 48
5.5 Stabilizing the ECDL . . . 50
5.5.1 Reference cavity . . . 50
5.5.2 Cavity decay time . . . 51
5.5.3 Stabilization system optics . . . 52
5.5.4 Stabilization system electronics . . . 53
5.5.5 Optical table . . . 54

6 Microscope for single ion detection 57
6.1 Confocal microscopy . . . 58
6.1.1 Diffraction limit . . . 59
6.1.2 Resolution limit for a confocal microscope . . . 61
6.1.3 Point spread function . . . 62
6.2 Optical aberrations . . . 62
6.2.1 Aberrations in the ray-picture . . . 63
6.2.2 Wavefront aberrations . . . 64
6.2.3 Case 1: Focusing through a cryostat window . . . 65
6.2.4 Case 2: Focusing into a crystal . . . 65
6.3 Microscope design . . . 66
6.3.1 A Blu-ray lens . . . 67
6.3.2 Sample scanning . . . 68
6.3.3 Intracryostat assembly . . . 69
6.3.4 Optics and detection . . . 70
6.4 Test of the microscope . . . 72

7 Cerium spectroscopy 79
7.1 Zero phonon line . . . 79
7.2 Homogeneous linewidth . . . 81
7.3 Fluorescence spectrum . . . 82
7.4 Single ion detection attempts . . . 83
7.4.1 Method . . . 83
7.4.2 Sample 1: Low concentration Ce:Y_2SiO_5 . . . 84
7.4.3 Sample 2: Undoped Y_2SiO_5 . . . 85
7.4.4 Sample 3: Pr:Y_2SiO_5 . . . 86
7.4.5 Improvements and outlook . . . 86
7.5 Charge transfer and trapping . . . 88
7.5.1 Possible trapping mechanisms . . . 89
7.5.2 Rate equation model . . . 90
7.5.3 Consequences for single ion detection . . . 91
7.6 Summary of the results . . . 92

8 Ion-ion interaction 93

8.1 Electric ion-ion interactions 93
8.2 Static electric dipole interaction 95
8.2.1 Measurement of the change in static electric dipole moment of cerium 96
8.3 Satellite lines 99
8.4 Energy transfer 102
8.5 Overlapping transitions 104
8.6 Summary of the results 105

9 Conclusion and outlook **107**

The Author's Contribution to the Papers **109**

Acknowledgements **113**

Papers

I Hole burning and frequency selective trapping in Ce:Y_2SiO_5 at liquid helium temperatures **131**

II A confocal optical microscope for detection of single impurities in a bulk crystal at cryogenic temperatures **141**

III Measurement of line-widths and permanent electric dipole moment change of the Ce 4f-5d transition in Y2SiO5 for a qubit readout scheme in rare-earth ion based quantum computing **151**

IV Satellite line mapping in Eu^{3+}-Ce^{3+} and Pr^{3+}-Ce^{3+} codoped Y_2SiO_5 **161**

V Impact of ion-ion energy transfer on quantum computing schemes in rare-earth doped solids **173**

VI High-fidelity readout scheme for rare-earth solid-state quantum computing **183**

Chapter 1

Introduction

Since the invention of the transistor in 1948 computers have become smaller and increasingly powerful. Gordon E. Moore predicted in 1965 that the number of components on a chip would double every year [1]. This predicted exponential growth rate in computer power has been amazingly accurate, and Moore's law has been widely used as a guideline for industry and development.

However, today the size of a transistor is less than 20 nm, and it is approaching fundamental limits. As components get smaller, quantum mechanics comes into play, and quantum tunnelling through the gates of a transistor will eventually make it difficult to reduce the size any further. Moore's law will most probably slow down within the next few years, and there will be a need for new designs and new inventions [2].

A quantum computer is, at least in the versions of today, not a replacement for a normal PC. A quantum computer is not always faster than a normal computer, and the versions we work with today are certainly not smaller, they occupy large rooms. But a quantum computer could solve some specific problems much faster than a normal computer. Such problems include simulating large quantum systems, like molecules, which for example could allow us to calculate how proteins in our body interact with a certain medication.

Most of all, learning to control quantum systems would open up a door to previously unexplored territory, to new technical possibilities. In that sense a quantum computer is just a symbol for a much wider range of possible devices based on quantum mechanics.

Today, much research is focused on developing hardware for quantum computers. This thesis concerns quantum computer hardware based on a particular physical system, namely rare-earth-ion-doped crystals.

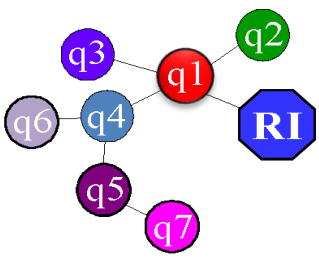

Figure 1.1. *A conceptual image of a quantum processor in a rare earth ion doped crystal. The circular dots (q1-q7) are qubit ions, which can be for example praseodymium ions or europium ions. Each of them absorb at a unique frequency within the inhomogeneous profile. Some of them sit close enough to each other to interact strongly, which is shown as black lines, and together they create a chain structure of interacting ions. One readout ion, RI, which in this case is a cerium ion, interacts with at least one of the qubits in the chain. The readout ion acts like an indicator lamp, fluorescing if a qubit is in state 1, but not if it is in state 0.*

1.1 Aim of the project

Rare-earth ions, sitting in a crystal, is a system with properties very suitable for quantum computer hardware. Two hyperfine levels of a single rare-earth ion can be used to represent the states '0' and '1' of a qubit. If one ion is promoted to an optically excited state, it shifts surrounding ions out of resonance with the laser and prevents them from being excited. This interaction between ions, called the dipole blockade effect, can be used to create a quantum transistor, where the state of one qubit is changed only if another ion is in state 1. It is however very difficult to detect which state a single ion is in. With most detection methods the information we want to read would be destroyed by the measurement itself before the readout is finished. To read the information from the quantum processor we need to introduce another degree of freedom, to be able to do a so called non-demolition measurement.

The aim of this project has been to investigate one potential readout mechanism for a rare-earth quantum processor. A single cerium ion is introduced into the crystal, which interacts with the qubit ions via the dipole blockade effect. The cerium ion could be used like an indicator lamp, fluorescing if a qubit is in state 1, but not if it is in state 0.

A conceptual image of a small quantum processor is shown in Figure 1.1. The qubit ions, named q1 to q7, interact with each other in a chain structure. A readout ion marked RI, in this case a cerium ion, interacts with at least one qubit ion. The same readout ion can be used to determine the state of all qubits in the chain, since the states can be exchanged between qubit pairs and moved to the qubit that interacts with the readout ion.

In this thesis properties of the cerium ions relevant for the readout scheme are studied, as well as interactions between cerium ions and praseodymium or europium ions. A microscope set-up was developed and tested to detect fluorescence from single ions inside a crystal immersed in liquid helium. Single ion detection in an experimental situation which also allows for cerium-qubit interaction and implementation of gate operations puts high requirements on the set-up, and is believed to be within reach in the near future.

1.2 A personal perspective

Reality is much more complex then the simple models and images we often have in our minds. Behind the simple illustration in Figure 1.1 there is a whole universe of particles, bound together by different forces into molecules, which are connected into a crystal structure and interacting with each other in different ways. The simple image is still very useful, if we would take everything into account at once we would drown in information. Nonetheless, to

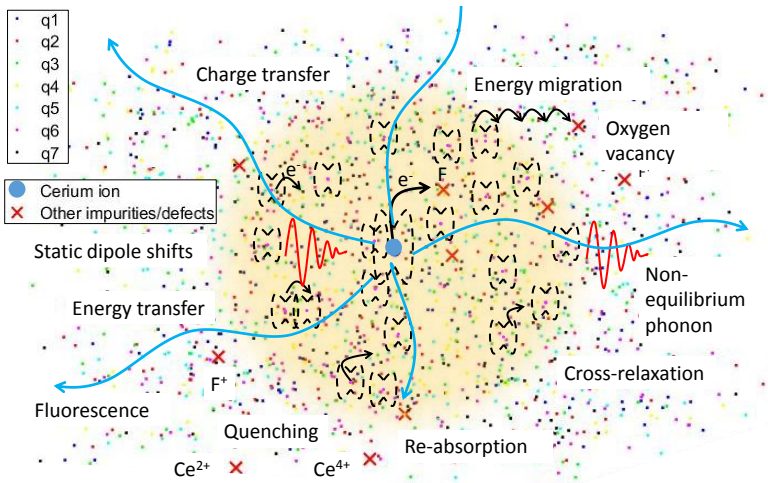

Figure 1.2. *An artistic view showing the complexity of a rare-earth-ion-doped crystal. The image shows the laser focus in a crystal doped with around 1% qubit ions and a very low concentration of cerium ions ($\approx 10^{-7}$). q1-q7 in this case refers to ions absorbing at 7 different frequencies within the inhomogeneous line. Around 100 million qubit ions that are not part of the 7 frequency channels q1-q7 are excluded from the picture, otherwise the picture would be completely black. Around 2000 cerium ions that are not resonant with the laser frequency of the readout laser are also excluded. The butterfly structures show excited ions with a different static dipole moment. The image illustrates some effects we might need to take into account when developing quantum computer hardware in a rare-earth-ion-doped crystal.*

make real progress, and to actually build a quantum computer, we need to start breaking the picture down into smaller parts, and start investigating what is behind each part. Figure 1.2 is my effort to illustrate the result of this process in my own mind, after spending 5 years trying to understand what is going on in a rare-earth-ion-doped crystal.

The progression from the image in Figure 1.1 towards the image in Figure 1.2 summarizes my view of this thesis. Within the scope of this thesis we have moved from a simple idea to a more realistic picture of what needs to be considered in order to create a quantum processor in a rare-earth-ion-doped crystal.

1.3 Outline of the thesis

The thesis is structured as follows; In Chapter 2 and 3 the background and context of the project is introduced. Chapter 4-6 describes the experimental set-up that was partly developed and improved within the scope of this work. Chapter 7-8 presents ex-

perimental findings and Chapter 9 concludes the thesis.

Chapter 2

Rare-earth-ion-doped crystals

The main topic of this thesis is rare-earth ions, their spectral properties and their application in the field of quantum computing.

Rare-earth minerals were discovered in Sweden in 1787, in the village Ytterby close to Stockholm. The first rare-earth element was named Yttrium after the village, and Ytterbium, Terbium and Erbium were named in the same tradition. The Swedish scientists later adopted a slightly broader perspective and named other discovered elements Scandium (for Scandinavia), Thulium (old Latin name for Scandinavia) and Holmium (medieval name for Stockholm). The naming convention might have inspired the French scientists that later discovered Lutetium (ancient Roman name for Paris) and Europium (for Europe) [3].

Rare-earth-ion-doped crystals have been extensively studied for more than 50 years. In this chapter some relevant properties of rare-earth-ion-doped crystals will be summarized with a focus on the materials used in this thesis; praseodymium (Pr), europium (Eu) and cerium (Ce) doped into yttrium orthosilicate (Y_2SiO_5) crystals.

My aim is to describe the relevant properties of the materials in an intuitive way that can be useful when working experimentally. For a more rigorous description I recommend reading Reference [4].

2.1 Chemical properties of the Rare Earths

According to the definition by the International Union of Pure and Applied Chemistry (IUPAC), the rare earth elements consist of scandium, yttrium and the 15 so called lanthanides from the third and fourth group of the periodic table of elements. The lanthanides are all sitting in the same little square in the periodic table of elements (sometimes with an exception for lutetium), and

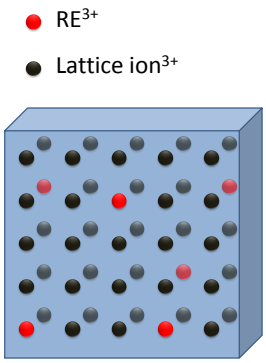

Figure 2.2. *Ions in the crystal lattice is replaced by rare-earth ions in a process called doping.*

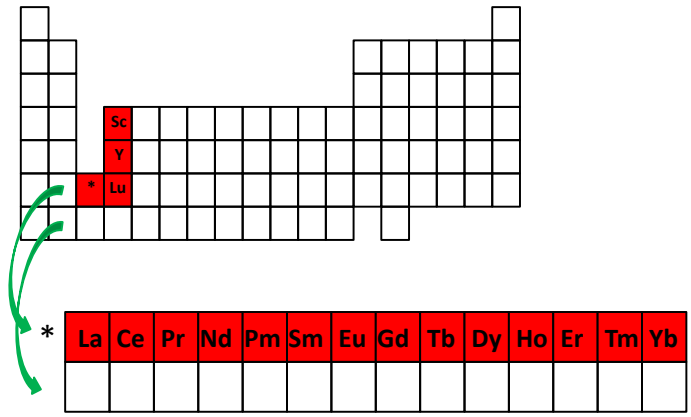

Figure 2.1. *The location of the rare earths in the periodic table of elements*

are often presented in a fold out together with the actinides, as shown in Figure 2.1. The reason is that although the lanthanides are sitting in the sixth row of the periodic table of elements they represent a gradual filling of the fourth electron shell, more exactly the 4f-subshell, which has lower energy than the 5d-subshell.

It is possible to capture rare earths inside a transparent crystal in a process called doping, see Figure 2.2. As the crystal is grown a small amount of a rare-earth element is added to the chemical mixture. Ions of the rare-earth element will then replace other ions inside the crystal at random positions. Once the rare-earth ions are captured in the crystal structure, they can be investigated optically by shining light into the crystal.

When doping rare-earth elements into a crystal they most often appear as trivalent ions (3+). The trivalent lanthanide ions all have configuration $[Xe]4f^n$, a xenon core and the valence electrons in the 4f-subshell, where n goes from 0 to 14 from lanthanum to lutetium.

2.1.1 Lanthanide contraction and screening

The nuclear charge of an atom is partly screened by inner electron orbitals, causing the outer orbitals to feel a lower effective charge and extend further away from the nucleus. The screening ability is dependent on the shape of the charge distribution of an orbital,

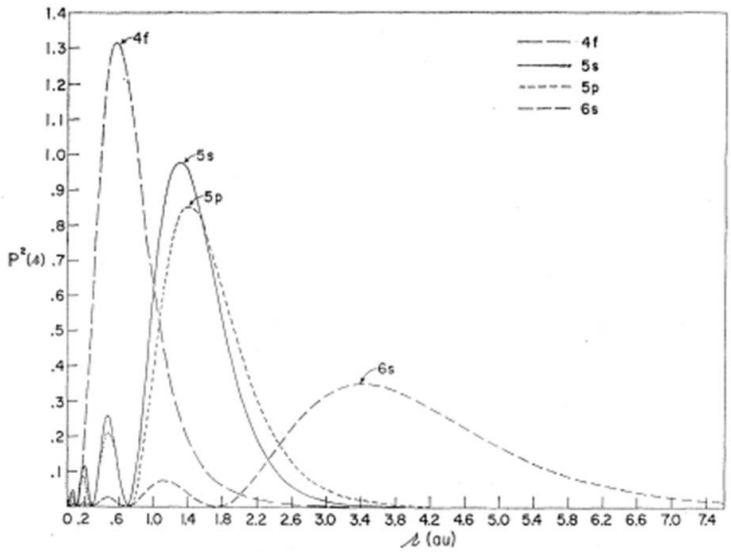

Figure 2.3. *The radial distribution of the 4f, 5s, 5p and 6s electron orbitals, from right to left, of Gd. The 4f-orbital is shielded from the environment by the outer orbitals. The figure is reprinted with permission from [5].*

with s-orbitals screening very efficiently and p,d and f orbitals getting successively worse.

The 4f-subshell of the lanthanides screens the nucleus very badly, causing what is called the lanthanide contraction. As the nuclear charge is getting larger with increasing atomic number the badly screened outer electrons are pulled harder towards the nucleus and the radius of the atom decreases by roughly 15 % from lanthanum to lutetium. The mutual screening among the 4f-electrons is almost negligible, causing the 4f-subshell to contract more than the filled 5s and 5p orbitals [3]. An example of this can be seen in Figure 2.3, where the radial extension of the 4f, 5s, 5p and 6s orbitals of gadolinium are calculated by Freeman and Watson [5]. Since the 4f-subshell is closer to the nucleus, the filled orbitals of the fifth shell will act like a Faraday cage, screening the 4f-electrons efficiently from the surroundings.

Since the bonding electrons in the outermost orbitals are the same for all lanthanides the chemical differences that exist between different lanthanides are mostly due to differences in size of the atoms [3].

2.1.2 Implications for quantum computing

For rare-earth ions doped into a crystal the contraction of the 4f-subshell means that the valence electrons are screened from electric and magnetic fields in the crystal. Thus, as long as we keep the valence electrons inside the Faraday cage of the fifth shell, which means that we only do transitions within the 4f-subshell, the ions act almost as if they were hoovering in empty space, unaffected by the crystal environment. At the same time they are stationary, can be conveniently investigated without escaping and can possibly in the future be placed on a chip.

The lack of disturbance from the environment is just what is needed for quantum information applications, where wave function coherence needs to be preserved for a long time. 4f-4f transitions in rare-earth-ion-doped crystals can have coherence times that are very close to being limited only by the lifetime of the excited state [6]. To obtain such long coherence times the crystal needs to be cooled down to liquid helium temperatures, to depopulate vibrational modes of the crystal lattice, so called phonons, that would otherwise cause decoherence. Phonons and coherence will be discussed more in detail in sections 2.3 and 2.4.

2.2 Spectroscopic properties of the Rare Earths

Rare-earth-ion-doped crystals provide a versatile spectroscopic platform for quantum information applications. Hyperfine states in the electronic ground state of the ions have extremely long lifetimes and very long coherence times, which make them suitable for storing qubits. Optical transitions within the $4f^n$ configuration provides a method for qubit manipulation with very little disturbance from the surrounding crystal environment. In addition, short-lived 5d-states with high fluorescence yield makes it possible to detect single ions in a crystal, which could allow scalability of a qubit system.

In this section the basic spectroscopic properties of rare-earth-ion-doped crystals will be presented.

2.2.1 $4f^n$ energy levels

Almost all transitions in the visible spectrum in rare-earth-ion-doped crystal are so called 4f-4f transitions, transitions within the $4f^n$ configuration.

Transitions within the 4f-subshell are electric dipole forbidden for a free atom, because an electric dipole transition require a change of parity. In a non-centrosymmetric crystal, the transitions become weakly allowed because of mixing with opposite parity

states. The weak oscillator strengths of 4f-4f transitions makes them long lived, with lifetimes in the μs to ms range.

Because of screening from the crystal environment discussed in section 2.1 the energy levels associated with the $4f^n$ configuration in a rare earth material are atom-like in the sense that the influence from the crystal can be treated as a perturbation.

To a first approximation the energy levels can be represented with the fine structure levels of a free ion $^{2S+1}L_J$, where S is the total electron spin quantum number, L is the total orbital angular momentum and J is the total angular momentum of the electrons. It should however be noted that L and S are not good quantum numbers for the rare earths, levels with the same J but different L and S are mixed in the so called intermediate coupling scheme. The notation is still used, with L and S as the strongest contributing quantum numbers. The levels are 2J+1 times degenerate.

The perturbation from the crystal environment can be considered as a static electric field caused by all surrounding ligands. The crystal field cause a splitting of the atom-like energy levels, depending on the local crystal symmetry around the rare-earth ion and the number of valence electrons of the ion. For an ion with an even number of valence electrons, a so called non-Kramers ion, the degeneracy of the atom-like energy levels can be fully lifted in a non-axial crystal site. This is the case for Pr:Y_2SiO_5 and Eu:Y_2SiO_5 used in this thesis. For a so called Kramers-ion, with an odd number of valence electrons, there is a remaining two-fold degeneracy of the resulting energy levels. This is true in the case of Ce:Y_2SiO_5.

The energy levels of the 4f-subshell of the rare earths are only slightly disturbed by the crystal surroundings, and they are very similar from one crystal to another. Figure 2.4 shows a diagram of the $4f^n$ energy levels of the trivalent rare-earth ions in a LaF_3-crystal. The crystal field splitting is sometimes not resolved but is indicated by the width of the levels. The first chart presenting the energy levels of the $4f^n$ configuration, a so called Dieke diagram, was published by Dieke in 1968 [7] for a $LaCl_3$ crystal, and has since then been reprinted many times and extended to higher energies. Here I use a diagram by Carnall [8] from 1989 since it contains more detailed information on the crystal field splitting of some levels. There is also a more recent version by Meijerink [9] which is extended to even higher energies.

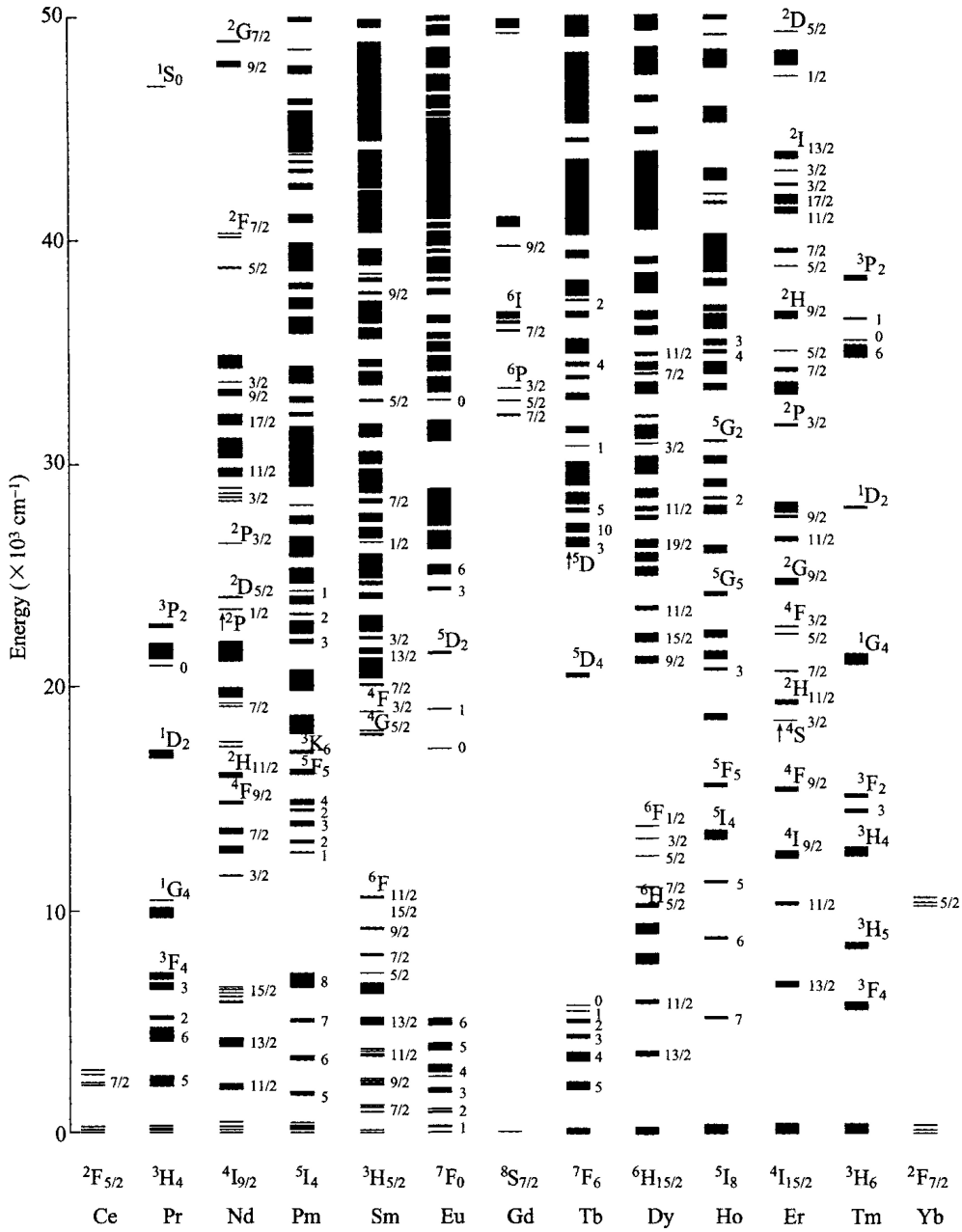

Figure 2.4. *Calculated $4f^n$ energy levels of the trivalent rare-earth ions in LaF_3. The figure is reprinted with permission from [8].*

2.2.2 $4f^{n-1}5d$ energy levels

The 5d-orbitals of rare-earth ions in crystals are much more exposed to the crystal environment than the 4f-orbitals. As a consequence, the energy of the $4f^{n-1}5d$-configuration of rare-earth ions varies a lot with crystal host material; For a free (gaseous) cerium ion the transition from 4f to the lowest 5d-level is resonant with 201 nm. A cerium ion doped into LaF_3 has the same transition at 249 nm, in $Y_3Al_5O_{12}$ (YAG) it is at 458 nm and in $MgSc_2S_4$ at 625 nm [10]. Another consequence of lack of shielding is that the crystal field is felt much more strongly by the electron, and the splitting caused by the crystal field is larger than the spin-orbit splitting.

Most $4f^n$ to $4f^{n-1}5d$ transitions are in the ultraviolet or even x-ray spectrum, but there are a few exceptions where the 5d-level can be reached with visible wavelengths. Cerium has the lowest 5d-energy of all rare-earth ions. The second lowest 5d-level is found in praseodymium and is located at about 12500 cm^{-1} (375 THz or about 200 nm at blue wavelengths) higher energy than the cerium level for the same host crystal [11].

Transitions between a $4f^n$ ground state to a $4f^{n-1}5d$-state are electric dipole allowed and about 10000 times stronger than the strongest transitions within the $4f^n$ configuration. in many cases $4f^{n-1}5d$-states can give rise to strong fluorescence [4].

2.2.3 Hyperfine structure

Rare earths that have nuclear spin also have hyperfine structure, where each crystal field level is further split into several levels, with separations in the MHz to GHz range. Several different mechanisms contribute to the hyperfine structure of the rare earths.

Magnetic interaction between the electron angular momentum and the nuclear angular momentum of the rare-earth ion causes a first order splitting of each level. For electronic singlet states, as for example all crystal field levels of a non-Kramers ion in a crystal site with no axial symmetry, the orbital angular momentum of the ion is quenched. In systems where the orbital angular momentum is quenched there is no first order hyperfine splitting. This is for example the case in Eu:Y_2SiO_5 and Pr:Y_2SiO_5.

The second order magnetic interaction between the electron angular momentum and the nuclear spin causes a hyperfine splitting that depends on the nuclear spin to second order. Each level is then doubly degenerate.

The interaction between the nuclear electric quadrupole moment and the local electric field gradient at the nucleus causes a hyperfine splitting that is also of second order in nuclear spin. The local electric field gradient depends both on the electron configuration of the rare-earth ion, and the crystal field [4].

The hyperfine levels of the ground state in a rare-earth ion can have extremely long lifetimes. For example a lifetime of 20 days have been measured in Eu:Y_2SiO_5 [6].

2.3 Influence of the crystal

We might like to imagine the rare-earth ions in a crystal as floating in empty space, but they are not, and the crystal surroundings of an ion can have a large impact in some situations. In the previous section it was mentioned that the crystal field will split up the free-ion energy levels and even make some transitions allowed that are otherwise forbidden.

In this section a few more effects of the crystal surroundings will be mentioned.

2.3.1 Static dipole moment

Since the ions are sitting in a static crystal field the electrons will be slightly shifted relative to the nucleus and the ions will gain a static dipole moment. This dipole moment is dependent on the electronic state of the ion and will change if the ion is excited to a higher energy state. The change of dipole moment as an ion is excited has a back action on the local crystal field and can shift the energy levels of other nearby rare-earth ions.

This can have negative effects as in the case of excitation induced dephasing, when the phase of an ion is randomized due to excitations of other ions, see Section 2.4. It can also be turned into a useful effect when creating gate operations, see Chapter 3.

2.3.2 Charge transfer processes

Charge transfer occurs when an electron is either added or subtracted from a dopant ion, and the ion is left in a state with a different charge.

Charge transfer can happen if an electron is excited from a ligand ion of the crystal lattice into a 4f-state of the dopant ion. The dopant ion ends up in a state $4f^{n+1}$ as a divalent ion (2+) and a neighbouring ligand ion is left with a hole after the missing electron. The energy required for charge transfer is strongly dependent on the host crystal and can in some cases be lower than the energy of the $4f^n$ - $4f^{n-1}5d$ transition. This is for example the case in Eu:YPO_4 [12].

Ionization of an ion is another charge transfer process where an electron is excited from a dopant ion to the conduction band of the host crystal.

In some cases some levels of the $4f^{n-1}5d$-configuration overlap in energy with the conduction band of the crystal. An electron can then resonantly escape the ion from these levels, which results

in very short lifetimes and broad structureless absorption bands. Emission from the $4f^{n-1}5d$-configuration can then be completely quenched. This is believed to be the case for example in Ce:Y_2O_3 where there is no emission from the 5d-level [13].

2.3.3 Phonons

A crystal consists of different kinds of ions, held together in a regular structure by electric forces. Looking at one such ion the electric forces holding the ion in it's equilibrium position can be thought of as springs. Then it's easy to imagine that the ion can vibrate around it's equilibrium position, with a certain eigenfrequency ω, as illustrated in Figure 2.5.

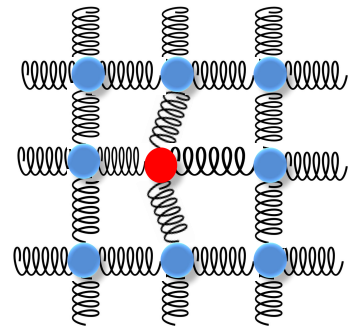

Figure 2.5. *A phonon can be imagined as an energy quanta $\hbar\omega$ of a vibrational mode in a system of coupled springs.*

The simplest model of vibrations of an ion in a crystal structure is a three dimensional harmonic oscillator. We know from quantum mechanics that the energy of such a system is quantized, with energy quanta $\hbar\omega$. This quanta of vibrational energy is called a phonon.

When we imagine the crystal lattice as a three dimensional structure of many ions held together by springs, we also realize that there are many different ways in which the ions can vibrate relative to each other. We can describe every possible vibration as a combination of certain normal modes of the lattice, travelling waves characterized by a wave vector q. Each normal mode has a phonon energy $\hbar\omega_q$. The number of possible normal modes and their phonon energy depends on the crystal structure.

The average number of phonons present in each normal mode (n_q) of a crystal follows a Bose-Einstein distribution according to Equation (2.1).

$$n_q = \frac{1}{e^{\hbar\omega_q/k_BT} - 1}, \tag{2.1}$$

where k_B is the Bolzmann constant and T is the temperature.

At room temperature many phonons are present in the crystal, while at absolute zero there are none. At liquid helium temperatures around 4K only low energy phonons are present.

Coupling to the phonon modes of the crystal can allow non-radiative decay to lower energy levels by emission of phonons. The process will make the lifetime of the excited state shorter. Non-radiative decay gets more unlikely the larger the gap is between energy levels of the ion, since multi-phonon processes are needed to bridge the gap.

For transitions involving 5 or more phonons non-radiative decay is considered less significant than radiative decay. For Y_2SiO_5 with a maximum phonon energy of about 400 cm^{-1} (12 THz), this would mean that transitions above 2000 cm^{-1} or 60 THz would not be affected very much by non-radiative decay [14], [15].

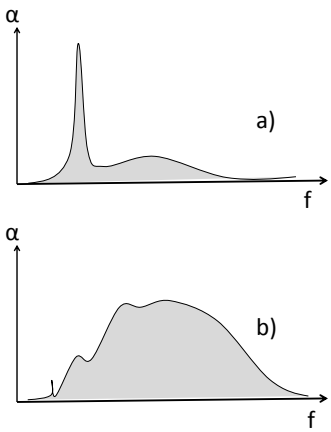

Figure 2.6. *Schematic illustration of the absorption (α) as a function of frequency (f) of a transition in a rare-earth-ion-doped crystal. a) 4f-4f transitions often have strong zero-phonon lines and weak phonon sidebands. b) On the contrary 4f-5d transitions have weak zero-phonon lines and strong phonon wings.*

2.3.4 Zero-phonon lines

When exciting an ion from the ground state to an excited state a number of vibrational modes can also be excited, if there is enough energy. This will broaden the absorption spectrum of the transition by adding a so called phonon wing corresponding to excitation of the ion + a number of phonons. At the low energy edge of the phonon wing there is often a sharp peak which corresponds to the transition where no phonons are created, a so called zero-phonon line (ZPL).

An excitation from a $4f^n$ configuration to a $4f^{n-1}5d$ configuration means that the electron orbital will expand much further away from the nucleus. This expansion of the electron distribution is likely to result in a displaced equilibrium position of the ion relative to other ions, to give other ions in the nearby crystal structure a push and excite vibrational modes. Thus 4f-5d transitions have strong phonon wings, and weak or sometimes no zero-phonon lines.

For excitations within the $4f^n$ configuration the situation is the opposite. The electrons stay within the same configuration and they are efficiently shielded from the surrounding lattice by the outer-lying electron orbitals. The transitions within the $4f^n$ configuration have strong zero-phonon lines and weak phonon wings, see Figure 2.6 [16].

The zero-phonon lines are similar to transitions in free ions. In the rest of this section only zero-phonon lines will be considered.

2.3.5 Inhomogeneous linewidth

Zero-phonon lines of rare-earth-ion-doped crystals typically have absorption linewidths in the GHz range. This is however not the case if we look at a single ion for which the linewidth can be much narrower. The absorption line is inhomogeneous, which means that there is a spread in absorption frequency between individual ions, that are all summed up to create the collective absorption line.

The spread in absorption frequency is due to irregularities in the crystal lattice, so that each ion experience a slightly different crystal field. The crystal lattice gets distorted as we dope rare-earth ions into the crystal, since they have a slightly different size than the ions that would normally occupy the crystal site. The higher concentration of dopant ions the crystal has, the wider the inhomogeneous line is. Figure 2.7 shows a simple illustration of the broadening mechanism.

Other defects in the crystal lattice can also contribute to the inhomogeneous broadening. Usually, however, the concentration of rare-earth ions is much larger than the concentration of any other defect and accounts for most of the broadening [6].

2.4 Coherence and homogeneous linewidth

Coherence can mean many things, depending on the situation. It can mean that ions in an ensemble oscillate in phase with each other. It can mean that one or an ensemble of ions oscillate in phase with the laser. The opposite of coherence, decoherence or dephasing, is a limiting process that makes the systems go out of phase with each other. If dephasing happens in a deterministic way it is sometimes possible to reverse it. If we have enough knowledge about the mechanisms of dephasing it might also be possible to eliminate or reduce the effect. Thus, a measure of coherence has a lot to do with our knowledge about the phases of a system and our ability to control them.

What I mean by coherence in this section is the ability to predict and keep our laser tuned to the phase of a single ion. This is what determines the homogeneous linewidth of the ion. Decoherence is then random or seemingly random events that change the phase of the ion in a way that we can not predict.

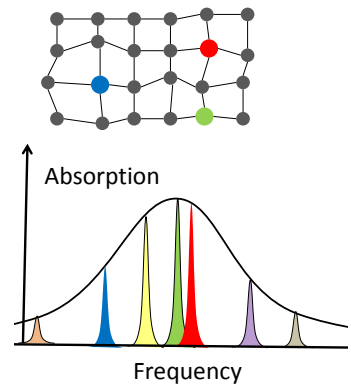

Figure 2.7. *The dopant ions have a slightly different size than the ions they are replacing in the crystal lattice. The difference induces strain in the lattice and random shifts of the local electric fields. Each ion is shifted in absorption frequency due to it's local environment and a broader inhomogeneous line appears.*

2.4.1 Homogeneous linewidth

The absorption linewidth of each ion in the crystal, the so called homogeneous linewidth, Γ_{hom}, depends on the coherence time, T_2, of the transition, as in Equation (2.2).

$$\Gamma_{hom} = \frac{1}{\pi T_2} \tag{2.2}$$

The coherence time is in turn ultimately limited by the lifetime, T_1, of a state, as in Equation (2.3).

$$T_2 \leq 2T_1 \tag{2.3}$$

This is easy to understand considering that coherence has to do with a quantum mechanical phase relationship between two eigenstates involved in a superposition state. When the excited state has decayed, there is no longer any superposition between the two, and no coherence. The factor of two between the lifetime and the coherence time simply reflects the fact that when we measure coherence, we measure an amplitude, but when we measure lifetime we measure the population of a level which is the square of the amplitude, see Figure 2.8.

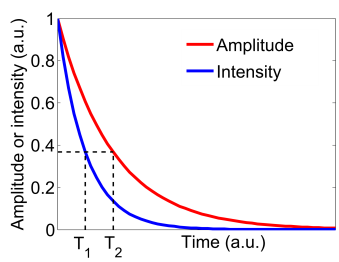

Figure 2.8. *The figure shows the exponential decay of population in the excited state with the lifetime T_1 (blue curve) and (the absolute value of) the amplitude of the excited state (red curve). If the coherence time, T_2, is lifetime limited, the coherence will decay as the amplitude of the excited state. The figure is reprinted with permission from [17].*

Usually the coherence time is shorter than twice the lifetime because of additional dephasing mechanisms. The homogeneous linewidth can be written as in Equation (2.4), where T_2^* corresponds to an additional decoherence time due to influence from the environment of the ion.

$$\Gamma_{hom} = \frac{1}{2\pi T_1} + \frac{1}{\pi T_2^*} = \Gamma_0 + \Gamma_{dephasing} \tag{2.4}$$

The contributions to additional dephasing, $\Gamma_{dephasing}$, is described more in detail below.

2.4.2 Dephasing mechanisms

There are four main contributors to the homogeneous linewidth, Γ_{hom}:

$$\Gamma_{hom} = \Gamma_0 + \Gamma_{phon} + \Gamma_{field} + \Gamma_{ISD}. \tag{2.5}$$

Γ_0 is the lifetime limited linewidth.

Γ_{phon} is a broadening caused by phonon scattering. This random process leads to a phase shift, and after many such events we successively lose information about the phase of the ion. At room temperature phonon scattering is the biggest contributor to dephasing. Scattering of phonons is however unlikely at liquid helium temperatures, since the scattering probability scales as T^7 for low temperatures.

At low temperatures ($\leq$ 4K) it is instead random changes of the electric or magnetic field felt by the ion that causes dephasing, Γ_{field}. Changes in crystal field is typically caused by spin flips in ligand ions. Spin flips can be reduced by applying a magnetic field to the crystal, that splits up the spin levels.

If we excite a number of ions in the crystal their static electric dipole moments will change and cause a change in the crystal field, which will shift the energy levels of ions nearby. This will cause so called excitation induced dephasing, or instantaneous spectral diffusion (ISD). This effect is only present when some ions are in an excited state [18].

2.5 Summary: Europium, Praseodymium and Cerium in Y_2SiO_5

In this thesis yttrium orthosilicate (Y_2SiO_5) crystals doped with Eu, Pr, Ce or combinations thereof, are investigated. For convenience the relevant properties of these materials are summarized.

2.5.1 The Y_2SiO_5-crystal

Y_2SiO_5 is a host material that is often chosen for quantum information applications because of it's low nuclear magnetic moments. Spin flips in the crystal lattice close to a rare-earth ion is the limiting factor for the coherence time at low temperatures. The most common isotopes of silicon and oxygen have no nuclear spin. Yttrium has nuclear spin 1/2, but a low magnetic moment of -0.137 μ_N, where μ_N is the nuclear magneton [6].

Y_2SiO_5 is a monoclinic crystal, with eight Y_2SiO_5 molecules per cell. It is biaxial with a refractive index around 1.8. A

schematic picture of the crystal structure can be seen in Figure 2.9 where a,b and c denotes the crystal axis and D_1, D_2 and C_2 denotes the principal axis of refractive index.

A Y_2SiO_5 crystal can have two slightly different monoclinic structures, called X_1 and X_2. For annealing temperatures above 1190 °C the structure is X_2 [19]. This is the case for crystals grown with the Czochralski-method, where the melt is at temperatures around 2000 °C. All crystals used in this thesis are grown with this method.

rare-earth ions occupy the yttrium-sites in the crystal. There are two inequivalent yttrium-sites, which for an X_2 structured crystal has 6 or 7 surrounding oxygen ions respectively. They are simply called site 1 and site 2. Site 1 and site 2 give rise to different transition energies in the dopant ions [20].

There are $1.83 \cdot 10^{10}$ yttrium ions per μm^3 in the crystal [21], and the concentration of rare-earth ions is usually given relative to yttrium.

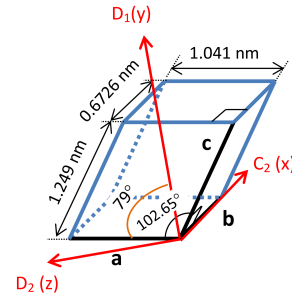

Figure 2.9. *A schematic image of the Y_2SiO_5 crystal unit cell. a, b and c are the crystal axis and D_1, D_2 and C_2 are the principal axis of refractive index. The figure is reprinted with permission from Reference [17].*

2.5.2 Eu:Y_2SiO_5 and Pr:Y_2SiO_5

Europium and Praseodymium are similar in many ways. They are both non-Kramers ions, and have non-degenerate crystal field levels. There is only one stable isotope of Pr, ^{141}Pr, and two of Eu, ^{151}Eu and ^{153}Eu with roughly equal abundance. All have nuclear spin 5/2, and they have no first order hyperfine splitting. The second order hyperfine interaction splits up each crystal field level into three doubly degenerate hyperfine levels. The two Eu isotopes have different hyperfine splittings, but the optical transitions overlap. Figure 2.10 shows a sketch of the relevant energy levels for Pr and ^{151}Eu in site 1.

The $^7F_0$ - $^5D_0$ transition in Eu, and the $^3H_4$ - $^1D_2$ transition in Pr both have long lifetimes and coherence times, and can be used for qubit manipulation. Some properties of these transitions as well as the hyperfine levels are summarized in Tables 2.1 and 2.2.

The $^7F_0$ - $^5D_0$ transition in Eu is exceptional in the way that it is a transition between two states with angular momentum J = 0, and hence there is no first order magnetic moment. This makes it even more insensitive to fluctuations in crystal field [6].

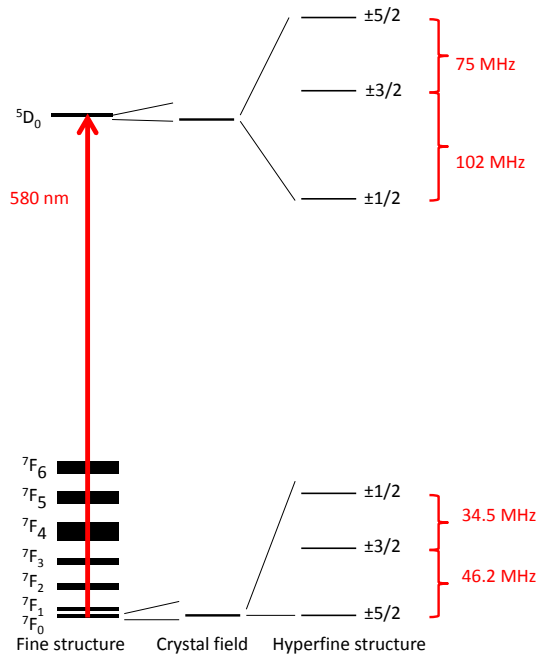

a) ^{151}Eu (site 1)

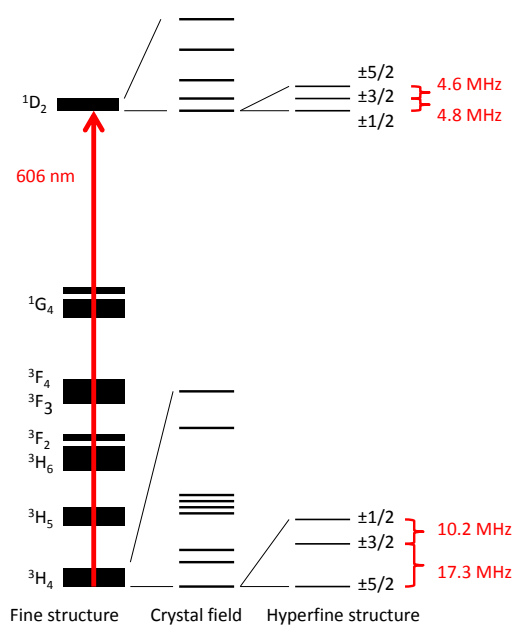

b) Pr (site 1)

Figure 2.10. *A sketch of the relevant energy levels for a)* ^{151}Eu *and b)* Pr *in site 1 of* Y_2SiO_5.

	Eu (site 1)	Eu (site 2)	Ref
λ_{vac}	579.879 nm	580.049 nm	[18]
T_1 optical	1.9 ms	1.6 ms	[18]
T_2 optical (B = 0 T)	1.5 ms	1.1 ms	[18]
T_2 optical (B = 10 mT)	2.6 ms	1.9 ms	[18]
T_1 hyperfine	$>$ 20 days	$>$ 20 days	[6]
T_2 hyperfine (B = 0 T)	19 ms (^{151}Eu)	-	[22]
T_2 hyperfine (B = 1.35 T)	6 hours* (^{151}Eu)	-	[23]

Table 2.1: Some properties of Eu:Y_2SiO_5 at liquid helium temperatures. If nothing else is stated the crystal contains roughly equal abundance of ^{151}Eu and ^{153}Eu. *To obtain this record coherence time the ZEFOS-technique was used [24].

	Pr (site 1)	Pr (site 2)	Ref
λ_{vac}	605.977 nm	607.934 nm	[25]
T_1 optical	164 μs	222 μs	[25]
T_2 optical (B = 0 T)	114 μs	318 μs	[25]
T_2 optical (B = 7.7 mT)	152 μs	377 μs	[25]
T_1 hyperfine	$\approx$ 100 s	$\approx$ 100s	[26]
T_1 hyperfine (B = 10 mT)	$>$ 1000 s	-	[27]
T_2 hyperfine (B $\approx$ 80 mT)	42 s*	-	[28]

Table 2.2: Some properties of Pr:Y_2SiO_5 at liquid helium temperatures. *To reach this coherence time several tricks were employed, ZEFOS [24], and dynamical decoupling sequences.

2.5.3 Ce:Y_2SiO_5

Cerium has only one valence electron as a trivalent ion, which makes the energy level structure very simple, see Figure 2.11. It also means that the only 4f-level of cerium is the electronic ground state, split up into two fine structure levels $^2F_{5/2}$ and $^2F_{7/2}$. There are no optical 4f-4f transitions. The separation between the ground state levels is about 2000 cm^{-1}, or 60 THz.

Cerium is a Kramers-ion with doubly degenerate crystal field levels. There are four cerium isotopes occurring naturally (^{140}Ce, ^{142}Ce, ^{138}Ce and ^{136}Ce), all without nuclear spin, and hence there is no hyperfine structure.

The transition of interest in Ce:Y_2SiO_5 is a 4f-5d transition. The 5d-level experience a strong crystal field, which dominates over the spin-orbit coupling. The transition also has strong and wide phonon wings. The zero-phonon transition to the lowest crystal field level occurs at 371 nm for site 1. For site 2 no zero-phonon line has been reported to my knowledge, but the low energy edge of the absorption is at longer wavelength, around 400 nm [20].

Since there are no intermediate levels between the lowest level

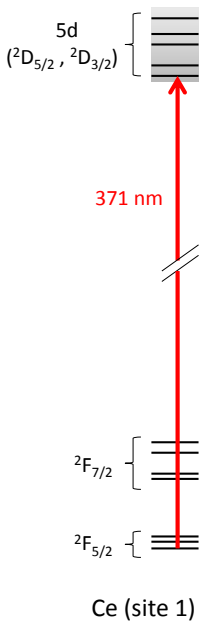

Figure 2.11. *A sketch of the relevant energy levels for Ce in site 1 of Y_2SiO_5.*

of the 5d-configuration and the electronic ground state, the 4f-5d transition can be cycled many times with continuous excitation. The lifetime of the 5d-state is 40 ns [19], which can give a good photon count rate and allow for single ion detection at short time scales [29].

Chapter 3

Quantum Computing

In 1982 Feynman suggested to build a quantum mechanical computer for the purpose of simulating quantum systems [30]. Since then it has been realized that some quantum algorithms, that take advantage of superpositions and entanglement, could solve some particular problems faster than any known classical algorithm. Examples are the famous Shor's algorithm for factorizing large prime numbers [31], and Grover's algorithm for searching large databases [32].

But a quantum computer isn't just a computer where the bits are replaced by qubits and transistors are replaced by entangling quantum gates. It is a concept that spans much more than that. A quantum computer is a controllable and scalable quantum system, for which many applications are yet to be discovered.

For physicists like myself a quantum computer is interesting from a very fundamental perspective. Quantum mechanics is the theory that predicts how things work on the very small scale, where the atoms are the main players. Quantum theory predicts some weird effects, very different from our everyday experience of the world. What if it would be possible to see these effects, in real life? To somehow scale them up to the macroscopic world where we live? The question is beautifully although slightly brutally expressed in the famous Schrödingers Cat thought experiment [33]. A cat is placed in a closed chamber with some poison and a quantum system gets to decide weather or not the poison is released to the cat. If we do not measure the quantum system, it will be in a superposition of it's two states. Does that imply that the cat is in a superposition between being dead and alive until we open the box?

We do not work with cats, but we do try to create a scalable quantum system. A system where we could potentially create large entangled states and see very real and direct consequences of

quantum mechanics. When we can see and control the effects of quantum mechanics we can also put them to use. This opens up a door to a whole range of new and unexplored technical possibilities and in the future there might very well be a range of devices working based on quantum mechanical principles.

3.1 Requirements for quantum computing

To actually build a quantum computer is not easy. Quantum states are very fragile and extreme control of the system and all noise that could interfere with it is necessary.

To build a quantum computer one needs:

(i) Controllable two-level quantum systems (qubits), with coherence times much longer than the gate operation time

(ii) A method to initialize the qubits to a known state

(iii) Interaction between qubits, a quantum transistor

(iv) A universal set of quantum gates

(v) Scalability, one qubit is not a computer, we need a lot of them

(vi) A method to read out each qubit

The items listed here are slightly modified versions of the requirements put up by DiVincenzo in 2000 [34]. The requirements should not be seen in a too stringent way, but more as a guide to what kind of physical system could be suitable.

A universal set of quantum gates can for example consist of arbitrary single qubit operations (arbitrary change of population and phase relation of the two states of a qubit), together with a controlled-NOT (cNOT) gate. A cNOT-gate, can act as a quantum transistor, where the state of one qubit is changed conditionally on another qubit state. This requires interaction between the qubits.

The major challenge when creating hardware for quantum computing lies in a conflict of interests: while fast manipulation and read out of qubits require strong interaction, a long coherence time require weak interactions with the noisy environment. Thus there is a need to switch on and off the qubit interactions, and to avoid interactions that are not controlled [35].

3.2 Quantum computing implementations

A number of different physical systems are currently being explored and developed for rudimentary quantum computing. Here

is a brief description of some examples, chosen to show the diversity of techniques used in quantum computing. A more detailed review can be found in [35].

3.2.1 Trapped ions

Single ions that are trapped by electric fields can be very well isolated from external sources of noise, and have very long coherence times, on the second time scale [36]. A qubit can be represented by two hyperfine levels of an ion. Ions interact with each other via motional modes in the trap [37].

The drawback of ion trapping is that it's rather demanding. It requires vacuum, electrodes for trapping and several stable lasers for laser cooling and manipulation. To scale the quantum system to many ions, there is a need to shuttle ions in and out of a trap, since only a limited number of ions can interact inside a single trap.

Among other things, ion traps have been used to run a quantum error correction protocol [38] and to create the first quantum byte with 8 entangled qubits [39]. In 2011 the record in number of entangled qubits was beaten once again, with 14 entangled ions in a trap [40].

3.2.2 Superconducting circuits

Quantum behaviour is associated with microscopic systems. Macroscopic ($\approx$ 100 μm) superconducting circuits can however also have quantized energy. A simple LC-circuit works like an oscillator and in combination with a so called Josephson junction, a thin insulating layer, the circuit can be made into a qubit.

Superconducting qubits need to be cooled down to extremely low temperatures, about 1 mK, to avoid thermal noise. The qubits are manipulated with microwave pulses and different qubits can be coupled capacitively or inductively, or via single microwave photons in a transmission line cavity. They can have coherence times of a few to tens of μs [41], but decoherence is still a limiting factor.

In 2009 two superconducting qubits were used to run Grovers algorithm [42].

D-Wave, a commercial system

In 2011 a spin-off company from the University of British Columbia called D-Wave released D-Wave One, which was claimed to be the first commercially available quantum computer in the world, with a register of 128 superconducting qubits. In 2013 D-Wave Two was released, with a 512 qubit register.

The D-Wave systems are not general purpose quantum computers, and do not work with the conventional gate operations.

They are so called adiabatic processors, designed to solve one particular class of problems. A problem is formulated in such a way that the ground state of a particular configuration of the quantum computer represents the solution. The quantum computer is then slowly driven to the desired configuration while it's kept in the ground state. The state can be read out, and a solution of the problem is found.

There has been quite a lot of controversy about weather the D-Wave processors are actually quantum computers and whether they can offer any speed up compared to classical computers. The issue is still not fully resolved. In May 2014 researchers from D-Wave together with Google, University of Southern California, Simon Fraser University and national Research Tomsk Polytechnic University published a paper containing proof of entanglement between the D-Wave qubits [43]. One month later a publication in Science concluded that the researchers couldn't see any speed up in D-Wave compared to a classical computer. Representatives from D-Wave however claim that the test problems were not chosen fairly [44].

3.2.3 NV-centres in diamond

A nitrogen-vacancy centre (NV-centre) in diamond is a defect of the crystal lattice consisting of a nitrogen atom substituting for a carbon atom with a neighbouring vacancy. The electron spin of the defect can be used as a qubit. Electronic spin states of NV-centres in pure diamond can have coherence times on the 1 ms time scale at room temperature [45]. Nearby nuclear spins, for example the nuclear spin of the nitrogen atom, can be coupled to the electronic spin levels. The nuclear spin states can have coherence times of seconds at cryogenic temperatures and allow for a qubit storage mechanism.

The spins of an NV-centre can be manipulated with microwaves, and read out by optical fluorescence detection [46].

One NV-centre can be used to create two qubits (nuclear and electronic spin). In 2012 such a two-qubit register was used to run Grover's algorithm at room temperature [47]. Entanglement between two different NV-centres has also been shown at room temperature [48].

3.2.4 Photons

A qubit can be represented by two polarization states of a photon, or sometimes also by the position, timing or phase of the photon.

A benefit of using photons for quantum computing is the long coherence times, without the need for vacuum or cooling procedures, since photons don't interact much with the environment.

They also offer processing and network capability in the same system.

The fact that photons don't interact much with the environment (and very little with each other) is also a drawback, since it is difficult to create two-qubit gates.

Five-photon entanglement has been shown [49] and in 2009 four single photon qubits were used to run a version of Shor's algorithm, to factorize 15 into it's prime numbers 3 and 5 [50].

3.2.5 Combining different systems

Each of the quantum systems mentioned above has benefits and drawbacks for quantum computing applications. It was already mentioned that there is a conflict of interest between having weak coupling to the environment for achieving long coherence times and strong coupling for gates and read out. For this reason it is interesting to combine different quantum systems to create a more versatile platform for quantum experiments.

One very interesting combination is to couple photons (flying qubits) to some kind of stationary qubits. Photons could be used to send quantum information in a network, and could create entanglement between different smaller quantum computers. That would lead to scalability, since several smaller quantum systems could be coupled to each other and form a large system. Entanglement between remote quantum systems using photons has been shown for ion traps [51] and NV-centres [52].

An option to tailor the interactions of a quantum system with the environment is to combine qubits with cavities. This has been done with several types of cavities and several types of quantum systems, for example quantum dots [53], NV-centres [54], atoms [55] , superconducting qubits [56] and rare-earth ions [57].

Combining systems offer more degrees of freedom for quantum computing, but to the price of increased complexity and resources needed.

3.3 Rare-earth quantum computing

This thesis concerns a quantum computing scheme using rare-earth ions doped into a crystal. Rare-earth ions have very suitable properties for quantum information applications such as very long coherence times and suitable energy levels for manipulation and storage of quantum states. When doped into a crystal the ions are stationary, but still keep their good coherence properties and sharp atom-like transitions.

To use hole burning and narrow spectral peaks in rare-earth-ion-doped crystals for quantum computing was suggested in 1999 by Pryde, Sellars and Manson, Canberra [58]. A detailed description of a quantum computing scheme was later put together by

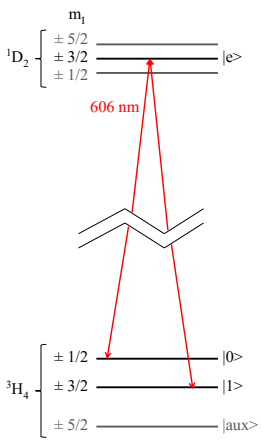

Figure 3.1. *A schematic showing the hyperfine levels of Pr used for qubit states $|0\rangle$ and $|1\rangle$ and the optical transition used for qubit manipulation.*

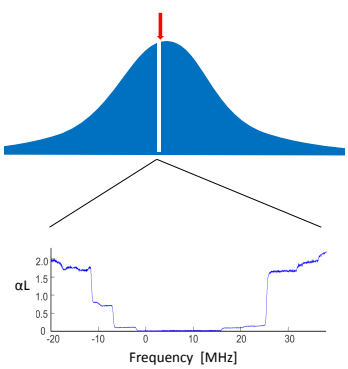

Figure 3.2. *A spectral pit is burnt within the inhomogeneous absorption profile of the Pr ions. The lower graph shows experimental data [62].*

Ohlsson, Mohana and Kröll, Lund [59]. The scheme has been pursued experimentally by both groups. Very similar suggestions has also been put forward by for example Ichimura [60] and Hemmer [61].

3.3.1 Creation and characterization of one ensemble qubit

In the ensemble approach one qubit is represented by two hyperfine levels in an ensemble of rare-earth ions. The qubit is defined by it's unique absorption frequency within the inhomogeneous line of an optical transition, for example the $^3H_4$ - $^1D_2$ transition in Pr, see Figure 3.1.

To create and initialize a qubit, spectral hole burning is used. A wide spectral hole, a so called spectral pit, is created within the inhomogeneous absorption line of the optical transition by applying a sequence of frequency scanned pulses, see Figure 3.2. By applying a pulse at a specific frequency outside the pit, an ensemble of ions can be burnt back into the pit, all sitting in e.g. their m_I=1/2 ground state, which we can call $|0\rangle$. Three peaks will appear in the absorption spectrum, inside the spectral pit, corresponding to the three possible transitions to the excited state hyperfine levels, see Figure 3.3 a). At this stage we have created one qubit containing about 10^9 ions, initialized to it's $|0\rangle$ ground state.

After initialization the qubit can be put into an arbitrary superposition of the ground state hyperfine levels labelled $|0\rangle$ and $|1\rangle$, by applying optical pulses containing two frequency components. The state can be read out by straight forward absorption spectroscopy. The result of the readout for three different states are shown in Figure 3.3.

Quantum state tomography of a rare-earth ensemble qubit shows single qubit transition fidelities above 90% [62] [63].

3.3.2 Two-qubit gates

Rare-earth ions in a crystal have a static electric dipole moment, which is dependent on the electronic state of the ions. When an ion is excited from the ground state to an optically excited state, the static dipole moment will change. The resulting change in electric field in the close vicinity of the excited ion can shift the transition frequency of other ions by many linewidths, causing them to go out of resonance with the laser. The phenomenon is called dipole blockade, since it blocks close by ions from being excited.

The induced shift of a transition in ion (i) due to excitation of another ion (j) is:

$$\Delta\nu = \eta(0)\frac{\Delta\mu_i\Delta\mu_j\kappa}{4\pi h\epsilon_0 r_{ij}^3}. \tag{3.1}$$

Ion in site 1	$\Delta\mu$	Ref
Pr ($^3H_4$ - $^1D_2$)	$2.4 \cdot 10^{-31}$ Cm	[66]
Eu ($^7F_0$ - $^5D_0$)	$7.7 \cdot 10^{-32}$ Cm	[66]
Ce ($^2F_5/2$ - 5d)	$9.6 \cdot 10^{-30}$ Cm	Paper **III**

Table 3.1: The change of static electric dipole moment between the ground and excited state of the ions used in this thesis.

$\eta(0) = 1.28$ is a factor taking into account near field effects inside the crystal [64], $\Delta\mu$ is the difference in static electric dipole moment between the ground state and the optically excited state of an ion, κ is in the order of 1 and accounts for the relative orientation of the dipoles, and r_{ij} is the distance between the ions [65].

Table 3.1 lists the change of static electric dipole moment $\Delta\mu$ between the ground and excited state of the ions relevant for this thesis.

Two praseodymium ions sitting 1 nm apart (which is roughly true for nearest neighbours) shift each other by about 1 GHz, and 10 nm apart by 1 MHz, both which are much larger than the 1 kHz homogeneous linewidth.

Say that we create a superposition $c_0 |0\rangle + c_1 |1\rangle$ in one ion, called qubit$_A$. We then excite qubit$_A$ from the $|0\rangle$-state to the optically excited state, which will create the superposition $c_0 |e\rangle + c_1 |1\rangle$. A nearby ion, qubit$_B$ is initialized to the $|0\rangle$-state. It will be shifted out of resonance with the laser (at it's own unique absorption frequency within the inhomogeneous line) only if qubit$_A$ is excited. We then apply a pulse to bring qubit$_B$ to the excited state, which only has an effect if it qubit$_B$ is not shifted out of resonance. This creates an entangled state between qubit$_A$ and qubit$_B$, see Equation (3.2):

$$c_0 |e\rangle_A |0\rangle_B + c_1 |1\rangle_A |e\rangle_B \tag{3.2}$$

Adding a couple of more pulses to the manipulation of qubit$_B$ creates a cNOT-gate, where qubit$_B$ is switched on the condition that qubit$_A$ is in state $|1\rangle$.

The argument above was given for single ion qubits. The same mechanism works for ensembles, but a distillation process must make sure that all ions in ensemble qubit$_A$ interacts with at least one ion in ensemble qubit$_B$. The ions that do not interact can be pumped away to a third hyperfine level called $|aux\rangle$, not used in computations. This distillation process has been shown to work, but reduces the number of ions in each ensemble qubit [67].

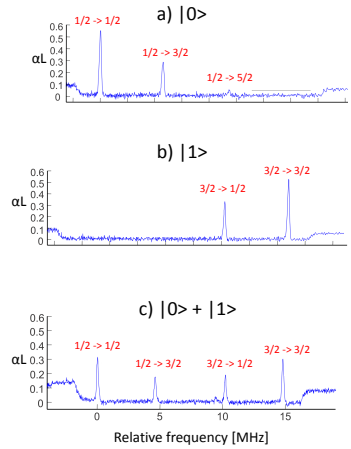

Figure 3.3. *Three different quantum states as shown in absorption spectroscopy. The figures shows absorption versus frequency relative to the 1/2-1/2 transition [62].*

3.3.3 Scalability

In the previous section it was mentioned that using ensemble qubits for two-qubit gates require a distillation process where ions in each qubit are chosen, so that they all interact strongly with at least one ion in the other qubit. As the qubit register grows from two to many qubits this process scales very badly for reasonable dopant concentrations; the more qubits we want to couple, the fewer ions there will be in each qubit, until the absorption is so weak that we can no longer read out the state of the qubits.

One can imagine a few different solutions to this. One way to look at it, is to conclude that the dopant concentration is too small. If we could work with a crystal of very high doping more ions would sit closer to each other and the scaling would not be as bad.

Another approach is to say that the detection method is not sensitive enough. The distillation process described above could be carried out until there is only one ion in each qubit, provided that we had the ability to read out the state of a single ion. For a single instance quantum computing scheme, where each qubit is represented by a single ion in a crystal, the scaling properties are much better. It is then only necessary to find a single chain of interacting ions, all with different absorption frequencies.

3.3.4 Stochiometric crystals - The Canberra scheme

The group of Matthew Sellars in Canberra has developed a scheme for quantum computing using stoichiometric crystals [68].

A stoichiometric crystal is a crystal with 100% doping, or looking at it another way; a crystal with no doping where the active ion is a ligand ion of the crystal. An example of this is $EuCl_3{\cdot}6H_2O$, where europium is the active ion. In a crystal like this, every qubit ion has other qubit ions in the close vicinity which they interact strongly with.

By doping a stoichiometric crystal with another ion, some of the active ions will be shifted in frequency by the distortion of the crystal lattice caused by the dopant ions. The shift depends on the relative distance between a dopant and the active ion. So called satellite lines appear outside the inhomogeneously broadened absorption profile of the active ion. One specific satellite line can be identified as a particular configuration of dopant ion and active ion [69]. Thus, each satellite line is an ensemble of europium ions in identical sites, with identical neighbours, and can be used as a qubit. Another satellite line represents another site, also neighbouring to the dopant and hence also sitting spatially close to the ions of the first satellite line. The set of satellite lines (about 20 in $EuCl_3{\cdot}6H_2O$) can be used as a set of qubits, each containing mil-

lions of identical ions and all interacting strongly with each other [68].

3.3.5 Single instance quantum computing - The Lund scheme

In Lund we have focused our attention on improving the detection method to be able to read out the state of single ions, and work with single ion qubits.

The first ever conclusive optical detection of single rare-earth ions in a crystal was done by Kolesov et. al. in 2012 [70]. Single praseodymium ions were detected in nano-crystals and on the surface of a bulk crystal at room temperature. The bulk crystal consisted of undoped high purity YAG, with only small traces of praseodymium to get low enough concentration to enable spatial separation of ions with a confocal microscope. The praseodymium ions were excited to the 5d-state by a two-photon process and fluorescence from the short-lived 5d-state was collected.

In 2013 the same group detected single cerium ions in a similar way, on the surface of a high purity YAG crystal at room temperature, by detecting fluorescence emitted from the 5d-state [71].

Later the same year Utikal et. al. detected and manipulated single praseodymium ions in Y_2SiO_5 nano-crystals at liquid helium temperatures [72]. This time a 4f-4f transition was used for detection, which allowed for spectral separation of individual ions. Since the lifetime of the excited state is long, the signal was very low, only about 60 photons per second were collected. State sensitive readout was achieved with repeated state preparation and readout cycles. In 1000 cycles about 10 photon counts were detected, which was enough to discriminate a populated hyperfine level from an unpopulated one.

The most sensitive way to optically detect a signal from a single ion is by fluorescence microscopy. There are however several complications when detecting fluorescence from the qubit ion. First of all, the excited state lifetime is very long to enable high fidelity gate operations. That means that we will get a very weak fluorescence signal. It could however be the case that there is another energy level available with a shorter lifetime, for example a 5d-level. But as the qubit ion decays, it has a probability to end up in any of the ground state hyperfine levels ($|0\rangle$ or $|1\rangle$), thus we immediately lose the information we are trying to read out. Single shot read out is then not possible, but the computation would have to be repeated multiple times to get a reliable result. For a single computation readout a non-demolition measurement is needed, to discriminate the qubit states with high fidelity.

One way to solve the problem is to introduce an extra degree of freedom; to couple the qubit ion to another ion, with more suitable properties for single ion detection.

Cerium is an ion that can easily be doped into the same type of crystal as Pr and Eu that are used as qubits. The simple energy level structure of cerium with only a ground state and a 5d-level, allows for cycling the transition with a high fluorescence yield. The lifetime of the 5d-level is 40 ns [19], short enough to generate about 20 000 photons during the excited state lifetime of a Eu ion.

The qubit ion can be coupled to the cerium ion via the dipole blockade effect, with exactly the same mechanism described previously for two-qubit gates. The qubit ion is excited with a pulse on the $|0\rangle$ to $|e\rangle$ transition. The cerium ions is then excited continuously. By the dipole blockade effect, the cerium ion will be shifted out of resonance with the laser on the condition that the qubit was in state $|0\rangle$, and there will be no fluorescence generated. On the other hand if the qubit was in state $|1\rangle$ it was never brought to the excited state and there is fluorescence. In this way the cerium ion can act like a state sensitive probe of the qubit ion [73].

To obtain good enough qubit properties all qubit operations and readout must be performed at liquid helium temperatures. The qubit ions, and hence also the readout ion, should preferably sit a small distance below the surface of the crystal to ensure that the surface environment does not disturb the coherence properties of the ions.

3.3.6 The aim of this thesis

The aim of this thesis has been to investigate the possibility to use cerium as a state sensitive probe for a qubit ion. The qubit ions of choice have been praseodymium and europium, because of their long coherence times and suitable energy level structure.

The task involves investigating the static dipole interaction between cerium and a qubit ion, as well as other ion-ion interactions that could play a role for the scheme.

The ultimate goal of this work has been to detect a single cerium ion in a situation where gates could be implemented and the cerium ion could be used for read out of actual qubit states. This goal has not been achieved to date, but is believed to be within reach.

Chapter 4

Dye laser system for qubit manipulation

To manipulate the fragile quantum states of a quantum computer there is a need for good lasers. Coherence is a crucial property of a quantum computer. It was mentioned in Section 2.4 that by coherence we often mean the ability to predict and keep our laser tuned to the phase of a qubit, in this case a rare-earth ion. If the laser has random phase shifts the coherence of the system will be limited by the laser. Thus, we want our laser to be at least as stable as the ions, which means that it should have a linewidth at least as narrow as the homogeneous linewidth of the transition it is targeting.

Laser frequency stabilization is a field of it's own, with applications not only within quantum information, but also for example in optical clocks [74] and gravitational wave detectors [75]. Today, the most stable laser system in the world has a linewidth of 40 mHz over a few seconds, which should be compared to the laser frequency of 200 THz and gives a fractional stability of 10^{-16} [76]. To achieve this extreme laser stability a very stable reference, for example a cavity with an extremely stable length, is necessary.

The technique most commonly used for stabilizing the frequency of a laser to a stable reference is Pound-Drever-Hall locking [77, 78]. Before describing the laser systems used in this thesis I will give an introduction to the Pound-Drever-Hall technique.

4.1 Pound-Drever-Hall laser stabilization

Pound-Drever-Hall stabilization [77, 78] is a widely used technique for ultra stable lasers. It can be used to stabilize a laser to different types of frequency references, like for example a cavity, a spectral hole or an absorption line.

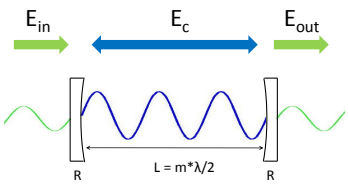

Figure 4.1. *A matched Fabry-Perot cavity on resonance. All the incident light is transmitted through the cavity.*

Here I will describe the Pound-Drever-Hall technique using a Fabry-Perot cavity as a frequency reference. An advantage of the Pound-Drever-Hall technique is that the speed of the feedback system is not limited by the response time of the reference cavity. Thus, high finesse cavities can be used without trade off. This is not the case when for example locking to the transmission line of a cavity.

4.1.1 Transmission and reflection from a Fabry-Perot cavity

A Fabry-Perot cavity consists of two mirrors with reflectivities R_1 and R_2 facing each other. If we couple light into the cavity the light can bounce back and forth between the mirrors and interfere constructively if the length of the cavity L, is a multiple of half the wavelength of the light, $m * \frac{\lambda}{2}$.

In a matched cavity the reflectivity of the first mirror is the same as the reflectivity of the second mirror, $R_1 = R_2 = R$, so that equally much light leaks out in the forward as in the backward direction. An incident light wave for which the resonance condition holds, and which does not experience any losses inside the cavity, is completely transmitted through the cavity, as illustrated in Figure 4.1. At a first glance this is not obvious; as a light wave hits the first mirror a fraction R, which is usually very high, is reflected straight back. How can then everything be transmitted?

The key is in the build up of a strong field inside the cavity. As we turn on our light field it is true that a big part, say 99.99%, of the power is reflected, and only 0.01% of the light enters the cavity. But also 0.01% of the power inside the cavity leaks out in the backward direction, and overlaps with the light that is directly reflected from the first cavity mirror. The field that leaks out from the cavity is 180° out of phase with the directly reflected light and cancels part of it. More and more light will enter the cavity, in phase with the field that is already there. This will happen until the power inside the cavity is so high that the 0.01% that leaks out in the backward direction can completely cancel the directly reflected light. At the same time, the 0.01% leaking out in the forward direction corresponds exactly to the incident power on the cavity. Hence, the reflection is zero and the transmission is 100%.

The time it takes for this to happen is called the cavity build up time, τ_c, and depends on the mirror reflectivity R and the length of the cavity L. If we would suddenly switch off the light source it would also take the same amount of time for all the light to leak out from the cavity. More exactly the intensity coming out of the cavity would decay as $I = I_0 e^{-t/\tau_c}$. The build up time is directly related to the frequency linewidth of the cavity, as in Equation (4.1):

$$\nu_c = \frac{1}{2\pi\tau_c}. \tag{4.1}$$

4.1.2 Cavity response to laser noise

Imagine that we have built up a strong field in the cavity, and that the phase of the laser suddenly changes a little bit. If this happens faster than τ_c, the field inside the cavity will not have time to change, and the field that leaks out from the cavity will still have the same phase. But the directly reflected light will now have a slightly different phase, and the two will not cancel completely. There will be a small reflected power from the cavity, and the phase of this reflected beam depends on if the laser drifted up or down in phase compared to the cavity field, see Figure 4.2. For small errors there is a 180° phase difference of the signal depending on if the phase drifted up or down. Thus, the power and phase of the reflected beam provides the magnitude and sign of an error signal for locking the phase of the laser to a delayed version of itself; the cavity field.

Instead imagine that the frequency of the laser drifts on a slower time scale, longer than τ_c, so that the cavity field has time to follow the change. The laser will then drift away from the cavity resonance, and the cavity length is no longer an exact multiple of half the wavelength. The field that leaks out of the cavity will then be slightly shifted in phase compared to the directly reflected beam, and again they don't cancel and we get some reflected power. The power and phase of the reflected beam act like an error signal for the laser frequency, to keep it locked to the cavity resonance.

Thus, the reflected beam from a Fabry-Perot cavity provides an error signal for the laser phase on short time scales, and an error signal for the laser frequency on longer time scales. This is in fact the basis of Pound-Drever-Hall locking [79].

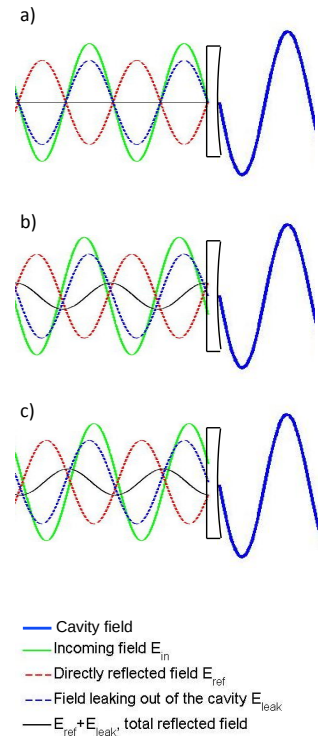

Figure 4.2. *The reflected amplitude from a Fabry-Perot cavity is the sum of the field leaking out from the cavity, and the directly reflected incident field. In a) the incident field is exactly matched to the cavity resonance, and nothing is reflected. In b) there is a negative phase shift of the incident field compared to the cavity field (the incident field is delayed slightly), and some light is reflected off the cavity. In c) there is a positive phase shift of the incident light compared to the cavity field.*

4.1.3 Generating the error signal

The power and phase of the cavity reflection contains information about the phase and frequency error of the laser. To use this error signal for laser feedback, we want to convert it to a DC-signal containing the same information.

To determine the phase of the light that is reflected from the cavity we need to convert it to a lower frequency. The way to do this is to overlap it with a reference beam that has a slightly different frequency (heterodyning). The overlapped beams will beat at the difference frequency. The phase of this beating signal will depend on the relative phase of the cavity reflection and the reference beam. To get a deterministic phase of the beating signal,

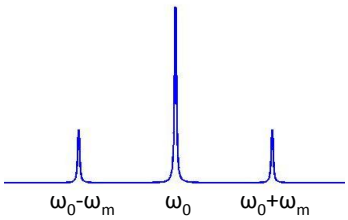

Figure 4.3. *Sending the laser beam through the EOM creates sidebands in frequency, shifted from the carrier by the EOM modulation frequency ω_m.*

the reference beam needs to be phase locked to the laser beam that enters the cavity. The easiest way to achieve this is to use the laser beam itself as a reference.

To create our frequency shifted reference beam we send the laser beam through a phase modulator, for example an electro-optic modulator (EOM), before it reaches the cavity. If we modulate the phase of the laser beam in a sinusoidal way with a small amount, it can be described as a sum of three overlapped beams; the unmodulated carrier and two sidebands shifted by plus and minus the modulation frequency respectively, see Equation (4.2) and Figure 4.3.

$$\begin{aligned} E_{mod}(t) =& E_0 e^{-i\omega_0 t - im\sin(\omega_m t)} \\ \approx& J_0(m) E_0 e^{-i\omega_0 t} \\ &+ J_1(m) E_0 e^{-i(\omega_0+\omega_m)t} \\ &- J_1(m) E_0 e^{-i(\omega_0-\omega_m)t} \\ &+ \text{higher order terms} \end{aligned} \tag{4.2}$$

Here m is the modulation depth which describes the strength of the modulation, $J_n(m)$ are Bessel functions and ω_m is the modulation frequency.

If the modulation frequency is much larger than the cavity linewidth, the sidebands will always be completely reflected off the cavity, while the carrier will couple into the cavity. Thus, the reflection from the cavity consists of three overlapped beams; the reflected carrier that contains information of the phase and frequency error, and the two sidebands that are shifted in frequency and can act as references.

The reflection from the cavity consists of three frequency components, a carrier and two sidebands. When the reflected light power is measured by a photo detector the signal will beat at the modulation frequency ω_m (carrier-sideband) and also on twice the modulation frequency $2\omega_m$ (sideband1-sideband2). The signal at the modulation frequency ω_m can then be picked out from the rest by a mixer with a reference signal from the same source (and hence phase locked to) the RF-signal used to modulate the laser.

The output of a mixer is the product of it's two inputs. Sending in two sinusoidal signals in phase with each other we get:

$$\begin{aligned} &\sin(\omega_{ref} t)\sin(\omega_m t) \\ =& \frac{1}{2}\cos((\omega_{ref}-\omega_m)t) - \frac{1}{2}\cos((\omega_{ref}+\omega_m)t). \end{aligned} \tag{4.3}$$

The reference signal and the beating signal from the cavity reflection have the same frequency ($\omega_{ref} = \omega_m$), which means that we get one DC-signal and one signal at twice the modulation

frequency. We are only interested in the DC-signal, which can be selected with a low-pass filter. This DC-signal is positive if the reference signal and the error signal are in phase. If they are completely out of phase it is negative.

Thus, with an appropriate choice of phase in the reference signal the DC-signal generated by the mixer depends both on the phase and power of the beam that is reflected off the cavity. With the right amplification it can drive the laser up or down in frequency to compensate for the error detected by the cavity.

To summarize; conversion of the cavity reflection into a DC-signal that can be fed back to the laser is done in two steps.

(i) The reflected optical beam is converted to a lower frequency (RF). This is done by beating it with a reference beam, for example the sidebands of the laser beam.

(ii) The RF signal is converted to a DC signal by mixing it with a reference signal with a stable phase relative to the modulation of the laser (e.g. from the same source).

Figure 4.4 is a sketch showing a vary basic Pound-Drever-Hall set-up.

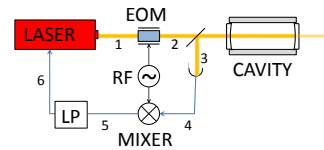

Figure 4.4. *A very simple Pound-Drever-Hall laser stabilization set-up. The laser beam (1) is phase modulated in an EOM and two sidebands are added to the laser frequency (2). The sidebands are always reflected from the cavity, and beats together with the reflected carrier containing information on the phase and frequency error of the laser (3). The beating signal is detected with a photo detector (4). The beating signal is transformed to a DC-signal (5) in a mixer. The signal from the mixer is low-pass filtered and fed back to the laser to correct the frequency or phase error (6). In a real set-up several additional optical and electronic components are required, such as an isolator, lenses, polarizers, amplifiers etc.*

4.2 Dye laser system

The $^3H_4$-$^1D_2$ transition in Pr:Y_2SiO_5 has a homogeneous linewidth of about 1 kHz. The same laser linewidth was previously reached by locking our dye laser to a spectral hole in a Pr crystal using the Pound-Drever-Hall technique [80]. Locking to a Pr crystal however means that we can only lock at the Pr wavelength of 606 nm. Since one goal was to use Eu, with even better coherence properties than Pr, for some experiments, there was a need for a system with larger tunability. For that reason the dye laser stabilization system was rebuilt during 2011 and the start of 2012. Instead of a spectral hole, the laser was locked to an ultra stable Fabry-Perot cavity. The $^7F_0$-$^5D_0$ transition of Eu has a homogeneous linewidth around 100 Hz, and the design goal for laser stability was set to 10 Hz. This work was initialized as a master thesis project by Adam Wiman [81], and continued as a joint venture for the Ph.D.-students in the group. Here I will present an overview of the system with a special focus on my contributions.

4.2.1 Dye laser

The dye laser is a Coherent 699-21 with some modified parts for increased stability. The lasing medium of a dye laser is a liquid dye jet, in this case Rhodamine 6G dissolved in ethylene glycol. The dye is pumped by a Verdi-V6 solid state laser giving 6W at

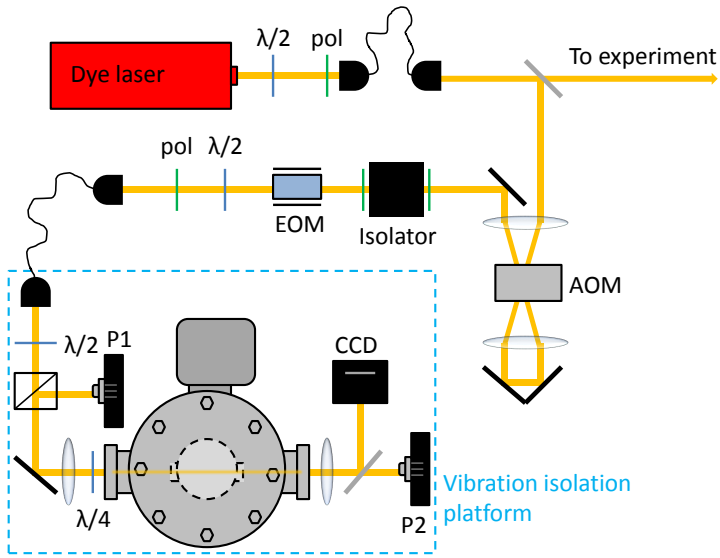

Figure 4.5. *The vital components of the dye laser stabilization system. P1 and P2 are home built photo detectors. The reference cavity is sitting inside a vacuum chamber on a vibration isolation platform. Further details are presented in the text.*

532 nm. The dye laser is tunable from about 570 nm to 635 nm with this dye, giving 600 mW at the Pr wavelength of 606 nm and about 1 W at the Eu wavelength of 580 nm.

The linewidth of the laser is limited by fluctuations in the dye stream. The liquid dye is cooled to a stable temperature around 9°C by a feedback loop heat exchanger and it is pumped by a Micropump GJN25-JF1SJ at a pressure of 4.2 bar. The quality of the dye pump has turned out to be important for laser stability. When the laser works poorly the reason has frequently been degradation of the dye pump leading to fluctuations in the dye stream.

The dye laser contains an external invar cavity used for stabilizing the frequency to a linewidth of 1 MHz. The laser can be scanned 30 GHz mode hop free from the control box, by tilting a galvo-mounted glass plate sitting in Brewster angle in the laser cavity.

4.2.2 Stabilization system optics

The dye laser is further stabilized by Pound-Drever-Hall locking to an ultra stable cavity, with the aim to reach a linewidth around 10 Hz.

Figure 4.5 shows a sketch of the important optical components of the stabilization system. The laser beam is sent through a polarization preserving single mode optical fibre to obtain a better spatial profile and beam stability.

A double pass AOM (Brimrose GPF-1125-750-590) giving a tuning range of 1.5 GHz is used to shift the frequency of the laser beam to match the cavity resonance.

An optical isolator is placed in the beam to avoid back-reflected light from the cavity to reach the laser. It consists of a Faraday rotator, which rotates the polarization 45 degrees, with polarizers on each side. Since the direction in which the polarization is rotated is defined by the magnetic field of the Faraday rotator, light propagating backwards will be rotated 90° in total and will be blocked by the first polarizer.

The EOM (New Focus 4002) is driven by a direct digital synthesizer (DDS) at 50 MHz to put sidebands 50 MHz on each side of the laser frequency. To amplify the signal from the DDS, a resonance tank is built and attached to the EOM. A polarization preserving single mode fibre after the EOM assures that the spatial mode of the laser is good enough to couple well to the TEM_{00}-mode of the cavity and brings the beam to the stabilization platform where the cavity sits.

The light that is reflected off the cavity is picked out by placing a quarter wave plate and a polarizing beam splitter in front of the cavity. The quarter wave plate converts the initially linearly polarized light into circularly polarized. Upon reflection at the cavity the direction of circular polarization is changed (from σ^+ to σ^-). The reflected light passes through the quarter wave plate once more and the polarization is turned 90 degrees in total compared to the incoming light. The beam is reflected off the polarizing beam splitter and detected with a photo detector (P1).

The cavity spacer used as a reference is a 5 cm in diameter spherical piece of ultra low expansion (ULE) glass. Two high reflectivity mirrors are optically contacted to the spacer, creating a cavity with a free spectral range of 3 GHz. The ring down (decay) time of the cavity was measured to 6.5 μs which gives a linewidth of 24 kHz.

The cavity is clamped to a holder at an angle which makes the length between the mirrors insensitive to the pressure from the clamp to first order [82]. The cavity is placed inside a three-layer temperature shield, to reduce the influence of heat radiation from the environment. The outer part of the shield is stabilized to a specific temperature where the first order thermal expansion of the ULE glass is zero. The cavity and shield assembly is put into a vacuum chamber that is kept at a pressure of $4 \cdot 10^{-9}$ mbar by an ion pump. The chamber is placed on a platform for active vibration cancellation.

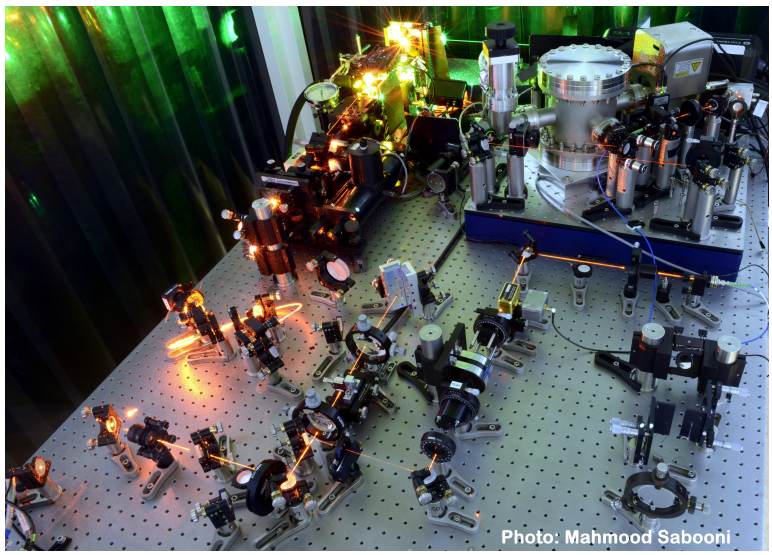

Figure 4.6. *A picture of the dye laser stabilization set-up. The dye laser is visible in the upper left corner. The vibration isolation platform with the vacuum chamber containing the cavity is standing in the upper right corner.*

A photo detector (P2) is placed after the cavity to measure the transmitted power. A beam splitter also sends part of the transmitted beam to a camera, where the spatial mode of the cavity resonance can be analysed.

Figure 4.6 shows how the system looks like in real life.

4.2.3 Low noise photo detectors

To obtain a laser linewidth as narrow as 10 Hz it is important not to introduce additional noise in the error signal. The photo detector for measuring the reflected light from the cavity (P1 in Figure 4.5) has to be fast enough to detect a 50 MHz beating signal (sideband-carrier) without distortions. At the same time it should ideally have low enough noise to obtain a shot noise limited error signal. The photo detectors used in the dye stabilization system were home built to obtain as good properties as possible. For light levels of 20-30 μW a photo diode in combination with a transimpedance amplifier is the most convenient choice.

The photo detector for the error signal was home built by combining a low capacitance photo diode (Hamamatsu S9055) with a low noise transimpendance amplifier evaluation circuit board. This transimpedance amplifier (MAX3658AETA) consists of a operational amplifier with negative feedback, a voltage amplifier stage,

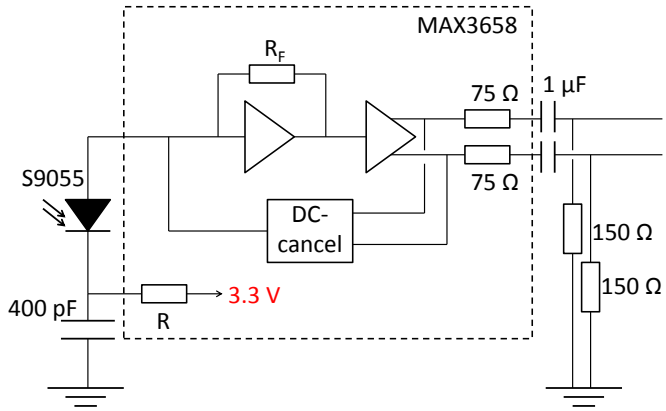

Figure 4.7. *A simplified circuit for detector P1, after modification of the evaluation board MAX3658A.*

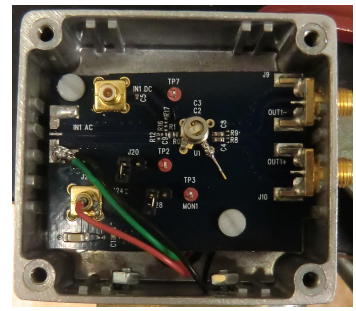

Figure 4.8. *The error detector (P1). A photo diode (S9055) is soldered directly onto a circuit board (MAX3658A evaluation board). The board is mounted in an aluminium casing and the signal is fed out via SMA-connectors.*

a DC cancellation circuit and some filter stages, on the same chip. The evaluation board was modified to enable current input from the photo diode, with a reverse voltage of about 1V. A simplified version of the resulting circuit is drawn in Figure 4.7. The photo diode was soldered directly onto the circuit board surface solder points to avoid increasing the capacitance more than necessary by using cables, see Figure 4.8. Capacitance at the input of the amplifier slows down the circuit and amplifies the high frequency voltage noise.

Some measured properties of the detector are summarized in Table 4.1. For power levels above 17 μW the shot noise from the signal is larger than the inherent detector noise, see Figure 4.9. The input referred noise of this detector is better than any photo detector with similar bandwidth we could find on the market, except some avalanche photo diodes (APD's) which require a high voltage supply.

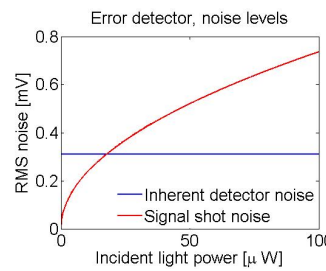

Figure 4.9. *The inherent noise of the error detector (P1) and the shot noise from the incident light. For light levels above 17 μW the shot noise is larger than the detector noise.*

There is also a need for a detector placed after the cavity to monitor the transmission of the cavity (P2 in Figure 4.5). This detector will be used to find the resonance of the cavity, measure the ring-down time of the cavity and monitor the transmission when the laser is locked. This detector was home built in the same manner as the error detector, but with lower requirements on speed and with higher gain. A photo diode with a larger chip (S5971) was soldered directly onto a modified transimpedance amplifier evaluation board (THS4631 DDA EVM). A drawing of the resulting circuit is shown in Figure 4.10. The diode is in this case DC coupled and has a reverse voltage that can be switched between 0 V (no reverse voltage), 9 V and 15 V. Some properties of the

P1: Error detector (cavity reflection)	
Diode chip size	100 μm
Diode capacitance (1V reverse voltage)	0.5 pF
Diode responsivity (606 nm)	0.35 A/W
Diode dark current (1V reverse voltage)	1 pA
Transimpedance gain (at 50 MHz)	11 kΩ
Bandwidth	400 MHz
Noise level, dark detector	0.3 mV RMS
Noise, input referred	4.2 pW/$\sqrt{\text{Hz}}$

Table 4.1: Some specifications and measured properties of the home built error detector.

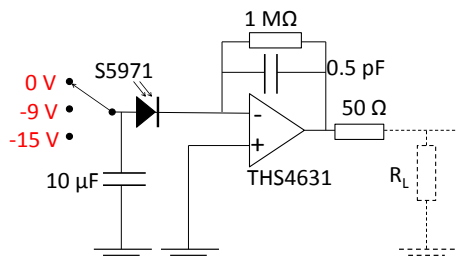

Figure 4.10. *The circuit for detector P2, after modification of the evaluation board THS4631 DDA EVM.*

detector are summarized in Table 4.2.

P2: Transmission detector	
Diode chip size	1.2 mm
Diode capacitance (9V reverse voltage)	3 pF
Diode responsivity (606 nm)	0.35 A/W
Max transimpendance gain (in a 50Ω load)	500 kΩ
Bandwidth	3 MHz
Noise level, dark detector (9V reverse voltage)	2.5 mV RMS
Noise, input referred (9V reverse voltage)	8.2 pW/$\sqrt{\text{Hz}}$

Table 4.2: Some specifications and measured properties of the home built transmission detector.

4.2.4 Feedback actuators

The error signal generated from the cavity should be fed back to actuators in the dye laser to change it's frequency. The commercial dye laser is already equipped with one stabilization system, with

an external invar cavity as a reference. The laser is locked to the slope of a transmission fringe from this cavity. The feedback signal is in this case sent to a piezo electric stack behind one mirror in the laser cavity, to change the length of the cavity. The piezo has a limited bandwidth of about 1 kHz, and this is too slow to reach a laser linewidth of 10 Hz.

For that reason an EOM (Linos PM25) is placed inside the laser cavity. Changing the voltage over the EOM will change it's refractive index and hence the optical length of the cavity. The EOM responds very fast to an applied voltage, and the feedback speed will be limited by the time it takes for a frequency or phase error to propagate from the laser, through all optics to the error detector and through all electronics to the EOM in the laser (the delay time in the feedback loop). The measured self oscillation frequency of the feedback system is 3 MHz, which is the frequency where the phase delay in the feedback loop is 180°. The time it takes for an error to propagate through the system and for a correction signal to be picked up by the laser is then half a self oscillation cycle, in this case 170 ns. The bandwidth of the feedback loop also depends on the gain setting of the system. To avoid self oscillation the system must be damped at 3 MHz, and the actual bandwidth where the gain is larger than one is then slightly lower than 3 MHz.

The piezo mounted mirror in the cavity can be used to compensate for slower errors in the laser frequency, that occur on the few ms time scale. There is also a galvo controlled glass plate in the laser cavity, sitting in Brewster angle, which is used for scanning the laser. This can be used to compensate for slow but large drifts in laser frequency, with a response time of about 100 ms.

In summary there are three actuators in the laser cavity, a fast EOM, a slower piezo mounted mirror and a very slow galvo mounted Brewster plate. They are used in parallel to compensate for fast phase fluctuations and slow frequency drift of the laser. To feed back the error signal from the locking cavity to the actuators in the laser an analogue as well as a digital control system is used.

4.2.5 Feedback electronics

The electronics for the dye laser stabilization system was home built for the previous laser stabilization system, where the dye laser was locked to a spectral hole in a crystal [80]. It was not re-built during my time as a Ph.D.-student. Despite this I spent several months tracking down the error signal through the electronic boxes to find the cause to why the laser did not lock as it should. Finally a broken potentiometer was found on one of the many circuit boards. As it was replaced, the new laser system locked for the first time in the summer of 2012.

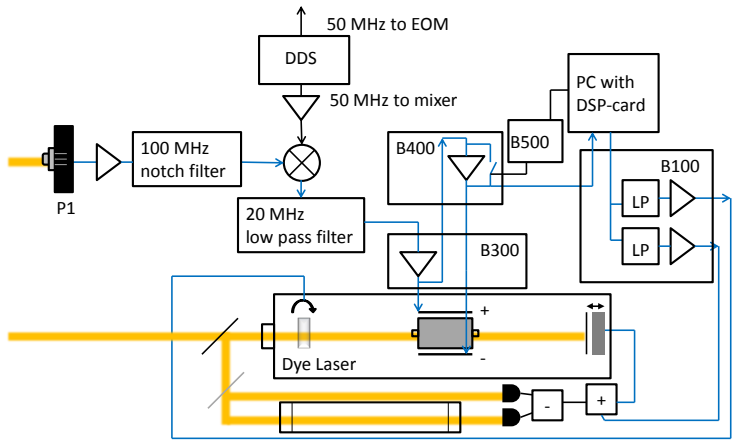

Figure 4.11. *A sketch of the main components of the feedback electronics of the dye laser stabilization system. The boxes are labelled according to the labels in reference [83]. The error signal is marked as blue lines, starting from the error detector P1.*

I will not describe the electronics in detail here, but will give an overview of the basic function of each part of the system. A much more detailed description of the electronics can by found in the Ph.D.-thesis of Lars Rippe [83].

A drawing of the major components of the stabilization electronics is shown in Figure 4.11. Amplifiers are shown as triangular boxes, and each amplifier in the image can correspond to a combination of several amplifiers and attenuators in real life. Each box contains many components, not shown in the image. The function of each of the boxes are described briefly below. I do not include detailed schematics of the electronics, as it can be found in reference [83].

The 50 MHz signal picked up by photo detector P1 is amplified and sent through a 100 MHz notch filter. It is mixed with a 50 MHz reference signal from a DDS. The DDS is based on a 500 mega-samples per second DDS-card (AD9959), with 4 digital-to-analogue output channels. The relative phase of the reference signal can be adjusted accurately from a computer via the DDS USB port. The signal from the mixer is sent through a low pass filter to obtain a DC-signal.

Low voltage P-regulator, B300

B300 contains an adjustable amplifier to set the proportional gain of the fastest feedback signal. After the amplifier the signal is sent to one contact of the intra-cavity EOM. B300 is mounted

directly on top of the EOM to avoid adding capacitance by using cables. The maximum voltage sent to the EOM is ±10 V, and the bandwidth of this feedback is around 3 MHz.

High voltage PI-regulator, B400

The error signal from B300 is also sent to B400 where it is further amplified. B400 contains a high voltage amplification stage and an integrating circuit. The proportional and integrator gain can be adjusted from the outside. The signal is inverted and sent to the second contact of the EOM, for larger frequency and phase adjustment. The output voltage range is ±200 V and the bandwidth of this feedback is a few hundred kHz.

Suspend regulation controller, B500

The task of B500 is to control the integrators, both in B400 and in the digital system, to prevent them from railing. It can freeze the integrator if the laser power goes low, for example because of a piece of dust in the beam. When initializing the laser lock, the digital system sends out a signal to reset the integrator in B400 and force integration to be on for a short time. The force integration function was useful when locking to a spectral hole, since there was no transmission through the crystal before the lock was initialized. Then the laser power was always low, and to prevent the freeze integrator function to stop the integrator, force integration was turned on.

Break out box, B100

The error signal from B400 is also sent to B100, the so called break out box. This is an interface between the digital signal processing (DSP) card in the PC and the analogue circuits. The error signal is sent through a 5 kHz low pass filter before going to the DSP-card.

B100 also filters the signals coming from the DSP-card and sends out two error signals. One goes to the internal stabilization system of the laser where it is added to the error signal from the detectors after the invar cavity. The control box of the dye laser picks up this signal and sends a correcting signal to the piezo stack behind a mirror in the laser cavity. The second signal goes to the external scan input on the dye laser control box. This will cause the galvo controlled Brewster plate to turn.

Digital PID-regulator, PC with DSP-card

The slow part of the feedback system is controlled from a computer. A digital signal processing (DSP) card (model SI-C6713DSP-PCI-256) is installed in the computer and can be controlled from LabView. Analogue to digital converters at the inputs

are used to digitize the incoming error signal. The digital signal is sent through a PID-regulator where the parameters can be set in the software. Amplified error signals are sent out to B100, and distributed to the piezo mounted mirror and the galvo controlled Brewster plate in the laser cavity.

4.2.6 Pulse shaping system

The laser beam going to the experiment is first sent through a pulse shaping system. The system consists of one double pass AOM (AA St.200/B100/A0.5-VIS) and one single pass AOM (AA St.360/B200/A0.5-VIS) in series. The double pass AOM is aligned in a butterfly configuration allowing the frequency shifted beam to be picked off. The beam can be scanned 200 MHz (double pass) in frequency without spatial shift. The first order diffracted beam from the single pass AOM is sent through a single mode optical fibre to the experiment.

The AOMs are controlled with an arbitrary waveform generator (Tektronix AWG520) and can be used to change the frequency and amplitude of the laser beam and create complex pulses.

Chapter 5

Diode laser system for readout

For cerium detection an external cavity diode laser (ECDL) at 371 nm is used. My very first task as a Ph.D.-student in 2010 was to rebuild an external cavity that was previously used for an infrared laser diode, to fit with a 371 nm laser diode. The design and characteristics of the ECDL are presented in this chapter.

For single ion detection it is important that the excitation laser doesn't drift out of the homogeneous absorption line of the ion while a measurement is being done. For that reason the ECDL was stabilized to a Fabry-Perot cavity using Pound-Drever-Hall locking in a similar way as the dye laser used for qubit manipulations. The aim was in this case not to get an ultra narrow laser linewidth, but rather to prevent the laser from drifting more than 1 MHz during a full working day. The system was built by Ying Yan together with Xingqiu Zhao [84]. I contributed with simulations to optimize the cavity design, I characterized the system and optimized the gain parameters.

Figure 5.1. *The Toptica LD-0375-0020-2 laser diode.*

5.1 Laser diode

A laser diode (LD) is a PIN-junction in a semiconductor. When a forward voltage is applied across the diode, electrons and holes are injected into the intrinsic (I) region where they recombine and generate photons. Two surfaces of the semiconductor chip form a cavity and at a certain threshold current lasing starts.

Laser diodes at red wavelengths have been available for more than 50 years [85], but the blue laser diode was developed as late as in the 90's in conjunction with the blue light emitting diode (LED), which was rewarded the Nobel prize in physics 2014 [86].

Today laser diodes are manufactured for wavelengths down to 372 nm in the ultraviolet, and odd examples of diodes with centre emission as low as 370 nm can be found. A diode laser can be tuned

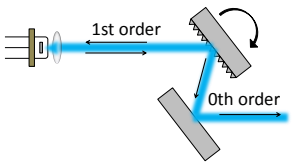

Figure 5.2. *A laser diode in a Littrow configuration. The first order reflection from a grating is fed back into the laser diode creating an external cavity. The output beam is the direct reflection from the grating. A mirror that is always parallel to the grating is used for out-coupling to keep the beam angle constant as the grating is turned.*

a few nm in wavelength by changing the temperature of the chip, which shifts the gain profile of the material and also changes the length of the chip and hence the length of the lasing cavity. This can be done in two ways; either directly by heating or cooling the laser from the outside or indirectly by changing the drive current to the laser, which will in turn change the temperature by a small amount. Changing the drive current also has the effect of changing the output power of the diode.

In this thesis two different laser diodes were used. One was bought from Toptica (LD-0375-0020-2) selected with a centre wavelength of 372 nm. It was later replaced by a diode from Sacher (SAL-372-10) selected with a centre wavelength of 371 nm. Both diodes are manufactured by Nichia. The maximum output power is specified to 20mW for the Toptica diode and 70mW for the Sacher diode. The Sacher diode has one anti-reflection coated chip surface, which can be beneficial when used in an external cavity configuration. Both can be tuned to the cerium 4f-5d zero phonon transition at 370.83 nm. The Toptica diode is shown in Figure 5.1.

5.2 Littrow cavity design

By placing a laser diode in an external cavity the linewidth can be reduced from 10-100 MHz in free running mode to below 1 MHz. In a Littrow type external cavity the first order reflection from a grating is used to create a cavity together with the back surface of the laser diode, see Figure 5.2. The wavelength of the laser can be tuned by either changing the length of the external cavity or by turning the grating and thereby changing the first order feedback angle.

As the grating is turned the angle of the output beam will change, which can be very annoying if many optical components are aligned after the laser. An output mirror can be placed parallel to the grating, and turn together with the grating so that the beam angle will be fixed. The beam position will still shift a little bit as the grating is turned, but this usually does not cause any major problems.

For the diode laser used in this thesis, a housing that was originally built for an infra-red laser diode was re-used. The 370 nm laser diode is smaller than the infra-red diode, the cavity should be shorter, the grating should sit in a different angle and the lens is different, so all the mounts had to be re-built to fit. The 3D mechanical design software SolidWorks was used to draw the new parts.

A sketch of the design is shown in Figure 5.3. The cavity is about 2.5 cm long which gives a free spectral range (FSR) of 6 GHz. The grating surface should have a rather large angle to the

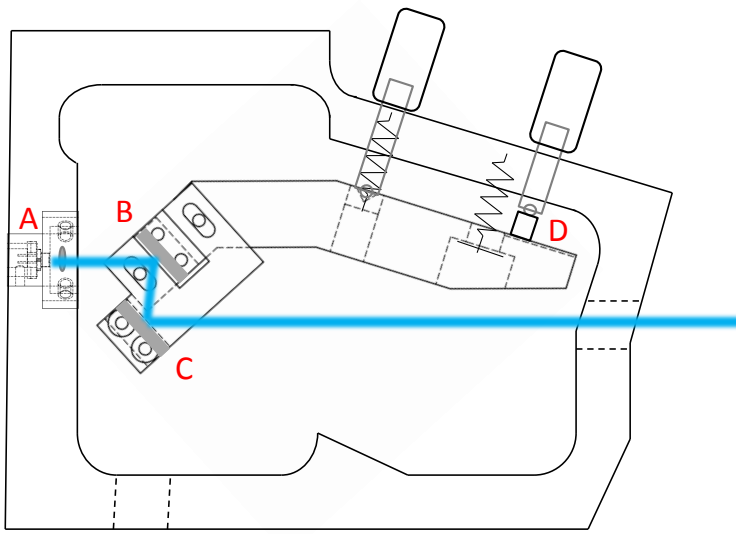

Figure 5.3. *A sketch of the Littrow external cavity. The main housing was re-used from another ECDL. A: A copper holder for the laser diode and a separate holder for the collimation lens that can be adjusted in three directions. B: Grating holder containing a UV reflective holographic grating (Thorlabs GH13-36U) C: Out-coupling mirror (Thorlabs PFSQ05-03-F01) D: A piezo stack for fine tuning of the grating angle (Thorlabs AE0203D04F)*

beam (48°), which was not the case for the infra-red laser diode, thereof the strangely shaped grating holder. A piezo stack is glued between the horizontal adjustment screw and the grating holder to allow fine tuning of the grating angle.

The laser diode is mounted in a copper housing. The collimation lens is glued into a mount made of brass, which can be adjusted both along the beam for optimal collimation, and transverse to the beam to make sure the beam hits the centre of the lens, see Figure 5.4.

The temperature of the whole metal housing is controlled by four thermoelectric elements mounted between the housing and a bottom plate, as in Figure 5.5. The laser diode temperature can be finely adjusted by another thermoelectric element sitting just below the copper mount of the diode. The laser driver (Vescent D2-105) has two temperature controllers with sub-mK stability, used for the housing and the laser diode respectively.

Figure 5.4. *The copper mount for the laser diode and the collimation lens glued into a brass mount.*

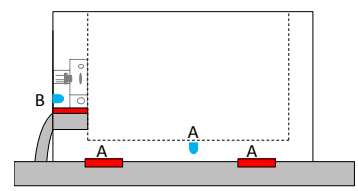

Figure 5.5. *The laser housing seen from the side. A: Four thermoelectric elements (red) are mounted under the main housing of the laser, onto an aluminium plate acting like a heat sink. A temperature sensor (blue), at the bottom of the housing, is used to measure the temperature. B: One thermoelectric element (red) is mounted just underneath the copper holder for the laser diode, onto a copper braid connected to the bottom plate. A sensor (blue) sitting close to the diode monitors the temperature. The laser driver can actively control both the housing and the diode temperature.*

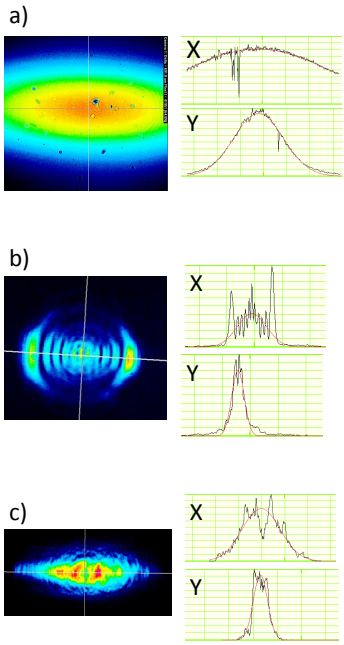

Figure 5.6. *The spatial profiles of: a) The beam directly from the laser diode. Since the beam is very divergent it is cut by the camera chip. b) The beam after the wrong collimation lens 352610-A c) The beam after the correct collimation lens 352671-A. To the right the intensity along the horizontal (X) and vertical (Y) direction is plotted and Gaussian fits are shown as red lines.*

5.3 Collimation lens

The laser beam from a laser diode is elliptical and very divergent. A lens with a high numerical aperture is needed to collimate the beam. Most often an aspheric lens is used, since it is small and still gives a good quality beam.

Most laser diodes have a cover glass to protect the diode from damage. The cover glass will introduce spherical aberration in the beam if a lens without correction is used. Aspheric lenses specially designed for different cover glass thickness and refractive index are available.

The laser diodes used in this thesis have 0.25 mm thick borosilicate windows. By mistake a lens was bought that is designed for a 1.2 mm thick window (Thorlabs 352610-A). The lens caused a very strange spatial pattern in the laser beam, with deep minima and several maxima, as can be seen in Figure 5.6.

A new lens was bought, specially designed for a blue Nichia laser diode, compensating for a 0.25 mm thick borosilicate window (Thorlabs 352671-A, also Lightpath 352671). The new lens improved the spatial mode of the beam. But one big problem still remains, the beam has a minimum in the centre.

It is still not completely understood why this lens destroys the spatial mode of the beam. One possibility is that the anti-reflection coating on the lens is not good enough, which could cause some interference or etalon effects. The specified AR-coating should give a reflectivity below 0.5%. When placed inside a cavity this might however not be good enough.

Since the laser locks well to the external cavity with this lens, and because of time constraints we decided not to investigate this further but to move on with experiments.

5.4 Tuning characteristics

The external cavity diode laser can be tuned in frequency by changing the drive current to the diode or by applying a voltage to the piezo stack behind the grating. It is also possible to directly change the temperature of the laser diode with the thermoelectric element, but this often leads to bigger frequency jumps, since the adjustment knob for the temperature is not precise enough.

In Figure 5.7 the laser was scanned by a) applying a ramp to the piezo stack to move the grating, and b) ramping the drive current of the laser diode. The wavelength was monitored with a wave meter (HighFinesse WS6) with 100 MHz resolution. Two kinds of mode jumps can be seen. The smaller 6 GHz mode jumps are due to jumps between the external cavity modes. Between the jumps the laser has a mode hop free scan range of about 6 GHz when tuning the grating.

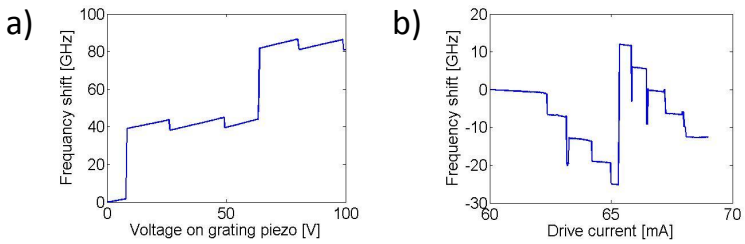

Figure 5.7. *The laser diode is scanned by a) moving the grating by ramping the voltage applied to a piezo stack behind the grating or b) ramping the drive current.The threshold current for lasing is just below 60 mA.*

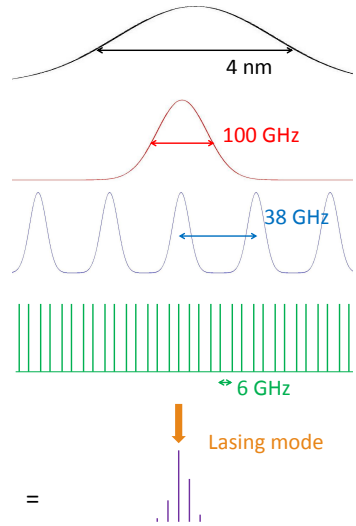

Figure 5.8. *The image is illustrating the frequency selecting elements of the ECDL. The black curve illustrates the gain of the laser diode, which sets the ultimate tuning range of the laser. In red is shown the grating feedback curve. In blue is the mysterious cavity modes which are probably caused by reflections from the lens. In green are the external cavity modes. As all the curves are multiplied the total gain is illustrated by the purple curve at the bottom. Only the strongest mode will lase. When the grating is moved, the green external cavity modes move the most. When the drive current is changed, the external cavity modes shift, but the 38 GHz blue modes shift the most. The figure is not to scale.*

There are also larger mode jumps of 38 GHz. Normally this would be interpreted as jumps between internal modes of the laser diode. In this case however, an anti-reflection coated laser diode was used, which should disable the internal modes of the laser chip. 38 GHz free spectral range corresponds to a cavity length of 4 mm in air. After communication with Sacher it was concluded that the large mode jumps can not be due to the diode chip. In fact, the large mode jumps matches better to the optical distance between the back surface of the chip and the collimation lens. This would support the assumption that the anti-reflection coating of the collimation lens is not good enough. Considering the shape of the lens surfaces however, the reflected beam should be very divergent, and it seems like not much light would be coupled back into the small active area of the laser diode.

Still, the lens seems like the strongest candidate for the mysterious mode jumps. The big mode jumps has the effect that we can't reach some frequencies by just tuning the grating.

When tuning the grating, both the grating first order feedback angle changes (red curve in Figure 5.8 shifts), and the length of the external cavity changes (green lines in Figure 5.8). But the 38 GHz modes (blue curve) does not change, and hence lasing will always take place close to the peak of one of these modes, and just jump from one external cavity mode to another as they are swept. Eventually the grating feedback curve has moved enough so that another one of the 38 GHz spaced modes will give more feedback and the laser will make a big jump.

When the current to the laser diode is scanned the length of the external cavity (green modes in Figure 5.8) will shift a little bit and the length of the cavity defined by the lens (blue curve in Figure 5.8) will shift more, but the grating angle is fixed. As the blue curve moves across the external cavity modes the laser jumps 6 GHz from one mode to another to lower and lower fre-

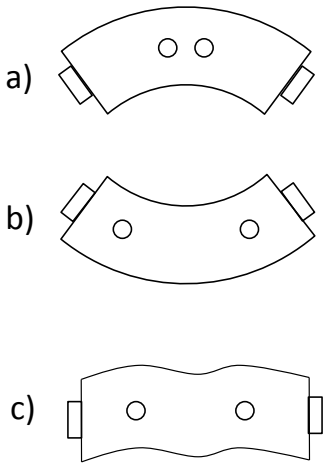

Figure 5.9. *The position of the holes in which the cavity hangs will influence it's deformed shape and sensitivity to vibrations. a) The holes are too close to each other. b) The holes are too far apart. c) The holes in good positions. The deformations are grossly exaggerated.*

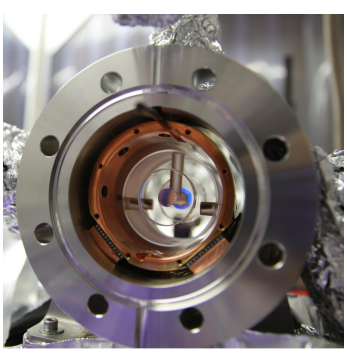

Figure 5.10. *The ULE cavity mounted inside the vacuum chamber and a gold coated radiation shield.*

quencies, until the next 38 GHz mode enters under the grating feedback curve. Then the laser makes a big mode jump back to high frequencies.

5.5 Stabilizing the ECDL

To prevent the laser to drift out of resonance with a single cerium ion while a measurement is in progress the ECDL is actively stabilized to an ultra stable cavity using Pound-Drever-Hall locking. The system is rather similar to the dye laser locking system, and here I will focus on the differences between the systems.

5.5.1 Reference cavity

The reference cavity spacer is in this case a cylindrical piece of ultra low expansion (ULE) glass , with two mirrors optically contacted to the end surfaces. The spacer is 55 mm long which gives a free spectral range of 2.7 GHz. The diameter is 44 mm.

The cavity is held inside a temperature shield by four spring wires inserted into holes in the glass. The exact positions of the holes determines how sensitive the cavity is to vibrations, see Figure 5.9. The positions of the holes were determined using a finite element method simulation originally written by the group of Professor Uwe Sterr at Physikalisch-Technische Bundesanstalt, Braunschweig, Germany. The program was modified with the dimensions of our cavity and the first order sensitivity of the length of the cavity to vibrations was calculated.

The mirrors in this cavity are high reflectivity coated both around 370 nm and in the range 575nm-615nm. It enables us to couple the dye laser to the same cavity, which is useful for some experiments. The dye laser can then be locked separately, to it's own cavity, and the stability of the 370 nm cavity can be analysed using the stable dye laser. This method was used to find the zero-crossing temperature for the thermal expansion of this cavity as well as the cavity in the dye laser system.

The cavity and the temperature shield are mounted inside a small specially designed vacuum chamber, as shown in Figure 5.10. The temperature shield is mounted on top of four thermoelectric elements to stabilize the temperature at the point where the first order expansion of the ULE glass is zero. The vacuum chamber is kept at a pressure of 10^{-8} mbar.

The required stability of this system is not as high as for the dye laser system, and for that reason no active vibration cancellation is necessary. Vibrations are partly damped by the spring wires in which the cavity is hanging.

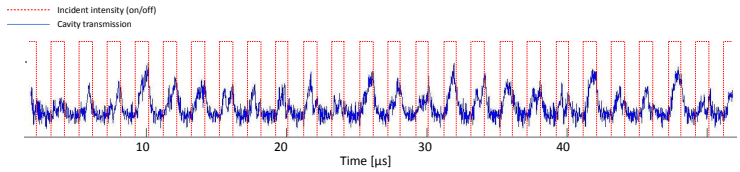

Figure 5.11. *The cavity decay time was measured by modulating the incident light with a square wave, and monitoring the cavity transmission.*

5.5.2 Cavity decay time

The decay time of the cavity was measured by turning the laser beam on and off, while monitoring the cavity transmission. The laser beam was turned on and off by modulating the RF-signal sent to the double pass AOM with a 500 kHz square wave. As the laser is turned on a field builds up in the cavity, and as the laser is turned off the field decays. The modulation frequency thus has to be slow enough to allow the cavity to decay during half a period of the square wave. The result can be seen in Figure 5.11. The transmission varies a bit from period to period since the laser jitters a bit in frequency and might not always hit the exact resonance of the cavity.

The decay time was measured in three of the periods from the sequence in Figure 5.11 where the coupling to the cavity happened to be good. An exponential function was fitted to the decaying transmission when the laser was turned off. An example can be seen in Figure 5.12. The resulting cavity decay time τ_c = 120-150 ns.

The measured decay time gives a cavity linewidth of 1.1-1.3 MHz. This is larger than we expected. According to specifications the mirror reflectivity should be 99.97 % at 370 nm, which would lead to a finesse of about 10 000 and a linewidth of 270 kHz. The reason might be that there is some dirt or grease stuck to the surface of the mirrors. It is also possible that the coating degraded because of the high intensity UV-radiation inside the cavity.

One consequence of the larger linewidth is that the cavity only work as a phase reference on very short time scales, smaller than 120 ns. The feedback loop is not fast enough to correct for phase errors, but our locking system will only work as a frequency lock. For single ion detection however, where we don't need a very narrow linewidth, this should not be a problem.

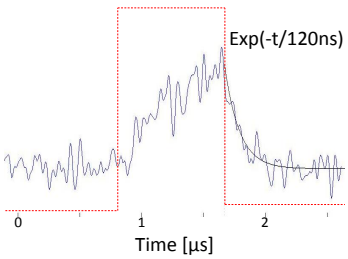

Figure 5.12. *An exponential fit to the cavity decay as the input laser is abruptly turned off gives a decay time of 120 ns.*

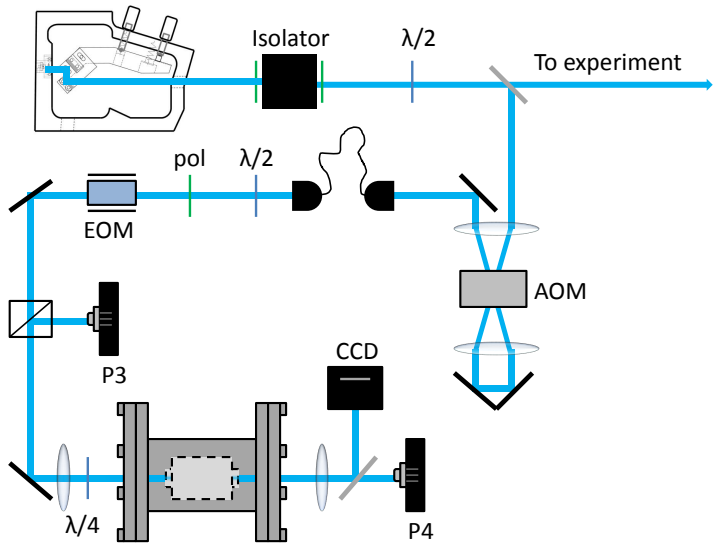

Figure 5.13. *The vital components of the diode laser stabilization system.*

5.5.3 Stabilization system optics

Figure 5.13 shows a sketch of the optical set-up for the diode laser frequency stabilization system. The isolator is in this case placed closer to the laser to protect it from reflected light. An AOM (Isomet 1250C-829A) in double pass configuration is used to scan the laser a maximum of 200 MHz while it is locked. In this case the bandwidth of the AOM is small compared to the free spectral range of the locking cavity. To tune the laser to the cavity resonance it is not enough to use the AOM, but the grating of the ECDL has to be tuned with a small offset voltage on the piezo stack on the grating mount. Tuning the grating also effects the frequency of the experimental beam. For that reason it is not possible to lock the laser at any frequency, but only to the cavity resonances which are 2.7 GHz apart.

A single mode fibre after the AOM is cleaning up the laser mode to match the TEM_{00}-mode of the cavity better. An EOM with a modulation frequency of 20 MHz puts sidebands on the laser beam. In front of the cavity the beam passes a quarter wave plate to convert the polarization from linear to circular. The beam that is reflected from the cavity and passes the quarter wave plate once more, will get it's polarization turned 90° compared to the incoming beam. The reflected beam is picked out with a polarizing beam splitter and detected on a photo detector. Another photo

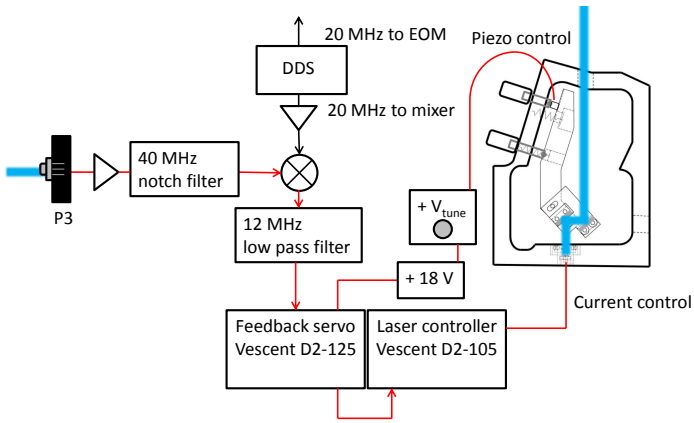

Figure 5.14. *A sketch of the main components of the feedback electronics of the diode laser stabilization system. The detected reflection from the cavity is demodulated in a mixer. The DC error signal is sent to a servo which sends control signals to the laser driver to change the current and to a piezo on the grating mount to change the grating angle.*

detector is used to monitor the cavity transmission and a CCD camera (PointGrey Firefly) behind the cavity is used to see the transversal mode profile of the cavity resonance.

The photo detectors are in this case bought from Femto. The error detector (P3) is a modified version of a Femto HCA-S-200M-SI-FS, specially ordered for our needs. It consists of a photo diode (S5973-02) with a responsivity of 0.3 A/W at 370 nm in combination with a transimpedance amplifier. The amplifier has a bandwidth of 60 MHz, is AC-coupled and has a transimpedance gain of 100 kV/A. The detector for the cavity transmission (P4) consists of the same type of photo diode (S5973-02) in combination with the amplifier Femto HCA-10M-100k, with a 10 MHz bandwidth and 100 kV/A transimpedance gain.

5.5.4 Stabilization system electronics

For the 370 nm diode laser stabilization system only commercially available electronics is used. The laser servo Vescent D2-125 is used in combination with the laser controller Vescent D2-105. The servo is used in side lock mode, which means that it locks to a slope in the error signal. An offset knob can be used to choose the zero-point of the error signal, which is the locking point. Demodulation of the Pound-Drever-Hall signal is done externally. A sketch of the main parts of the electronic system can be seen in Figure 5.14.

A fast correction signal is sent from the servo to the laser controller to change the drive current of the laser diode to compensate for phase and frequency fluctuations. The bandwidth of the servo signal is 10 MHz, but the feedback bandwidth is limited to about 3 MHz by the delay time in optics and electronics.

A slow integrated signal with a bandwidth of a few tens of Hz is also sent to the piezo stack behind the grating in the ECDL to compensate for slow drifts. Since the piezo can be damaged by negative voltages and since the error signal is bipolar, a voltage offset on the piezo is needed. This is achieved by connecting two 9V batteries in series with the error signal. On top of that we also need to tune the grating to find the cavity resonance, and this is achieved by also adding a tunable voltage supply in series with both the batteries and the error signal.

Proportional gain, the time constant of two integrators and a derivative gain can be set on the servo.

5.5.5 Optical table

All optics and electronics of the diode laser stabilization system are sitting on a mobile optical table. The table consists of an optical breadboard (Thorlabs PBI51511), with 90x75 cm surface area, sitting on a table frame (Thorlabs PFR7590-8) which has been mounted on wheels (Thorlabs PWA061). Between the table and the breadboard there are passive isolation mounts to damp vibrations (Thorlabs PWA074).

In this way the stabilized laser can be easily moved from one lab to another. This was important to us since until 2014 we did not have a microscope set-up in our own lab, but borrowed a set-up in a neighbouring lab for the initial single ions detection experiments. A photograph of the optical table can be seen in Figure 5.15.

Figure 5.15. *The 370 nm laser stabilization system. Both the optics and the electronics are placed on a table with wheels.*

Chapter 6

Microscope for single ion detection

One major goal of my thesis work has been to detect fluorescence from single cerium ions in a crystal. In a typical hole burning experiment using Pr:Y_2SiO_5 which is done on a regular basis in our lab, the laser beam will pass about 10^{13} ions on it's way through the crystal. Due to spectral selection the laser only interacts with about one million Pr ions. Since cerium has a wider homogeneous linewidth using the same concentration and set-up would mean interacting with one billion cerium ions.

The example above shows that with our normal set-up we are very far from the single ion level. Pursuing the single instance quantum computing scheme requires taking the experiment to the microscopic scale.

The first step is to reduce the concentration of dopant ions in the crystal. We have during the years had the privilege to cooperate with the group of Philippe Goldner and Alban Ferrier at Chimie ParisTech, Laboratoire de Chimie de la Matire Condense de Paris. They have grown Ce:Y_2SiO_5 crystals with successively lower concentrations of cerium. The final one has a doping level around 10^{-7}, which is on the limit of what they can measure in the chemical composition.

With a doping concentration of 10^{-7} there will still be 1000 cerium ions per μm^3 in the crystal. With a frequency stabilized laser we could selectively interact with on average 0.1 ions per μm^3. To see single ions we thus need a spatial resolution close to 1 μm^3. This is achievable with a confocal microscope.

While having plenty of expertise in the fields of spectroscopy and laser stabilization, microscopy was something new to the group when this project started. We got a lot of help and support from Mats-Erik Pistol and David Lindgren at Solid State Physics, Lund

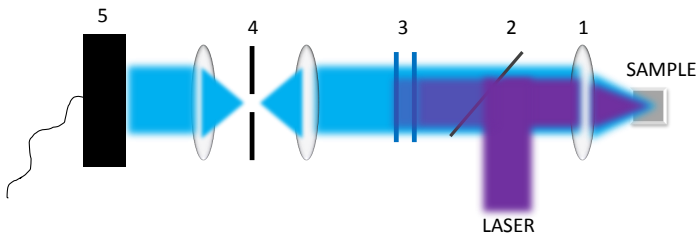

Figure 6.1. *The vital components of a confocal fluorescence microscope. The laser is reflected off a dichroic mirror (2) and focused onto the sample with a lens (1). Fluorescence generated in the sample is collected by the objective lens (1), transmitted through the dicroic mirror (2) and a set of frequency selective filters (3) which are chosen to block reflected laser light. The fluorescence is focused through a pinhole (4) and measured with a sensitive detector (5). The laser can also be focused onto the sample with a separate lens, incident from the side or from the backside of the sample. Only one point of the sample is measured at each instance of time, and either the laser focus or the sample has to be scanned to build up an image.*

University, and also from Ivan Scheblykin at Chemical Physics, Lund University. We got the chance to do initial experiments both in the lab at Solid State Physics and at Chemical Physics.

In 2013 we started building our own scanning confocal microscope set-up. The initial design was done by me, and for the detailed mechanical design and optical set-up I got help from my two master students, Tobias Bladh [87] and Martynas Soloveius [88].

Since confocal microscopy was new to the group I will dwell on the background theory a little bit. In this way I hope to give a new Ph.D.-student a head start when continuing this project.

6.1 Confocal microscopy

In wide field microscopy the sample is illuminated by a large and uniform beam of light and a small area of the sample is magnified and imaged onto a camera or directly into the eyes of an observer by an eyepiece.

Wide field fluorescence microscopy is very convenient when using a thin sample. When using a thick sample however, there are some problems. In a thick sample fluorescence generated below or above the focal plane will create a blurred image that is added to the sharp image from the focus and the contrast will be low. In the case of single ion detection this means that fluorescence from

ions that are sitting below or above the focus will contribute to the signal.

Confocal fluorescence microscopy is a simple way to exclude light that is generated outside the focal plane and improve the contrast and resolution of an image. The price to pay is that either the sample or the laser beam has to be scanned in order to build up an image point by point.

The principle of a confocal fluorescence microscope is shown in Figure 6.1. The improvement in contrast and resolution with a confocal microscope comes about because of two things; limitation of the excitation volume and limitation of the collection volume.

Instead of wide field illumination, a focused laser beam is used for excitation of the sample. To limit the volume from which fluorescence is efficiently collected in the sample, a pinhole (or an equivalent aperture, for example the small chip of a detector), is placed in the image plane of the sample. Fluorescence generated in the point inside the crystal corresponding to the image of the pinhole will be efficiently transmitted through the pinhole, while fluorescence generated outside this point will be partly blocked, see Figure 6.2.

In a well-aligned confocal microscope the image of the pinhole in the crystal overlaps completely with the laser focus, hence the word *confocal*.

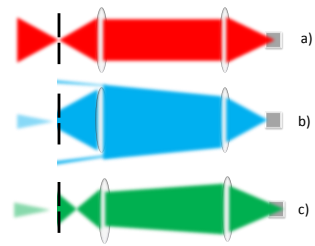

Figure 6.2. *In a) light originating from the image plane of the pinhole is focused through the pinhole with good transmission. Light generated in front of the image plane, b), or behind the image plane, c), is partly blocked by the pinhole.*

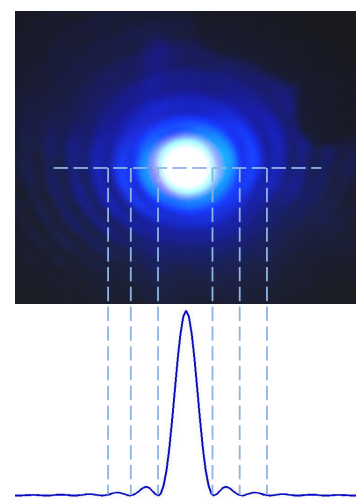

Figure 6.3. *An Airy pattern from a laser beam passing through a small pinhole.*

6.1.1 Diffraction limit

Ultimately the resolution of a standard optical microscope is limited by diffraction. Diffraction has the effect that a laser beam can not be focused to a point, and similarly the image of a point will be blurred to a spot of limited area. In the following section I consider a perfect, aberration free optical system.

There are two limiting cases which are relevant when focusing a beam with a lens. The first case is transmission of a plane wave of uniform amplitude through a circular lens. The resulting focus will show a ring pattern with maxima and minima, see Figure 6.3. The central peak is called the Airy disc, and contains 84 % of the energy in the beam. The diameter of the Airy disc is $1.22\lambda/NA$ where λ is the wavelength of light and NA is the numerical aperture of the lens. The numerical aperture is a measure of the size of the focused light cone and is defined as $NA = nsin(\theta)$, where n is the refractive index of the medium in which the beam is focused and θ is the half angle of the light cone. The most widely used criterion for resolution of an optical system, Rayleigh's criterion, states that two points can be resolved if the maxima of the Airy disc originating from one of them overlaps with the first minima in the ring pattern of the other one. Thus the diffraction limited resolution is half the diameter of the Airy disc, as in Equation (6.1) [89].

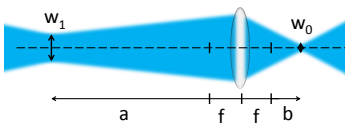

Figure 6.4. *A Gaussian beam focused by a lens.*

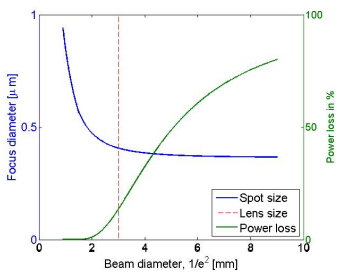

Figure 6.5. *The resulting diameter of the focal spot, and power loss as a function of incident beam diameter. The lens is 3 mm in diameter and has a focal length of 1 mm.*

$$\text{Diffraction limited resolution} = \frac{0.61\lambda}{NA} \tag{6.1}$$

The second limiting case is focusing a plane wave Gaussian beam by an infinitely large lens. In this case the lens does not cause diffraction of the beam, and the aperture is defined by the beam diameter. A Gaussian beam has a a radial intensity distribution of the form $I(r) = I_0 e^{-2r^2/w^2}$ where I_0 is the intensity in the centre of the beam, r is a radial variable, and w is the radius where the intensity of the beam has fallen to I_0/e^2. When focusing a Gaussian beam it remains a Gaussian beam, but the radius of the beam, w, is reduced to w_0 at the new beam waist [89].

The radius and position of the beam waist of a Gaussian beam after a lens can be calculated using Equation (6.2) and Equation (6.3). Here a refers to the distance between the first focal point of the lens and the beam waist of the incident beam, w_1 is the radius of the beam waist in the incident beam, f is the focal length of the lens, b is the distance from the second focal point of the lens to the new beam waist after the lens and λ is the wavelength [89, 90]. a and b are positive if the beam waists are further away from the lens than the focal points on each side, see Figure 6.4.

$$b = \frac{af^2}{a^2 + \left(\frac{\pi w_1^2}{\lambda}\right)^2} \tag{6.2}$$

$$w_0^2 = w_1^2 \left(\frac{b}{a}\right) \tag{6.3}$$

In a real situation a close to Gaussian beam is passing through a lens of finite size. Depending on how much the beam is truncated by the lens, the situation can resemble one of the two cases above. For a lens that is much smaller than the beam, the part of the beam passing through the lens resembles a wave of uniform amplitude. For a beam that is much smaller than the lens, the lens seems infinitely large. When moving from one situation to the other the Airy disc with a ring pattern will slowly be washed out and transform into a smooth Gaussian focus [91].

For a fixed lens size the smallest spot size is obtained with a uniform incident wave, which means with a truncated Gaussian beam. But truncating the beam also means throwing away power, so there is a trade off.

In Figure 6.5, the spot size after a lens with a diameter of 3 mm and a focal length of 1 mm is calculated as a function of beam diameter (at $1/e^2$ of the maximum intensity), using equations in reference [91]. The lens parameters are chosen to roughly match the actual lens used in the microscope set-up in this thesis. The power loss due to truncation of the beam is also shown. For a beam

truncated at the $1/e^2$-diameter the focus is about 12% larger than for a uniform beam, and the power loss is about 14%.

6.1.2 Resolution limit for a confocal microscope

Confocal microscopy offers a better resolution than wide field microscopy thanks to the double spatial selection; both the excitation volume and the collection volume are limited. This can be understood in the following way.

In each point of the sample, there is a certain probability for an emitter to be excited by the laser, depending on how far from the laser focus the emitter sits. Correspondingly there is a certain probability that a photon from the emitter will be collected by the lens and pass through the pinhole, depending on how far from the pinhole-image the emitter is. The total probability for detecting a photon from a certain point of the sample is then the product of the excitation probability and the collection probability. The spatial distribution of this product drops faster as we move away from focus, then the excitation probability or the collection probability alone, as illustrated in Figure 6.6. This gives an improved spatial resolution in a confocal microscope.

Assuming that both the laser focus and the image of the pinhole at the sample have a Gaussian intensity distribution in the plane perpendicular to the beam (which is approximately true for an Airy pattern), the product of the two is also Gaussian with a beam waist which is given by Equation (6.4).

$$w_{confocal} = \frac{1}{\sqrt{\frac{1}{w_{laser}^2} + \frac{1}{w_{pinhole}^2}}} \tag{6.4}$$

When the laser focus and the image of the pinhole overlap completely the confocal geometry gives a factor $\sqrt{2} \approx 1.4$ improvement in transversal resolution. This is however only true for an infinitely small pinhole, and in a practical situation the improvement is marginal.

The intensity along the axis of a Gaussian beam has a Lorentzian distribution with a maximum at the beam waist. The product of two Lorentzian functions is not a Lorentzian, and the improvement in depth resolution depends on which intensity level we measure at. The full width at half maximum (FWHM) of the spot is reduced by a factor 1.6 in a confocal geometry, while the $1/e^2$ width of the spot is reduced by a factor 1.9.

Above I calculated the spot size along the axis of the beam, and this is what gives an improved depth *resolution*. But I did not take into account that the beam widens as we move away from the waist, and interacts with a larger area of the sample. If we look at a Gaussian beam propagating through a sample, the intensity will drop at the same rate as the area will grow as we move away

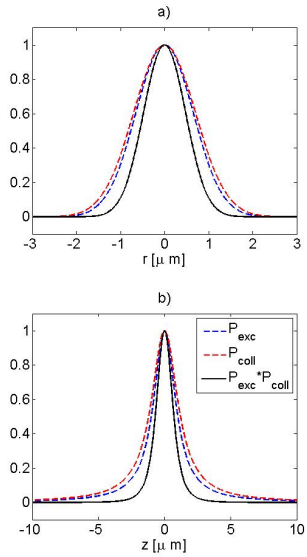

Figure 6.6. *The combination of a diffraction limited excitation volume and collection volume gives an improved resolution in a confocal microscope. The total detection probability is the product of the excitation probability, P_{exc}, and the collection probability, P_{coll}. This is illustrated for a) the transverse direction, and b) along the beam axis.*

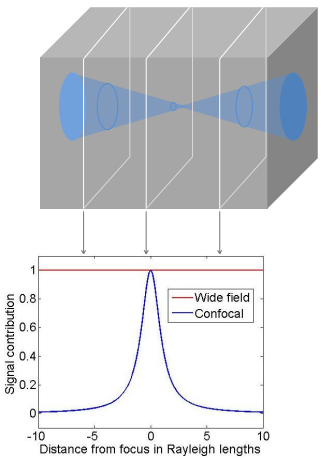

Figure 6.7. *Relative signal contribution in each point of a microscope image from different sections of a sample with a uniform distribution of emitters. The blue cone illustrates the collection volume. In wide field excitation (assumed to be uniform throughout the sample) there is no depth discrimination. In a confocal geometry most of the signal originates from the focal plane.*

from the waist. Assuming that the excitation probability of the sample goes linearly with intensity (no saturation) and that the fluorescing centres are homogeneously distributed in the sample, we will excite equally many centres in each plane perpendicular to the beam. Thus, there is no depth discrimination at all, if we collect all fluorescence generated by the beam.

The situation is very similar if we instead imagine that the photon collection probability has the shape of a beam going through the sample. If we excite the whole sample uniformly, as in wide field microscopy, there will be no depth discrimination at all.

In a confocal geometry the combination of a limited excitation volume and a limited collection volume will add a sectioning ability which is lacking in wide field microscopy, see Figure 6.7. The sectioning ability excludes light generated outside the focal plane, and in that way it improves the contrast of the image, and allows for 3-dimensional imaging. This ability is crucial for single ion detection in a thick crystal since the crystal, even with low concentration, contains a lot of ions spread out in the full volume of the crystal and the out of focus contribution would otherwise drown the signal.

6.1.3 Point spread function

The point spread function (PSF) of an imaging system is simply the image of an infinitesimal point. It is the *impulse response* of the system, and an image of a known object can be calculated by convolution of the object with the point spread function.

In sample scanning confocal microscopy the point spread function is identical to the detection volume, which is the product of the excitation volume and the collection volume shown in Figure 6.6. Note that a *volume* in the sample is imaged onto another *volume* in the image plane, and the point spread function is three dimensional.

6.2 Optical aberrations

So far it was assumed that the optical imaging system used for microscopy is perfect. In a real system there will be optical aberrations which will worsen the performance. Optical aberrations can be defined and calculated in many ways. Here I will briefly introduce two ways, one using the ray picture of light and one using the wave picture. For small aberrations, the ray picture does not tell us much about how our focus look like since it does not include diffraction. On the other hand, if the aberrations are large the wave picture gets very messy since there will be phase shifts of hundreds of multiples of 2π across the beam. For large aberrations the ray picture can give a good indication of where the light goes.

6.2.1 Aberrations in the ray-picture

In the ray picture we simply trace the rays originating from an object or from a source through an optical system and map out where they end up. In a perfectly focused beam all rays will meet in one point. Aberrations will cause the positions of the rays to spread and the focus will no longer be a single point. The position of a ray in the image plane (x',y') can be expressed as a function of the position in the object plane (x,y) and the point where the beam cross the optical system, which is usually expressed in polar coordinates (ρ,θ), see Figure 6.8. Without loss of generality we can turn our coordinate system so that the ray originates from the y-axis in the object plane (0,y). We can now express the position in the image plane as a function of three coordinates: $(x', y') = f(y, \rho, \theta)$. By assuming that the optical system is axially symmetric this relationship can be expanded as a sum of polynomials, as in Equation (6.5), where A and B are expansion coefficients [92].

$$\begin{aligned} x' =& A_1\rho sin\theta \\ &+B_1\rho^3 sin\theta + B_2\rho^2 y sin2\theta + (B_3+B_4)\rho y^2 sin\theta + ... \\ y' =& A_1\rho cos\theta + A_2 y \\ &+B_1\rho^3 cos\theta + B_2\rho^2 y(2+cos2\theta) + (3B_3+B_4)\rho y^2 cos\theta \\ &+B_5 y^3 + ... \end{aligned} \tag{6.5}$$

The A-terms in Equation (6.5) are of first order in ρ and y, and corresponds to the paraxial case, where the incidence angle onto the optical system is small and we can make the approximation $sin(\alpha_{in}) \approx \alpha_{in}$.

The third order aberrations (the B-terms) are often referred to as the *Seidel aberrations* since they were investigated and classified by Philipp Ludwig von Seidel. The five Seidel aberrations are: spherical aberration (B_1), coma (B_2), astigmatism (B_3), field curvature (B_4) and distortion (B_5).

For a beam that is propagating along the symmetry axis of the optical system (y=0), as is the case in sample scanning confocal microscopy, the only Seidel aberration present is spherical aberration. Spherical aberration causes the periphery of a beam to focus in a different spot along the optical axis compared to the centre of the beam, so that the focus gets stretched out. An illustration is shown in Figure 6.9 where the longitudinal aberration (LA), transverse aberration(TA) and circle of least confusion (CLC) are defined.

Spherical aberration is most commonly seen when using a spherical lens to focus a beam. It is also present when a converging or diverging beam goes trough a plane surface of different

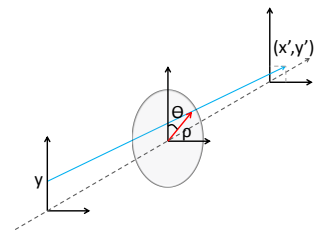

Figure 6.8. *A ray originating from a point (0,y) in the object plane propagates through the optical system at (ρ, θ) and is imaged onto a point (x',y').*

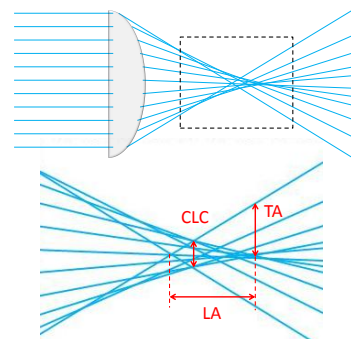

Figure 6.9. *Spherical aberration in the focus after a lens. The longitudinal aberration (LA) is defined as the spread in focus along the optical axis. The transverse aberration (TA) gives the spot radius in the paraxial focal plane. The circle of least confusion (CLC) is the smallest spot size along the beam.*

refractive index, for example when focusing a beam through a glass window, or below the surface of a crystal.

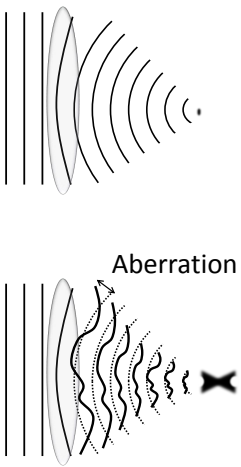

Figure 6.10. *Aberrations from a spherical wavefront in a focused beam changes the intensity distribution in the focus and makes the spotsize larger.*

6.2.2 Wavefront aberrations

Wavefront aberrations is another way of expressing deviations from a perfect focus. When expressing an aberration as a deviation from a perfect wavefront, it is possible to propagate the beam to an arbitrary plane and map out the intensity distribution, taking diffraction into account.

In a perfectly focused beam the wavefronts are spherical with the centre of the sphere located in the focal point. Wavefront aberrations are deviations from a perfect spherical wavefront and will cause the intensity distribution in the focal plane to change. This is illustrated in Figure 6.10.

Strictly speaking, the definition of wavefront aberration in not quite the one of Figure 6.10, which shows the wavefront errors along the surface of a spherical reference wavefront. The definition of aberration is the phase deviation, compared to a spherical wave, on a plane surface.

The deviation in phase, or in optical path, can be expanded in a basis of polynomials. The most commonly used basis of polynomials are the Zernike polynomials, which expands the wavefront aberration in a circular aperture, for example a lens, as in Equation (6.6) [94].

$$\Delta OP = \sum_{n=0}^{\infty} \sum_{m=0}^{n} a_{n,m} {}^{o}Z_n^m(\rho,\theta) + b_{n,m} {}^{e}Z_n^m(\rho,\theta) \tag{6.6}$$

Here ΔOP is the difference in optical path caused by the optical system, $a_{n,m}$ and $b_{n,m}$ are expansion coefficients, ${}^{o}Z_n^m$ and ${}^{e}Z_n^m$ are the odd and even Zernike polynomials respectively, and ρ and θ are the polar coordinates of the circular aperture of the optical system. The Zernike polynomials are defined in Equations (6.7). They are orthogonal and the expansion coefficients are unique.

$$\begin{aligned}
&{}^{o}Z_n^m(\rho,\theta) = R_n^m(\rho) sin(m\theta) \\
&{}^{e}Z_n^m(\rho,\theta) = R_n^m(\rho) cos(m\theta) \\
&R_n^m(\rho) = \sum_{k=0}^{(n-m)/2} \frac{(-1)^k (n-k)!}{k!((n+m)/2-k)!((n-m)/2-k)!} \rho^{n-2k} \\
&\text{(if n-m is even)} \\
&R_n^m(\rho) = 0 \text{ (if n-m is odd)}
\end{aligned} \tag{6.7}$$

The low order terms in the Zernike-expansion of wavefront aberrations can be approximately related to the Seidel aberrations

discussed in the ray-picture. Figure 6.11 shows an example of wavefront aberrations and their effect on the point spread function.

Piston is the lowest order wavefront aberration, which is not present in the ray optics version. It's just a uniform phase shift, or time delay, which has no effect on the focusing properties. *Tilt* is, just as is sounds, a linear tilt of the wavefront, which shifts the focal position in the transverse direction. For paraxial rays, the *defocus* aberration corresponds exactly to a shift of the focus along the optical axis, as one might expect from the name. For systems of high numerical aperture where the outer part of the beam comes in at a steep angle this is not exactly true.

6.2.3 Case 1: Focusing through a cryostat window

Figure 6.12 a) shows spherical aberration by focusing through a glass window in the ray model. By tracing a paraxial ray and a marginal ray to the optical axis, the longitudinal and transverse spherical aberration, as defined in Figure 6.9, can be estimated. With a bit of trigonometry the aberrations are expressed as in Equation (6.8). It is assumed that the window is surrounded by air with refractive index $n_{air} = 1$.

$$\begin{aligned} LA &= \frac{d}{n} - d\sqrt{\frac{1-NA^2}{n^2-NA^2}} \\ TA &= LA\frac{NA}{1-NA^2} \end{aligned} \tag{6.8}$$

In the equation d is the thickness of the window, n is the refractive index of the window and NA is the numerical aperture of the focused beam.

Focusing with NA=0.6 through a 2 mm thick glass window with refractive index 1.5 gives a longitudinal aberration of 170 μm. The transverse aberration is 128 μm. The smallest spot size along the beam (the circle of least confusion), has a radius of approximately half the transverse aberration, around 64 μm.

6.2.4 Case 2: Focusing into a crystal

Figure 6.12 b) shows spherical aberration by focusing below the surface of a crystal. Exactly as above the longitudinal and transverse aberrations can be estimated by tracing a paraxial ray and the marginal ray to the optical axis. The result is expressed in Equation (6.9). It is assumed that the crystal is surrounded by air with refractive index $n_{air} = 1$.

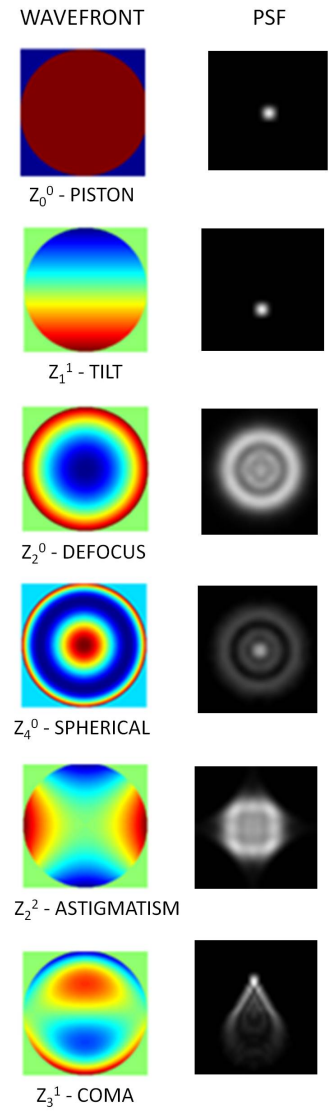

Figure 6.11. *Examples of low order wavefront aberrations and the resulting point spread function (PSF) in the paraxial focal plane. The colours show negative (red) and positive (blue) wavefront shifts in a circular aperture. The figure is reprinted and adapted from [93] under the creative commons licence: https://creativecommons.org /licenses/by/3.0/.*

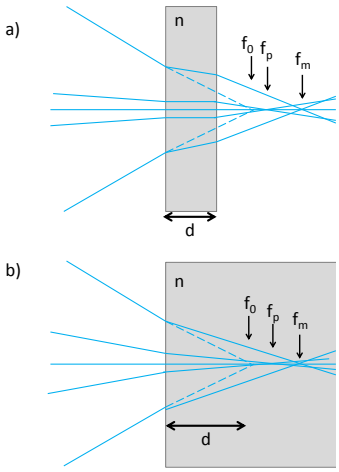

Figure 6.12. *Focusing through a glass window (a) or below the surface of a crystal (b) introduces spherical aberration in the beam. f_0 denotes the focus position in air (ignoring the window or the crystal), f_p is the paraxial focus and f_m is the focus of the marginal ray.*

$$LA = d\left(\sqrt{\frac{n^2 - NA^2}{1 - NA^2}} - n\right)$$
$$TA = LA\frac{NA}{n^2 - NA^2} \tag{6.9}$$

Here d is the distance the lens has been moved towards the crystal compared to when it is focused on the surface (the focal depth f_0 ignoring the shift of focus caused by the surface), n is the refractive index of the crystal and NA is the numerical aperture of the focused beam.

Focusing with NA=0.6, assuming a crystal with refractive index n=1.8 and a focal depth of f_0=100 μm gives a longitudinal aberration of 32 μm and a transverse aberration of 7 μm. The smallest spot along the beam then has a radius around 3.5 μm.

This is rather far from the diffraction limited spot size, which has a radius of roughly 380 nm, assuming a wavelength of 370 nm and NA=0.6. The aberrations gets worse for larger NA, which normally would give a smaller focus. By setting the radius of the CLC equal to the diffraction limited radius we can get a rough measure of the maximum focal depth into the crystal that does not destroy the focus too much. For NA=0.6 this depth is 3.3 μm and for a larger NA of 0.85 the depth is only 0.4 μm.

6.3 Microscope design

The most important properties for a set-up for single ion detection is resolution and collection efficiency. The resolution has to be good enough to see fluorescence from one ion instead of many, which in a bulk crystal is not trivial. The aim was in this case to achieve a resolution of about 1 μm^3, which should be possible with a confocal microscope.

The signal from one single ion is weak, and the collection efficiency determines how big part of all the emitted photons we can catch. When detecting light from an emitter inside a high refractive index crystal, most of the photons do not even exit the crystal surface, because of total internal reflection. If an emitter sits below the surface of a crystal of refractive index 1.8, only about 7% of the emitted photons will exit the surface of the crystal, and they will be spread out in a half sphere. This number assumes that the emitted photons are unpolarized and takes into account angle dependent reflection of the crystal-air interface. The best possible collection efficiency (without using an immersion lens) is then in the few percent range.

Properties of the Blu-ray lens:	
Focal length (f)	$\approx$ 1.2 mm
Working distance (WD)	$\approx$ 0.5 mm
Diameter (D)	3 mm
Numerical aperture (NA)	0.85
Transmission @ 370 nm	$\approx$ 87%

Table 6.1: Some properties of the Blu-ray lens. The focal length, working distance and transmission were measured in our lab at 370 nm. The size and numerical aperture are known from specifications [95].

6.3.1 A Blu-ray lens

The design of the microscope set-up was done with a quantum computing scheme in mind. The coherence time of a qubit needs to be long, which requires the qubit ions to sit some distance below the surface of the crystal. This requires the microscope to have good resolution below the crystal surface, which can be a problem due to aberrations.

The crystal have to be cooled to liquid helium temperatures which requires a cryostat. Focusing a beam through the thick windows of a cryostat would cause spherical aberration that would destroy the resolution of the microscope. The best solution is to put a lens inside the cryostat, to allow a short distance between the sample and the lens, and eliminate aberrations caused by the window.

To be able to put the objective lens of the microscope inside the cryostat it has to be small. The sample space of the helium bath cryostat used in this thesis is only 25 mm in diameter, and should also fit the sample and the scanning system. This excludes most commercial microscope objectives.

Because of a suggestion from one of my supervisors we started investigating the properties of the focusing lens in a Blu-ray player. A Blu-ray disc has a 100 μm transparent cover layer to protect the tracks on the disc. The laser in a Blu-ray-player has the wavelength 405 nm, which is not all that far from 371 nm. The laser has a diffraction limited focus at the disc-tracks, since the lens is compensating for the aberrations caused by focusing through the cover layer [95]. In addition the lens is very small.

Some properties of a Blu-ray lens is listen in Table 6.1.

The crystal has a higher refractive index than the cover layer on a Blu-ray disc. By slightly adjusting the focal depth into the crystal it should however be possible to obtain an aberration free focus. The optimal focus can be calculated to be 108 μm below the surface of the crystal with this lens. This point is found by focusing on the surface of the crystal and then moving 36 μm closer

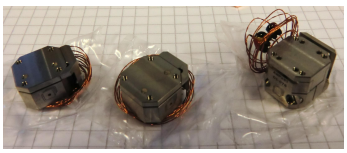

Figure 6.13. *Attocube ANPx51RES (left and centre) and Attocube ANPz51RES (right) nano-positioners used for scanning and positioning in three dimensions. The small squares on the paper are 5mm, and the positioners have a footprint of 15x18 mm.*

to the the crystal (f_0 = 36 μm).

The diffraction limited spot size at 370 nm when focusing with NA=0.85 is 531 nm (Airy disc diameter). The Rayleigh length is 600 nm. The intensity along the optical axis of a Gaussian beam drops to a fraction $1/e^2$ of the intensity in the focus over a distance of 2.5 times the Rayleigh length, which in this case is 1.5 μm. Thus, the excitation volume with this lens is at best π*(0.531/2)^2*3 μm^3 = 0.66 μm^3. In a confocal set-up the detection volume can be reduced by a factor of 4, in the ideal case. This gives a detection volume which is a factor 6 smaller than the requirement of 1 μm^3.

Since we have some margin in the detection volume we can allow for small aberrations caused by the fact that the lens is not designed for 370 nm, and for misalignment. It should however be noted that the margins are very small. For a Gaussian beam the interaction volume scales like the beam radius to the power of four. A slightly larger focal spot would quickly make the interaction volume much larger.

The collection efficiency of the lens can be calculated from the numerical aperture. The total collection efficiency for photons emitted by an ion below the surface of the crystal is 5.2%, taking refraction and reflection at the crystal surface into account. The collection efficiency is severely limited by refraction at the crystal surface.

The Blu-ray lens used in this microscope was dismounted from a commercial Blu-ray player (LG CH10LS20).

6.3.2 Sample scanning

To obtain an image from a confocal microscope either the sample or the laser beam has to be scanned. From the perspective of optical aberrations, scanning the sample is preferable. Scanning the laser beam will cause additional aberrations since the beam is not always perpendicular to the lens or the cryostat windows. In addition, with a short focal length lens, scanning the laser gives a rather small scan range, while scanning the sample can allow a very large scan range.

To be able to scan the sample the scanning system has to sit inside the cryostat and will be immersed in liquid helium. It should have a position resolution smaller than the optical resolution and it should not drift over long times. On top of that it should fit into a cylinder of 25 mm diameter.

For this purpose three nano-positioners were bought from Attocube, two ANPx51RES and one ANPz51RES, for positioning in three dimensions, see Figure 6.13. In stepping mode, the positioners use so called *slip-stick motion* to translate the sample, which means that there is no voltage applied to the piezos when the sample is standing still, and hence no drift.

The ANP51-positioners together have a footprint of only 18x18 mm including the full travel range, and can be immersed in liquid helium. The minimum step size is about 10 nm at 4K, and the travel range is 3 mm. By applying a constant voltage to the piezos the position can be adjusted with sub-nm resolution.

ANP51RES has resistive position feedback, with a sensor resolution of 200 nm according to specifications. The observed feedback resolution when the positioner is mounted inside the cryostat is however on the μm-scale. This is probably because of the long home made cables used to connect the positioners to the feedthrough of the cryostat. The cables have a few solder points and are about 1.5 m long, and they introduce additional resistance.

6.3.3 Intracryostat assembly

The group had two different cryostats available for this set-up, one liquid helium bath cryostat (Oxford Instruments Spectromag) and one cold finger cryostat (Oxford Instruments Optistat). The cold finger cryostat has the advantage of a larger sample space, which makes it easier to fit sample, lens and scanning system inside. The disadvantage is that the thermal conductivity between the sample and the cold finger has to be very good to reach 4K. This makes it more complicated to scan the sample. In the end a decision was made to construct holders for both cryostats, so that both could be used.

Cold finger cryostat assembly

The holder for the cold finger cryostat was designed and built by Tobias Bladh and Martynas Solovejus as part of their master projects, [87, 88]. It consists of a plastic structure to carry the Attocube nano-positioners, the sample mount, the lens mount and a thermal bridge consisting of a copper plate and a very thin, flexible copper foil, see Figure 6.14. The thermal bridge connects the sample holder, which sits on the positioners, to the cold finger of the cryostat. The crucial part of the design was to make the thermal bridge, and in particular the thin copper foil, conduct enough heat to cool the crystal to 4K. The copper foil has to be thin enough to move and bend as the sample is scanned, but at the same time thick enough to transport heat away from the sample very efficiently.

High purity copper (with an amount of impurities below 10 ppm) was used for the sample holder and the thermal link. All copper pieces were oxygen annealed in a specific procedure to reduce the number of impurities and increase the thermal conductivity at low temperatures. For details regarding the annealing procedure, see reference [87]. Finally all copper pieces were gold coated to

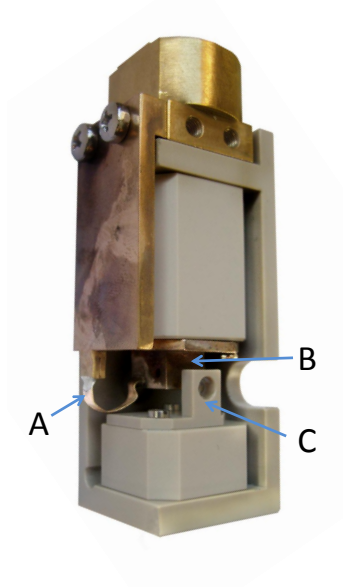

Figure 6.14. *The sample holder (B) and lens holder (C) for the cold finger cryostat. The thin copper foil (A) should conduct enough heat to cool the sample to 4K. The positioning system is in this picture replaced by plastic dummies.*

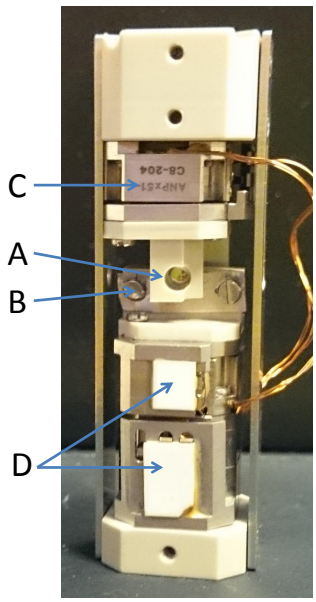

Figure 6.15. *The sample holder (B) and lens holder (A) for the helium bath cryostat. An Attocube ANPx51RES is used for focusing by moving the lens (C) and a combination of Attocube ANPx51RES and Attocube ANPz51RES is used for scanning the sample (D).*

Components:	
CCD camera 1 (CCD1)	Hamamatsu ORCA-03G
Dichroic mirror (DM)	Semrock BrightLine FF380-Di01
Band pass filter 1 (BP)	Chroma NC217171-ET405/40m
Band pass filter 2 (BP)	Chroma OS007401-HQ465/170m
Spectrometer	Oriel Instruments
CCD camera 2 (CCD2)	Andor DH501-25U-01
Photo multiplier (PMT)	Hamamatsu R943-02
Photon counter (SPAD)	Laser Components Count Blue 250B
Pinhole (PH)	Thorlabs 25/30/50 μm

Table 6.2: Some components of the microscope set-up.

reflect heat radiation efficiently and to protect the surface from oxidation.

After annealing, the copper foil was very soft and flexible. Scanning the sample with the thermal bridge clamped to the sample holder was tested in room temperature with good results.

Cooling the sample to 4K with the copper foil clamped to the sample holder proved difficult. After many hours of cooling the sample finally reached 4K, but the cooling procedure was simply too slow. To improve the thermal conductivity between the sample holder and the thermal link, the copper foil was silver soldered to the crystal holder. After soldering the link, cooling the sample went faster, but the high temperature soldering process made the copper foil very stiff. Scanning the sample with the Attocube positioners turned out to be impossible.

As a result the cold finger cryostat can only be used for experiments which do not require moving the sample. This assembly was used in Paper **IV**.

Helium bath cryostat assembly

A similar holder for the crystal, lens and positioning system was built for the liquid helium bath cryostat, see Figure 6.15. In this case the sample space is smaller, so the holder design had to be adjusted to fit. There is no need for a thermal link since the whole assembly is immersed in liquid helium.

The footprint of the full assembly is 19x19 mm.

This assembly was used in Paper **I** and Paper **II**.

6.3.4 Optics and detection

Figure 6.16 shows a sketch of the full optical set-up. The components are listen in Table 6.2.

The set-up contains standard optics mounted on a breadboard, which can be easily exchanged to for example allow excitation

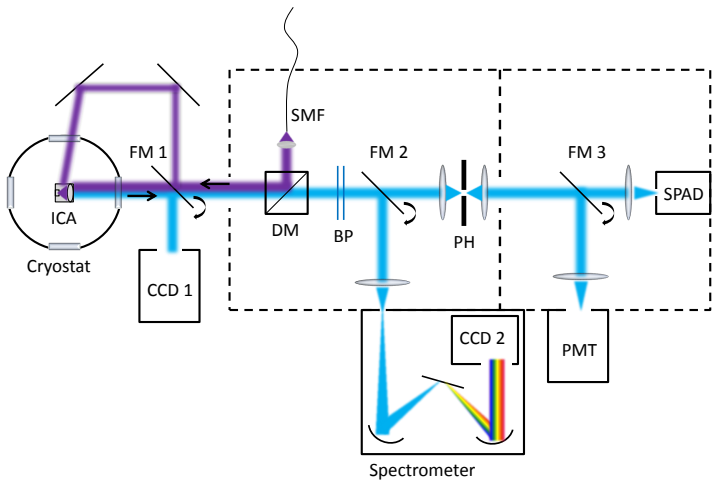

Figure 6.16. *The full optical microscope set-up. The dashed line corresponds to a black box to shield the set-up from room light. The purple beam represents the excitation laser and the blue beam represents fluorescence collected from the sample. Notation: ICA - Intra Cryostat Assembly, FM - Flip Mirror, DM - Dichroic Mirror, BP - Band Pass Filters, PH - Pinhole, CCD - Charged Coupled Device (camera), PMT - Photo Multiplier Tube, SPAD - Single Photon Avalanche Diode*

at a different wavelength. A flip mirror in front of the cryostat can be used to excite the sample in wide field from a different angle and image the sample on a camera. This is useful when aligning the set-up and the sample since it is very difficult to see the sample inside the cryostat by eye. Another flip mirror sitting before the pinhole can re-route the fluorescence into a spectrometer for spectral analysis. In the last stage of the detection set-up there is a choice to use either a photo multiplier tube for stronger fluorescence signals or a single photon counter for weak signals.

The single photon counter, Count Blue 250B, has a quantum efficiency around 50% for the cerium (site 1) fluorescence range 380-425 nm. The maximum dark counts for this model is 250 counts/s, and our specific detector has around 60 dark counts/s.

The size of the pinhole should ideally match the point spread function of the set-up, taking magnification into account. The lens for focusing into the pinhole has a focal length of 50 mm, and the magnification is around 42 times. A diffraction limited focus for the longest fluorescence wavelength (425 nm) would correspond to 26 μm in the plane of the pinhole. Normally a 25 μm pinhole is

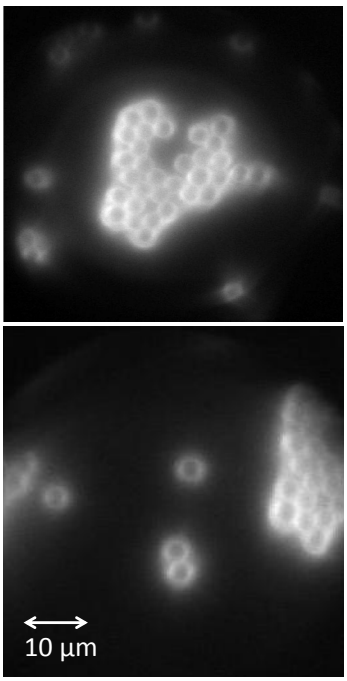

Figure 6.17. *Fluorescing microspheres which are 4 µm in diameter, imaged in wide field excitation.*

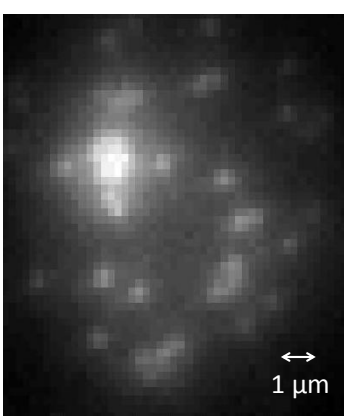

Figure 6.18. *Fluorescing microspheres which are 0.5 µm in diameter, imaged in wide field excitation.*

used, but if for example a larger signal is required it can be changed to a larger size.

Taking the collection efficiency of the lens, the transmission of all optics and the detection efficiency of the photon counter into account, the total detection efficiency of the set-up is calculated to 1.6%.

6.4 Test of the microscope

The microscope set-up was tested by wide field imaging in room temperature and confocal imaging in liquid helium.

In room temperature a sample consisting of fluorescing polystyrene beads (TetraSpeck Fluorescent Microspheres) was imaged (onto CCD1 in Figure 6.16) in wide field illumination. A drop of a solution containing microspheres was put on a microscope slide. The slide was left for a few hours to dry. The microspheres were imaged from the backside of the slide, through the glass, which is about 100μm thick.

Figure 6.17 shows examples of images of microspheres which are 4 μm in diameter.

Figure 6.18 shows an example of an image of microspheres that are 0.5 μm in diameter. The resolution of the camera chip is of the same order as the optical resolution which makes it hard to get a good estimate of the optical resolution. The magnification of the set-up was determined by imaging the 4 μm spheres, which occupy 20 pixels on the camera. The diameter of one 0.5 μm sphere roughly corresponds to 2-4 pixels, which with this magnification corresponds to 0.4-0.8 μm. It thus seems like the optical resolution is at least better than 1 μm.

In this case the resolution might be limited by chromatic aberration since we are detecting fluorescence in the full wavelength range 380-425nm. It thus seems like chromatic aberration still allows imaging with a resolution below 1 μm, which is better than expected.

Next the set-up was tested in confocal mode, at 2K with both the sample, the lens and the scanning system immersed in liquid helium. Since the fluorescing microspheres can not be cooled to 2K without breaking, a gold coated silicon plate with a pattern made by ion beam milling was used instead. This sample did not fluoresce, so the imaging was done by measuring the reflection of the laser beam from the sample, point by point. The resulting image was compared to a scanning electron microscope (SEM) image of the sample. The result is shown in Figure 6.19.

The optical image of the etched structures has a strange shadow like pattern, like if two bright and diagonally slightly displaced images were placed on top of the normal, dark one. This is particularly clear looking at the square in the lower centre of the image

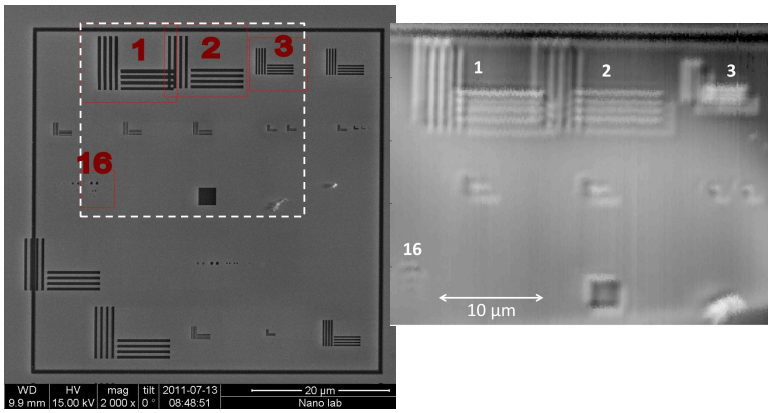

Figure 6.19. *a) A scanning electron microscope image of a sample created by focused ion beam milling. A region of the sample (the white dashed box) was imaged by the confocal optical microscope. b) The resulting optical image taken by measuring reflection from the sample in confocal mode. The features number 1,2,3 and 16 were used to estimate the resolution of the confocal set-up.*

in Figure 6.19. The reason for this is not fully understood. The look of the image reminds me of differential interference contrast microscopy, were two coherent beams of different polarization interfere after interaction with a sample. Since we are using a reflected coherent beam to image the sample it is not impossible that something similar happen.

The etched structures on the sample are 25-50 nm deep, which give rise to a phase shift in the beam depending on if it is reflected on the gold surface or on the silicon at the bottom of an etched structure. After reflection parts of the beam reflected at different places could interfere which could explain the bright and dark parts of the image. Exactly how this creates two diagonally displaced shadows remains to be explained.

The SEM image of the sample was used to measure the spacing of the lines in the L-shaped structures as well as the spacing between the dots, see Figure 6.20. By comparing the optical image to the SEM image, the transverse resolution of the set-up can be estimated to 300-350 nm. For a detailed description of the resolution measurement, see Paper **II**.

By scanning the lens along the beam, so that the focus point will cross the sample surface, the sectioning ability of the set-up can be estimated, see Figure 6.21. When the surface of the sample is out of focus, the amount of light that is reflected from the sample

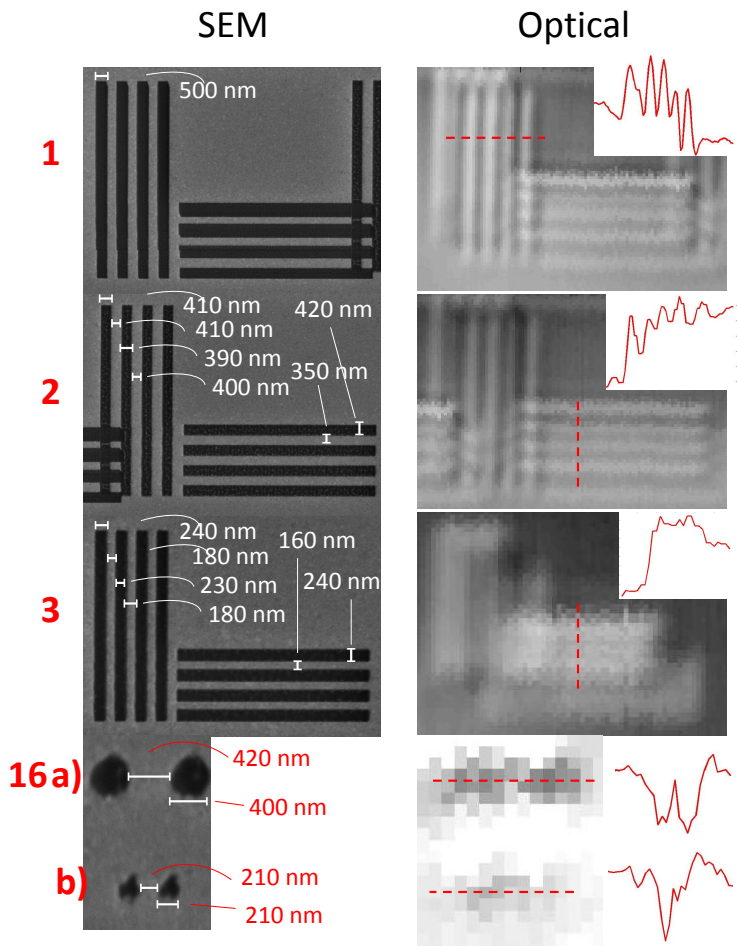

Figure 6.20. *To the left is the SEM image of features 1,2,3 and 16 of the sample, showing some of the distances measured by the SEM. To the right is the corresponding optical images. The lines in L-shaped structures 1 and 2 can be resolved, while the lines in L-shaped structure 3 can not be resolved. Similarly the dots in 16 a) can be resolved but not the dots in 16 b).*

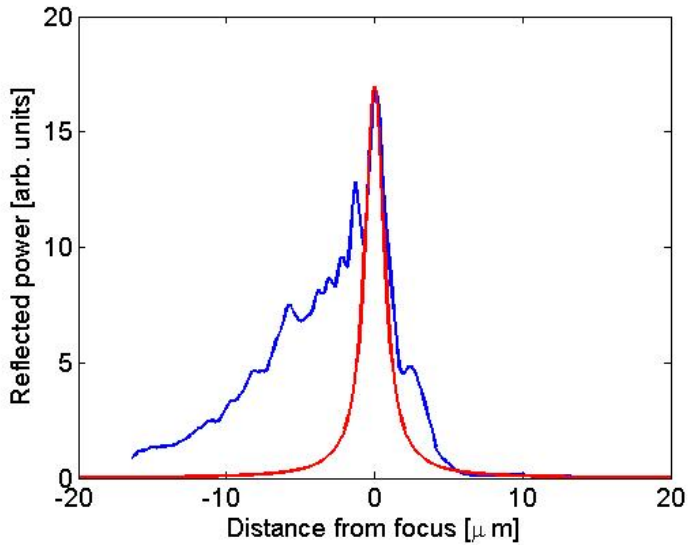

Figure 6.21. *By scanning the lens along the optical axis and hence moving the focus point across the surface of the sample the sectioning ability in the axial direction can be estimated. The FWHM of the curve is 5 μm. The red curve shows an ideal calculated curve, assuming perfectly Gaussian excitation and collection volumes, with focal radi 300 nm.*

and collected by the set-up gives the out of focus contribution to an image. Along the optical axis the curve has a long tail with sub-maxima. This indicates that there is spherical aberration in the beam. The FWHM of the figure is 5 μm, and the $1/e^2$ width in the axial direction is 15 μm. In Figure 6.21, an ideal curve is shown in red, calculated from a Gaussian excitation beam as well as a Gaussian collection volume, both with focal radius 300 nm.

The bad sectioning ability of the set-up might be a problem when trying to detect single ions since a large part of the signal will come from ions that are not in the focus. Since there is no cover layer on the gold sample, and the lens is designed for a cover layer, there should be some spherical aberration present in the beam. This should be improved when focusing at the correct depth below the surface of a crystal.

The curve in Figure 6.21 is however not a measure of the axial *resolution* since we are not measuring the reflection from a single point, but rather the integrated reflection over a plane (the integrated point spread function over each plane). The resolution would ideally be measured in a situation where we have a single point emitter that we move out of focus and measure the detected

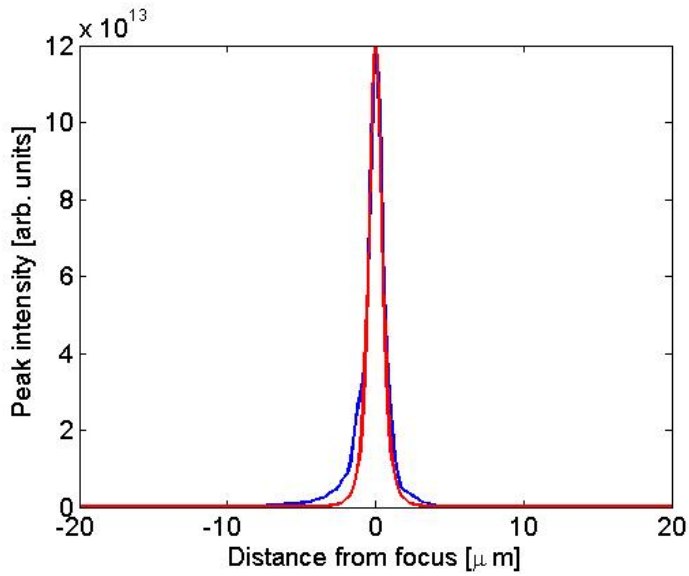

Figure 6.22. *By assuming that the beam diameter widens like a Gaussian beam as we move away from focus the reflected intensity along the optical axis can be calculated. This gives the axial resolution. The FWHM of the curve is 1 μm and the $1/e^2$ length is 2.6 μm. The red curve shows an ideal calculated curve, assuming perfectly Gaussian excitation and collection volumes, with focal radius 300 nm.*

signal as a function of position, rather than a reflecting plane.

To estimate the axial resolution we want to know the detected intensity originating from points on the optical axis, rather than the integrated reflected power from each plane in the beam. We can get a rough estimate of this by assuming that the detection efficiency has a distribution of a perfect Gaussian beam as we move away from focus. Since we know that there are aberrations present, the diameter in each plane might be underestimated.

Figure 6.22 shows the detected reflection from axial points assuming a Gaussian signal distribution in each plane perpendicular to the beam (blue curve). This was calculated from the data in Figure 6.21 by making the assumption mentioned above. The red curve shows an ideal curve calculated from a perfect Gaussian excitation and collection volume. Here the curves match rather well, so even though the sectioning ability of the set-up is compromised my aberrations, the axial resolution is good. The $1/e^2$ distance along the axis is 2.6 μm.

A very rough estimate of the detection volume (up to $1/e^2$ of the maximum intensity) is $\pi * (0.3\mu\text{m})^2 * 2.6\mu\text{m} = 0.7\mu\text{m}^3$.

It should however be pointed out that the detection volume is

not necessarily the most interesting parameter. Here I put the limit of the detection volume at points from where the detected signal is reduced by a factor of $1/e^2$ compared to the signal from the focal point. But the volume not included in the detection volume is very large, and the integrated signal contribution from this large volume might still by stronger the signal from the focus. In that sense the sectioning ability of Figure 6.21 is a better measure of the performance of the microscope.

Chapter 7

Cerium spectroscopy

The single instance quantum computing scheme investigated in this thesis relies on a readout mechanism where the fluorescence emitted by a single cerium ion acts like an indicator lamp, telling whether a qubit ion is in state 0 or 1. The scheme require a single cerium ion to shift out of resonance with the laser as a nearby qubit ion is optically excited. This is only possible within the zero phonon absorption line of the cerium ion. If the transition involve phonon emission, absorption is possible within a wide band of energies, and the cerium can not go off resonance.

The induced frequency shift of the cerium ion due to the change in permanent electric dipole moment of a nearby qubit must be larger than the homogeneous linewidth of the cerium ion. Thus the homogeneous linewidth must be reasonably narrow, in the MHz range.

In this chapter our investigations of the 4f-5d transition of Ce:Y_2SiO_5 are described. The measurements started a couple of years before I entered the group by my predecessor Yan Ying [17]. At first a crystal with a rather high content of cerium, which is shown in Figure 7.1, was investigated. Later on, at about the same time as I started my Ph.D., we moved on to very low concentration crystals. At the stage when we finally tried to detect fluorescence emission from single cerium ions, we also used an undoped Y_2SiO_5-crystal and praseodymium doped Y_2SiO_5 which should contain traces of cerium.

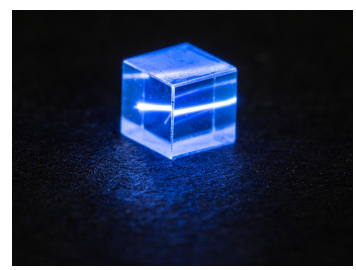

Figure 7.1. *A 0.088% Ce:Y_2SiO_5-crystal fluorescing brightly when excited with a laser beam at 371 nm.*

7.1 Zero phonon line

The zero phonon absorption line of a 4f-5d transition can be very weak due to poor overlap of the wave functions of the 4f and the 5d state.

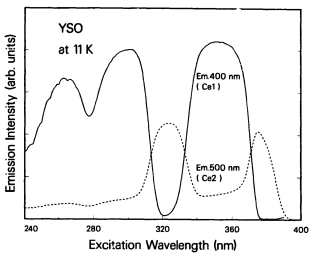

Figure 7.2. *The excitation spectrum for Ce:Y_2SiO_5. The zero phonon line for each site should be located at the low energy, long wavelength, edge of the excitation band. This is around 370 nm for cerium in site 1 and around 390 nm for cerium in site 2. The figure is reprinted with permission from reference [20].*

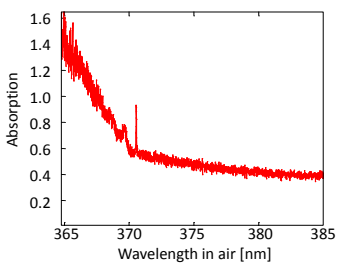

Figure 7.3. *The absorption of 0.088% Ce:Y_2SiO_5 between 365 nm and 385 nm (air wavelength). A zero phonon line is found around 371 nm, and a steep and strong phonon wing shows up at shorter wavelengths. The data was taken by Philippe Goldner and Olivier Guillot-Noël at Chimie ParisTech, Laboratoire de Chimie de la Matière Condensée de Paris.*

In Figure 7.2 a low resolution excitation spectrum of Ce:Y_2SiO_5 is shown. The zero phonon line is the lowest energy excitation (at low temperatures), and should be located at the low energy edge of the excitation band. In our investigations a zero phonon line for cerium ions in site 1 has been found and characterized. For cerium ions in site 2 no zero phonon line has been detected, probably because it is too weak.

The initial search for the zero phonon line was done by Philippe Goldner and Olivier Guillot-Noël at Chimie ParisTech, Laboratoire de Chimie de la Matière Condensée de Paris. A crystal with a rather high cerium concentration of 0.088% was used. The zero phonon line and the start of the phonon wing can be seen in Figure 7.3.

The zero phonon line of the same crystal was measured with higher spectral resolution in our lab by Yan Ying [17]. The result is shown in Figure 7.4. The line centre is found at 370.829 nm (or 370.724 nm in air) and the FWHM is 50 GHz.

There is a broad and rather strong background absorption around the zero phonon line in Figure 7.4. This is due to absorption by cerium ions in crystal site 2. The broad phonon band of the 4f-5d transition for cerium in site 2 overlaps with the zero phonon line of cerium in site 1 in this region, as can be seen in the excitation spectrum in Figure 7.2. As will be clear in Section 7.3, the fluorescence emission from cerium ions in site 2 is at longer wavelengths compared to that of cerium ions in site 1, and can be filtered away [20, 96].

The inhomogeneous linewidth is concentration dependent and for single ion detection 0.088% cerium doping is much too high. For that reason another crystal was investigated, with a cerium concentration around 10^{-7}. A measurement of the zero phonon line in this crystal can be seen in Figure 7.5. In this case the fluorescence emission from the crystal was measured, instead of the absorption as for the higher concentration crystal. The data fits well to a Lorentzian line profile with a FWHM of 37 GHz. The line centre was in this case found at 371.824 nm (or 371.719 nm in air). The line is shifted by 50 GHz towards higher energy compared to the higher concentration crystal.

The inhomogeneous broadening of the zero phonon line comes about because of differences in the local environment of the ions, which shifts the resonance frequency of the individual transitions. The differences in local environment can for example be due to differences in local electric field, caused by the permanent electric dipole moment of other impurities and dopant ions in the crystal. Using this model it has been shown that the inhomogeneous lineshape is Lorentzian for low concentrations of dopants and becomes more and more Gaussian for higher concentrations [97]. This is reflected in the data presented above, where the low concentration crystal has a Lorentzian lineshape, see Figure 7.5, while the

higher concentration crystal has a lineshape which is a sum of a Lorentzian and a Gaussian curve, as in Figure 7.4.

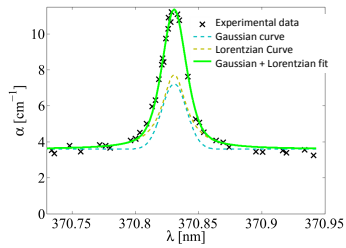

Figure 7.4. *The zero phonon line of 0.088% Ce:Y_2SiO_5. The line is fitted by a combination of a Gaussian and a Lorentzian line profile. The line is centred around 370.829 nm (or 370.724 nm in air) and has a FWHM of 50 GHz. The figure is reprinted with permission from reference [17].*

7.2 Homogeneous linewidth

The homogeneous linewidth of the 4f-5d transition in Ce:Y_2SiO_5 was measured by saturation spectroscopy in our lab by Yan Ying [17]. A strong laser beam was sent through the sample to partly saturate the 4f-5d transition at a certain frequency within the inhomogeneous zero phonon line. A weaker probe beam was spatially overlapped with the pump beam inside the crystal. The probe beam was scanned in frequency by an acousto-optic modulator and the transmission of the probe beam was measured after the crystal. To get better signal to noise, both the probe beam and the pump beam were chopped with different frequencies, f_{pump} and f_{probe} respectively, and the transmission was detected at the sum frequency $f_{pump} + f_{probe}$.

When the pump beam and the probe beam overlap in frequency, they interact with the same ions and an increased transmission can be detected at the sum frequency. The transmission peak is shown in Figure 7.6. The FWHM of the transmission peak is 5.8 MHz.

The transmission peak will be a convolution of the homogeneous line with itself, assuming that the laser linewidth is much narrower than the homogeneous line and does not contribute to the width of the peak. Since the homogeneous line is Lorentzian, the convolution is simply a new Lorentzian function with twice the width. Hence the homogeneous linewidth is limited by half the width of the transmission peak, which is 2.9 MHz (FWHM).

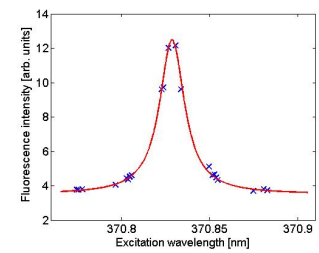

Figure 7.5. *The zero phonon line of 0.00001% Ce:Y_2SiO_5. The fluorescence intensity from the sample is measured for different excitation wavelengths. The red line shows a Lorentzian fit to data. The FWHM of the line is 37 GHz and the line centre is at 371.824 nm.*

The lifetime of the 5d-state of Ce:Y_2SiO_5 is 40 ns [19], which means that the upper limit of the coherence time is 80 ns, and the lower limit on the homogeneous linewidth is 4 MHz. Thus, the measured linewidth of 2.9 MHz is too narrow. This was explained by a slight change in the position of the probe beam as the frequency was tuned to higher values, which made the overlap of the beams worse, and caused the transmission to decrease faster on the higher frequency side of the curve. For more details on this measurement, see Reference [17] and Paper **III**.

The homogeneous linewidth can also be estimated by hole burning measurements. By applying a small magnetic field to the crystal the doubly degenerate crystal field levels will split up into two Zeeman components. By exciting the cerium ions at a fixed frequency within the inhomogeneous line for a short time, they will be transferred to another Zeeman-level, and a spectral hole is created. The spin-lattice relaxation time is around 70 ms, which is considerably longer than the lifetime of the excited 5d-state. The spectral hole can be detected by sweeping the laser

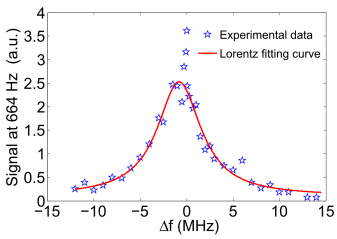

Figure 7.6. *The transmission peak of a saturation spectroscopy measurement. The peak is a Lorentzian with FWHM 5.8 MHz. The homogeneous linewidth is limited by half the width of the transmission peak, 2.9 MHz. Reprinted with permission from reference [17].*

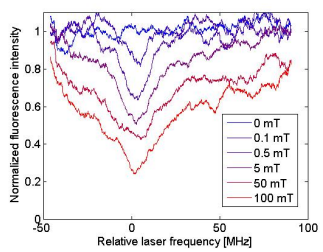

Figure 7.7. *Spectral holes created by redistribution of ions in the Zeeman levels of Ce:Y_2SiO_5 in a small magnetic field.*

frequency quickly over a larger spectral region while monitoring the transmission, or the fluorescence emission of the crystal.

The measurement described above was done with a very low concentration (10^{-7}) cerium crystal. The reason why such a low concentration crystal was used is that the experiment was done in connection to attempts to see a single ion. When we failed to see spectral lines from single ions, we wanted to confirm that the homogeneous linewidth was narrow.

The created spectral holes got wider and deeper for higher magnetic fields, as shown in Figure 7.7. For low magnetic fields there might still be considerable spectral overlap between the Zeeman-levels of the ground state. This makes the hole burning less efficient and the created spectral hole will be shallow.

The narrowest spectral holes for low magnetic fields (0.1 mT-0.5 mT) were about 9 MHz wide (FWHM). This puts an upper limit of the homogeneous linewidth to 4.5 MHz. The measurement confirms that the homogeneous linewidth of the 4f-5d transition in Ce:Y_2SiO_5 is close to lifetime limited. More details on this measurement can be found in Paper **I**.

7.3 Fluorescence spectrum

The fluorescence emission from a 0.088% Ce:Y_2SiO_5 crystal was characterized by exciting the sample within the ZPL at 370.83 nm and detecting the emission with a spectrometer followed by a CCD camera. The fluorescence spectrum can be seen in Figure 7.8. A reference spectrum (offline spectrum) was taken by tuning the laser to longer wavelengths, about 0.7 nm (1.5 THz) away from he ZPL. The offline spectrum shows emission from cerium ions in site 2, while the online spectrum shows emission from cerium ions in both site 1 and site 2 [20, 96, 98, 99]. The offline emission (site 2 emission) is shifted towards longer wavelengths compared to the emission from site 1. Using a band pass filter to block the emission for wavelengths longer than 425 nm would exclude almost all emission from cerium in site 2, while transmitting around 75% of the emission from cerium in site 1.

The fluorescence spectrum from cerium ions in site 1 has three peaks at 402 nm, 425 nm and 440 nm. The spectrum from cerium ions in site 2 has two peaks at 465 nm and 482 nm. The emission spectra found in literature however only show two peaks in the emission from cerium in site 1, located around 395-400 nm and 425-430 nm, and one single broad peak for cerium in site 2 with maximum around 480-500 nm. The two peaks in the emission from site 1 is interpreted as emission from the lower edge of the 5d-band to the two fine structure levels of the ground state, $^2F_{7/2}$ and $^2F_{5/2}$, separated by roughly 2000 cm^{-1} or 60 THz, which at the emission wavelength would correspond to 35 nm [96, 98–100].

Figure 7.9 shows a comparison between our measured fluorescence spectrum and one that was previously published.

The fine structure levels of cerium are further split by the crystal field, into four and three Stark levels for the $^2F_{7/2}$ state and the $^2F_{5/2}$ state respectively. The splitting of the $^2F_{7/2}$ state is such that the Stark levels are grouped two and two, with a larger energy separation between the pairs (level separation 80 cm^{-1} or 1.3 nm, 395 cm^{-1} or 6.6 nm and 210 cm^{-1} or 3.6 nm respectively), see Figure 2.11 in Chapter 2 [8]. This could explain the two peaks around 425 nm and 440 nm for the site 1 emission. The peak at 402 nm would then correspond to emission to the Stark levels of the $^2F_{5/2}$ state.

The fluorescence spectrum from the crystal with a cerium concentration of 10^{-7} has the same structure, see figure 7.10. In this case the fluorescence contribution from cerium in site 2 (the offline spectrum) is weaker compared to the site 1 spectrum. This indicates that at lower doping concentration a larger part of the cerium ions occupy site 1.

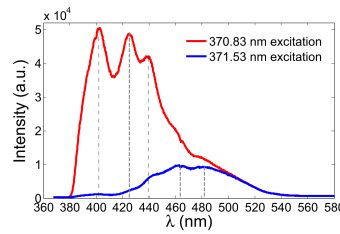

Figure 7.8. *Fluorescence emission from 0.088% Ce:Y_2SiO_5 with excitation on the peak of the ZPL (red curve) and outside the ZPL (blue curve). When exciting outside the ZPL only cerium ions in site 2 will fluoresce. When exciting in the ZPL cerium ions in both site 1 and site 2 will fluoresce. A bandpass filter with transmission between 380 nm and 550 nm was placed in the fluorescence beam.*

7.4 Single ion detection attempts

A few attempts to see emission from single cerium ions were done in our lab during the last couple of years. So far none were successful. Our approach to single ion detection has been to work in an experimental situation were we could potentially also implement quantum gates. We have always worked at or below 4K, exciting cerium ions sitting below the surface of a bulk crystal with an actively stabilized laser at the zero phonon absorption line. To my knowledge all solid proof of single rare earth ion detection published so far are done in experimental situations which are less favourable for quantum computing, in room temperature [70, 71], in nano-crystals [72] or at the surface of a bulk crystal [29, 101], with a possible exception for Reference [29] where a single cerium ion sitting below a half sphere etched into the surface of the crystal is detected. Praseodymium ions detected in a nano-crystal and on the surface of a bulk crystal had linewidths of a few MHz, which is an order of magnitude wider than ions sitting deeper below the crystal surface [72, 101].

Here I will describe a couple of attempts to see a single ion and analyse the results.

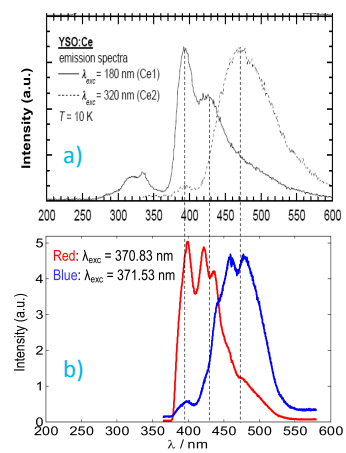

Figure 7.9. *Comparison between the emission spectra for Ce:Y_2SiO_5 (site 1 and site 2 respectively) which was a) previously published, and b) measured in our lab. The figure in a) is reprinted with permission from reference [99]. The spectrum from cerium ions in site 2 has been magnified to allow for easier comparison.*

7.4.1 Method

The single ion detection attempts were done with bulk crystals placed either in a cold finger cryostat or immersed in liquid helium, kept at or below 4K. The excitation intensity of the laser was adjusted to roughly match the saturation intensity of the cerium

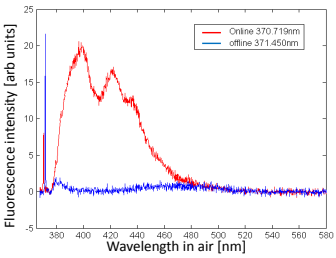

Figure 7.10. *Fluorescence spectra from 0.00001% Ce:Y_2SiO_5. The red curve shows fluorescence when exciting at the peak of the zero phonon line of cerium in site 1 and the blue curve shows fluorescence from cerium in site 2 when exciting far away from the zero phonon line. Some laser light was transmitted through the filters and shows up at 371 nm.*

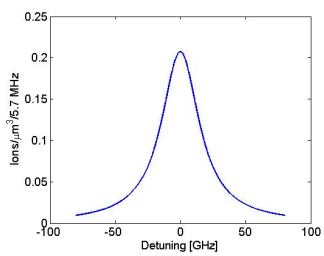

Figure 7.11. *The number of ions per μm^3 within a 5.7 MHz excitation range as a function of detuning from the inhomogeneous line centre. The inhomogeneous line is Lorentzian, and there are in total 2000 cerium ions/μm^3.*

4f-5d transition. The focus of the laser was placed about 100 μm below the surface of the crystal. The focus adjustment was done by first optimizing the laser focus on the surface of the crystal by looking at reflected laser light and then moving the lens towards the crystal in a controlled way with the Attocube nano-positioners.

The frequency of the laser was adjusted to a position within the inhomogeneous line were the fluorescence strength is barely detectable. In the cerium doped samples this implied going offline into the wing of the absorption line, while in the undoped crystal the frequency was kept as close to the line centre as possible. A frequency scan of 10-200 MHz was done by scanning an AOM in the laser system. Single ions would show up as 4 MHz wide fluorescence peaks as the excitation laser is scanned. Since the signal was sometimes low the frequency scan had to be very slow to collect enough signal in each point, or repeated many times to accumulate data. Alternatively an image of the sample was taken in a confocal geometry by scanning the sample. Single ions would show up as randomly placed bright spots in an image.

A single cerium ion should emit about 6 million photons per second when excited at the saturation intensity. About 75% of the photons will be within the spectral range we detect (this is limited by our need to block unwanted fluorescence from cerium ions in site 2). With a detection efficiency of 1.6% in this spectral range this would give us around 70 000 counts per second, which should be clearly visible on our measured background level of 100-500 counts/s. The background consists of dark counts from the photon counter (60 counts/s), reflected laser light and fluorescence from cerium ions in site 2.

7.4.2 Sample 1: Low concentration Ce:Y_2SiO_5

In the Ce:Y_2SiO_5-crystal with a doping concentration of 10^{-7} there is around 2000 ions/μm^3 in the crystal. At the saturation intensity we broaden the absorption region spectrally to about $\sqrt{2}$ times the homogeneous linewidth, which is around $\sqrt{2}$*4 MHz = 5.7 MHz. This crystal has an inhomogeneous linewidth of 37 GHz.

How many ions we interact with depends on where in the inhomogeneous profile we excite. The density of ions within a 5.7 MHz spectral interval as a function of excitation frequency is given in Figure 7.11. At the line centre there are about 0.21 cerium ions/μm^3 interacting with the laser.

With this low concentration of ions there shouldn't be a smooth inhomogeneous line, given that the detection volume is of the order of 1 μm^3, but rather a collection of more or less densely spaced lines from single ions. Thus, already the measurement of the inhomogeneous line profile shown in Figure 7.5, which was taken with the microscope set-up, tells us that something is wrong. Despite the fact that the curve does not have many data points, it is clear

that the signal is not discrete, in the wings the signal decreases rather smoothly at a fluorescence level which is about 10% of the fluorescence level on the peak. Figure 7.12 shows a more recent measurement of the inhomogeneous line. The wings are zoomed in to show the continuous decrease in signal.

The maximum signal we have detected on the peak of the inhomogeneous line in this crystal when exciting at the saturation intensity is 300 000 counts/s, which is more than four times as high as expected for a single ion.

It is possible that the detection volume of the confocal microscope is too large, so that we see much more ions than we expect. It is also possible that the concentration of cerium ions in the crystal is higher than expected, since it is very difficult to measure such small amounts of dopants.

By tuning the laser offline, into the wings of the inhomogeneous profile, there should be fewer ions resonant with the laser in the confocal volume and there should still be a chance to see single ions. Examples of frequency scans taken at the point of the inhomogeneous profile where the signal is just above or at the background level are shown in Figure 7.13, and an example of an image of the sample is shown in Figure 7.14. Despite many spatial and spectral scans at different positions within the inhomogeneous line there has been no obvious trace of single ions.

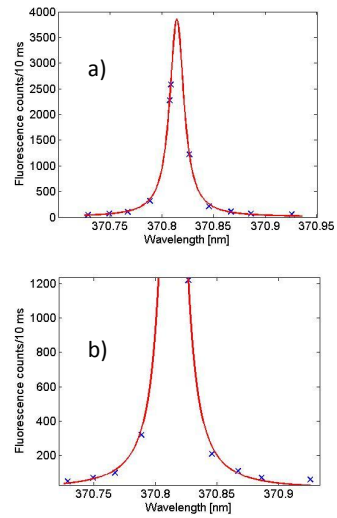

Figure 7.12. *The inhomogeneous line of the 10^{-7} $Ce{:}Y_2SiO_5$-crystal. The signal decreases continuously far out in the wings.*

7.4.3 Sample 2: Undoped Y_2SiO_5

One way to reduce the number of ions in the detection volume is to use an undoped sample. Undoped Y_2SiO_5 contains traces of rare-earth ions, due to the chemical similarity of the rare-earth species. How much cerium there is in the undoped sample is not known. The Y_2SiO_5 sample is bought from Scientific Materials Corp. and they can only tell us that it contains less cerium than a doping level of 10^{-6}.

In this crystal we have failed to see any signal from cerium ions. It is possible that the absorption line is shifted a bit in frequency, and that we simply have not managed to find it. The other alternative is that our set-up is not sensitive enough to detect single ions, or that there are so few ions in the crystal that they are very hard to find. If the detection sensitivity of the set-up is not good enough, the most probable causes are related to the lens. Misalignments of the lens like for example the wrong focal depth into the crystal or a tilt between the lens and the surface can introduce aberrations which lower the collection efficiency from one or few ions. Chromatic aberrations can also have this effect.

Figure 7.15 shows an example of a spatial scan of the undoped crystal. The signal (or rather background) level is around 100 counts/s at the saturation intensity. In Figure 7.15 a higher intensity was used, which has the effect of completely saturating the

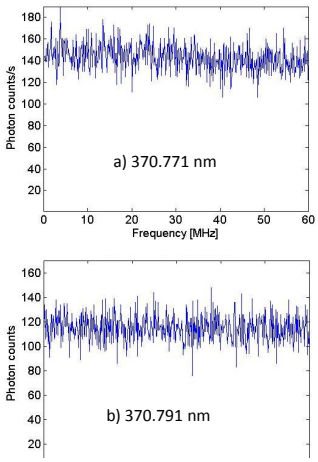

Figure 7.13. *A 60 MHz scan of the low concentration cerium sample. The scan starts at the spectral position where the fluorescence signal is just above the background level (a) and at the background level (b).*

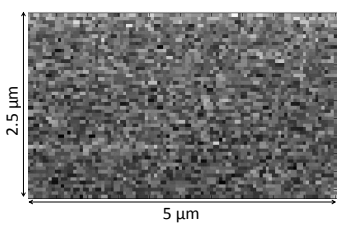

Figure 7.14. *A spatial scan of the low concentration cerium sample. The image is taken about 100 µm below the surface of the crystal, with excitation at 370.799 nm, which is 174 GHz from the line centre. The step size is around 50 nm and the signal varies between 70 counts/s (black) and 150 counts/s (white).*

cerium transition and broadening the frequency range we excite, to increase the chance to see a signal from cerium. There is however no sign of cerium ions. The noise level corresponds well to shot noise from the background signal.

7.4.4 Sample 3: $Pr:Y_2SiO_5$

Since we are in a situation where we see a too strong signal from the cerium doped sample, and no signal from the undoped crystal, we would like to have a sample with a concentration of cerium somewhere between the two. Since cerium and praseodymium are very similar they are hard to separate. In a praseodymium-doped crystal there is always some amount of cerium present, which comes together with the dopant. A 1% $Pr:Y_2SiO_5$-crystal was tested, which should contain more cerium than the undoped sample.

In this sample a signal from cerium was found, which is characterized by the fluorescence spectrum, see Figure 7.16 where the spectrum from a cerium doped crystal is also shown for reference. The fluorescence signal was about 10 times weaker than the maximum signal from the 10^{-7} $Ce:Y_2SiO_5$ sample. The signal disappeared as the laser was tuned far away from the cerium absorption line, but no clear line profile could be mapped out which might indicate that there are few ions in the line. The online spectrum of cerium in site 1 could be found at wavelengths between 370.68 nm and 370.96 nm. Since the crystal contains a rather high concentration of praseodymium it is possible that the inhomogeneous cerium line is very broad.

Despite the promising start no homogeneous lines from single ions have been measured in this crystal, nor any signs of single ions in the spatial images.

7.4.5 Improvements and outlook

After multiple tries to detect a single ion, none have been successful. Starting out from a situation where we can implement quantum gates was possibly a too ambitious plan, and maybe we should have started out with detecting single ions in a simpler situation. My conclusion from the single ion detection attempts is that we don't have good enough control of the confocal volume. This can be improved in several ways. In the end working with a thick sample will always be difficult, and even with a confocal microscope the ability to exclude out of focus light might not be good enough. Below I list some improvements to the detection set-up, which I think will be crucial for future experiments.

Focal depth control

The Blu-ray lens is designed to focus exactly 100 μm below a surface of refractive index 1.5. The tolerance in the thickness of the cover layer is only 3 μm. This should translate to a focal depth tolerance of the same order (a few percent) when focusing into the crystal. If the focal depth is wrong, there will be aberrations which makes the detection volume larger and the collection efficiency per unit volume worse. In principle the Attocube nano-positioners have the required accuracy to position the crystal correctly. It has been noticed however, when imaging standard samples of known size, that the position sensors in the nano-positioners are not showing distances correctly in μm.

If the Blu-ray lens is going to be used for detection below the surface of the crystal the focal depth into the crystal has to be controlled with around 100 nm accuracy. The problem with the feedback sensors of the Attocube positioners must be solved. It might be as simple as changing the cabling going from the cryostat feed-through to the positioners.

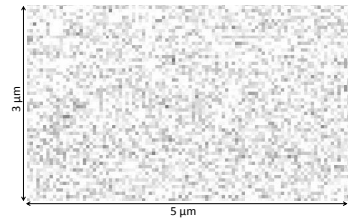

Figure 7.15. *A spatial scan of the undoped cerium sample. The image is taken about 100 μm below the surface of the crystal, with excitation at 370.719 nm, which is on the line centre, and a power which is about 20 times higher than the saturation intensity. The step size is around 50 nm and the grey scale in the image corresponds to 0 counts/s (black) to 600 counts/s (white). The maximum signal of 600 counts/s can be compared to the expected signal from a single ion of 70 000 counts/s.*

Chromatic aberrations

Already in the design process of the microscope set-up the presence of chromatic aberrations when using a single lens was noted but not thoroughly investigated. A lens will focus different wavelengths in slightly different positions. When detecting wide band fluorescence from a sample it can cause a larger detection volume, and a lower collection efficiency from each point of the sample. As the wide field imaging of the microspheres described in the previous chapter worked out well, it was assumed that chromatic aberrations is not a big problem. The microsphere sample fluoresce in a much broader spectral region than the cerium sample. But in that case we had a thin sample, and did not require any depth discrimination. It is possible that chromatic aberration is a problem for single ion detection in a thick sample, and in that case the Blu-ray lens has to be replaced by for example a mirror objective, similar to the one described in Reference [102], which was also successfully used for single rare-earth ion detection [101].

A solid immersion lens

One of the major reasons to use a Blu-ray lens was that it is designed to focus below a surface of higher refractive index. Refraction at the crystal surface does not only require aberration correction, it also makes the collection efficiency much lower. Only 7% of the emitted fluorescence from a single ion is transmitted through the surface of the crystal. One solution to both of these problems is to use a solid immersion lens (SIL), a small half sphere of high refractive index on the crystal surface. A solid immersion lens will

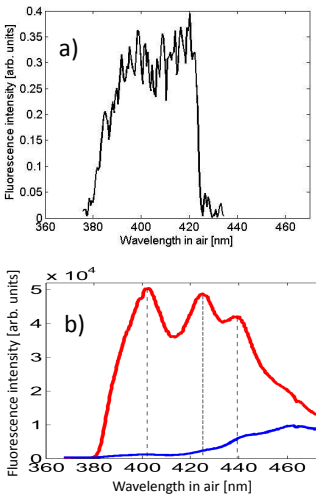

Figure 7.16. *a) shows a fluorescence spectrum from a 1% Pr:Y_2SiO_5-crystal when exciting at 370.71 nm. A bandpass filter cutting at 380 nm and at 425 nm was used. In b) is a reference spectrum from a 0.088% Ce:Y_2SiO_5-crystal when excited at 370.83 nm (red line) and 371.53 nm (blue line).*

make all rays from a single ion sitting exactly at the centre of the SIL on the sample surface to cross the outer surface of the SIL at normal incidence, and they will not be refracted.

In combination with a SIL a collection lens of high NA should be used to collimate the fluorescence, and to focus the laser beam into the SIL. The downside of using a SIL is that the scan range is reduced to a fraction of the diameter of the SIL. To have a good probability to find a single ion close to the centre of the SIL, several SILs can be placed on the sample at different positions.

A SIL can be etched directly into the crystal by ion beam milling, which is done in reference [29]. This has the advantage that the investigated ions are not sitting directly at the sample surface, but are covered by the SIL half sphere. As long as the SIL is reasonably large (100 μm or so) the dopant ions should not be disturbed too much by the milling process.

Outlook

Single ion detection in a bulk crystal is a more challenging task then I first realized. Building a microscope set-up and doing the first attempts to see a single ion has taught us a lot and given us the experience we need to improve the experiment. With a few improvements I think single ion detection is within reach in the near future.

7.5 Charge transfer and trapping

During the cerium florescence experiments it was noted that when the 10^{-7} Ce:Y_2SiO_5 sample was continuously excited within the zero phonon line, the fluorescence signal slowly decreased, as can be seen in Figure 7.17. The signal came back to full strength again after changing the laser frequency to another position within the ZPL, or alternatively after moving the sample a small distance spatially. Afterwards a new decay started. The signal decreased to about 50% of the initial value over a couple of minutes, and then seemed to stabilize. After blocking the laser for 40 minutes and then unblocking it again, the signal showed no sign of recovery, but was still as low as before the laser was blocked.

The width of the created spectral hole was estimated by making frequency jumps of different amplitude and recording the increase in fluorescence. The measurement was very rough, but shows that the spectral hole has a width in the tens of MHz range (10-50 MHz).

It seems like there is a very long-lived trap state to which the ions can be very inefficiently transferred while the 4f-5d transition is cycled. The trap mechanism can for example be charge transfer of an electron in a cerium ion to a charge trap in the crystal lattice. It is well known that various such charge traps exist in Ce:Y_2SiO_5.

They can have very long lifetimes and give rise to afterglow, an emission that can last for hours after excitation [103–110].

Since jumping to a new frequency within the inhomogeneous line brought back the signal, and started a new decay, the trapping must be local in space, and frequency selective. Even if it seems like all traps fill up when exciting at one frequency, moving to another frequency starts a new decay, which shows that new traps are available for a different set of ions in the same focal region. Very similar frequency selective trapping (hole burning) with long trap lifetimes was previously measured in Ce:$LuPO_4$ and Ce:YPO_4 [111].

By studying the intensity dependence of the trapping rate it was concluded that the trapping is not a multi-photon process, and hence the electron can not be transferred to a trap via the conduction band of the crystal. The intensity dependence of the trap rate follows the saturation behaviour of the population in the 5d-state as the intensity is increased, see Figure 7.18.

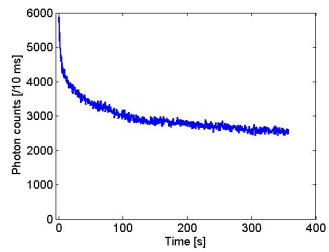

Figure 7.17. *The detected fluorescence from 10^{-7} Ce:Y_2SiO_5 while continuously exciting the 4f-5d transition within the ZPL. The first few seconds the signal drops fast and after that the signal decreases slowly over a couple of minutes. The fluorescence strength approaches a value slightly below 50% of the initial strength.*

7.5.1 Possible trapping mechanisms

Several different mechanisms have previously been suggested to cause charge trapping and afterglow in Ce:Y_2SiO_5. On the basis of our experiments it is possible to exclude some mechanisms that can not be responsible for the decrease in fluorescence, but it is not possible to draw final conclusions regarding which trap mechanisms are actually happening in the crystal. A few examples are given below.

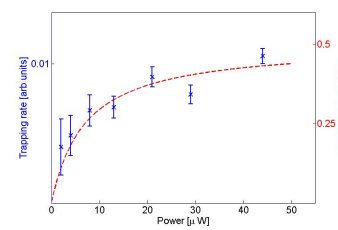

Figure 7.18. *The rate of fluorescence decrease the first 20s of excitation is shown by the blue crosses together with an 80% confidence interval, on the leftmost y-axis. The calculated population in the 5d-state is shown by the dashed red line on the y-axis to the right.*

(i) **Excitation to the conduction band and decay into a trap state**

An electron from a cerium ion that is promoted to the conduction band of the crystal can move freely in the crystal lattice and decay into a trap state. The trap state can be another defect, for example an oxygen vacancy [105, 108, 110].

In our case we excite cerium ions with an energy that is lower than the required energy to promote an electron to the conduction band. The intensity dependence of the process shows that it is not a multi-photon process, and hence trapping does not happen via the conduction band.

(ii) **Excitation of a ligand electron into the cerium ground state**

An electron from the valence band of the crystal, which is normally bound to one of the ligand ions, can be excited into the ground state of cerium, creating a Ce^{2+} ion [105]. This process is however not frequency selective. The electron could end up in the ground state of *any* cerium ion, not only

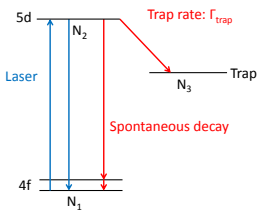

Figure 7.19. *A very simple model of trapping of electrons from a cerium ion.*

cerium ions which are resonant with the laser. In that case, moving the laser 50 MHz in frequency would not bring back the cerium fluorescence signal.

(iii) **Energy transfer from the Ce 5d-state to another defect**

A cerium ion in the excited 5d-state can transfer energy to another defect sitting close by, with a transition of similar energy [106].

The excited defect could potentially cause a change in local electric field and shift the energy of the cerium 4f-5d transition out of resonance with the laser. In this case it requires the excited state of the defect to have a lifetime of hours, which is unlikely.

(iv) **Tunnelling from the 5d-state into a trap state**

An electron which is promoted to the 5d-state could tunnel out of the cerium ion, into another defect, leaving behind a Ce^{4+} ion. This seems to be the most likely process in this case. The other defect can for example be an oxygen vacancy, which can trap an electron and create a so called F^{+}-centre. The tunnelling process is distance dependent and it's possible that only ions with an oxygen vacancy in the close vicinity can be ionized [104, 109].

7.5.2 Rate equation model

A simple toy model was created, assuming that an electron in the 5d-state of cerium spontaneously decays into a trap state, see Figure 7.19. Since the signal decreases on a time scale of seconds, while the excited 5d-state has a lifetime of 40 ns, it can be assumed that the 4f-5d transition is always in a steady state, with a distribution of population in the two levels that depends on the excitation intensity. Spectral saturation broadening was taken into account, since we work close to the saturation intensity of the 4f-5d transition. It was also assumed that there is a limited number of traps available for each set of ions, to account for the fact that the fluorescence signal does not tend to zero.

The rate equation describing the population in the trap state (N_3) can be written as in Equation (7.1), where Γ_{trap} is the probability to tunnel into a trap from the 5d-state and N_{traps} is the fraction of cerium ions with an available trap. All populations are written as a fraction of the total number of participating ions N. The population in the 5d excited state (N_2) can be written as the steady state distribution of the remaining Ce^{3+} ions, as in Equation (7.2), where $I_{sat}(\omega)$ is the frequency dependent saturation intensity. The 4f ground state was treated as a single level and the splitting into fine structure levels and crystal field levels was not

taken into account, since these levels should decay non-radiatively to the ground state on time scales faster than 40 ns.

To take saturation broadening into account, the rate equations were solved numerically one frequency at a time for frequency steps spaced by 300 kHz, in a frequency range of 200 MHz within the inhomogeneous line, and then integrated (summed) over frequency.

$$\begin{aligned}\frac{dN_3(\omega)}{dt} &= \text{trap rate} * \text{5d population} * \text{Fraction with available trap} \\ &= \Gamma_{trap} * N_2(\omega) * (N_{traps} - N_3(\omega))\end{aligned} \tag{7.1}$$

$$\begin{aligned}N_2(\omega) &= \frac{1}{2}(1 - N_3(\omega))(1 - \frac{1}{1 + I/I_{sat}(\omega)}) \\ I_{sat}(\omega) &= I_{sat}(\omega_0)\left(\frac{4(\omega - \omega_0)^2}{\Gamma_{hom}^2} + 1\right)\end{aligned} \tag{7.2}$$

The calculated decrease in fluorescence as a function of time was fitted to the data, using the trap rate, Γ_{trap}, and the number of available traps, N_{traps} as fitting parameters, by minimizing the root mean square (RMS) difference between the calculated curve and the experimental data. The resulting fit can be seen in Figure 7.20. The best fit gave a trap rate Γ_{trap}=0.17 /s and the fraction of available traps N_{traps}=55% of the number of cerium ions.

The calculated curve in Figure 7.20 fits well to data, except for the very few first seconds of fluorescence decrease. The initial fast drop in fluorescence can not be explained this way. It is possible that there is yet another trapping mechanism that happen on a time scale of seconds. It might also be possible that the ions sitting very close to a defect get ionized much faster than ions which are further away from a defect. To explain this behaviour more measurements would have to be done.

The permanent hole burning experiments are described more in detail in Paper **I**.

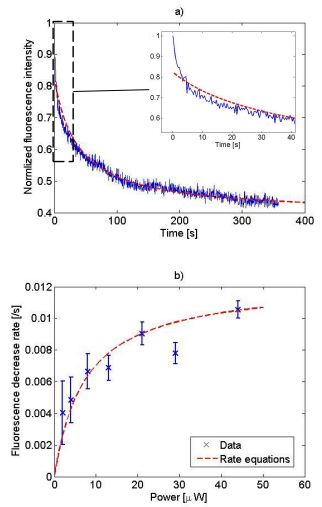

Figure 7.20. *A simple rate equation model is fitted by a least squares fit to the decrease in fluorescence shown in a). The same parameters are used to calculate the intensity dependence of the fluorescence decrease shown in b). No fitting or scaling is applied in b). The best fitted curve has a trap rate of 0.17 /s and the number of available traps is 55% of the number of cerium ions.*

7.5.3 Consequences for single ion detection

Charge transfer and trapping is not a good thing for single ion detection, since if an electron escapes the ion and gets trapped it might not recombine for hours and the ion is lost from view. However, in this case trapping happens on a very slow time scale of several seconds. We can cycle the 4f-5d transition about 14 million times, which lets the cerium ion emit 14 million photons, before the ion has a 10% risk of being trapped. That should be enough to detect a single ion.

7.6 Summary of the results

The zero phonon line for cerium ions in site 1 has been found at 370.829 nm for a higher concentration (0.088%) Ce:Y_2SiO_5 crystal and at 371.824 nm for a very low concentration (10^{-7}) Ce:Y_2SiO_5 crystal. For the high concentration crystal the inhomogeneous linewidth is 50 GHz (FWHM) and for the low concentration crystal it is 37 GHz (FWHM). The homogeneous linewidth of cerium ions in site 1 was measured with saturation spectroscopy and hole burning, which shows that it is around 4 MHz and close to lifetime limited. The characteristic cerium fluorescence spectrum is the same for both concentrations.

Attempts to detect a single cerium ion inside a crystal have not been successful. The reason can be that the detection volume of the microscope is too large. A permanent hole burning mechanism was discovered, and was interpreted as charge transfer from cerium to a charge trap in the crystal lattice.

Chapter 8

Ion-ion interaction

The quantum computing scheme investigated in this thesis requires qubit ions, and pairs consisting of one qubit ion and one readout ion, to interact via their static electric dipole moments. This require the ions to sit closer to each other then a certain critical distance which is set by the change in static dipole moment upon excitation of the ions. At the same time as a strong qubit-qubit interaction is desirable, unwanted interactions which can reduce the coherence time or the lifetime of the ions should be avoided.

The distance between two neighbouring yttrium ions in site 1 in Y_2SiO_5 is less than 0.5 nm. This distance is the smallest possible distance between two dopant ions. Since the dopant ions are randomly distributed in the crystal the distances will vary from pair to pair. The average distance between two ions for a concentration of 1% is about 3.5 nm.

In this chapter our attempts to quantify the interaction strength between ion pairs and to understand and control different interaction mechanisms are described.

8.1 Electric ion-ion interactions

All interactions described in this chapter are fully or partly explained by electric interactions between dopant ions. Since the interactions have the same origin, in the electric properties of the dopant ions, they are also related. In this section I intend to use a simplified case of a two-level system to clarify the relation between them.

I will assume that two ions, denoted A and B, have two energy levels each, denoted g for the ground state and e for the excited state. Thus $|ge\rangle_{AB}$ will be the combined state of ion A in the ground state and ion B in the excited state. For convenience I will drop the subscript and write only $|ge\rangle$.

The electric interaction between the ions can be described by a Hamiltonian H_e. H_e can be written as a multi-pole expansion, and often only the first dipole term is taken into account. In the dipole approximation $H_e \propto 1/r_{AB}^3$, where r_{AB} is the distance between the ions. We will write H_e in the two-ion basis with basis states: $|gg\rangle$, $|ge\rangle$, $|eg\rangle$ and $|ee\rangle$.

The cross terms $\langle ge| H_e |eg\rangle$ and $\langle ge| H_e |eg\rangle$ mixes the states $|eg\rangle$ and $|ge\rangle$. The probability for a transfer from one state to another is $|\langle ge| H_e |eg\rangle|^2$, which in the dipole approximation scales as $1/r_{AB}^6$ and also depends on the mismatch in excitation energy between ion A and ion B (since energy must be preserved). This is a resonant interaction which leads to energy transfer from one ion to another, which is described in Section 8.4. It should however be noted that in a real case one would have to take into account all possible excitation and decay paths of the ions and a two-level approximation is not suitable.

Assuming that the cross-terms are zero, which is the case for example when the transitions of the ions do not overlap, the matrix H_e is diagonal. The diagonal elements; $\langle gg| H_e |gg\rangle$, $\langle ge| H_e |ge\rangle$, $\langle eg| H_e |eg\rangle$ and $\langle ee| H_e |ee\rangle$, are the energy shifts of the basis states due to ion-ion interaction. In the dipole approximation the energy shift depends on the distance between ions as $1/r_{AB}^3$. Since the dopant ions in a crystal are randomly placed relative to each other, the energy shifts will be slightly different for different ions. In the case of ions sitting very close to each other the energy shifts will be particularly large, large enough to shift the transition frequency of the ions out from the main absorption line. Since the crystal structure only allow certain discrete positions of the ions, the nearest neighbour interaction gives rise to discrete satellite lines. As will be discussed further in Section 8.3, the electric interaction alone can not fully explain the position of the satellite lines, but also strain in the crystal lattice due to the introduction of dopant ions is believed to be a major contributor to the frequency shift of nearest neighbour ions.

Another consequence of the diagonal terms of the electric interaction is that the resonant energy of the transition $|gg\rangle \rightarrow |ge\rangle$ is in general not the same as that of $|eg\rangle \rightarrow |ee\rangle$. It means that the transition energy of ion B is dependent on the state of ion A. This gives rise to the frequency shifts that could be used for gate operations in a quantum computer, which are described in Section 8.2.

If the cross terms mentioned above are not zero, the matrix will not be diagonal. The cross terms will then also contribute to the energy of the ions as a second order perturbation, and strictly speaking the basis states used here are not eigenstates of the Hamiltonian. The relationship between diagonal and off-diagonal terms have been discussed for example in Reference [66].

8.2 Static electric dipole interaction

As an ion is promoted to an excited state it will change the static electric field in the local crystal surroundings. The change in local field will Stark shift the transition energies of other ions which are sufficiently close to the excited ion. The shift of transition frequency can, if it is large enough, cause the surrounding ions to go off resonance with the laser and prevent them from being excited.

In the dipole approximation, the shift of the transition frequency of one ion, $\Delta\nu_i$, due to the excitation of another can be quantified as in Equation (8.1) [112], where $\Delta\mu_i$ is the magnitude of the difference in static electric dipole moment between the ground and excited state of the i'th ion, r_{ij} is the distance between the two ions, ϵ_0 =8.854·10^{-12} As/(Vm) is the permeability of free space and h = 6.626·10^{34} Js is Planck's constant. $\eta(\nu)$ is a dielectric correction factor that arises because of polarization of the host crystal, which screens the electric field created by an excited ion. It is calculated as in Equation (8.2), where $\epsilon(\nu)$ is the dielectric function of the material at frequency ν [64]. $\kappa(\Omega)$ is the dependence on the orientation of the dipoles relative to each other, as given by equation 8.3, where $\delta\hat{\mu}_i$ is the unit vector along the dipole moment difference between the ground and excited state of the i'th ion and $\hat{r}_{ij}$ is the unit vector pointing from one ion to the other [112].

$$\Delta\nu_i = \eta(0)\frac{\Delta\mu_i\Delta\mu_j}{4\pi h\epsilon_0 r_{ij}^3}\kappa(\Omega) \tag{8.1}$$

$$\eta(\nu) = \frac{1}{\epsilon(\nu)}\left(\frac{\epsilon(\nu)+2}{3}\right)^2 \tag{8.2}$$

$$\kappa(\Omega) = \delta\hat{\mu}_i\cdot\delta\hat{\mu}_j - 3(\delta\hat{\mu}_i\cdot\hat{r}_{ij})(\hat{r}_{ij}\cdot\delta\hat{\mu}_j) \tag{8.3}$$

Since the difference in static electric dipole moment between the ground and excited state was known for praseodymium and europium [66], the qubit-qubit interaction could be directly estimated with the expressions given above. The dielectric function for static fields, $\epsilon(0)$, was estimated to $\epsilon(0) \approx 7$ for Eu:Y_2SiO_5 in reference [66], while $\epsilon(0) = 9.94$ is given for undoped Y_2SiO_5 in reference [113]. Using these values $\eta(0)$ is 1.28 and 1.6 respectively. Here I choose to use $\eta(0) = 1.6$. Since the directions of the dipoles are unknown, and the ions are randomly placed relative to each other, $\kappa(\Omega)$ is set equal to 1.

In Table 8.1 the frequency shift for a couple of different ion-ion distances are given.

The homogeneous linewidths of praseodymium and europium are approximately 1 kHz and 100 Hz respectively, which means that for realistic ion-ion distances the ions can be shifted by many

Ion-ion distance:	0.5 nm	3.5 nm	10 nm
Pr ($^3H_4$ - $^1D_2$)	8.0 GHz	23 MHz	1.0 MHz
Eu ($^7F_0$ - $^5D_0$)	820 MHz	2.4 MHz	0.1 MHz

Table 8.1: The frequency shift of an ion caused by excitation of another ion (of the same species) for ion-ion distances of 0.5 nm, 3.5 nm and 10 nm.

linewidths and go out of resonance with the laser. Thus, the dipole blockade effect can work as a quantum transistor, changing the state of one ion on the condition that another one is in the ground state. The critical ion-ion distance where the qubit ion is shifted by one homogeneous linewidth is 70 nm for Pr and 78 nm for Eu.

8.2.1 Measurement of the change in static electric dipole moment of cerium

For cerium the static electric dipole moment difference between the ground state (4f) and the excited state (5d) was not previously known. It was measured in Paper **III** using a photon echo technique.

A photon echo is just as it sounds a process where the crystal emits a copy of an input laser pulse some time after the pulse has been sent in. In a two-pulse photon echo two laser pulses are used to trigger the echo. The first pulse puts the ions in a superposition of the ground state and the optically excited state. With time, the superposition state will gain a phase depending on the resonance frequency of the transition. Since the transitions of the ions are inhomogeneously distributed, and have slightly different resonance frequencies, they will gain slightly different phases. After a time t_{12} a second laser pulse is sent in, that will flip the phases of the ions, which will now rephase, and come back to a point where they are in phase with each other, see Figure 8.1 a). A time t_{12} after the second pulse the ions are in phase and they will then emit a pulse of light.

The intensity of the emitted echo, I_{echo}, depends on how well the phases of the ions were preserved between the first pulse and the echo, and hence how well the ions rephased with each other. How well the phases are preserved can be expressed as a function of the coherence time of the ions, T_2, see Equation (8.4). I_0 is the maximum echo intensity when extrapolating to zero pulse separation time t_{12}.

$$I_{echo} = I_0 e^{-4t_{12}/T_2} = I_0 e^{-4\pi t_{12}\Gamma_{hom}} \tag{8.4}$$

If something disturbs the phase or resonance frequency of the ions in a way that is not identical in the dephasing and rephasing period, and not identical for all participating ions, the echo will

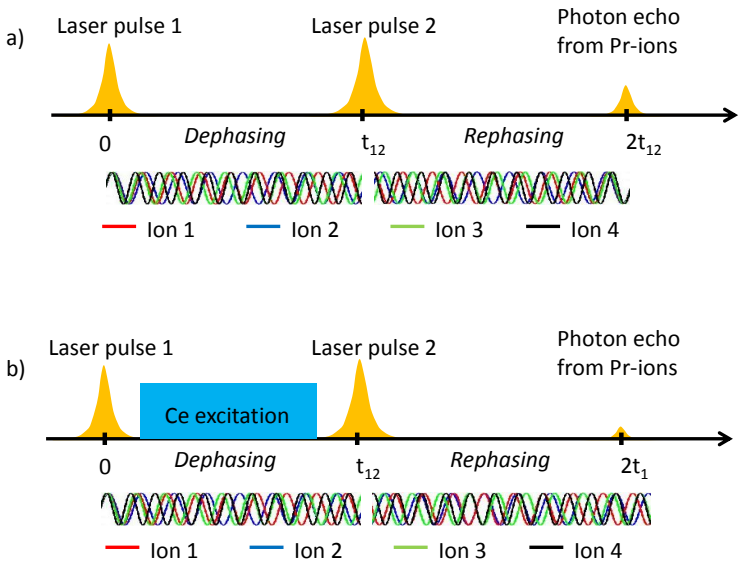

Figure 8.1. *a) The first laser pulse puts the Pr-ions in a superposition state. The ions dephase because of their different resonance frequencies. Laser pulse 2 flips the phases of the ions and they start rephasing. When all ions are in phase again a photon echo is emitted. b) Cerium ions are excited during the dephasing period. Thus, the resonance frequencies of the Pr ions are shifted in a random way during dephasing, but not during rephasing and the ions never completely rephase. The echo signal is attenuated by an amount depending on the interaction between the Ce ions and Pr ions.*

be attenuated. Such a disturbance can for example be excitation of other ions in the crystal which cause a position dependent shift of the resonance frequencies of some of the echo-ions via the static dipole-dipole interaction described previously.

To measure the static dipole moment change of the cerium 4f-5d transition a co-doped crystal containing both cerium (0.088%) and praseodymium (0.05%) was used. A two-pulse photon echo was initiated in the Pr ions. The phase relationship of the Pr ions was disturbed by exciting Ce ions during the dephasing period, as in Figure 8.1 b).

The reduction in the echo intensity due the random frequency shifts caused by excitation of cerium can be expressed as in Equation (8.5), [66, 112, 114]. I_{att} is the attenuated echo intensity, I_{ref} is the echo intensity without cerium excitation and $\nu_j(t)$ is the time dependent transition frequency of the jth Pr ion. The average is taken over all Pr ions participating in the echo.

$$\frac{I_{att}}{I_{ref}} = \left| \left\langle \exp\, i \left(\int_0^{t_{12}} \nu_j(t)dt - \int_{t_{12}}^{2t_{12}} \nu_j(t)dt \right) \right\rangle \right|^2 \tag{8.5}$$

The time dependent frequency of the jth Pr ion, $\nu_j(t)$, can be written as in Equation (8.6), where ν_{0j} is the unperturbed resonance frequency of the ion, $\Delta\nu_k$ is the frequency shift given in Equation (8.1), caused by a cerium ion sitting at lattice site k, ξ_k is a random variable which is 1 if site k is occupied by a cerium ion, and 0 otherwise and $u_k(t)$ is a random variable which is 1 if the cerium ion is excited, and 0 otherwise. The sum is taken over all lattice sites [66, 112].

$$\nu_j(t) = \nu_{0j} + \sum_k \Delta\nu_k \xi_k u_k(t) \tag{8.6}$$

After some mathematics given in reference [66], the echo reduction can be modelled as a broadening of the homogeneous linewidth of the ions, as in Equation (8.7) and Equation (8.8). Γ_{exc} is the additional linewidth contribution caused by cerium excitation. $\langle|\kappa|\rangle$ is the effect of the relative dipole orientation, averaged over all relative positions between the two ions. $\langle|\kappa|\rangle$ is equal to $\frac{4}{\sqrt{27}} \approx 0.77$ for parallel dipoles and $\frac{2}{\pi} \approx 0.64$ for perpendicular dipoles, and since the dipole orientation is unknown it is set to 0.7. ρ_0 is the density of sites for which the dopant ion could substitute (in this case yttrium site 1) and p is the cerium site occupation probability which depends on the cerium concentration. $\langle P_{exc}\rangle$ is the average excitation probability of a cerium ion, with the average taken over all ions in the inhomogeneous line. Since we excite continuously and since the excited state lifetime of cerium is much shorter than the total excitation time, $\langle P_{exc}\rangle$ can be calculated from the steady state population in the excited state and the homogeneous linewidth of cerium.

$$I_{att} = I_0 e^{-4\pi t_{12}(\Gamma_{hom}+\Gamma_{exc})} \tag{8.7}$$

$$\Gamma_{exc} = \frac{\pi}{3}\rho_0 p \langle|\kappa|\rangle \nu(0) \frac{\Delta\mu_{Pr}\Delta\mu_{Ce}}{4\pi\hbar\epsilon_0} \langle P_{exc}\rangle \tag{8.8}$$

Γ_{exc} was measured by varying the pulse separation time t_{12} and recording the echo intensity in two cases; with cerium excitation at 371.54 nm, which only excites cerium ions in site 2, and at 370.83 nm which excites the zero phonon line of cerium ions in site 1 as well as cerium ions in site 2. The contribution from cerium ions in site 2 should be equal in both cases since the phonon wing absorption profile is spectrally broad. The additional broadening measured at 370.83 nm should then correspond to excited cerium ions in site 1. The result is shown in Figure 8.2.

Qubit-cerium distance:	0.5 nm	3.5 nm	10 nm
Pr	320 GHz	930 MHz	40 MHz
Eu	100 GHz	300 MHz	13 MHz

Table 8.2: The frequency shift of a cerium ion caused by excitation of a qubit ion (Pr or Eu) for ion-ion distances of 0.5 nm, 3.5 nm and 10 nm.

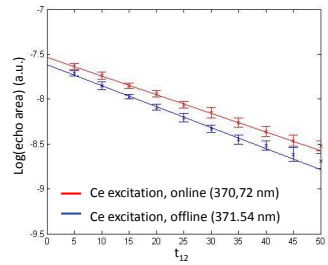

Figure 8.2. *The logarithm of the echo area as a function of pulse separation t_{12}. The slope of the curve is proportional to the homogeneous linewidth. For excitation of cerium in site 2 (offline) the homogeneous linewidth is 3.8 kHz, for excitation of cerium in site 1 and site 2 (online) the linewidth has been broadened to 4.3 kHz. Thus the broadening caused by excitation of cerium in site 1 is 0.5 kHz. By comparison to reference data taken with no cerium excitation (laser off) in connection to the online and offline measurement, the broadening was corrected to 0.6 kHz. For more details see Paper* ***III****.*

The additional broadening Γ_{att} caused by excitation of cerium ions in site 1 was measured to 0.6 kHz. By using Equation (8.8) the difference in static dipole moment between the cerium (site 1) 4f ground state and the excited 5d state was calculated to $9.6 \cdot 10^{-30}$ Cm. This is 40 times higher than the difference in static electric dipole moment for Pr ($2.4 \cdot 10^{-31}$) and 125 times higher than for Eu ($7.7 \cdot 10^{-32}$) [66].

The interesting property from the point of view of the quantum computing scheme is how much a cerium ion will be shifted by an excited qubit at a realistic distance. With the known static electric dipole moment difference this can be calculated, and the numbers are given in Table 8.2. The shifts are larger than the homogeneous linewidth of cerium (4 MHz), and hence an excited Pr or Eu ion could shift a cerium ion out of resonance with the laser via the dipole blockade effect. The critical distance from a cerium ion to an excited qubit where the cerium ion is shifted by one homogeneous linewidth is 14.7 nm in the case of Eu and 21.5 nm in the case of Pr.

8.3 Satellite lines

The inhomogeneous zero phonon line of a transition of rare-earth ions doped into a crystal is surrounded by a number of much weaker absorption lines, or satellite lines, with widths similar to the main line. The satellite lines are due to rare-earth ions sitting in perturbed crystal sites, with a defect or crystal impurity in the close vicinity. For good quality crystals with commonly used concentrations of dopants, the most likely impurity is another dopant ion.

The electric dipole-dipole interaction between ion pairs cause an energy shift of the transitions large enough to shift nearest neighbour ions out from the main absorption line. The shift depends on the distance between ions as $1/r^3$. Experimentally it has been shown that the frequency shift of the satellite lines do not follow the $1/r^3$ dependence on ion-ion distance, and the electric interactions alone can not fully explain the positions of the lines. Most probably crystal lattice distortions due to the introduction of a dopant ion of different radius than the host ion will also contribute to the satellite line positions [115].

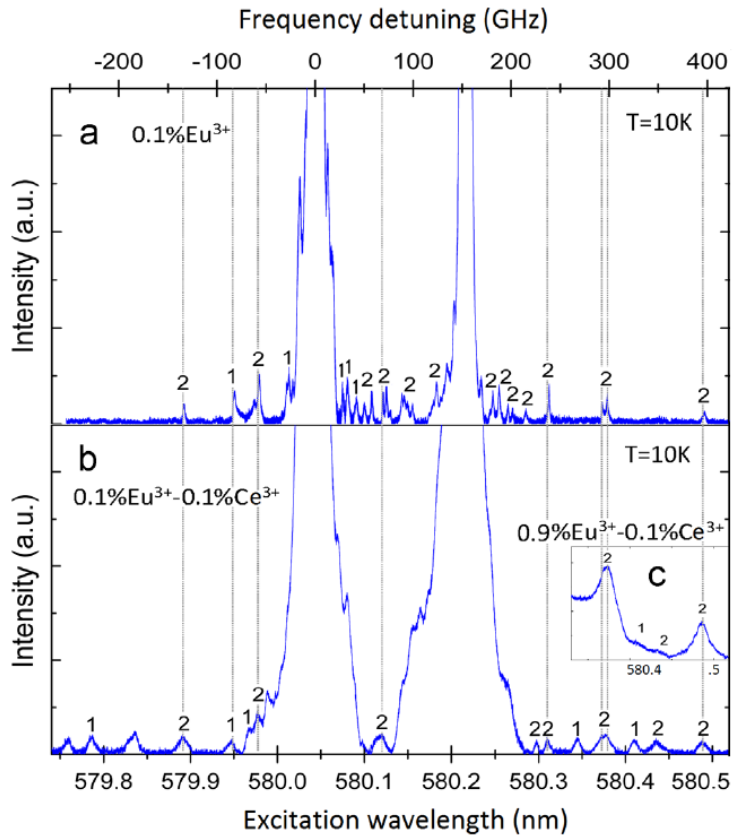

Figure 8.3. *The satellite lines of a) a singly doped Eu:Y_2SiO_5 crystal and b) a codoped Ce-Eu:Y_2SiO_5 crystal. The vertical bars connecting the spectra indicates overlapping lines, which originates from pairs of Eu ions. The additional lines in b) originates from Ce-Eu pairs.*

The quantum computing scheme investigated in this thesis require finding qubit ions that sit close to each other and interact strongly. For the readout of a qubit state a cerium ion must sit close enough to a qubit ion to interact strongly. The satellite lines contains subgroups of strongly interacting ions which can be selectively excited.

In Paper **IV** the satellite lines of Pr and Eu doped Y_2SiO_5 crystals was compared to those of Ce-Pr and Ce-Eu codoped crystals. The result is shown in Figure 8.3 for Eu and Eu-Ce doped samples, and in Figure 8.4 for Pr and Pr-Ce doped samples. The codoped crystals gave rise to the same satellite lines as the singly doped, plus a number of new lines. The lines that were only present in the

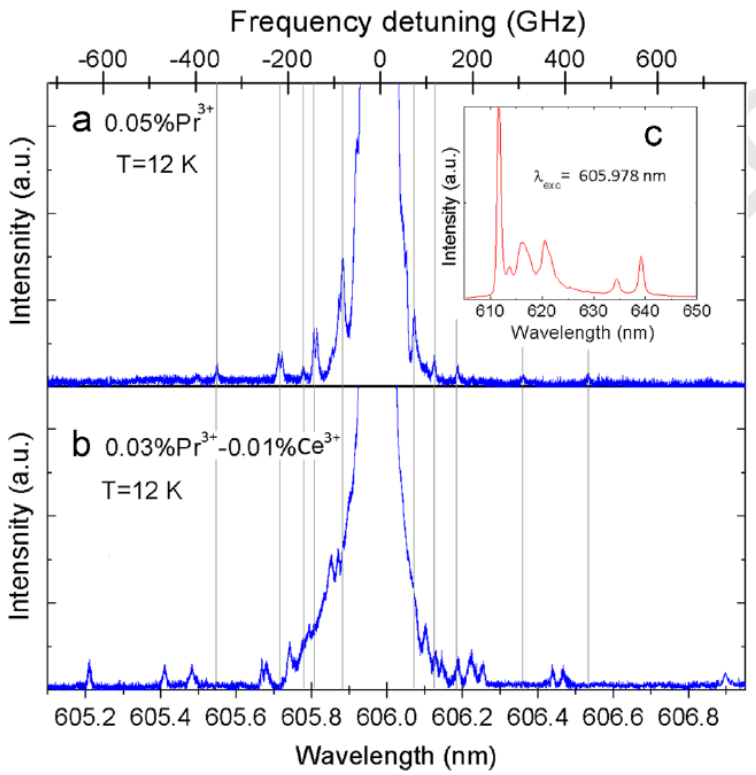

Figure 8.4. *The satellite lines of a) a singly doped Pr:Y_2SiO_5 crystal and b) a codoped Ce-Pr:Y_2SiO_5 crystal. The vertical bars connecting the spectra indicates overlapping lines, which originates from pairs of Pr ions. In b) these lines are very weak, barely visible. They were confirmed by detecting the fluorescence spectrum with a less noisy detector, as is shown in the inset. A possible reason for the weak Pr-Pr lines is cross-relaxation between the Pr ions, which quenches the fluorescence. Lines belonging to Ce-Pr pairs, which are only present in the codoped sample, are much stronger.*

codoped samples were interpreted as pairs consisting of a cerium ion and a qubit ion. Fluorescence spectra were recorded for selective excitation of individual satellite lines, confirming that they belong to Eu and Pr. In the case of Pr, lines belonging to Pr-Pr pairs were much weaker than lines caused by Ce-Pr pairs. This might be because of cross-relaxation between pairs of Pr ions, see Section 8.4.

The satellite lines of a codoped or singly doped sample can be used to explore interactions between pairs of ions. For example, using a codoped Ce-Pr:Y_2SiO_5 sample, and identifying satellite lines related to both the praseodymium absorption line and the cerium absorption line could potentially allow us to find pairs of satellite lines, one related to Pr and one related to Ce, caused by the same neighbouring Ce-Pr pairs. Excitation in the relevant Pr satellite line would then shift a large number of cerium ions out from the corresponding Ce satellite line, reducing the absorption within the line. Initial measurements of satellite line structure related to the cerium 4f-5d transition were done, but unfortunately the external cavity diode laser used for cerium excitation has too bad scanning characteristics to obtain reliable data. The laser can only be continuously scanned over a range of 6 GHz before mode jumping. Since the mode jumps are 38 GHz, which is of the same size as the inhomogeneous linewidth of the transition, we could only cover a small part of the spectrum.

8.4 Energy transfer

If the fluorescence spectrum of one ion (the donor) overlaps with the absorption spectrum of another ion (the acceptor), an excitation in the donor can be directly transferred to the acceptor without the intermediate creation of a photon, in a process of non-radiative energy transfer. This process in unwanted for the quantum computing scheme since it can destroy the information stored in qubits. The most sensitive step in terms of energy transfer is the readout of information from a qubit, since a cerium ion will be cycled between the ground and excited state thousands of times, and the probability that an energy transfer happens between the cerium ion and the qubit during this process must be very small.

Energy transfer only occurs if the ions sit sufficiently close to each other, but the static dipole interaction between ions that is necessary for the quantum computing scheme do require that they are not too distant. What saves the day is that the energy transfer probability scales as $1/r_{ij}^6$, while the energy shift induced by static dipole interaction decreases slower with distance, as $1/r_{ij}^3$ where r_{ij} is the ion-ion distance, assuming dipolar interactions. The scaling gives some room for finding an ion-ion distance where the static dipole shift is sufficiently large while the energy transfer

Qubit ion	Qubit-cerium distance
Pr	3-22 nm
Eu	2-15 nm

Table 8.3: Cerium-qubit distances that could lead to a successful readout of the qubit state, where the lower bound is set by the energy transfer probability, and the upper bound is set by the frequency shift of the cerium ions due to excitation of the qubit ion.

probability is sufficiently small.

In the dipole-dipole approximation the energy transfer rate can be written as in Equation (8.9), where C is a parameter depending on the spectral overlap, as in Equation (8.10). Here c is the vacuum speed of light, n is the refractive index of the crystal, σ_{Em} is the cross section for fluorescence emission by the donor and σ_{Abs} is the cross section for absorption by the acceptor, at the wavelength λ.

$$A_{ET} = \frac{C}{r_{ij}^6} \tag{8.9}$$

$$C = \frac{3c}{8\pi^4 n^2} \int \sigma_{Em}(\lambda)\sigma_{Abs}(\lambda)d\lambda \tag{8.10}$$

In Paper **??** the spectral overlap between the cerium fluorescence emission and the europium as well as praseodymium absorption was evaluated. For the case of europium also dipole-quadrupole interactions were taken into account, since some of the europium transitions are dipole forbidden. If we set the limit for the acceptable energy transfer rate to one energy transfer event per 2000 cerium 4f-5d cycles, which is approximately the number of cycles we need for a reliable readout, a minimum distance between ion pairs can be calculated. The minimum distance is around 3 nm for the case of Pr and 2 nm for Eu.

In the previous section we determined maximum ion-ion distances for sufficiently large energy shifts due to static dipole interaction. The range of distances between a cerium ion and a qubit ion which can lead to a successful readout of the qubit state are summarized in table 8.3.

The question immediately arises; how easy is it to find pairs of ions with an ion-ion distance in this range? To be able to form chains of interacting qubits it is desirable to use a high concentration of qubit ions. For a qubit ion concentration of 2% the probability to find a cerium ion with no qubit ions closer than 2 nm is only 4%. Since energy transfer also leads to a partial quenching of the cerium fluorescence, the task of finding such a cerium ion where the energy transfer probability is low is equivalent to finding a strongly fluorescing cerium ion. This is in principle easily done

by scanning the sample spatially or by scanning the 370.83 nm laser in frequency while recording cerium fluorescence.

The optical transitions of ion-ion pairs which sits closer than about 1.5 nm from each other are shifted out from the main absorption line, into a satellite line, as was explained in the previous section. One way to avoid energy transfer is then simply **not** to use the ions in the satellite lines, contrary to what was suggested previously.

Energy transfer between qubit ions can also be a problem for the quantum computing scheme. This has not been investigated in detail in the present work, but it is previously known that there is a cross-relaxation path for praseodymium ions sitting sufficiently close to each other [116, 117]. As one Pr ion decays via the $^1D_2 \rightarrow {}^1G_4$ transition, energy is transferred to a second ion which is promoted to the $^3F_4$-state (from the $^3H_4$ ground state). In Paper **IV** it is shown that the fluorescence from satellite lines caused by Pr-Pr pairs is weaker than expected, and a possible cause is cross-relaxation which quenches the Pr fluorescence. For the application as a quantum processor it might be necessary to carefully consider the concentration of Pr ions in the crystal, to reduce the probability for cross-relaxation.

For europium there is to the best of my knowledge no cross-relaxation paths, and the $^7F_0$ - $^5D_0$ transition is very weak, which makes energy migration unlikely.

8.5 Overlapping transitions

Overlapping transitions is not in itself an interaction between ions, but nonetheless important in this context. For cerium to work as a readout ion, it is important that the cerium transition at 370.83 nm is not resonant with any transitions of the qubit ions, since the readout laser would then also excite the qubit ions and destroy the information stored in them.

It turns out that europium ions absorb at the cerium wavelength of 370.83 nm. By exciting a pure Eu:Y_2SiO_5 crystal at 370.83 nm characteristic europium fluorescence was detected.

The conclusion is that europium and cerium is not a suitable pair for quantum processing and readout. This was discovered rather late in the process of this work and for that reason I have chosen to include data and results for both Pr and Eu in this thesis.

Since europium has longer lifetimes and coherence times than praseodymium it is more attractive for quantum computing applications. For that reason an investigation into alternative readout mechanisms also started. Some of the initial ideas can be found in Paper **VI**.

8.6 Summary of the results

The change of static electric dipole moment between the cerium 4f and 5d state was measured with a photon echo technique. The range of possible cerium-europium and cerium-praseodymium distances for a successful qubit readout was determined to 2-15 nm and 3-22 nm respectively. The upper limit is set by the static electric dipole shifts, which must be larger than the cerium homogeneous linewidth. The lower limit is set by the energy transfer probability during readout.

Satellite lines belonging to pairs of Pr and Ce as well as Eu and Ce were identified. It was noted that satellite lines belonging to Pr-Pr pairs are very weak, which was interpreted as quenching via cross-relaxation.

It was realised that Eu absorbs at the cerium excitation wavelength 370.83nm, which appears to prevent reading out the state of a Eu ion by looking at Ce fluorescence. ju

Chapter 9

Conclusion and outlook

In principle, all the building blocks of a quantum computer is contained in a Pr:Y_2SiO_5 or a Eu:Y_2SiO_5 crystal. Praseodymium and europium ions doped into Y_2SiO_5 have hyperfine levels in the ground state with extremely long coherence times, and an optical transition which can be used for qubit manipulation. The static electric dipole interaction between ions is strong enough to shift an ion out of resonance with the laser, by promoting the other ion to the excited state, and in that way create a quantum transistor.

Taking the rare-earth quantum computing scheme to the microscopic level and using single ions in the crystal as qubits is believed to allow the system to be scaled to several qubits. The first steps towards microscopic manipulation of rare-earth ions in a crystal have been taken during the course of this work.

Cerium has been investigated as a potential quantum state probe for reading out the state of the qubits. The cerium absorption and fluorescence spectrum has been characterized and the interaction between a cerium ion and a qubit has been shown to be strong enough for qubit readout.

A major challenge when implementing a quantum computing scheme in rare-earth-ion-doped crystals is to identify and control the unwanted processes taking place in the crystal, such as energy transfer. The problem of energy transfer between a cerium ion and a qubit is solved by finding interacting ions with ion-ion distances larger than 2-3 nm. This can be done by finding a strongly fluorescing cerium ion, which is not quenched by energy transfer. By monitoring the fluorescence while exciting different parts of the qubit absorption line, qubits which are coupled to the cerium ion can be mapped out. If the cerium fluorescence stops, there is a chance that a qubit ion is found which shifts the cerium ion out of resonance with the laser.

Eu:Y_2SiO_5 absorb at the resonance wavelength of the cerium zero phonon 4f-5d transition. This makes it difficult to use cerium

as a quantum state probe for europium ions. Ce-Pr is still believed to be a potential qubit-readout ion pair. Praseodymium however has a shorter excited state lifetime than europium which puts higher requirements on the cerium detection set-up, since fluorescence from a single cerium ion must be detected while the Pr ion is in the excited state. With the present microscope set-up only 12 counts would be recorded during the lifetime of a Pr ion. Cross-relaxation between Pr ion pairs can be another complication, which prevents the use of nearest neighbour Pr ions as qubits. Using ions absorbing in the satellite lines is probably impossible due to cross-relaxation.

Europium is more attractive as a qubit because of the longer coherence times and absence of cross-relaxation processes. It might be possible to find another readout ion that is compatible with europium. The most important consideration when choosing a readout ion is, apart from the fluorescence yield, also the spectral properties. Ideally there should not be any overlap between the absorption and emission spectra of the readout ion and the qubit ion, to prevent energy transfer and unwanted excitations.

Small mode volume cavities are interesting as a method to increase the emission rate of a resonant transition via the Purcell effect. It opens up the possibility to use a transition that normally has a long lifetime as a readout transition. This could in principle be any 4f-4f transition in a rare-earth ion.

Single ion detection is believed to be within reach in the near future. Reading out the state of a qubit is the next challenge which require finding a suitable pair of qubit species and readout species. Ce and Pr might still be a possible combination, with an improved single ion detection set-up. Another option is to use europium as a qubit, and to find another readout ion, for example a 4f-4f transition of a rare-earth ion in combination with a small mode volume cavity.

When the state of one single qubit can be prepared and detected, the remaining challenge is scaling the system to more qubits. The concentration of ions inside the crystal needs to be carefully considered, depending on the energy transfer properties of the ions, and the probability of finding interacting qubit chains.

The many degrees of freedom of rare-earth-ion-doped crystals makes the system complex, but also very versatile. When finding all the right combinations; the right dopants, the right concentrations, possible combinations with cavities etc., rare-earth-ion-doped crystals are still very promising for development of quantum computing hardware.

The Author's Contribution to the Papers

I **Hole burning and frequency selective trapping in Ce:Y_2SiO_5 at liquid helium temperatures**
J. Karlsson, A. N. Nilsson, D. Serrano, A. Walther, L. Rippe and S. Kröll
A. Ferrier and P. Goldner.
Manuscript in preparation.

In this paper we perform hole burning in Ce:Y_2SiO_5 by redistribution of ions in the Zeeman levels in a small magnetic field. The width of the created spectral holes confirms that the homogeneous linewidth of the 4f-5d transition in cerium is close to lifetime limited. We present a very slow and long lived hole burning mechanism which is interpreted as charge trapping via the 5d-state of cerium.
I built the set-up used in the experiment, performed all measurements together with Adam Nilsson, interpreted data and wrote the manuscript.

II **A confocal optical microscope for detection of single impurities in a bulk crystal at cryogenic temperatures**
J. Karlsson, L. Rippe, and S. Kröll.
(2015) *Submitted to Review of Scientific Instruments.*

In this paper we describe the design and test of a confocal microscope setup for detection of single cerium ions.
I did the design and construction of the microscope, performed all measurements and wrote the manuscript.

III **Measurement of line-widths and permanent electric dipole moment change of the Ce 4f-5d transition in Y2SiO5 for a qubit readout scheme in rare-earth ion based quantum computing**
Y. Yan, J. Karlsson, L. Rippe, A. Walther, D. Serrano, S. Kröll, P. Goldner, D. Lindgren, M-E. Pistol, L. Zheng and J. Xu.
Phys. Rev. B **87**, 184205 (2013).

In this paper we present some of the important spectroscopic properties of Ce:Y_2SiO_5 for the purpose of using it as a readout ion for single ion qubits. We measure the change of the static electric dipole moment between the 4f and 5d state of cerium.
I did the static dipole moment measurement together with Ying Yan and participated in discussions regarding the experiment, calculations and the manuscript. I helped with improving the set-up and in the re-building of a the laser system used for Pr-excitation.

IV **Satellite line mapping in Eu^{3+}-Ce^{3+} and Pr^{3+}-Ce^{3+} codoped Y_2SiO_5**
D. Serrano, J. Karlsson, L. Zheng, Y. Dong, A. Ferrier, P. Goldner, A. Walther, L. Rippe, and S. Kröll.
Accepted for publication in J. of Lumin , (2015).

In this paper we map out satellite lines in singly doped and codoped crystals, and identify lines that are caused by Ce-Eu and Ce-Pr pairs. Within these satellite lines a qubit ion (Eu or Pr) is strongly interacting with a readout ion (Ce) which is necessary for the quantum computing scheme presented in this thesis.
I did all measurements together with Diana Serrano, constructed part of the set-up and participated in discussions and interpretation of data.

V **Impact of ion-ion energy transfer on quantum computing schemes in rare-earth doped solids**
D. Serrano, Y. Yan, J. Karlsson, L. Rippe, A. Walther, S. Kröll, A. Ferrier and P. Goldner.
J. of Lumin. **151**, 93-99 (2014).

In this paper we study energy transfer between qubit ions (Pr and Eu) and the read out ion (Ce). Energy transfer can potentially destroy the information stored in a qubit, before read out is possible. In this paper we find bounds on the distance between ions required to avoid energy transfer but still have a strong enough dipole interaction between the ions.
I helped in some parts of the experiment and participated in discussions.

VI **High-fidelity readout scheme for rare-earth solid-state quantum computing**
A. Walther, L. Rippe, Y. Yan, J. Karlsson, D. Serrano, A. N. Nilsson, S. Bengtsson and S. Kröll.
Phys. Rev. A **92**, 022319 (2015).

In this paper we discuss alternative readout schemes involving small mode volume cavities. A buffer ion is introduced as a method to increase the fidelity of qubit readout. The fidelity of a CNOT-gate with readout is calculated and scalability to many qubits is discussed.
I did initial calculations regarding fluorescence collection efficiencies and the possibility to detect single ions, and I participated in discussions.

Acknowledgements

One of the major benefits with working in science is all the smart and kind people from all over the world I have had the privilege to get to know. Without the knowledge, skills and support of people around me this thesis would never have been written.

Many thanks to my main supervisor, Stefan Kröll, for always taking the time to discuss and for being very supportive. There were times when I was about to give up, but a kind word and a good advise from Stefan got my motivation up. I want to thank my co-supervisor Lars Rippe for teaching me a lot of useful things and for being a force that keeps the group moving forward. I am grateful to my second co-supervisor Anne L'Huillier for taking the time to understand my project even if it's not in her field of research and for contributing with good ideas and wisdom. Anne has always been a role model to me and her humble yet determined approach to research is very inspiring. I am greatly thankful to Yan Ying, who fought with this project before me. She taught me all about the lab, cerium ions and many other things that came up during our long experiments. Her work forms the basis for all results presented in this thesis.

The Quantum Information group has provided a creative and open atmosphere where no question is too stupid to ask, no idea too far fetched to be discussed and no one is too inexperienced to be listened to. For that I want to thank all current and former members of the group. I want to give special thanks to Diana Serrano, a world-citizen of great skill who I learned a lot from, Adam Nilsson for being as friendly and helpful as he is smart, Andreas Walther for being the one that best explains things so that I understand, Qian Li for all easy-going discussions and Mahmood Sabooni for always smiling while working. I also want to thank my master students, Martynas Solveius and Tobias Bladh, for all work with the microscope and for teaching me how to be a supervisor. You made my work too easy.

I am very grateful to Leif Magnusson and Stefan Schmiedel for providing us with liquid helium. We have no idea how lucky we are. I would like to thank all administrative staff at the Division of Atomic Physics, Minna Ramkull, Camilla Nilsson, Harriett Lin-

dahl, Anne Petersson Jungbeck and Jakob Testad, for being very patient with my complete lack of ability to write travel bills and for handling all my invoices for two screws at a time. A special thanks to Jakob for the Wednesday-running. Big thanks to Bertil Hermansson and Åke Johansson for fixing my computer, helping out with soldering and all other things I had no clue how to do.

Many thanks to the people we have cooperated with during the years, Philippe Goldner, Alban Ferrier, Mats-Erik Pistol, David Lindgren and Ivan Scheblykin. Thank you for all useful discussions and all faithful work you put into the projects, especially that which did not end up in a publication.

Doing a Ph.D. would not have been half as fun without the great social atmosphere at the division. I would like to thank the Attogroup for adopting me into the big atto-family. I can't thank all of you individually, you're just too many, but I think you can imagine what I would say to each of you.

I also want to thank the 2015 board of the SPIE/OSA student chapter for being more professional and ambitious than I could ever hope for, you rock!

Big thanks to all my wonderful office mates, coffee companions, and more.

Some people have grown closer and become an indispensable part of my life. I am greatly thankful to Linnea, my friend, colleague, neighbour, mentor and companion in all life's ups and downs for more than ten years. Also big thanks to Lovisa, a true friend in good times and bad times. A special greeting to Algot and Elise, I will never forget that a Däääääär says more than 1000 words.

I would like to thank all my non-physicist friends, Matlaget for keeping me well fed even in stressful times, Henrik and Jonas for keeping me fit, the great horse Zefir for keeping me calm, Turid and Sofia for letting me borrow him and Lysekilsfolket; Rebecca, Emma, Jenny for always letting me back in, and especially Malin for sharing the wisdom and worries of a Ph.D.-student. You all keep me sane.

I am very grateful to my dad for always being there when I need him, whether it means picking up horse shit or more serious things, and to my mum for making me brave enough to think that I can do whatever I want. I would like to thank my brother for giving me inspiration and courage, and for his two wonderful daughters, Ellen and Agnes, who I am sure will rule the world one day.

Finally, Diego, for taking me to Paris, for your patience and understanding, for our travels, for ice cream and Dr Who, for all your love, I am more than grateful.

References

1. Gordon E. Moore. *Cramming More Components onto Integrated Circuits*. In *Proceedings of the IEEE* volume 86 (1998).

2. Rachel Courtland. *Gordon Moore: The Man Whose Name Means Progress*. IEEE spectrum (2015).

3. Krishnamurthy A. and Gupta C. K. *Extractive Metallurgy of Rare Earths* chapter 1. The Rare Earths. CRC Press, Florida (2005).

4. Liu G. *Spectroscopic Properties of Rare Earths in Optical Materials* chapter Electronic Energy Level Structure. Springer-Verlag Berlin (2005).

5. A. J. Freeman and R. E. Watson. *Theoretical Investigation of Some Magnetic and Spectroscopic Properties of Rare-Earth Ions*. Phys. Rev. **127**, 2058–2075 (1962). URL http://link.aps.org/doi/10.1103/PhysRev.127.2058.

6. Flurin Könz, Y. Sun, C. W. Thiel, R. L. Cone, R. W. Equall, R. L. Hutcheson and R. M. Macfarlane. *Temperature and concentration dependence of optical dephasing, spectral-hole lifetime, and anisotropic absorption in* Eu^{3+}*:*Y_2SiO_5. Phys. Rev. B **68**, 085109 (2003). URL http://link.aps.org/doi/10.1103/PhysRevB.68.085109.

7. Dieke G. H., Crosswhite H. M. and Crosswhite H. . *Spectra and energy levels of rare earth ions in crystals*. Interscience Publishers New York (1968).

8. W. T. Carnall, G. L. Goodman, K. Rajnak and R. S. Rana. *A systematic analysis of the spectra of the lanthanides doped into single crystal* LaF_3. The Journal of Chemical Physics **90**, 3443–3457 (1989). URL http://scitation.aip.org/content/aip/journal/jcp/90/7/10.1063/1.455853.

9. Meijerink A. and Wegh R. T. . *VUV Spectroscopy of Lanthanides: Extending the Horizon*. Materials Science Forum **315-317**, 11–26 (1999).

10. P Dorenbos. *The 5d level positions of the trivalent lan-*

thanides in inorganic compounds. Journal of Luminescence **91**, 155 – 176 (2000). URL http://www.sciencedirect.com/science/article/pii/S0022231300002295.

11. P. Dorenbos. *The $4f^n$ - $4f^{n-1}5d$ transitions of the trivalent lanthanides in halogenides and chalcogenides*. Journal of Luminescence **91**, 91 – 106 (2000). URL http://www.sciencedirect.com/science/article/pii/S0022231300001976.

12. L. van Pieterson, M. F. Reid, R. T. Wegh, S. Soverna and A. Meijerink. *$4f^n \rightarrow 4f^{n-1}5d$ transitions of the light lanthanides: Experiment and theory*. Phys. Rev. B **65**, 045113 (2002). URL http://link.aps.org/doi/10.1103/PhysRevB.65.045113.

13. M. Raukas, S. A. Basun, W. van Schaik, W. M. Yen and U. Happek. *Luminescence efficiency of cerium doped insulators: The role of electron transfer processes*. Applied Physics Letters **69**, 3300–3302 (1996). URL http://scitation.aip.org/content/aip/journal/apl/69/22/10.1063/1.117286.

14. Ziqi Sun, Meishuan Li and Yanchun Zhou. *Thermal properties of single-phase Y_2SiO_5*. Journal of the European Ceramic Society **29**, 551 – 557 (2009). URL http://www.sciencedirect.com/science/article/pii/S0955221908003968.

15. Lutz Petersen. *High-resolution spectroscopy of praseodymium ions in a solid matrix: towards single-ion detection sensitivity*. PhD thesis ETH Zurich (2011).

16. Malkin B. Z. *Spectroscopic Properties of Rare Earths in Optical Materials* chapter Ion-phonon interactions. Springer-Verlag Berlin (2005).

17. Ying Yan. *Towards single Ce ion detection in a bulk crystal for the development of a single-ion qubit readout scheme*. PhD thesis Lund University, Lund (2013).

18. R. W. Equall, Y. Sun, R. L. Cone and R. M. Macfarlane. *Ultraslow optical dephasing in Eu^{3+}:Y_2SiO_5*. Phys. Rev. Lett. **72**, 2179–2182 (1994). URL http://link.aps.org/doi/10.1103/PhysRevLett.72.2179.

19. Tuomas Aitasalo, Jorma Hls, Mika Lastusaari, Janina Legendziewicz, Janne Niittykoski and Fabienne Pell. *Delayed luminescence of Ce^{3+} doped Y_2SiO_5*. Optical Materials **26**, 107 – 112 (2004). URL http://www.sciencedirect.com/science/article/pii/S0925346703003264. Proceedings of the Second International Conference on Sol–Gel Materials. Research, Technology, Applications (SGM'03).

20. H. Suzuki, T.A. Tombrello, C.L. Melcher and J.S. Schweitzer. *UV and gamma-ray excited luminescence of cerium-doped rare-earth oxyorthosilicates*. Nuclear Instruments and Methods in Physics Research Section A: Accelerators, Spectrometers, Detectors and Associated Equipment **320**, 263 – 272 (1992). URL http://www.sciencedirect.com/science/article/pii/0168900292907842.

21. Flurin Könz, Y. Sun, C. W. Thiel, R. L. Cone, R. W. Equall, R. L. Hutcheson and R. M. Macfarlane. *Temperature and concentration dependence of optical dephasing, spectral-hole lifetime, and anisotropic absorption in* Eu^{3+}*:*Y_2SiO_5. Phys. Rev. B **68**, 085109 (2003). URL http://link.aps.org/doi/10.1103/PhysRevB.68.085109.

22. Andrea Arcangeli, Marko Lovrić, Biagio Tumino, Alban Ferrier and Philippe Goldner. *Spectroscopy and coherence lifetime extension of hyperfine transitions in* $^{151}Eu^{3+}$*:*Y_2SiO_5. Phys. Rev. B **89**, 184305 (2014). URL http://link.aps.org/doi/10.1103/PhysRevB.89.184305.

23. Zhong M., Hedges M. P., Ahlefeldt R. L., Bartholomew J. G., Beavan S. E., Wittig S. M., Longdell J. J. and Sellars M. J. *Optically addressable nuclear spins in a solid with a six-hour coherence time*. Nature **517**, 177–180 (2015).

24. E. Fraval, M. J. Sellars and J. J. Longdell. *Method of Extending Hyperfine Coherence Times in* Pr^{3+}*:*Y_2SiO_5. Phys. Rev. Lett. **92**, 077601 (2004). URL http://link.aps.org/doi/10.1103/PhysRevLett.92.077601.

25. R. W. Equall, R. L. Cone and R. M. Macfarlane. *Homogeneous broadening and hyperfine structure of optical transitions in* Pr^{3+}*:*Y_2SiO_5. Phys. Rev. B **52**, 3963–3969 (1995). URL http://link.aps.org/doi/10.1103/PhysRevB.52.3963.

26. Keith Holliday, Mauro Croci, Eric Vauthey and Urs P. Wild. *Spectral hole burning and holography in an* Y_2SiO_5*:*Pr^{3+} *crystal*. Phys. Rev. B **47**, 14741–14752 (1993). URL http://link.aps.org/doi/10.1103/PhysRevB.47.14741.

27. Nicklas Ohlsson, Mattias Nilsson and Stefan Kröll. *Experimental investigation of delayed self-interference for single photons*. Phys. Rev. A **68**, 063812 (2003). URL http://link.aps.org/doi/10.1103/PhysRevA.68.063812.

28. Georg Heinze, Christian Hubrich and Thomas Halfmann. *Stopped Light and Image Storage by Electromagnetically Induced Transparency up to the Regime of One Minute*. Phys. Rev. Lett. **111**, 033601 (2013). URL http://link.aps.org/doi/10.1103/PhysRevLett.111.033601.

29. Siyushev P., Xia K., Reuter R., Jamali M., Zhao N., Yang N., Duan C., Kukharchyk N., Wieck A. D., Kolesov R. and Wrachtrup J. *Coherent properties of single rare-earth spin qubits*. Nature Communications **5** (2014).

30. Feynman R. P. *Simulating Physics with Computers*. International Journal of Theoretical Physics **21**, 467–488 (1982).

31. P. W. Shor. *Algorithms for Quantum Computation: Discrete Logarithms and Factoring*. In *Proceedings of the 35th Annual Symposium on Foundations of Computer Science* SFCS '94 pages 124–134 Washington, DC, USA (1994). IEEE Computer Society. ISBN 0-8186-6580-7. URL http://dx.doi.org/10.1109/SFCS.1994.365700.

32. Grover L. K. *A fast quantum mechanical algorithm for database search*. In *Proceedings, 28th Annual ACM Symposium on the Theory of Computing* page 212 (1996).

33. Schrödinger E. *Die gegenwärtige Situation in der Quantenmechanik*. Naturwissenschaften **23**, 807–812; 823–828; 844–849 (1935).

34. David P. DiVincenzo. *The Physical Implementation of Quantum Computation*. Fortschritte der Physik **48**, 771–783 (2000). URL http://dx.doi.org/10.1002/1521-3978(200009)48:9/11<771::AID-PROP771>3.0.CO;2-E.

35. Ladd T. D., Jelezko F., Laflamme R., Nakamura Y., Monroe C. and OBrien J. L. *Quantum Computers*. Nature **464**, 45–53 (2010).

36. W. H. Oskay, S. A. Diddams, E. A. Donley, T. M. Fortier, T. P. Heavner, L. Hollberg, W. M. Itano, S. R. Jefferts, M. J. Delaney, K. Kim, F. Levi, T. E. Parker and J. C. Bergquist. *Single-Atom Optical Clock with High Accuracy*. Phys. Rev. Lett. **97**, 020801 (2006). URL http://link.aps.org/doi/10.1103/PhysRevLett.97.020801.

37. J. I. Cirac and P. Zoller. *Quantum Computations with Cold Trapped Ions*. Phys. Rev. Lett. **74**, 4091–4094 (1995). URL http://link.aps.org/doi/10.1103/PhysRevLett.74.4091.

38. Chiaverini J., Leibfried D., Schaetz T., Barrett M. D., Blakestad R. B., Britton J., Itano W. M., Jost J. D., Knill E., Langer C., Ozeri R. and Wineland D. J. *Realization of quantum error correction*. Nature **432**, 602–605 (2004).

39. Häffner H., Hänsel W., Roos C. F., Benhelm J., Chek alkar D., Chwalla M., Körber T., Rapol U. D., Riebe M., Schmidt P. O., Becher C., Gühne O., Dür W. and Blatt R.

Scalable multiparticle entanglement of trapped ions. Nature **430**, 54–58 (2004).

40. Thomas Monz, Philipp Schindler, Julio T. Barreiro, Michael Chwalla, Daniel Nigg, William A. Coish, Maximilian Harlander, Wolfgang Hänsel, Markus Hennrich and Rainer Blatt. *14-Qubit Entanglement: Creation and Coherence*. Phys. Rev. Lett. **106**, 130506 (2011). URL http://link.aps.org/doi/10.1103/PhysRevLett.106.130506.

41. Hanhee Paik, D. I. Schuster, Lev S. Bishop, G. Kirchmair, G. Catelani, A. P. Sears, B. R. Johnson, M. J. Reagor, L. Frunzio, L. I. Glazman, S. M. Girvin, M. H. Devoret and R. J. Schoelkopf. *Observation of High Coherence in Josephson Junction Qubits Measured in a Three-Dimensional Circuit QED Architecture*. Phys. Rev. Lett. **107**, 240501 (2011). URL http://link.aps.org/doi/10.1103/PhysRevLett.107.240501.

42. DiCarlo L., Chow J. M., Gambetta J. M., Bishop L. S., Johnson B. R., Schuster D. I., Majer J., Blais A., Frunzio L., Girvin S. M. and Schoelkopf R. J. *Demonstration of two-qubit algorithms with a superconducting quantum processor*. Nature **460**, 240–244 (2009).

43. T. Lanting, J. Przybysz, A. Yu. Smirnov, A. M. Spedalieri, F. H. Amin, M. J. Berkley, A. R. Harris, F. Altomare, S. Boixo, P. Bunyk, N. Dickson, C. Enderud, P. Hilton, J. E. Hoskinson, W. Johnson, M. E. Ladizinsky, N. Ladizinsky, R. Neufeld, T. Oh, I. Perminov, C. Rich, C. Thom, M. E. Tolkacheva, S. Uchaikin, B. Wilson, A. and G. Rose. *Entanglement in a Quantum Annealing Processor*. Phys. Rev. X **4**, 021041 (2014). URL http://link.aps.org/doi/10.1103/PhysRevX.4.021041.

44. Adrian Cho. *Quantum or not, controversial computer yields no speedup*. Science **344**, 1330–1331 (2014). URL http://www.sciencemag.org/content/344/6190/1330.short.

45. Balasubramanian G., Neumann P., Twitchen D., Markham M., Kolesov R., Mizuochi N., Isoya J., Achard J., Beck J., Tissler J., Jacques V., Hemmer P. R., Jelezko F. and Wrachtrup J. *Ultralong spin coherence time in isotopically engineered diamond*. Nature Materials **8**, 383–387 (2009).

46. Lilian Childress and Ronald Hanson. *Diamond NV centers for quantum computing and quantum networks*. MRS Bulletin **38**, 134–138 (2013). URL http://journals.cambridge.org/article_S0883769413000201.

47. van der Sar T., Wang Z. H., Blok M. S., Bernien H. abd Taminiau T. H., Toyli D. M., Lidar D. A. Awschalom D.

D., Hanson R. and Dobrovitski V. V. *Decoherence-protected quantum gates for a hybrid solid-state spin register*. Nature **484**, 82–86 (2012).

48. Dolde F., Jakobi I., Naydenov B., Zhao N., Pezzagna S., Trautmann C., Meijer J., Neumann P., Jelezko F. and Wrachtrup J. *Room-temperature entanglement between single defect spins in diamond*. Nature Physics **9**, 139–143 (2013).

49. Zhao Z., Chen Y., Zhang A., Yang T., Briegel H. J. and Pan J. *Experimental demonstration of five-photon entanglement and open-destination teleportation*. Nature **430**, 54–58 (2004).

50. Politi A., Matthews J. C. F. and OBrien J. L. *Shor's Quantum Factoring Algorithm on a Photonic Chip*. Science **325**, 1221 (2009).

51. S. Olmschenk, D. N. Matsukevich, P. Maunz, D. Hayes, L.-M. Duan and C. Monroe. *Quantum Teleportation Between Distant Matter Qubits*. Science **323**, 486–489 (2009). URL http://www.sciencemag.org/content/323/5913/486.abstract.

52. Bernien H., Hensen B., Pfaff W., Koolstra G., Blok M. S., Robledo L., Taminiau T. H., Markham M., Twitchen D. J., Childress L. and Hanson R. *Heralded entanglement between solid-state qubits separated by three metres*. Nature **497**, 86–90 (2013).

53. Carter S. G., Sweeney T. M., Kim M., Kim C. S., Solenov D., Economou E., Reinecke T. L., Yang L., Bracker A. S. and Gammon D. *Quantum control of a spin qubit coupled to a photonic crystal cavity*. Nature Photonics **7**, 329–334 (2013).

54. Andrei Faraon, Charles Santori, Zhihong Huang, Victor M. Acosta and Raymond G. Beausoleil. *Coupling of Nitrogen-Vacancy Centers to Photonic Crystal Cavities in Monocrystalline Diamond*. Phys. Rev. Lett. **109**, 033604 (2012). URL http://link.aps.org/doi/10.1103/PhysRevLett.109.033604.

55. Aoki T., Dayan B., Wilcut E., Bowen W. P., Parkins A. S., Kippenberg T. J., Vahala K. J. and Kimble H. J. *Observation of strong coupling between one atom and a monolithic microresonator*. Nature **443**, 671–674 (2006).

56. Wallraff A., Schuster D. I., Blais A., Frunzio L., Huang R.-S., Majer J., Kumar S., Girvin S. M. and Schoelkopf R. J. *Strong coupling of a single photon to a superconducting qubit using circuit quantum electrodynamics*. Nature **431**, 162–167 (2004).

57. Zhong T., Hartz A., Miyazono E. and Faraon A. *Towards coupling rare earth ions to a Y_2SiO_5 nanophotonic resonator*. In *Proceedings, CLEO: QELS Fundamental Science, Quantum Interconnects* page FTh1B (2014).

58. G. J. Pryde, M. J. Sellars and N. B. Manson. *Solid State Coherent Transient Measurements Using Hard Optical Pulses*. Phys. Rev. Lett. **84**, 1152–1155 (2000). URL http://link.aps.org/doi/10.1103/PhysRevLett.84.1152.

59. Nicklas Ohlsson, R Krishna Mohan and Stefan Krll. *Quantum computer hardware based on rare-earth-ion-doped inorganic crystals*. Optics Communications **201**, 71 – 77 (2002). URL http://www.sciencedirect.com/science/article/pii/S0030401801016662.

60. Kouichi Ichimura. *A simple frequency-domain quantum computer with ions in a crystal coupled to a cavity mode*. Optics Communications **196**, 119 – 125 (2001). URL http://www.sciencedirect.com/science/article/pii/S0030401801013943.

61. M. D. Lukin and P. R. Hemmer. *Quantum Entanglement via Optical Control of Atom-Atom Interactions*. Phys. Rev. Lett. **84**, 2818–2821 (2000). URL http://link.aps.org/doi/10.1103/PhysRevLett.84.2818.

62. L. Rippe, B. Julsgaard, A. Walther, Yan Ying and S. Kröll. *Experimental quantum-state tomography of a solid-state qubit*. Phys. Rev. A **77**, 022307 (2008). URL http://link.aps.org/doi/10.1103/PhysRevA.77.022307.

63. J. J. Longdell and M. J. Sellars. *Experimental demonstration of quantum-state tomography and qubit-qubit interactions for rare-earth-metal-ion-based solid-state qubits*. Phys. Rev. A **69**, 032307 (2004). URL http://link.aps.org/doi/10.1103/PhysRevA.69.032307.

64. G. D. Mahan. *Local-Field Corrections to Coulomb Interactions*. Phys. Rev. **153**, 983–988 (1967). URL http://link.aps.org/doi/10.1103/PhysRev.153.983.

65. Felix R. Graf, Alois Renn, Gert Zumofen and Urs P. Wild. *Photon-echo attenuation by dynamical processes in rare-earth-ion-doped crystals*. Phys. Rev. B **58**, 5462–5478 (1998). URL http://link.aps.org/doi/10.1103/PhysRevB.58.5462.

66. Felix R. Graf, Alois Renn, Gert Zumofen and Urs P. Wild. *Photon-echo attenuation by dynamical processes in rare-earth-ion-doped crystals*. Phys. Rev. B **58**, 5462–5478 (1998). URL http://link.aps.org/doi/10.1103/PhysRevB.58.5462.

67. Lars Rippe, Mattias Nilsson, Stefan Kröll, Robert Klieber and Dieter Suter. *Experimental demonstration of efficient and selective population transfer and qubit distillation in a rare-earth-metal-ion-doped crystal.* Phys. Rev. A **71**, 062328 (2005). URL http://link.aps.org/doi/10.1103/PhysRevA.71.062328.

68. R. L. Ahlefeldt, D. L. McAuslan, J. J. Longdell, N. B. Manson and M. J. Sellars. *Precision Measurement of Electronic Ion-Ion Interactions between Neighboring Eu^{3+} Optical Centers.* Phys. Rev. Lett. **111**, 240501 (2013). URL http://link.aps.org/doi/10.1103/PhysRevLett.111.240501.

69. R. L. Ahlefeldt, W. D. Hutchison, N. B. Manson and M. J. Sellars. *Method for assigning satellite lines to crystallographic sites in rare-earth crystals.* Phys. Rev. B **88**, 184424 (2013). URL http://link.aps.org/doi/10.1103/PhysRevB.88.184424.

70. Kolesov R., Xia K., Reuter R., Stöhr R., Zappe A., Meijer J., Hemmer P. R. and Wrachtrup J. *Optical detection of a single rare-earth ion in a crystal.* Nature Communications **3** (2012).

71. Roman Kolesov, Kangwei Xia, Rolf Reuter, Mohammad Jamali, Rainer Stöhr, Tugrul Inal, Petr Siyushev and Jörg Wrachtrup. *Mapping Spin Coherence of a Single Rare-Earth Ion in a Crystal onto a Single Photon Polarization State.* Phys. Rev. Lett. **111**, 120502 (2013). URL http://link.aps.org/doi/10.1103/PhysRevLett.111.120502.

72. Utikal T., Eichhammer E., Petersen L., Renn A., Götzinger S. and Sandoghdar V. *Spectroscopic detection and state preparation of a single praseodymium ion in a crystal.* Nature Communications **5** (2014).

73. Janus H. Wesenberg, Klaus Mølmer, Lars Rippe and Stefan Kröll. *Scalable designs for quantum computing with rare-earth-ion-doped crystals.* Phys. Rev. A **75**, 012304 (2007). URL http://link.aps.org/doi/10.1103/PhysRevA.75.012304.

74. Andrew D. Ludlow, Martin M. Boyd, Jun Ye, E. Peik and P. O. Schmidt. *Optical atomic clocks.* Rev. Mod. Phys. **87**, 637–701 (2015). URL http://link.aps.org/doi/10.1103/RevModPhys.87.637.

75. Karsten Danzmann and the LISA study team. *LISA: laser interferometer space antenna for gravitational wave measurements.* Classical and Quantum Gravity **13**, A247 (1996). URL http://stacks.iop.org/0264-9381/13/i=11A/a=033.

76. Kessler T., Hagemann C., Grebing C., Legero T., Sterr U., Riehle F., Martin M. J., Chen L. and Ye J. *A sub-40-mHz-linewidth laser based on a silicon single-crystal optical cavity.* Nature Photonics **6**, 687–692 (2012).

77. Drever R. W. P., Hall J. L., Kowalski F. V., Hough J., Ford G. M., Munley A. J. and Ward H. *Laser phase and frequency stabilization using an optical resonator.* Applied Physics B **31**, 97–105 (1983).

78. R. V. Pound. *Electronic Frequency Stabilization of Microwave Oscillators.* Review of Scientific Instruments **17**, 490–505 (1946). URL http://scitation.aip.org/content/aip/journal/rsi/17/11/10.1063/1.1770414.

79. Eric D. Black. *An introduction to PoundDreverHall laser frequency stabilization.* American Journal of Physics **69**, 79–87 (2001). URL http://scitation.aip.org/content/aapt/journal/ajp/69/1/10.1119/1.1286663.

80. B. Julsgaard, A. Walther, S. Kröll and L. Rippe. *Understanding laser stabilization using spectral hole burning.* Opt. Express **15**, 11444–11465 (2007). URL http://www.opticsexpress.org/abstract.cfm?URI=oe-15-18-11444.

81. Adam Wiman. Laser stabilization to low-expansion Fabry-Pérot cavity. Master's thesis Lund University (2011).

82. David R. Leibrandt, Michael J. Thorpe, Mark Notcutt, Robert E. Drullinger, Till Rosenband and James C. Bergquist. *Spherical reference cavities for frequency stabilization of lasers in non-laboratory environments.* Opt. Express **19**, 3471–3482 (2011). URL http://www.opticsexpress.org/abstract.cfm?URI=oe-19-4-3471.

83. Lars Rippe. *Quantum Computing with sub-nanometre-spaced ions.* PhD thesis Lund University, Lund (2006).

84. Xingqiu Zhao. Diode laser frequency stabilization onto an optical cavity. Master's thesis Lund University (2013).

85. Nick Holonyak and S. F. Bevacqua. *Coherent (visible) light emission from Ga(As1xPx) junctions.* Applied Physics Letters **1**, 82–83 (1962). URL http://scitation.aip.org/content/aip/journal/apl/1/4/10.1063/1.1753706.

86. Shuji Nakamura, Masayuki Senoh, Shin ichi Nagahama, Naruhito Iwasa, Takao Yamada, Toshio Matsushita, Hiroyuki Kiyoku and Yasunobu Sugimoto. *InGaN-Based Multi-Quantum-Well-Structure Laser Diodes.* Japanese Journal of Applied Physics **35**, L74 (1996). URL http://stacks.iop.org/1347-4065/35/i=1B/a=L74.

87. Tobias Bladh. Single ion detection setup. Master's thesis

Lund University (2013).

88. Martynas Solovejus. Saturation intensity of rare earth ions doped crystals. Master's thesis Lund University (2014).

89. Warren J. Smith. *Modern Optical Engineering* chapter 9. McGraw-Hill Companies, New York 4th edition (2008).

90. Sidney A. Self. *Focusing of spherical Gaussian beams.* Appl. Opt. **22**, 658–661 (1983). URL http://ao.osa.org/abstract.cfm?URI=ao-22-5-658.

91. Hakan Urey. *Spot size, depth-of-focus, and diffraction ring intensity formulas for truncated Gaussian beams.* Appl. Opt. **43**, 620–625 (2004). URL http://ao.osa.org/abstract.cfm?URI=ao-43-3-620.

92. Warren J. Smith. *Modern Optical Engineering* chapter 5. McGraw-Hill Companies, New York 4th edition (2008).

93. Fuensanta A. Vera-Daz and Nathan Doble. *The Human Eye and Adaptive Optics, Topics in Adaptive Optics* chapter 6. InTech (2012).

94. Max Born, Emil Wolf and A. B. Bhatia. *Principles of optics: Electromagnetic theory of propagation, interference and diffraction of lignt* chapter 9. Cambridge Univeristy Press (1999).

95. Blu ray Disc association. White Paper, Blu-ray Disc^{TM} Format. Technical report Blu-ray Disc association (2012).

96. V. Jary, A. Krasnikov, M. Nikl and S. Zazubovich. *Origin of slow low-temperature luminescence in undoped and Ce-doped Y2SiO5 and Lu2SiO5 single crystals.* physica status solidi (b) **252**, 274–281 (2015). URL http://dx.doi.org/10.1002/pssb.201451234.

97. D L Orth, R J Mashl and J L Skinner. *Optical lineshapes of impurities in crystals: a lattice model of inhomogeneous broadening by point defects.* Journal of Physics: Condensed Matter **5**, 2533 (1993). URL http://stacks.iop.org/0953-8984/5/i=16/a=011.

98. Tuomas Aitasalo, Jorma Hölsä, Mika Lastusaari, Janne Niittykoski and Fabienne Pellé. *Delayed luminescence of Ce^{3+} doped X1 form of Y_2SiO_5.* Optical Materials **27**, 1511 – 1515 (2005). URL http://www.sciencedirect.com/science/article/pii/S0925346705000376. Proceedings of the Third International Conference on SolGel Materials: Research, Technology, Applications SGM04 Third International Conference on SolGel Materials.

99. Winicjusz Drozdowski, Andrzej J. Wojtowicz, Dariusz Winiewski, Piotr Szupryczyski, Sebastian Janus, Jean-Luc

Lefaucheur and Zhenhui Gou. *VUV spectroscopy and low temperature thermoluminescence of LSO:Ce and YSO:Ce.* Journal of Alloys and Compounds **380**, 146 – 150 (2004). URL http://www.sciencedirect.com/science/article/pii/S0925838804003081. Proceedings of the 4th International Spring Workshop on Spectroscopy, Structure and Synthesis of Rare Earth Systems.

100. He Feng, Vitezslav Jary, Eva Mihokova, Dongzhou Ding, Martin Nikl, Guohao Ren, Huanying Li, Shangke Pan, Alena Beitlerova and Romana Kucerkova. *Temperature dependence of luminescence characteristics of Lu 2 (1-x) Y 2 x SiO 5: Ce 3+ scintillator grown by the Czochralski method.* Journal of applied physics **108**, 033519 (2010).

101. Ippei Nakamura, Tatsuya Yoshihiro, Hironori Inagawa, Satoru Fujiyoshi and Michio Matsushita. *Spectroscopy of single Pr^{3+} ion in LaF_3 crystal at 1.5 K.* Scientific Reports **4** (2014).

102. H. Inagawa, Y. Toratani, K. Motohashi, I. Nakamura, M. Matsushita and S. Fujiyoshi. *Reflecting microscope system with a 0.99 numerical aperture designed for three-dimensional fluorescence imaging of individual molecules at cryogenic temperatures.* Scientific Reports **5**, 12833 (2015). URL http://dx.doi.org/10.1038/srep12833.

103. A Meijerink, W J Schipper and G Blasse. *Photostimulated luminescence and thermally stimulated luminescence of Y 2 SiO 5 -Ce, Sm.* Journal of Physics D: Applied Physics **24**, 997 (1991). URL http://stacks.iop.org/0022-3727/24/i=6/a=028.

104. Tuomas Aitasalo, Jorma Hölsä, Mika Lastusaari, Janina Legendziewicz, Janne Niittykoski and Fabienne Pellé. *Delayed luminescence of Ce3+ doped Y2SiO5.* Optical Materials **26**, 107 – 112 (2004). URL http://www.sciencedirect.com/science/article/pii/S0925346703003264. Proceedings of the Second International Conference on Sol–Gel Materials. Research, Technology, Applications (SGM'03).

105. V.V. Laguta, M. Nikl and S. Zazubovich. *Photothermally stimulated creation of electron and hole centers in Ce^{3+}-doped Y_2SiO_5 single crystals.* Optical Materials **36**, 1636 – 1641 (2014). URL http://www.sciencedirect.com/science/article/pii/S0925346713006587. SI: IWASOM'13.

106. V. Jary, A. Krasnikov, M. Nikl and S. Zazubovich. *Origin of slow low-temperature luminescence in undoped and Ce-doped Y_2SiO_5 and Lu_2SiO_5 single crystals.* physica status solidi (b) **252**, 274–281 (2015). URL http://dx.doi.org/10.1002/pssb.201451234.

107. P. Dorenbos, C.W.E. van Eijk, A.J.J. Bos and C.L. Melcher. *Afterglow and thermoluminescence properties of Lu2SiO5:Ce scintillation crystals.* Journal of Physics Condensed Matter **6**, 4167–4180 (1994).

108. E. Mihokova, K. Vavru, P. Horodysky, W. Chewpraditkul, V. Jary and M. Nikl. *Thermally Stimulated Luminescence in Ce-Doped Yttrium Oxyorthosilicate.* Nuclear Science, IEEE Transactions on **59**, 2085–2088 (2012).

109. T. Aitasalo, J. Hölsä, M. Lastusaari, J. Niittykoski and F. Pellé. *Defects in Ce^{3+} doped Y_2SiO_5.* physica status solidi (c) **2**, 272–275 (2005). URL http://dx.doi.org/10.1002/pssc.200460163.

110. V. V. Laguta, M. Buryi, J. Rosa, D. Savchenko, J. Hybler, M. Nikl, S. Zazubovich, T. Kärner, C. R. Stanek and K. J. McClellan. *Electron and hole traps in yttrium orthosilicate single crystals: The critical role of Si-unbound oxygen.* Phys. Rev. B **90**, 064104 (2014). URL http://link.aps.org/doi/10.1103/PhysRevB.90.064104.

111. R.S. Meltzer and S.P. Feofilov. *Spectral hole burning in the 4f5d transition of Ce3+ in LuPO4 and YPO4.* Journal of Luminescence **102,103**, 151 – 155 (2003). URL http://www.sciencedirect.com/science/article/pii/S0022231302004921. Proceedings of the 2002 International Conference on Luminescence and Optical Spectroscopy of Condensed Matter.

112. S. B. Altner, G. Zumofen, U. P. Wild and M. Mitsunaga. *Photon-echo attenuation in rare-earth-ion-doped crystals.* Phys. Rev. B **54**, 17493–17507 (1996). URL http://link.aps.org/doi/10.1103/PhysRevB.54.17493.

113. Fuensanta A. Vera-Daz and Nathan Doble. *Wide-gap luminescent materials, theory and applications* chapter 5. Kluwer academic publishers, Dordrecht (1997).

114. Jin Huang, J. M. Zhang, A. Lezama and T. W. Mossberg. *Excess dephasing in photon-echo experiments arising from excitation-induced electronic level shifts.* Phys. Rev. Lett. **63**, 78–81 (1989). URL http://link.aps.org/doi/10.1103/PhysRevLett.63.78.

115. R. L. Ahlefeldt, W. D. Hutchison, N. B. Manson and M. J. Sellars. *Method for assigning satellite lines to crystallographic sites in rare-earth crystals.* Phys. Rev. B **88**, 184424 (2013). URL http://link.aps.org/doi/10.1103/PhysRevB.88.184424.

116. Houtong Chen, Rui Lian, Min Yin, Liren Lou, Weiping Zhang, Shangda Xia and Jean-Claude Krupa. *Luminescence*

concentration quenching of $^1D_2$ *state in* YPO_4*:*Pr^{3+}. Journal of Physics: Condensed Matter **13**, 1151 (2001). URL http://stacks.iop.org/0953-8984/13/i=5/a=328.

117. R.C. Naik, N.P. Karanjikar and M.A.N. Razvi. *Concentration quenching of fluorescence from* $^1D_2$ *state of* Pr^{3+} *in* YPO_4. Journal of Luminescence **54**, 139 – 144 (1992). URL http://www.sciencedirect.com/science/article/pii/002223139290001P.

Papers

Paper I

Hole burning and frequency selective trapping in Ce:Y_2SiO_5 at liquid helium temperatures

J. Karlsson, A. N. Nilsson, D. Serrano, A. Walther, L. Rippe and S. Kröll
A. Ferrier and P. Goldner.

Manuscript in preparation.

Hole burning and frequency selective trapping in Ce^{3+}:Y_2SiO_5 at liquid helium temperatures

Jenny Karlsson,* Adam N. Nilsson, Diana Serrano,† Andreas Walther, Lars Rippe, and Stefan Kröll
Department of Physics, Lund University, P.O. Box 118, SE-22100 Lund, Sweden

Philippe Goldner and Alban Ferrier
Chimie ParisTech, Laboratoire de Chimie de la Matière Condensée de Paris, CNRS-UMR 7574, UPMC Univ Paris 06, 11 rue Pierre et Marie Curie 75005 Paris, France
(Dated: October 16, 2015)

We perform hole burning with an actively stabilized laser within the zero phonon line of the 4f-5d transition in Ce^{3+}:Y_2SiO_5 at 2K. The narrowest spectral holes appear for small applied magnetic fields and are 9 MHz wide (FWHM), which puts an upper bound to the homogeneous linewidth of the transition to 4.5 MHz which is close to lifetime limited. The spin level relaxation time is measured to 70 ms with a magnetic field of 10 mT.

A very slow and permanent hole burning mechanism is discovered, which reduces the fluorescence strength by more than 50% after a couple of minutes of continuous excitation. The created spectral hole has a width in the tens of MHz range, which shows that trapping happens via the 5d-state. The intensity dependence of the trapping rate follows the population in the 5d-level.

I. INTRODUCTION

Cerium doped yttrium orthosilicate (Ce^{3+}:Y_2SiO_5) crystals have been extensively studied for applications such as cathode ray tube phosphor[1–3], x-ray storage phosphor[4] and as a scintillator for fast detection of x-rays and γ-rays[5,6]. The 5d-state of cerium has a lifetime of about 40 ns, and gives rise to strong fluorescence in the 370-500 nm wavelength range[7–9].

The high yield of photons is an attractive property also for detection of single ions in a crystal[10,11], with possible applications in quantum information science. Currently, low concentration Ce^{3+}:Y_2SiO_5 is studied with the aim of implementing a quantum computing scheme where a single cerium ion is used for quantum state readout[12].The scheme requires cerium ions to interact with the qubit ions (for example praseodymium) via the difference in permanent electric dipole moment between the ground and excited state, which has been previously measured[13]. Depending on the quantum state of a qubit ion, the fluorescence from a single cerium ion can be switched on or off. The success of such a protocol will depend on some properties of Ce^{3+}:Y_2SiO_5 such as homogeneous linewidth and possible trap states.

The methods used for quantum information experiments are rather different from those traditionally used when studying cerium as a scintillator or phosphor. However, many of the results are related and relevant for both communities.

It is well known that γ-ray, x-ray or UV excitation of cerium ions in Y_2SiO_5 and similair crystals gives rise to afterglow, a very long lived luminescence emission that can last for hours[4,9,14–16]. The cause of afterglow is a slow recombination emission from electron and hole traps in the crystal lattice. The trapping of charge carriers worsens the performance of Ce^{3+}:Y_2SiO_5 as a scintillator[5], but enables the application as a storage phosphor[4]. Charge traps can be detrimental for single ion detection, since when an electron belonging to a cerium ion gets trapped it might not recombine for hours and the ion is lost from view. Many mechanisms that can lead to charge trapping have been suggested but exactly which mechanisms that are present in the crystal under certain conditions remains to be clarified.

Trapping mechanisms in Ce^{3+}:Y_2SiO_5 and undoped Y_2SiO_5 has previously been studied by means of thermally stimulated luminescence (TSL)[4,14,17–19], electron spin resonance (ESR)[18,19] as well as absorption, excitation and emission spectroscopy[4,9,15,18], with excitation by x-rays[4,19], γ-rays[17] or UV light[4,9,14,15,18]. These methods provide information about trap depths, the concentration of some defects in the crystal and possible charge trapping and recombination mechanisms.

In this work hole burning and charge trapping in a Ce^{3+}:Y_2SiO_5-crystal at a temperature of 2K is investigated. Contrary to most previous experiments an actively stabilized laser targeting the zero phonon line (ZPL) of the cerium 4f-5d transition is used. The high spectral resolution allows for new conclusions to be drawn regarding trapping and hole burning mechanisms.

When applying a magnetic field, redistribution of ions in the spin levels of the ground state within the ZPL gives rise to a spectral hole with a lifetime of 70 ms. The width of the spectral hole for the smallest fields is measured to 9 MHz, which puts an upper limit to the homogeneous linewidth of the transition to 4.5 MHz and confirms that the linewidth is close to lifetime limited[13].

A slower and much more long lived hole burning mechanism is observed as a decrease of the cerium fluorescence signal under continuous excitation for several minutes. The created spectral hole has a lifetime of hours. A similar observation was previously made in Ce^{3+}:$LuPO_4$ and Ce^{3+}:YPO_4[20]. To the best of our knowledge it is the first time a persistent trapping mechanism in Ce^{3+}:Y_2SiO_5 has been observed with high spectral resolution within

the ZPL. The width of the created spectral hole is in the tens of MHz range. The high frequency selectivity shows that trapping occurs via the excited 5d-state of cerium. The intensity dependence of the hole burning rate follows the intensity dependence of the steady state population in the 5d-state, which also suggests that trapping occurs via a spontaneous process originating from this state.

II. EXPERIMENTAL SETUP

A sketch of the optical setup can be seen in figure 1. An external cavity diode laser (ECDL) centered at 371 nm was used to excite the cerium ions and perform hole burning. The frequency of the ECDL was stabilized to a low drift cavity using the Pound-Drever-Hall technique[21]. An achousto-optic modulator (AOM) in double pass configuration allowed the laser frequency to be continuously scanned over a range of 200 MHz. After the AOM, the laser beam was sent through a single mode fiber to obtain a clean Gaussian TEM_{00}-mode before sending the beam to the sample. A maximum power of about 200 μW reached the sample. The polarization after the laser was linear, but when reaching the sample the polarization was probably slightly elliptical after passing several optical components.

To collect fluorescence from the sample a home built fluorescence detection setup was used[22]. The laser beam was reflected off a dichroic mirror with high reflectivity at 371 nm, and high transmission in the range 385-450 nm corresponding to the fluorescence emission from Ce^{3+}:Y_2SiO_5. The laser beam was sent into a liquid helium bath cryostat (Oxford Instruments Spectromag) where the sample was kept at a temperature of 2K. The laser beam was focused about 100 μm below the surface of the sample by a small lens with a numerical aperture of 0.85 mounted inside the sample space of the cryostat. Both the sample and the lens were sitting on translators with nanometer precision (Attocube ANP51RES). The laser focus was estimated to have a diameter of 1 μm in the crystal. The saturation intensity of the 4f-5d transition corresponds to a laser power of 14 μW[13].

The fluorescence was collected in the backward direction by the lens inside the cryostat. The dichroic mirror and three interference filters were used to block unwanted laser light. The interference filters transmits $<0.01\%$ at the laser wavelength of 371 nm, and transmits $> 90\%$ only in the range 385-425nm to select fluorescence from cerium in site 1 while blocking most of the fluorescence from cerium ions in site 2.[23] A 50 mm lens was used to focus the fluorescence through a 25 μm pinhole which blocks light generated out of focus in the crystal. The fluorescence was measured using a single photon counting avalanche diode (countBlue-250B).

III. SAMPLE

The sample used in the following experiments is a very low concentration Ce^{3+}:Y_2SiO_5 crystal grown by the Czochralski method. The concentration of cerium ions relative to yttrium is in the order of 10^{-7}. The crystal is kept at 2K in a liquid helium bath cryostat throughout all measurements. The inhomogeneous broadening of the zero phonon line is 35 GHz.

Ce^{3+} has a very simple energy level structure with two electronic levels, 4f and 5d, below the conduction band of the crystal. The 4f-5d transition is electric dipole allowed and gives rise to strong fluorescence. The 4f ground state is split into two fine structure levels, which are further split into crystal field levels, all of which are doubly degenerate at zero magnetic field. The energy level structure of Ce^{3+}:Y_2SiO_5 (site 1) is shown in figure 2 a). In this work the 4f-5d transition always refers to the transition between the lowest energy crystal field level in the 4f and 5d states respectively.

Cerium ions can occupy two crystal sites with different oxygen coordination[24]. In this work excitation of cerium takes place within the zero phonon line of ions in site 1. The detected fluorescence in the selected range 385-425 nm originates almost exclusively from cerium ions in site 1, with a signal to background ratio of 100 in the center of the line. The background is in this case measured by tuning the laser towards longer wavelengths 1 nm away from the zero phonon line of cerium in site 1, and consists mainly of overlapping fluorescence from cerium ions in crystal site 2.

When applying an external magnetic field the doubly degenerate fine structure levels will split into two Zeeman levels. In each of the two yttrium sites, the cerium ions can occupy two nonequivalent magnetic sites[25]. For a magnetic field applied along the b-axis of the crystal the Zeeman splittings of the two magnetic sites overlap. This is the case in the present study[26].

IV. HOLE BURNING IN A MAGNETIC FIELD

A small external magnetic field (0.05-100 mT) was applied to the crystal in the direction parallel to the laser beam, to split the doubly degenerate fine structure levels. A laser pulse of 300 μs duration and 20 μW of power ($\approx$ 1.43 times the saturation intensity) was applied close to the center of the inhomogeneous absorption profile to create a spectral hole. The hole was detected by scanning the laser frequency over a 200 MHz interval in 100 μs while recording the fluorescence from the sample. A wait time allowed the system to relax to thermal equilibrium. The experiment was repeated about 1000 times to average data.

As can be seen in figure 3, a spectral hole is created for an applied field as small as 0.1 mT. With increasing magnetic field the spectral hole gets both deeper and wider. At most about 80% of the ions are burnt away in

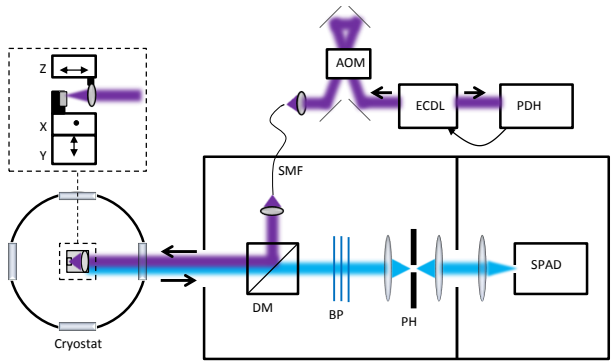

FIG. 1. Schematic of the optical setup. The purple beam represents the 371 nm laser excitation and the blue beam represents the collected fluorescence. The solid lines represents a dark enclosure. Labels are defined as follows: ECDL - External Cavity Diode Laser, PDH - Pound-Drever-Hall locking system, AOM - Acousto-Optic Modulator, DM - Dichroic Mirror, SMF - Single Mode Fiber, BP - Band Pass Filters, PH - Pinhole, SPAD - Single Photon Counting Avalanche Diode. Inside the cryostat the sample is sitting on two translators (X and Y) and the lens is attached to a third translator for focusing (Z). (color online)

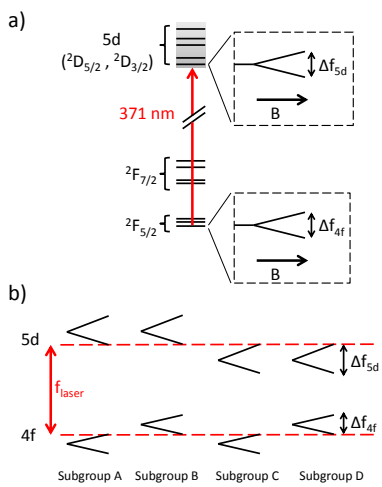

FIG. 2. a) The energy levels of Ce^{3+}:Y_2SiO_5. When applying a small magnetic field the lowest stark level of the ground state will split up into two Zeeman levels separated by Δf_{4f}, and the lowest level of the excited state will split up in two levels separated by Δf_{5d}. b) Because of the inhomogeneous broadening of the absorption line of Ce^{3+}:Y_2SiO_5, four different groups of ions absorb at each laser frequency f_{laser}. (color online)

the center of the hole.

The FWHM of the spectral holes was measured by fitting a Lorentzian curve to the data. The result is shown in figure 4. The smallest spectral holes for low magnetic fields were too noisy to obtain a reliable fit. More details about the data treatment can be found in the Supplementary Material. For a field of 0.1 mT the FWHM of the measured spectral hole is 9 MHz, which puts an upper limit on the homogeneous linewidth of the 4f-5d transition to 4.5 MHz. The widest hole for a magnetic field of 100 mT is around 80 MHz wide (FWHM).

Because of the inhomogeneous broadening of the zero phonon line, a fixed laser frequency f_{laser} interacts with four different groups of ions in a magnetic field, as shown in figure 2 b). The ground state splitting can be calculated using the known g-factor of Ce^{3+}:Y_2SiO_5[25,26]. For a field along the b-axis the splitting is 19 MHz/mT.

To measure the Zeeman splitting in our sample, the AOM in the laser beam was switched between two frequencies, separated by an amount Δf_{laser}, every 4 μs. If the two laser frequencies matches one transition from each ground state in the same subgroup of cerium ions hole burning will be less efficient since the ions will be repumped every 4 μs. This happens when Δf_{laser} is equal to the ground state Zeeman splitting Δf_{4f}, when it is equal to the sum of the ground state and the excited state splitting, $\Delta f_{4f} + \Delta f_{5d}$ (subgroup A and D), or when it is equal to the difference between the ground state and the excited state splitting, $\Delta f_{4f} - \Delta f_{5d}$ (subgroup B and C). To find these points, Δf_{laser} was kept fixed while the magnetic field was scanned from 0 to 6 mT, see figure 5 a). A strong resonance peak, and for small Δf_{laser} also a weaker peak at about twice the magnetic field, could be observed. The weaker peak shows a splitting of 17.9±1.5

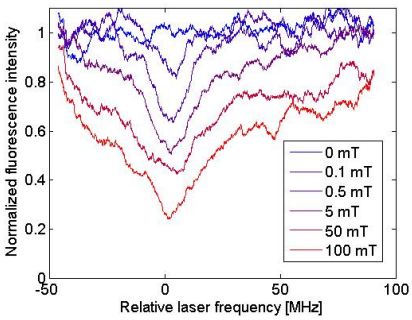

FIG. 3. A spectral hole is burnt in the inhomogeneous absorption profile by redistribution of ions in the Zeeman levels. Spectral holes created with different magnetic fields are shown in different colors, and the field strength is given in the inset. The data has been smoothed with a moving average over 100 points, corresponding to around 4 MHz on the frequency axis. (color online)

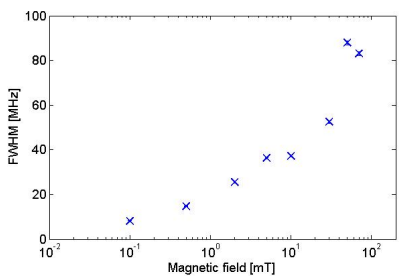

FIG. 4. The width (FWHM) of the spectral hole as a function of magnetic field. The horizontal axis is in logarithmic scale. For lower magnetic fields than 0.5 mT the spectral holes were too noisy to get a reliable fit. The narrowest spectral hole with a reliable fit has a FWHM of 9 MHz for an applied field of 0.1 mT. (color online)

MHz/mT (80% confidence interval) which corresponds to the known ground state Zeeman splitting of 19 MHz/mT. The stronger peak is at lower magnetic fields and should then correspond to the sum of the ground state and the excited state splitting. By repeating the experiment for different values of Δf_{laser} the sum of the ground state and excited state splitting as a function of magnetic field could be determined, see figure 5 b). The curve is linear with a slope of 43.4±1.7 MHz/mT, showing that the excited state splitting is similar to the ground state splitting with a value of 25.5±3.2 MHz/mT.

The peak corresponding to Δf_{4f} - Δf_{5d} is at much higher magnetic fields and can not be seen in figure 5.

In figure 5 a) a strong fluorescence peak around 0.2 mT can also be seen. This peak does not change with Δf_{laser} and thus has nothing to do with repumping by the two laser frequencies. It was first assumed that the peak corresponds to partial cancellation of the earth magnetic field, and hence to an overlap of the Zeeman levels. The field strength of 0.2 mT is however too large to be attributed to the earth magnetic field alone, which is around 50 μT at the lab location.

As the direction of the applied magnetic field was inverted, the peak around 0.2 mT did not show up. The resonance peaks caused by the frequency switching and hence repumping of ions had a small offset compared to the positive magnetic field direction. This indicates that the peak at 0.2 mT is the actual point of overlap of the Zeeman levels.

The lifetime of the spectral hole was measured by fixing the magnetic field at 10 mT and varying the wait time between the burn pulse and the scanned read out of the spectral hole. The burn pulse was in this case 1 ms long, with 30 μW of laser power. The spectral hole decays to 1/e of the initial area in 70 ± 8 ms (80% confidence interval), see figure 6. This is in the same order as the previously reported spin-lattice relaxation time of Ce:Y_2SiO_5[25].

It is interesting to note that even 500 ms after the burn pulse a small spectral hole remained. This persistent spectral hole can be related to another trapping mechanism, for example ionization of Ce^{3+} into Ce^{4+}. This will be discussed further in the next section.

V. PERMANENT TRAPPING

When exciting the cerium ions continuously for a few minutes it was noted that the fluorescence signal slowly decreases, see figure 7. Initially the signal drops fast, within a few seconds the signal has decreased by about 25%. After the initial quick drop the fluorescence slowly decreases over a time scale of minutes, indicating that the ions are slowly transferred to a long lived trap state. The fluorescence signal stabilizes slightly below 50 % of the initial value. The laser was turned off for up to 40 minutes and then turned on again without any sign of recovery of the signal. Thus the lifetime of the trap state is at least hours.

A sequence of frequency jumps was done with the AOM in the laser beam, with varying magnitudes from 10 to 100 MHz. Immediately after a sufficiently large frequency jump the fluorescence signal is back and a new decay starts. The increase of the fluorescence signal after a frequency jump was used to estimate the spectral hole width. The estimate gave a spectral hole width (FWHM) of 50 MHz. This is similar to the width of the short lived spectral holes created by redistribution in the spin levels (9-80 MHz), as described in the previous section. This shows that the trapping mechanism is frequency selec-

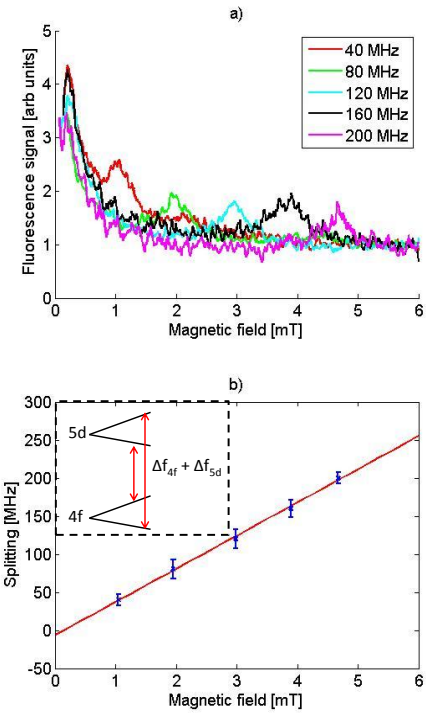

FIG. 5. The Zeeman splitting of the ground state and the excited state was measured by rapidly switching the laser between two frequencies separated by Δf_{laser} while scanning the magnetic field. a) When Δf_{laser} matches the Zeeman splitting of the ground state or the sum of the ground state and excited state splitting, a resonance peak is detected. Δf_{laser} for the different curves is shown in the inset. b) The measured sum of the ground and excited state level splitting as a function of magnetic field with a linear fit. (color online)

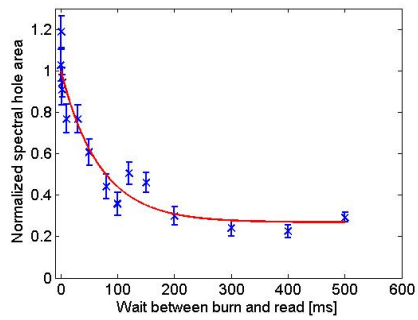

FIG. 6. The decay time of the spectral hole is 70 ± 8 ms. The error bars show the standard deviation of the data and the red curve is an exponential fit. (color online)

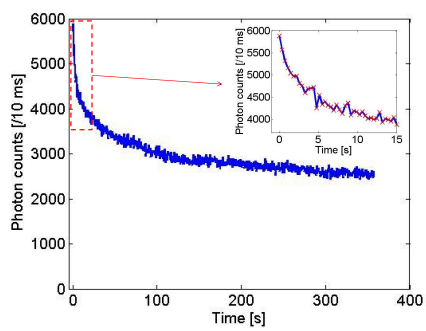

FIG. 7. At time zero the crystal is moved quickly so that the laser focus interacts with a new set of ions. The laser excitation is kept at constant power of 20 μW. The fluorescence signal slowly goes down over a couple of minutes and stabilizes around 50% of the initial signal strength. The data was taken at an applied magnetic field of 0.2 mT, where the hole burning due to redistribution in the Zeeman levels has a minimum. Other sets of data were taken at zero applied field and shows the same behavior. (color online)

tive. Thus trapping has to happen via the 5d-state of the cerium ions, since the zero phonon line of the 4f-5d transition is the only transition with narrow homogeneous linewidth.

To investigate the intensity dependence for the permanent hole burning mechanism, a similar fluorescence curve as in figure 7 was recorded for 7 different laser powers. The initial slope of the curves is a measure of the initial trapping rate. For this purpose a linear curve was fitted to the initial part of the data, from t=0 to 20 s. The time of 20 s was chosen as the shortest time giving acceptable errors in the linear fit due to noise in the signal, see Supplementary Material. The intensity dependence of the initial fluorescence decrease rate is shown in figure 9 b), where the fluorescence decrease rate during the first 20 s of continuous excitation is plotted versus laser power. The steady state population in the 5d-state is shown as a green dashed line in figure 9 b). It was calculated using the saturation intensity of the transition (1.4 W/m^2) which has been previously measured[13] and taking spectral broadening due to saturation into account. The measurement shows that the intensity dependent fluorescence decrease appears to follow the population in the

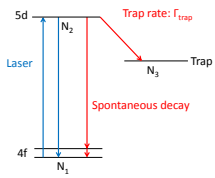

FIG. 8. A simple level diagram showing a model of the permanent trapping. The 4f-5d transition will reach steady state on the 100 ns time scale. The decay into the trap state happens on a much slower time scale of minutes. (color online)

5d-state. This seems to exclude multi-photon processes and indicates that the ions spontaneously decay into a trap state from the 5d-state.

The population in the 5d-state will decrease due to trapping of ions, which is not taken into account in the simple comparison above. To take this into account a simple set of rate equations can be used to model the trapping, assuming that a cerium ion decays spontaneously from the 5d-state to a trap state with a small trap rate Γ_{trap}, see figure 8. To match the fact that the signal seems to stabilize around 50 % of the initial value it is assumed that a limited number of traps are available, which means that not all ions can be trapped. Spectral broadening due to saturation also needs to be taken into consideration, since we are working close to or above the saturation intensity for the 4f-5d transition.

In figure 9 such a rate equation model is fitted to the fluorescence decrease with a least squares fit, with the trapping rate and the number of available traps as fitting parameters. The intensity dependence of the trapping is calculated using the parameters from the fit. The number of available traps for the best fit was 55 % of the number of cerium ions, and the resulting trapping rate from the 5d-state was $\Gamma_{trap} = 0.17$ /s. The model fits well to the slow decrease in fluorescence signal, but can not explain the initial fast drop during the first few seconds as shown in the inset of figure 9. This fast drop in signal is still too slow to be due to redistribution of ions in the Zeeman-levels which happens on the ms timescale. There might be yet another different trapping mechanisms present, where trapping happen on the few second time scale.

Since not all cerium ions get trapped (the fluorescence does not tend to zero), the trap state should not be an internal state of the cerium ion. It is possible that the electron in the 5d-level spontaneously tunnels into another crystal impurity, for example an oxygen vacancy.

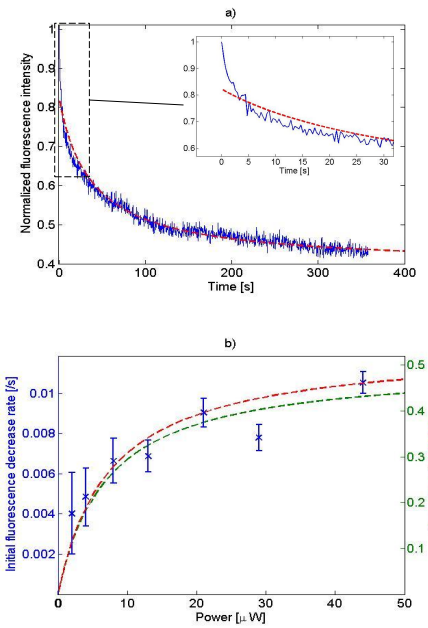

FIG. 9. In a) the decrease in fluorescence intensity as a function of time due to trapping of ions is plotted (blue line) together with a calculated fit using a rate equation model (red dashed line). The blue line is the same as in figure 7. In b) the intensity dependence of the initial trapping rate is plotted (blue crosses) with 80% confidence intervals. The calculated dependence using rate equations is shown as a red dashed line. The green dashed line with the y-scale to the right shows the calculated population of the 5d-state. (color online)

VI. CONCLUSION

Hole burning within the 4f-5d zero phonon line of cerium in site 1 in a very low concentration Ce^{3+}:Y_2SiO_5 crystal was performed with MHz spectral resolution. With a small applied magnetic field redistribution of population in the spin levels give rise to a spectral hole. The width of the created spectral hole shows that the homogeneous linewidth of the 4f-5d transition is around 4.5 MHz, which is close to lifetime limited. The lifetime of the spectral hole was measured to be 70 $\pm$ 8 ms.

A very slow hole burning mechanism was discovered which decreases the fluorescence signal to about 50% in a few minutes of continuous excitation. The created spectral hole has a width in the tens of MHz range and a lifetime of at least hours. The intensity dependence of the initial hole burning rate follows the steady state pop-

ulation in the 5d-state. In conjunction with the narrow spectral width this indicates that trapping occurs by a spontaneous process originating from the 5d-state. The fact that the fluorescence intensity does not tend to zero suggests that not all cerium ions in this crystal can become trapped.

One possibility is that an electron in the 5d-state of cerium spontaneously tunnels to another impurity in the crystal with a small probability. This impurity could for example be an oxygen vacancy, which traps an electron and leave behind a Ce^{4+}-ion. However, further studies are needed to draw final conclusions on the exact trapping mechanism.

Permanent trapping can be a serious problem for detection of single cerium ions in Y_2SiO_5. The time scale on which trapping happens is however long, many seconds, and the trapping probability for each excitation cycle to the 5d-state is low. With a lifetime of 40 ns in the 5d-state, it is possible to cycle one ion about 14 million times between the 4f and 5d states, and hence let the ion emit 14 million photons, before it has a 10% risk of being trapped. Thus it seems like single ion detection is still fully possible.

If the permanent trapping mechanism can be reversed, so that the cerium fluorescence signal comes back on demand, it might have interesting applications e.g. for long-lived spectrally tailored filters and data storage.

ACKNOWLEDGMENTS

This work was supported by the Swedish Research Council (VR), the Knut and Alice Wallenberg Foundation (KAW), (Marie Curie Action) REA Grant Agreement No. 287252 (CIPRIS), Lund Laser Center (LLC), and the Nanometer Structure Consortium at Lund University (nmC@LU).

* Jenny.Karlsson@fysik.lth.se
† Department of Chemistry, University of Zürich, Winterthurerstrasse 190, 8057 Zürich, Switzerland

[1] A. H. Gomes de Mesquita and A. Bril, Journal of The Electrochemical Society **116**, 871 (1969), http://jes.ecsdl.org/content/116/6/871.1.full.pdf+html.
[2] A. de Mesquita and A. Bril, Materials Research Bulletin **4**, 643 (1969).
[3] P. Born, D. Robertson, and P. Smith, Journal of Materials Science Letters **4**, 497 (1985).
[4] A. Meijerink, W. J. Schipper, and G. Blasse, Journal of Physics D: Applied Physics **24**, 997 (1991).
[5] M. Nikl, A. Vedda, and V. V. Laguta, in *Springer Handbook of Crystal Growth*, edited by D. G., B. K., P. V., and D. M. (Springer, Berlin, Heidelberg, 2010) Chap. 50, pp. 1663–1700.
[6] C. L. Melcher, J. S. Schweitzer, C. A. Peterson, R. A. Manente, and H. Suzuki, in *Inorganic scintillators and their application*, edited by P. Dorenbos and C. W. E. van Eijk (Delft University Press, 1995) pp. 309–316.
[7] M. Leskelä and J. Suikkanen, Journal of the Less Common Metals **112**, 71 (1985), proceedings of the International Rare Earth Conference.
[8] H. Suzuki, T. Tombrello, C. Melcher, and J. Schweitzer, Nuclear Instruments and Methods in Physics Research Section A: Accelerators, Spectrometers, Detectors and Associated Equipment **320**, 263 (1992).
[9] T. Aitasalo, J. Hölsä, M. Lastusaari, J. Legendziewicz, J. Niittykoski, and F. Pellé, Optical Materials **26**, 107 (2004), proceedings of the Second International Conference on Sol–Gel Materials. Research, Technology, Applications (SGM'03).
[10] R. Kolesov, K. Xia, R. Reuter, M. Jamali, R. Stöhr, T. Inal, P. Siyushev, and J. Wrachtrup, Phys. Rev. Lett. **111**, 120502 (2013).
[11] P. Siyushev, K. Xia, R. Reuter, M. Jamali, N. Zhao, N. Yang, C. Duan, N. K. A. D. Wieck, R. Kolesov, and J. Wrachtrup, Nature Communication **5**, 3895 (2014).
[12] J. H. Wesenberg, K. Mølmer, L. Rippe, and S. Kröll, Phys. Rev. A **75**, 012304 (2007).
[13] Y. Yan, J. Karlsson, L. Rippe, A. Walther, D. Serrano, D. Lindgren, M.-E. Pistol, S. Kröll, P. Goldner, L. Zheng, and J. Xu, Phys. Rev. B **87**, 184205 (2013).
[14] V. Laguta, M. Nikl, and S. Zazubovich, Optical Materials **36**, 1636 (2014), sI: IWASOM'13.
[15] V. Jary, A. Krasnikov, M. Nikl, and S. Zazubovich, physica status solidi (b) **252**, 274 (2015).
[16] P. Dorenbos, C. v. Eijk, A. Bos, and C. Melcher, Journal of Physics Condensed Matter **6**, 4167 (1994).
[17] E. Mihokova, K. Vavru, P. Horodysky, W. Chewpraditkul, V. Jary, and M. Nikl, Nuclear Science, IEEE Transactions on **59**, 2085 (2012).
[18] T. Aitasalo, J. Hölsä, M. Lastusaari, J. Niittykoski, and F. Pellé, physica status solidi (c) **2**, 272 (2005).
[19] V. V. Laguta, M. Buryi, J. Rosa, D. Savchenko, J. Hybler, M. Nikl, S. Zazubovich, T. Kärner, C. R. Stanek, and K. J. McClellan, Phys. Rev. B **90**, 064104 (2014).
[20] R. Meltzer and S. Feofilov, Journal of Luminescence **102,103**, 151 (2003), proceedings of the 2002 International Conference on Luminescence and Optical Spectroscopy of Condensed Matter.
[21] X. Zhao, *Diode laser frequency stabilization onto an optical cavity*, Master's thesis, Lund University (2013).
[22] J. Karlsson, L. Rippe, and S. Kröll, Manuscript in preparation (2015).
[23] W. Drozdowski, A. J. Wojtowicz, D. WiÅŻniewski, P. SzupryczyÅĎski, S. Janus, J.-L. Lefaucheur, and Z. Gou, Journal of Alloys and Compounds **380**, 146 (2004), proceedings of the 4th International Spring Workshop on Spectroscopy, Structure and Synthesis of Rare Earth Systems.
[24] H. Suzuki, T. Tombrello, C. Melcher, and J. Schweitzer, Nuclear Instruments and Methods in Physics Research Section A: Accelerators, Spectrometers, Detectors and Associated Equipment **320**, 263 (1992).
[25] I. Kurkin and K. Chernov, Physica B+C **101**, 233 (1980).
[26] M. S. Buryi, V. V. Laguta, D. V. Savchenko, and M. Nikl, Advanced Science, Engineering and Medicine **5**, 1 (2013).

Paper II

A confocal optical microscope for detection of single impurities in a bulk crystal at cryogenic temperatures

J. Karlsson, L. Rippe, and S. Kröll.

(2015) *Submitted to Review of Scientific Instruments.*

A confocal optical microscope for detection of single impurities in a bulk crystal at cryogenic temperatures

Jenny Karlsson,[1,a)] Lars Rippe,[1] and Stefan Kröll[1]
Department of Physics, Lund University, P.O. Box 118, SE-22100 Lund, Sweden

(Dated: 19 October 2015)

A compact sample-scanning confocal optical microscope for detection of single impurities below the surface of a bulk crystal at cryogenic temperatures is described. The sample, lens and scanners are mounted inside a helium bath cryostat and have a footprint of only 19x19 mm. Wide field imaging and confocal imaging using a Blu-ray lens immersed in liquid helium is demonstrated with excitation at 370nm. A spatial resolution of 300 nm and a detection efficiency of 1.6 % was achieved.

I. INTRODUCTION

Optical detection and manipulation of single emitters, as for example ions in a trap[1], quantum dots[2] and NV-centers in diamond[3], play an important role in quantum optics and quantum information science. Rare-earth ions doped into a crystal host can have very long coherence times[4,5], which makes them ideal for quantum information applications. Rare-earth systems have showed very promising results in the development of quantum memories[6–9], but for quantum computing the results are so far few. One reason for this is the difficulty to detect and manipulate single rare-earth ions, which is believed to be necessary for a scalable quantum computing approach[10].

Indirect proof of emission from single rare-earth ions in a bulk crystal was presented already in 1988[11–13]. Solid proof of single rare-earth ion detection in room temperature was reported for the first time in 2012[14], and since then single rare-earth ions have been detected at liquid helium temperatures in both nano-crystals[15] and in bulk crystals[16,17].

When detecting single emitters confocal fluorescence microscopy is often used to achieve sub-micrometer resolution in three dimensions and good background rejection[18]. The technique is relatively simple and flexible, but single rare-earth ion detection for quantum computing still imposes several additional requirements for the confocal microscope, compared to standard systems.

1. The crystal has to be cooled to liquid helium temperatures to obtain the long coherence times needed for quantum computing, which require the sample to sit inside a cryostat. Collecting fluorescence through the windows of a cryostat causes spherical aberrations as well as a low collection efficiency because of the long distance between the sample and the objective lens. The problems can be solved by placing the objective lens inside the cryostat. This requires a cryostat with a large sample space or very compact optics[19]. In some cases the cryostat has been custom made or re-built to accommodate the detection optics[20], while in other cases a cryostat with a large sample space has been used[21].

2. To obtain an image in a confocal geometry either the laser beam or the sample has to be scanned. Scanning the laser beam puts higher requirements on the microscope objective[22]. Good imaging quality can be difficult to achieve with a compact objective sitting in vacuum or liquid helium. Scanning the sample puts lower requirements on the objective lens since the beam is always axial, but requires scanners compatible with low temperatures[19–21,23].

3. To obtain a long coherence time it is desirable to use rare-earth ions that sit a small distance below the surface of the crystal. Focusing through a high refractive index surface causes spherical aberrations in the beam which can limit resolution. In addition, refraction at the crystal surface severely limits the collection efficiency of the lens. This can be improved by using a solid immersion lens (SIL)[24,25]. The size of the SIL will however limit how short the working distance, and hence the numerical aperture, of the focusing lens can be. It will also limit the possible scan range and make it a bit more cumbersome to change samples.

4. Quantum computing schemes involving rare-earth ions are dependent on the ions having narrow absorption linewidths. To prevent the excitation laser to drift out of resonance with the observed ion during a measurement, an actively stabilized laser source is needed.

In this work we present the design of a simple and versatile sample scanning confocal microscope setup, optimized for detection of a single cerium ion below the surface of a bulk crystal at cryogenic temperatures. A single cerium ion has been suggested as a readout mechanism in a scalable quantum computing scheme[10].

a)Jenny.Karlsson@fysik.lth.se

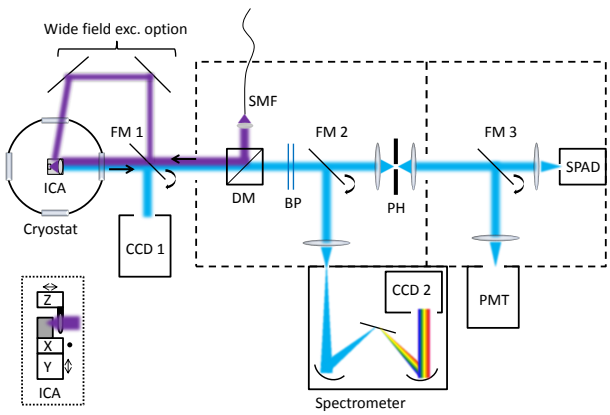

FIG. 1. Scheme of the optical setup. The purple beam represents the 371 nm laser excitation and the blue beam represents the collected fluorescence. The dashed lines represents shielding from room light and scattered laser light. Labels are defined as follows: ICA - Intracryostat Assembly, FM - Flip Mirror, DM - Dichroic Mirror, SMF - Single Mode Fiber, BP - Band Pass Filters, PH - Pinhole, SPAD - Single Photon Counting Avalanche Diode, PMT - Photomultiplier Tube, CCD - Charged Coupled Device (Camera). The intracryostat assembly consists of a lens sitting on a translator for focusing (Z), and a sample holder sitting on two translators (X and Y) for scanning. A detailed view of the ICA is shown in figure 2. (color online)

A lens dismounted from a Blu-ray player is used for fluorescence collection. This type of lens is designed for diffraction limited focusing below a surface[26].

The sample and the lens are mounted on commercially available nano positioners which give a total positioning range of 3 x 2.5 x 3 mm (x y depth) with nanometer precision. Only patience limits the possible scan size within this range. Similair types of nano positioners have previously been used at cryogenic temperatures for sample scanning and shown good stability and repeatability[21,23].

The mounted sample, lens and scanners have a very compact design. The full assembly has a footprint of no more than 19x19 mm and fits inside the 25 mm sample tube of a helium bath cryostat.

A close to diffraction limited spatial resolution of 300±111 nm is obtained in liquid helium. The estimated collection efficiency is 1.6 %.

II. DESIGN

A. Optical setup

Figure 1 shows a sketch of the setup. The setup is composed of standard optics, most of which is covered by a box (dashed line) to prevent room light from reaching the detectors.

The excitation laser is coupled through a single mode fiber (SMF) and reflected off a dichroic mirror (DM) which reflects 98 % at the excitation laser wavelength of 371 nm and transmits $\geq$ 95% in the fluorescence range 385 - 450 nm. The collimated laser beam goes through two cryostat windows and into a so called intracryostat assembly (ICA) containing a focusing lens, a positioning system and a sample holder.

A flip mirror (FM 1) in the laser beam path allows for wide field excitation from a side window of the cryostat. A cooled CCD-camera, Hamamatsu ORCA-03G, can be used to image the sample.

In confocal mode, the fluorescence generated at the sample is collected by the same lens used for focusing the laser beam and exits the cryostat counter propagating with the excitation beam. The fluorescence beam passes through the dichroic mirror (DM) and two spectral bandpass filters (BP) that together transmits more than 90 % in the range 385-425 nm, and less than 0.01 % of the laser light at 371 nm.

The fluorescence can be sent via a flip mirror (FM 2) to a spectrometer from Oriel Instruments with an intensified CCD-camera, Andor DH501-25U-01, for spectral analysis.

If the flip mirror is folded down the fluorescence is focused through a spatial filter consisting of a pair of lenses with 50 mm focal length and a 25μm pinhole (PH) to ex-

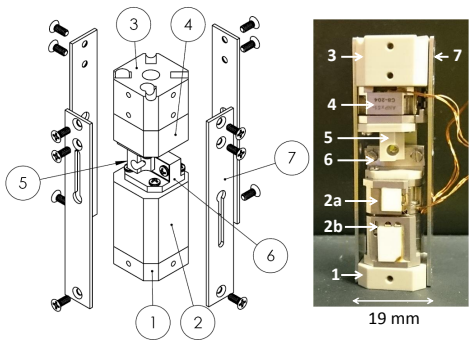

FIG. 2. Drawing and photograph of the intracryostat assembly (ICA). 1. Bottom plate (PEEK) 2a. X-positioner (ANPx51RES) 2b. Y-positioner (ANPz51RES) 3. Sample rod connector (PEEK) 4. Z-positioner (ANPx51RES) 5. Lens holder (PEEK) with a Blu-ray lens 6. Sample holder (PEEK) with a 100 μm thick clamp (stainless steel) 7. Side bars (stainless steel). (color online)

clude fluorescence generated out of focus. The size of the pinhole is selected to roughly match the Airy disc diameter for the longest detected fluorescence wavelength of 425 nm. The signal can be sent to either a single photon counting avalanche diode (SPAD) with less than 250 dark counts per second, Laser Components Count blue 250B, or a photomultiplier tube (PMT), Hamamatsu R943-02, depending on the signal strength. To obtain an image of the sample, the sample is scanned and the fluorescence intensity is measured point by point using the SPAD or the PMT.

B. Intracryostat assembly

The intracryostat assembly, shown in figure 2, is composed of a compact holder that fits inside the 25 mm wide sample tube of a helium bath cryostat, Oxford Instruments Spectromag. The holder contains the focusing lens, a sample mount and a positioning system. The full assembly has a footprint of 19x19 mm and is 65 mm high.

A lens dismounted from a Blu-ray player (LG CH10LS20) is used for focusing the laser beam as well as collecting the generated fluorescence. The lens is designed for 405 nm, is 3 mm in diamater and has a numerical aperture of 0.85. The focal length is estimated to be 1.2 mm by measuring the magnification in an otherwise known setup, and the working distance is less than 1 mm. The Blu-ray lens is designed to focus 100 μm below the surface of the cover layer on a Blu-ray disc. The shape of the lens is compensating for spherical aberration caused by the cover layer to obtain a diffraction limited focus below the surface[26]. In rare-earth quantum computing it is desirable to use ions sitting a small distance below the surface of the crystal, since surface effects will otherwise limit the coherence time of the ions. The crystal has a slightly different refractive index compared to the cover layer of a Blu-ray disc. By adjusting the focal depth in the crystal this can be compensated for, and it should be possible to obtain a diffraction limited focus in the crystal with this lens.

The lens is mounted on an Attocube ANPx51RES positioner to allow focus adjustment (Z-translation) with nanometer precision.

The sample is mounted on two positioners, Attocube ANPx51RES and ANPz51RES, for positioning in the horizontal (X) and vertical (Y) direction respectively. The positioners are very small, 18x15 mm, and work well in liquid helium. They have a total range of 3 x 2.5 mm, with nanometer precision and active position feedback.

Each positioner has two wires for the driving voltage and three wires for the position sensors, so in total 15 wires has to be fed out from the cryostat. A KF40 flange with a 15-wire connector is used for this purpose, and thin copper wires, about 1.5 m long, are pulled down along the sample rod to reach the positioners.

To obtain an image the positioners are stepped in the vertical and horisontal direction, with a minimum step size of about 50 nm, and the fluorescence strength is recorded for each step. During a scan the active position feedback is only used once for each column of the image to make sure that each column start at the same vertical position. The reason for not using feedback in each step is that the active feedback of the positioner is very slow, it takes several seconds to stabilize the position at a given point. The step size is very repeatable, so this does not impose any major problems. The end position variations from one scan to another is less than 1% of the scan length.

No special care was taken to stabilize the spatial position of the sample relative to the lens or the laser beam.

C. Excitation laser

An external cavity diode laser (ECDL), containing a laser diode selected with a center wavelength at 370.7 nm, Sacher SAL-0372-010, is used for excitation of the sample. The laser can be tuned over 2 nm to reach any point within and around the 4f-5d zero phonon absorption line of cerium ions doped into a bulk Y_2SiO_5-crystal. The ECDL can be actively locked to a stable cavity using the Pound-Drever-Hall locking technique to reduce the linewidth and prevent drift. The locking cavity spacer is made of ultra low expansion (ULE) glass and is sitting inside a temperature stabilized vacuum chamber. The system is designed to drift less than 100 kHz over 8 hours[27].

The laser beam is coupled to a single mode optical fiber, and at the output of the fiber a maximum of 1 mW in a Gaussian TEM_{00}-mode is obtained. The laser can

be scanned 160 MHz in locked mode using a double pass AOM, Isomet 1250C-829A, or 6 GHz in unlocked mode by applying a voltage ramp to a piezo crystal attached to the grating of the external cavity.

D. Software

A LabVIEW interface was developed to control all equipment and collect data. The LabVIEW program run directly on a Windows-based oscilloscope, Le Croy Waverunner HRO 66Zi. The oscilloscope connects to the control box of the Attocube positioners for sample scanning and to a DDS, Novatech 425A, controlling the AOM in the laser system for frequency scanning. The pulses from the SPAD can be counted directly in the acquisition program of the oscilloscope. The signal is imported into LabVIEW and plotted versus laser frequency for excitation spectroscopy or in a grid as a function of spatial position to create an image of the sample.

III. PERFORMANCE

A. Resolution

The setup was tested in room temperature using fluorescing polystyrene beads, Invitrogen TetraSpeck Fluorescent Microspheres, and in liquid helium using a gold and silicon sample with a pattern created by focused ion beam milling (FIB).

Fluorescing polystyrene spheres, with a diamater of 4 μm or 0.5 μm, were applied to the backside of a 100 μm thick microscope cover slide. The sample was placed inside a cryostat in room temperature and was imaged through the cover slide onto a camera (CCD 1) in wide field excitation by the 371 nm laser. The fluorescence from the spectral region 385 - 425 nm was selected using a bandpass interference filter.

Images of the microspheres are seen in in figure 3. The images in figure 3 a) and b) are taken with different magnification, and in both cases the 4 μm microspheres are used as size reference. In figure 3 a), 1 μm is imaged onto 10 pixels on the camera, and in figure 3 b) 1 μm is imaged onto 5 pixels on the camera. In figure 3 b), the 0.5 μm sized spheres cover 2-4 pixels, which corresponds to 0.4-0.8 μm. The resolution is in this case limited by the pixels of the camera chip. The images show that the Blu-ray lens can be used for wide field imaging 100 μm below a glass surface with a resolution below 1 μm. The optical resolution can in this case be limited by chromatic aberration, since fluorescence in the spectral region 385-425 nm is collected and imaged. The images show that sub-μm resolution is still possible.

Since the fluorescing polystyrene spheres can not be cooled to liquid helium temperatures another sample had to be used. A sample created by focused ion beam milling was used to test the resolution of the setup in confocal

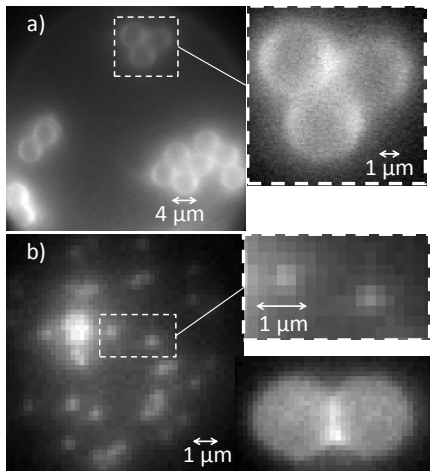

FIG. 3. a) 4 μm and b) 0.5 μm fluorescing polystyrene spheres imaged in wide field illumination. In b) 4 μm spheres imaged with the same magnification are shown to the bottom right for size reference.

mode with the sample and lens immersed in liquid helium. The sample consists of a silicon plate with a 25-50 nm layer of gold evaporated onto it. The gold has been milled away in some places by a focused ion beam to create a pattern. A scanning electron microscope (SEM) image of the sample can be seen in figure 4. For testing the resolution of the confocal optical microscope, features no. 1, 2, 3 and 16 as shown in the image were used.

Figure 5 shows an optical image of the sample that was taken with both the lens and the sample immersed in liquid helium at 2K. The sample did not fluoresce, and the image was created in a confocal geometry by detecting the reflection of the focused laser beam from the sample with the PMT while scanning the sample.

The optical image has a strange feature. It looks like there are three overlapping sets of patterns, one dark and two bright ones, slightly shifted relative to each other. The reason for this is not fully understood. The etched patterns on the sample has a height difference of 25-50 nm compared to the plane gold surface. Since a coherent beam is reflected off the sample it is possible that the sharp edges of the etched pattern give rise to phase shifts and interference in the reflected beam.

Figure 6 shows a comparison between the image obtained with SEM and with the confocal optical microscope. Some distances have been measured with an accuracy of about $\pm$ 5 nm using the SEM software. The patterns in L-shaped structures number 1 and 2 can be optically resolved while the pattern in the smaller L-shape number 3 can not be resolved. Similarly the two

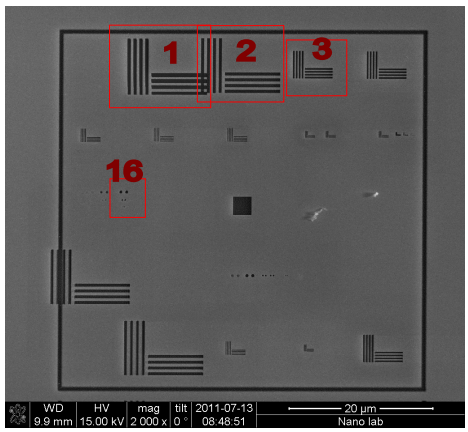

FIG. 4. Test sample imaged by scanning electron microscopy (SEM). Features number 1, 2, 3 and 16 were used to determine the resolution of the optical microscope. (color online)

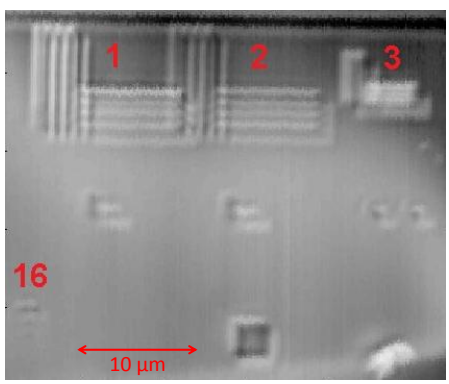

FIG. 5. Part of the test sample imaged by the scanning optical confocal microscope. Both the sample and the objective lens are immersed in liquid helium and at 2K. Since no fluorescence is emitted from the sample, the image is taken by detecting reflected laser light. (color online)

upper dots in feature number 16 a) can be optically resolved, but not the lowest ones in 16 b). According to the resolved patterns, the resolution limit of the setup is between 210 nm and 350 nm.

The step size of the positioners can be determined by comparing the optical image and the distances measured by the SEM. The step size was in this case 110 nm in the horisontal direction and 85 nm in the vertical direction.

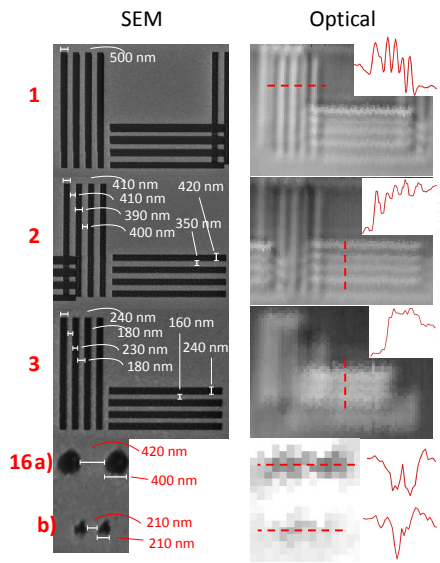

FIG. 6. A comparison between parts of the SEM image and the optical image. Some distances were measured in the SEM software, with an accuracy of ± 5 nm. Plots of the detected signal along a section of the optical image is shown in the insets to the right. The relevant section is indicated with a dashed line. (color online)

In figure 7 the image intensity across a vertical section of the unresolved dot in feature 16 b), is plotted versus scan distance. A least squares fit of a Gaussian curve on a linear background slope is shown in blue. The fitted curve has a full width at half maximum (FWHM) of 327±69 nm (80% confidence interval). The uncertainty in the fitting is large, since the cross section only contains very few data points. The number of data points is limited by the step size of the sample positioners.

The image is a convolution of the object, which is 210 nm in size, and the point spread function (PSF) of the setup. Assuming both profiles have Gaussian shapes, the convolution is also a Gaussian function, with $\mathrm{FWHM}^2_{image} = \mathrm{FWHM}^2_{obj} + \mathrm{FWHM}^2_{PSF}$. The FWHM of the point spread function can then be calculated to 251±93 nm. It corresponds to a resolution limit of 300±111 nm according to Rayleigh's criterion[28].

The diffraction limited Airy disc radius for a wavelength of 371 nm and a numerical aperture of 0.85 is 266 nm. A confocal geometry can improve the resolution by a factor 1.4[29], assuming the pinhole to be infinitesi-

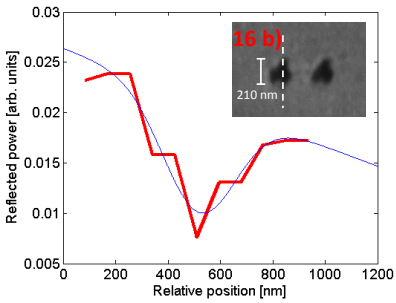

FIG. 7. A vertical section of a dot in feature 16 b), plotted against relative scan distance in the image. A Gaussian fit is made to the data (blue curve). The FWHM of the image is 327±69 nm (80% confidence interval). (color online)

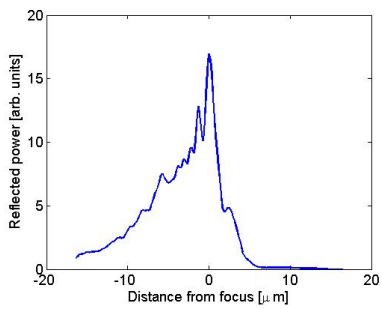

FIG. 8. The detected reflection from the sample as a function of lens position relative to the sample surface. The FWHM of the curve is 5 μm.

mal, which would give a diffraction limited resolution of 190 nm. The measured resolution of 300 nm is slightly larger than the 190 nm calculted from the diffraction limit above. One reason is spherical aberration, at least partly caused by a lack of cover layer on the sample, since the lens is designed for a 100 μm cover layer. Another possible cause is deformations of the lens due to the low temperature.

The depth discrimination of the confocal setup can be estimated by scanning the focal point across the sample surface. Figure 8 shows the measured reflected power from the sample as a function of lens position. As the lens is scanned the sample surface will cross the focus point, where the reflection will have a maximum. The figure shows a long wing with several maxima on the side where the lens is closer to the sample, which is a sign of spherical aberration in the beam[30].

B. Detection efficiency

The collection efficiency of the Blu-ray lens can be calculated to 5.2 % assuming that the fluorescence is emitted in the full 4π solid angle inside a crystal with refractive index 1.8 (as in the case of Y_2SiO_5), and taking refraction and reflection at the crystal surface into account. The reason for such a low collection efficiency is refraction at the high refractive index crystal surface which limits the angle of the light cone that can be collected from the emitter.

This could be improved by using a small solid immersion lens. The SIL would have to be smaller than about 500 μm to fit between the Blu-ray lens and the sample. The price to pay would be a much smaller scan range (in the order of 10 μm) and slightly more cumbersome procedures for changing the sample.

The total detection efficiency of the setup can be calculated by considering the transmission through all optical elements, which is estimated to 60 %, as well as the quantum efficiency of the most sensitive detector, the SPAD, which is around 50 % in the fluorescence range of interest, 385-425 nm.

The total detection efficiency from emitted photons in the sample to counts on the oscilloscope is in this way estimated to 1.6 %.

IV. CONCLUSION

The design and test of a sample-scanning confocal optical microscope for detection of single impurities below the surface of a bulk crystal immersed in liquid helium is described. A lens from a Blu-ray player is used for wide field imaging and scanning confocal imaging. The resolution with the lens and sample immersed in liquid helium was measured to 300±111 nm. The detection efficiency was estimated to 1.6 %.

A single cerium ion in a Y_2SiO_5 crystal can emit about 10 million photons per second if excited continuously at 371 nm. With this detection efficiency it is possible to detect 160 000 counts per second, or 160 counts per millisecond, from a single cerium ion. This is good enough for single ion detection at short time scales.

Rare-earth ions sitting below the surface of a crystal can have very long coherence times at liquid helium temperatures and are suitable qubit systems. It has been suggested to use cerium as a read-out ion in a quantum computing scheme[10]. Single cerium detection with this setup could enable read out of single ion qubits inside a crystal. In the long perspective this could enable scalable quantum computing in a solid state material.

ACKNOWLEDGMENTS

The authors thank Eleonora Lorek for providing the FIB-sample and the SEM images. This work was sup-

ported by the Swedish Research Council (VR), the Knut and Alice Wallenberg Foundation (KAW), (Marie Curie Action) REA Grant Agreement No. 287252 (CIPRIS), Lund Laser Center (LLC), and the Nanometer Structure Consortium at Lund University (nmC@LU).

[1]C. Monroe and J. Kim, Science **339**, 1164 (2013), http://www.sciencemag.org/content/339/6124/1164.full.pdf.
[2]A. V. Kuhlmann, J. H. Prechtel, J. Houel, A. Ludwig, D. Reuter, A. D. Wieck, and R. J. Warburton, Nature Communications **6**, 8204 (2015).
[3]D. D. Awschalom, L. C. Bassett, A. S. Dzurak, E. L. Hu, and J. R. Petta, Science **339**, 1174 (2013), http://www.sciencemag.org/content/339/6124/1174.full.pdf.
[4]Z. M., H. M. P., A. R. L., B. J. G., B. S. E., W. S. M., L. J. J., and S. M. J., Nature **517**, 177 (2015).
[5]R. W. Equall, Y. Sun, R. L. Cone, and R. M. Macfarlane, Phys. Rev. Lett. **72**, 2179 (1994).
[6]M. Afzelius, I. Usmani, A. Amari, B. Lauritzen, A. Walther, C. Simon, N. Sangouard, J. c. v. Minář, H. de Riedmatten, N. Gisin, and S. Kröll, Phys. Rev. Lett. **104**, 040503 (2010).
[7]C. C., U. I., B. F., S. N., A. M., de Riedmatten H., and G. N., Nature **469**, 508 (2011).
[8]H. M. P., L. J. J., L. Y., and S. M. J., Nature **465**, 1052 (2010).
[9]S. E., J. J., V. V. B., S. M. D., M. F., N. S. W., O. D., and T. W., Nature photonics **9**, 83 (2015).
[10]J. H. Wesenberg, K. Mølmer, L. Rippe, and S. Kröll, Phys. Rev. A **75**, 012304 (2007).
[11]L. R., G. W., and M. W., Europhysics Letters **6**, 499 (1988).
[12]A. P. Bartko, L. A. Peyser, R. M. Dickson, A. Mehta, T. Thundat, R. Bhargava, and M. Barnes, Chemical Physics Letters **358**, 459 (2002).
[13]Y. Malyukin, A. Masalov, and P. Zhmurin, Physics Letters A **316**, 147 (2003).
[14]R. Kolesov, K. Xia, R. Reuter, R. Stöhr, A. Zappe, J. Meijer, P. Hemmer, and J. Wrachtrup, Nature communications **3**, 1029 (2012).
[15]T. Utikal, E. Eichhammer, L. Petersen, A. Renn, S. Götzinger, and V. Sandoghdar, Nature communications **5**, 3627 (2014).
[16]P. Siyushev, K. Xia, R. Reuter, M. Jamali, N. Zhao, N. Yang, C. Duan, N. Kukharchyk, A. D. Wieck, R. Kolesov, and J. Wrachtrup, Nature communications **5**, 3895 (2014).
[17]I. Nakamura, T. Yoshihiro, H. Inagawa, S. Fujiyoshi, and M. Matsushita, Scientific reports **4**, 7364 (2014).
[18]W. E. Moerner and D. P. Fromm, Review of Scientific Instruments **74**, 3597 (2003).
[19]H. Inagawa, Y. Toratani, K. Motohashi, I. Nakamura, M. Matsushita, and S. Fujiyoshi, Scientific Reports **5**, 083701 (2015).
[20]J.-M. Segura, A. Renn, and B. Hecht, Review of Scientific Instruments **71**, 1706 (2000).
[21]M. Hussels, A. Konrad, and M. Brecht, Review of Scientific Instruments **83**, 123706 (2012).
[22]L. Zhang, S. Aite, and Z. Yu, Review of Scientific Instruments **78**, 083701 (2007).
[23]A. Högele, S. Seidl, M. Kroner, K. Karrai, C. Schulhauser, O. Sqalli, J. Scrimgeour, and R. J. Warburton, Review of Scientific Instruments **79**, 023709 (2008).
[24]S. M. Mansfield and G. S. Kino, Applied Physics Letters **57**, 2615 (1990).
[25]K. Koyama, M. Yoshita, M. Baba, T. Suemoto, and H. Akiyama, Applied Physics Letters **75**, 1667 (1999).
[26]B. ray Disc association, "White paper, blu-ray disc^{TM} format," Tech. Rep. (Blu-ray Disc association, 2012).
[27]Y. Yan, *Towards single Ce ion detection in a bulk crystal for the development of a single-ion qubit readout scheme*, Ph.D. thesis, Lund University, Lund (2013).
[28]S. W. J., "Modern optical engineering," (SPIE Press, McGraw-Hill Companies, Inc, 2008) pp. 192–193.
[29]W. T., ed., "Confocal microscopy," (Academic Press Limited, 1990) p. 26.
[30]W. T., ed., "Confocal microscopy," (Academic Press Limited, 1990) p. 230.

Paper III

Measurement of line-widths and permanent electric dipole moment change of the Ce 4f-5d transition in Y2SiO5 for a qubit readout scheme in rare-earth ion based quantum computing

Y. Yan, J. Karlsson, L. Rippe, A. Walther, D. Serrano, S. Kröll, P. Goldner, D. Lindgren, M-E. Pistol, L. Zheng and J. Xu.

Phys. Rev. B **87**, 184205 (2013).

PHYSICAL REVIEW B **87**, 184205 (2013)

Measurement of linewidths and permanent electric dipole moment change of the Ce $4f$-$5d$ transition in Y_2SiO_5 for qubit readout scheme in rare-earth ion based quantum computing

Ying Yan,* Jenny Karlsson, Lars Rippe, Andreas Walther, Diana Serrano, David Lindgren, Mats-erik Pistol, and Stefan Kröll
Department of Physics, Lund University, P.O. Box 118, SE-22100 Lund, Sweden

Philippe Goldner
Chimie ParisTech, Laboratoire de Chimie de la Matière Condensée de Paris, CNRS-UMR 7574, UPMC Université Paris 06, 11 rue Pierre et Marie Curie 75005 Paris, France

Lihe Zheng and Jun Xu
Key Laboratory of Transparent and Opto-Functional Inorganic Materials, Shanghai Institute of Ceramics, Chinese Academy of Sciences, Shanghai 201800, China

(Received 18 February 2013; revised manuscript received 2 May 2013; published 30 May 2013)

In this work the inhomogeneous (zero-phonon line) and homogeneous linewidths and the permanent electric dipole moment change (averaged value of all dipole orientations) for the Ce $4f$-$5d$ transition in Y_2SiO_5 were measured in order to investigate the possibility for using Ce as a sensor to detect the hyperfine state of a spatially close-lying Pr or Eu ion. The experiments were carried out on Ce doped or Ce-Pr co-doped single Y_2SiO_5 crystals. The homogeneous linewidth is essentially limited by the excited state lifetime. Based on the linewidth measurements, the oscillator strength, absorption cross section, and saturation intensity were calculated to be about $6.2(\pm1.7) \times 10^{-7}$, $4.5(\pm1.3) \times 10^{-19}$ m^2, and $1.4(\pm0.4) \times 10^7$ W/m^2, respectively. The difference in permanent dipole moment, $\triangle\mu_{Ce}$, between the ground and excited states of the Ce ion was measured as $9.6(\pm5.3) \times 10^{-30}$ C m. These measurements indicate that Ce is a promising readout ion to probe a single-ion qubit state for the quantum computing scheme using rare-earth ions.

DOI: 10.1103/PhysRevB.87.184205 PACS number(s): 33.70.Jg, 78.47.jh, 42.50.Md

I. INTRODUCTION

The quantum computing research field has attracted extensive interest for its potential to give a tremendous boost in computational ability for certain types of problems. Many physical systems have been investigated as test beds for quantum computing:[1] trapped ions,[2] nuclei in molecules,[3] Josephson junctions in superconductors,[4] nitrogen vacancy centers in diamond,[5] rare-earth ions in inorganic crystals,[6] etc. Regardless of the physical system, one of the necessary criteria for a quantum computing scheme is that it should be scalable. In this paper rare-earth ions based quantum computing (REIQC) is under concern, and the results in this paper are a part of the work to develop an ability to read out the hyperfine state of single ions in a rare-earth crystal in order to obtain a scalable system. In REIQC qubit-qubit interaction and arbitrary single qubit rotations have been carried out.[7,8] In these experiments each qubit, where the qubit states ($|0\rangle$ and $|1\rangle$) are two ground-state hyperfine levels of the ion, was represented by an ensemble of ions and addressed via their optical transition frequencies.[8] The optical transition lines of rare-earth ions in a crystal are inhomogeneously broadened as a result of the random substitutions of the rare-earth ions (qubit ions) in the solid matrix, which causes slight crystal-field variations for the sites of the individual ions. The ratio between the inhomogeneous and homogeneous broadening in these systems can be larger than 10^6. Thus a very large number of subensembles of ions can be singled out in frequency space within the inhomogeneous line. Each subensemble can then act as a frequency-selectively addressed qubit although they consist of many ions randomly distributed in space. The conditional gate operations in these systems can be realized via the permanent electric dipole-dipole interaction between the strong-interacting ions in each qubit (see Figs. 3 and 11 in Ref. 9 for details). The strength of the dipole-dipole interaction between two ions depends on the spatial distance between them, r, as $1/r^3$. Because of this spatially dependent coupling and the random spatial distribution of the ions in each qubit, the average probability P of an ion in one qubit being sufficiently close to an ion in another qubit to control its state is often $\ll 1$ for reasonable dopant concentrations. This means that the number of active ions in one ensemble qubit that interact strongly with one ion in each of the rest of the $n-1$ qubits scales as P^{n-1}. In order to improve this poor scalability, Wesenberg *et al.* proposed several schemes.[10] One approach is to discard the ensemble qubits and instead let each single ion represent a qubit. With sufficient dopant concentration, for instance 0.2% for Pr:Y_2SiO_5, there is a large possibility to find sequences of ions which sit $\sim$3 nm (on average) away from each other and where each of these absorbs at a specific and unique optical frequency and represents one single qubit. With that separation the dipole-dipole interaction between the qubits are strong enough for carrying out gate operations.[11]

However, in this single instance quantum computing approach a technique to read out the quantum state of a single-ion qubit needs to be developed. The straightforward typical fluorescence measurement for detecting a single molecule does not work because, first, the transitions of the qubit ion (in Ref. 8 this has been a Pr ion), which can discriminate the qubit states, have excited state lifetimes of more than 10 μs, which provides too low an emission rate for a high signal-to-noise detection; second, and more importantly, the qubit ion candidates have

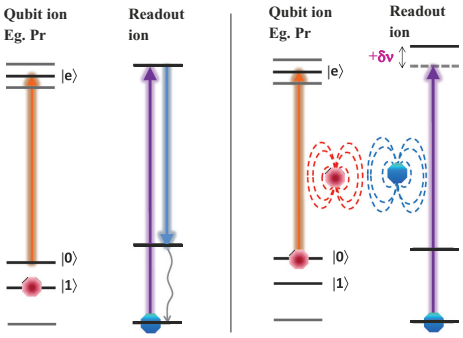

FIG. 1. (Color online) Permanent dipole-dipole interaction between a qubit ion and a readout ion that sits spatially close to this qubit ion. Two lasers interact with the ions, one for the qubit ion and one for the readout ion. The qubit laser sends out a pulse with pulse area of π on the $|0\rangle \rightarrow |e\rangle$ transition and following this pulse the readout laser is turned on and continuously excites the readout ion. If the Pr ion is in state $|1\rangle$ (left panel), the qubit laser is not on resonance with the Pr ion transition so it will not pump the Pr ion to state $|e\rangle$. There is no interaction between the qubit and readout ion in this case. The readout ion continuously sends out fluorescence photons (ON). On the other hand, if the Pr ion is initially in state $|0\rangle$ (right panel), it will be excited by the qubit laser pulse. Since the permanent dipole moment of the Pr ion in state $|e\rangle$ is different from that in state $|0\rangle$, the change of this local electric field induces a frequency shift ($\delta\nu$) of the nearby readout ion transition line. If the shift is larger than the homogeneous linewidth, the readout ion will be out of resonance with the readout laser and never excited so there is no fluorescence (OFF).

more than one ground-state hyperfine level to which they can decay, thus there is no transition that can be cycled until the number of emitted photons is sufficiently large to provide state selective information. A single-ion readout idea was proposed in Ref. 10 to accomplish single-qubit ion detection: an additional ion (hereafter called a readout ion) can be co-doped into the crystal, with such low concentration that there is only one readout ion fluorescing within the laser focal volume. This ion serves as a sensor for reading out the state of nearby qubit ions through the interaction between the qubit and readout ion, illustrated in Fig. 1. As a result the fluorescence signal from the single readout ion, either ON or OFF, depends on whether the single qubit ion is in state $|1\rangle$ or in $|0\rangle$.[12] For the other qubits, which are not directly coupled to the readout ion, their state can be transferred consecutively to its nearby ions through conditional gate operations until the qubit, which is directly coupled to the readout ion, is reached. Then its state can be read out in the way described above (see Sec. III B in Ref. 10 for details).

The readout scheme above requires that the readout ion has the following characteristics: (i) short excited-state lifetime in order to obtain a large contrast in photon emission number per unit time between when the qubit is in the ground state and when it is in the excited state; (ii) narrow homogeneous absorption linewidth such that the permanent dipole-dipole interaction with a nearby qubit shifts the readout ion resonance frequency by several homogeneous linewidths; (iii) large dipole moment change between ground and excited state (again such that the shift due to the permanent dipole-dipole interaction is sufficiently large); (iv) no fluorescence quenching mechanisms, e.g., a long-lived trapping state or energy transfer from the readout ion to the qubit ion. In this work Ce^{3+} (doped in an Y_2SiO_5 crystal) is considered as a readout ion.[13] Ce ions in Y_2SiO_5 have a short excited-state lifetime of about 40 ns,[14–16] to be compared with an excited-state lifetime of possible qubit ions as, e.g., Pr and Eu which are about 0.2 and 2 ms, respectively. The $4f$-$5d$ zero-phonon absorption line of Ce^{3+} doped in Y_2SiO_5 lies around 370.83 nm, which is well separated from the qubit transition frequencies (e.g., 606 nm for Pr ions in site 1). However, other than the excited-state lifetime, the spectroscopic parameters relevant for the readout scheme are not known. In this paper, the second and third spectroscopic requirements, (ii) and (iii) above, for a readout ion were measured for Ce ions in Y_2SiO_5 crystals. The inhomogeneous zero-phonon line (ZPL) measurement is described in Sec. II A, the homogeneous linewidth measurement is discussed in Sec. II B, and the measurement (based on the Ce-Pr interaction) of the Ce permanent dipole moment difference between the ground and excited state is described in Sec. II C. The work is concluded in Sec. III.

II. DETERMINATION OF SPECTROSCOPIC PARAMETERS OF Ce IONS

We focused on the parameters that are of special interest to the single-ion readout scheme in REIQC.

A. Zero-phonon line (ZPL) of Ce ions in an Y_2SiO_5 crystal

The absorption line of interest is the $4f$-$5d$ transition of Ce ions as illustrated in Fig. 2(a). Since the $5d$ levels are less shielded from the environment than the $4f$ levels, the $4f$-$5d$ transitions are often largely broadened by the external perturbations, for instance, defects in the crystal or electron-phonon coupling to the crystal lattice. The experiments were carried out at 2 K to greatly reduce the phonon broadening influence. In this and the following experiments, an external cavity diode laser in a Littrow configuration was used as an excitation source.

The inhomogeneous ZPL of Ce^{3+} was measured on a Ce:Y_2SiO_5 crystal with a nominal dopant concentration of 0.088 at.% relative to the yttrium ions. The result is shown in Fig. 3. Crosses are the experimental data and the solid curve is a Gaussian fit. The measured inhomogeneous linewidth is about 50 GHz (full width at half maximum of the absorption coefficient) with the line center at 370.83 nm. No significant polarization dependence was observed for the absorption. Based on the data shown in Fig. 3, the oscillator strength of the zero-phonon transition was calculated to be $\sim 6.2(\pm 1.7) \times 10^{-7}$ using the relations shown in Refs. 17 and 18.

The ZPL shown in Fig. 3 sits on a background absorption with $\alpha \simeq 3.6$ cm^{-1}, which most likely comes from the absorption by Ce ions in site 2. More information about this is provided by a fluorescence spectrum with an online excitation

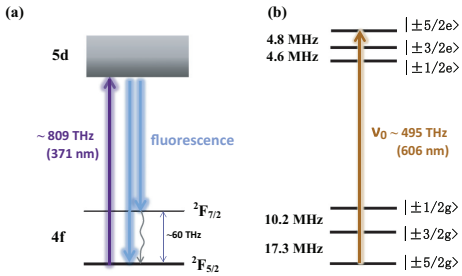

FIG. 2. (Color online) (a) Schematic level structure of Ce^{3+} in Y_2SiO_5 . (b) Schematic level structure for the $^3H_4 \rightarrow {}^1D_2$ transition of Pr^{3+} in Y_2SiO_5.

(at 370.83 nm) and an offline exciation (at 371.53 nm), shown as the solid and dashed curves in Fig. 4. The solid (dashed) curve matches reasonably well with the spectrum from a site 1 (site 2) excitation, shown in Refs. 19 and 14. However, the solid curve contains an extra shoulder sitting around 440 nm, the origin of which is unknown to us. In the rest of the paper, all calculations on Ce^{3+} refer to the ions in site 1, with the site 2 contribution being subtracted as a background.

B. Homogeneous linewidth of the ZPL

The homogeneous linewidth was measured by intensity modulated saturation spectroscopy, where both the pump and probe beams were generated from the external cavity diode laser by a beam splitter (70 : 30). Both beams were focused by a 200 mm focal length lens (focal diameter ~85 μm) onto the $Ce:Y_2SiO_5$ crystal, which was immersed in liquid helium. The probe beam propagated at an angle of ~3° relative to the pump beam in order to separate the two beams for the detection. Two acousto-optical modulators (AOMs) were used in series in the probe beam line. The +1 order deflected beam from the first AOM was used and followed by the −1 order deflected beam from the second AOM. In this way the probe beam frequency could be tuned within a ±50-MHz range relative to the pump

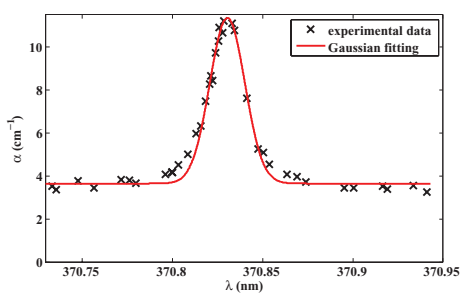

FIG. 3. (Color online) The inhomogeneous ZPL of Ce^{3+} (site 1) in an Y_2SiO_5 crystal. The linewidth is about 50 GHz. α is the absorption coefficient.

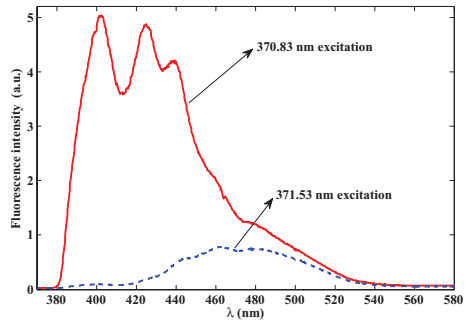

FIG. 4. (Color online) Fluorescence spectrum of Ce^{3+} in a $Ce:Y_2SiO_5$ crystal with 370.83-nm excitation (online of site 1) (solid line) and 371.53-nm excitation (offline of site 1) (dashed line).

beam frequency by adjusting the radio frequency of the second AOM. The probe beam position movement caused by the AOM at different detuning frequencies was compensated by slightly adjusting the mirror in front of the cryostat to overlap the two beams by maximizing the probe beam transmission. The probe beam was monitored by a photodiode after the cryostat. However, it is hard to directly detect an increase of the transmitted power caused by the saturation of the pump beam, since the top-hat pump beam intensity is only of the level of 1% of the estimated saturation intensity. To improve the signal-to-noise ratio, a chopper wheel was used to modulate the intensities of the pump and probe beam with modulation frequencies of 302 and 362 Hz, respectively. Due to the nonlinear interaction, the transmitted probe beam not only has the primary frequency modulation but also has an intensity modulation at the sum (664 Hz) and difference frequency (60 Hz). The signal strength at 664 Hz was extracted from the Fourier transform of the transmitted power of the probe beam and recorded as a function of the detuning frequencies between the pump and probe beams, Δf.

In the experiment, the observed signal at 664 Hz was 16 times as high as the noise floor when Δf is zero but only 1.3% of the signal strength at 362 Hz. The measurement data are shown in Fig. 5, where the vertical axis shows the sum frequency signal normalized by the square of the input probe beam power to compensate for the change in laser power between the data points. Figure 5 reveals a spectral hole width (full width at half maximum) of about 5.8 MHz, which results from a convolution of the laser line (Lorentzian) with the homogeneous line of the transition (Lorentzian) for both the pump step and probe step.[20] However, only fast laser frequency fluctuations within the time scale of the excited-state lifetime (~40 ns) would affect the measurement. This contribution should be negligible considering that the typical linewidth of an external cavity diode laser is 300 kHz over 100 μs. So the homogeneous linewidth we measured has an upper bound of 2.9 MHz. The 40-ns lifetime stated in the literature[14–16] poses a lower limit on the linewidth of ~4 MHz. The reason for measuring a linewidth <4 MHz might be that the signal at positive detuning frequencies was not properly maximized

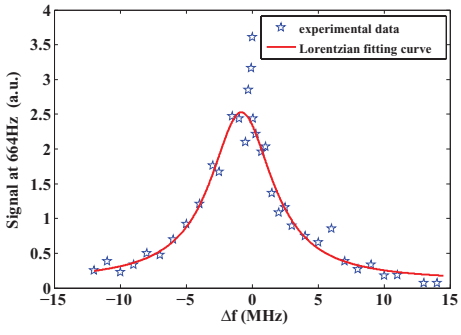

FIG. 5. (Color online) Ce ion homogeneous linewidth measured using saturation spectroscopy. The pentagrams are the measured data points. The solid curve is a Lorentzian fitting of the points excluding the central four which we believe are affected by population trapping.

by adjusting the spatial overlap between the pump and probe beam. While in principle we have no reason to suspect this, the fact that the center of the Lorentzian fitting curve is not at zero detuning but shifted to the left would indicate this as a possible explanation.

Based on the coherence time (lifetime limited value) and the frequency integrated absorption cross section (in m^2 rad/s) calculated from the inhomogeneous line,[21] the absorption cross section of the Ce ion in site 1 and the corresponding saturation intensity were calculated to be $\sim 4.5(\pm 1.3) \times 10^{-19}$ m^2 and $\sim 1.4(\pm 0.4) \times 10^7$ W/m^2, respectively.

The experimental data indicate an increased interaction between the beams within a narrow range (~400 kHz) of frequency detuning close to the line center. The origin of this resonance was not investigated but narrow resonances of this type can occur if the upper state can also decay to a third level which (compared with the relaxation from the excited state) relaxes slowly to the ground state; see, e.g., Refs. 22 and 23. The linewidth of the resonance is then determined by the decay rate of this third level. In the present experiment the third level could possibly be one of the lowest Kramer's doublets on the $^2F_{5/2}$ $(4f)$ ground state, compared with, e.g., Ref. 24, and the intrinsic width of the narrow resonance would then be given by the spin-lattice relaxation rate of the ground state. Using the calculated saturation intensity, the signal at the sum frequency (664 Hz) should be about 0.1% of the signal at 362 Hz at zero detuning frequency. However, the actual sum frequency signal is a factor of 8 higher than expected. The existence of a third level may not only give rise to the narrow structure mentioned above but also could provide a larger saturation effect due to the trapping of ions in this level. This could be part of the reason why the signal at 664 Hz (0.8% of the signal at 362 Hz) is larger than expected.

C. Ce-Pr interaction

The Ce and Pr ions in Y_2SiO_5 have different permanent electric dipole moments in their ground and excited states as they sit in noncentrosymmetric sites. This difference in the ground- and excited-state permanent dipole moment is denoted as $\Delta\mu$. When one ion is changing its state from ground to excited state or vice versa, the surrounding electric field is changed. This permanent dipole-dipole interaction causes a frequency shift Δf of the transition lines of the nearby ions, which depends on the spatial distance r between those two ions and $\Delta\mu$ of both ions as[25]

$$\Delta f \propto \frac{\Delta\mu_{\mathrm{Ce}}\Delta\mu_{\mathrm{Pr}}}{r^3}\kappa(\Delta\hat{\mu}_{\mathrm{Pr}}, \Delta\hat{\mu}_{\mathrm{Ce}}, \hat{r}), \tag{1}$$

where

$$\kappa(\Delta\hat{\mu}_{\mathrm{Pr}}, \Delta\hat{\mu}_{\mathrm{Ce}}, \hat{r}) = \Delta\hat{\mu}_{\mathrm{Ce}} \cdot \Delta\hat{\mu}_{\mathrm{Pr}} - 3(\hat{r} \cdot \Delta\hat{\mu}_{\mathrm{Ce}})(\hat{r} \cdot \Delta\hat{\mu}_{\mathrm{Pr}}) \tag{2}$$

stands for dependence of the interaction on the dipole orientations and displacement. $\Delta\hat{\mu}_{\mathrm{Pr,Ce}}$ and $\hat{r}$ are the unit vectors of the permanent dipole moment change and the displacement between these two dipoles (in our case they are a Pr dipole and a Ce dipole). Since the shift arises from the permanent dipole moment changes and not the transition dipole interactions, the shifts are the same regardless of which ion is excited for two ions with a specific distance. The value of $\Delta\mu_{\mathrm{Ce}}$ of the Ce^{3+} $4f$-$5d$ transition in Y_2SiO_5 is not previously known. It can, e.g., be determined by measuring the Stark shift caused by the interaction between the ions and an external electric field.[26] Here we instead used a sample doped with both Ce^{3+} and Pr^{3+} and implemented a two-pulse photon echo experiment on Pr ions, where Ce ions were excited during the dephasing period of the Pr ions, and the reduction of the echo intensity was observed.[25] The reduction is caused by the fact that a subgroup of Pr ions experience a frequency shift induced by the excitation of nearby Ce ions. When this happens the phases of the Pr superposition states evolve at different rates in the dephasing and rephasing periods, which causes an echo intensity decrease which depends on the magnitude of the shift and the evolution time. Thus the Pr-Ce ion-ion interaction introduces an additional dephasing channel for the excited Pr ions, which broadens the Pr homogeneous linewidth. From this extra broadening $\Delta\mu_{\mathrm{Ce}}$ can be calculated.[27]

In this experiment, an actively stabilized dye laser with a linewidth of less than 1 kHz was used to excite the Pr $^3H_4 \rightarrow {}^1D_2$ transition at 606 nm. Two weak Gaussian pulses with power of ~0.5 mW (0.15-μs duration time) were created with an AOM and the photon echo from the Pr ions was recorded. Ce ions were excited during the dephasing time of the Pr ions using an external cavity diode laser and another AOM. The pulse sequence is shown in Fig. 6, where eraser pulses refer to several frequency scanning pulses at 606 nm. These were applied to shuffle the Pr ions between the hyperfine states and prevent persistent hole burning that would otherwise be created by the two Gaussian pulses (pulse 1 and pulse 2) over

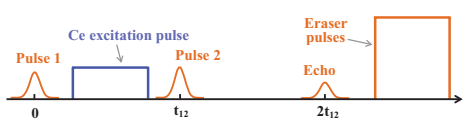

FIG. 6. (Color online) Pulses sequence for the Ce-Pr interaction measurement.

time. Each laser beam was coupled into a single mode fiber for spatial mode cleaning, and the collimated output beams from the fibers were coupled together by a dichroic mirror with 90% transmission (reflection) for 606 nm (371 nm). Those two beams were focused onto the crystal with focal diameters of about 130 and 170 μm, respectively, by a low dispersion CaF_2 lens. The spatial mode overlap between the two beams within the crystal was ascertained by using a beam profiler to ensure that the center of the two beam profiles overlapped with each other within 10 μm over the 40-cm distance between the dichroic mirror and the common focusing lens. The echo signal was deflected by a third AOM into a photomultiplier tube (PMT). Right before the PMT an electronic shutter with 100-μs rise time was used to prevent the strong frequency scanning pulses from reaching the PMT after the echo was recorded.

The intensity of the echo from the Pr ions was recorded as a function of the separation time t_{12} in two situations: Ce ions being excited or not excited (Ce laser blocked) in between the two Pr excitation pulses. The excitation of Ce ions was implemented at wavelengths of either 370.83 nm (hereafter referred to as online) or 371.54 nm (referred to as offline). Here online (offline) refers to the fact that the excitation wavelength is on (off) the ZPL of Ce ions in site 1. It is worthwhile to note that even at the offline wavelength there is still considerable background absorption as can be seen in the absorption spectrum in Fig. 3. We believe that this comes from ions in site 2, and they will also cause a reduction of the photon echo from Pr ions, by the interaction shown in Eq. (1). The experimental data from a Pr:Ce:Y_2SiO_5 crystal (grown by Shanghai Institute of Ceramics in China) with 0.05% of Pr and 0.088% of Ce dopant concentration relative to the Y ions are shown in Fig. 7.

Four series of data were recorded. The circles are the echo signals from the Pr ions when Ce ions were excited online (excitation power ~0.5 mW) during the dephasing time t_{12}. Each point is an average value of ~30 shots, and the error bar shows the standard deviation. To verify the experimental data, a complimentary data point corresponding to each circle, shown as a star, was recorded as well with the Ce excitation laser blocked. At each value of t_{12} in Fig. 7, all shots of the circle point were recorded first followed by the shots of the corresponding star point. After recording all data points at various t_{12}, the Ce laser was tuned to the offline position. The corresponding set of data was recorded, shown by the diamonds (Ce laser offline) and crosses (Ce laser blocked). The solid, dotted, dashed, and dash-dotted lines are the logarithmic fits of the experimental data for the cases when the Ce laser is online, blocked, offline, and blocked, respectively. The two blocked cases are equivalent, but show an offset on the echo signal possibly caused by laser power drift. However, the slopes are the same within the margin of error, as expected. The echo intensity as a function of the pulse separation time is

$$I_{\text{echo}} = I_0 e^{-4t_{12}/T_2}, \tag{3}$$

where I_0 is the maximum echo intensity when extrapolating the separation time to zero. Results of the measurements are shown in Table I, where T_2 and Γ_{hom} refer to the coherence time (with 70% confidence interval) and homogeneous linewidth of the Pr ions transition, respectively.

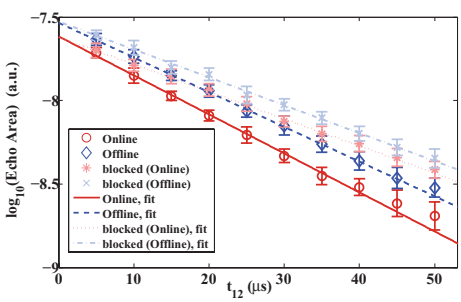

FIG. 7. (Color online) Decay curve of the echo from the Pr ions on the Pr:Ce:Y_2SiO_5 crystal. The circles (diamonds) are the experimental echo signal when the Ce ions were excited at an online (offline) wavelength. Error bar shows the standard deviation. The solid, dashed lines are logarithmic fits corresponding to those two cases. The stars (crosses) are the experimental data when the Ce excitation laser was blocked. The difference between them is explained in the text.

TABLE I. Measured homogeneous linewidths of Pr ions $^3H_4 \rightarrow {}^1D_2$ transition with Ce excitation laser being at an online wavelength, offline wavelength, and turned off.

	Ce online		Ce offline	
Measured values (Pr)	Laser on	Laser off	Laser on	Laser off
T_2 (μs)	74 ± 2	107 ± 3	83 ± 1	104 ± 3
Γ_{hom} (kHz)	4.3 ± 0.1	3.0 ± 0.1	3.83 ± 0.05	3.1 ± 0.1

Table I shows that the homogeneous linewidth broadening caused by the Ce online excitation Γ_{br} is 1.3 kHz with $\pm$0.14 kHz for a 70% confidence interval, while for the Ce offline excitation the broadening is ~0.7 kHz ($\pm$0.11 kHz). The difference between these two values tells the broadening contribution only from the Ce ions in site 1, which is ~0.6 ($\pm$0.18) kHz. This value was used for calculating $\Delta\mu_{\text{Ce}}$ in the following passage.

However, the reduction in echo intensity could conceivably be caused by other reasons than a frequency shift resulting from the permanent dipole-dipole interaction. For instance, (1) the Pr ions directly absorb the ultraviolet (UV) photons leading to processes shortening the coherence time, which causes the echo intensity to decrease, although this is unlikely to happen, as seen from the literature.[28] (2) The energy is transferred from Ce ions to Pr ions so that Pr ions are excited to a higher level, which also can cause an echo reduction. To clarify the influence of suggestion (1) above we did exactly the same measurement as before but on an Y_2SiO_5 crystal with the same Pr dopant concentration but no Ce ions. The result is shown in Fig. 8, where the Pr homogeneous linewidths are the same when the laser pulse at the Ce absorption wavelength was present and absent, which means that the linewidth broadening shown in Fig. 7 does not result from direct UV absorption by the Pr ions. For clarifying whether the interaction can be induced by energy transfer [argument (2) above], we did an

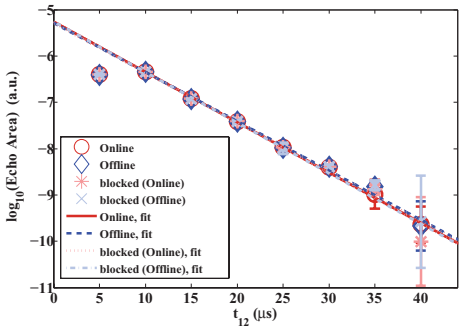

FIG. 8. (Color online) Echo decay curve on the pure Pr:Y_2SiO_5 crystal. Notation of the data symbols is the same as in Fig. 7. Circles, diamonds, stars, and crosses are for the cases when the Ce laser is online, offline, blocked (online), and blocked (offline), respectively. Deviation of the first data point from the fitting line was caused by the saturation of the PMT.

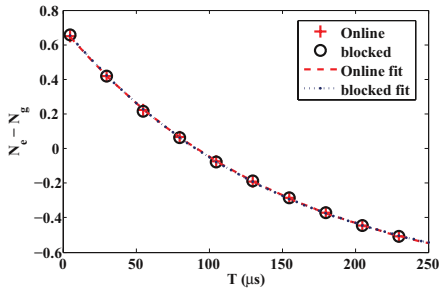

FIG. 9. (Color online) Population difference between the excited and ground state of Pr ions in a Pr:Ce:Y_2SiO_5 crystal as a function of time with Ce online excitation (+) and Ce laser blocked (◯). The dashed and dot-dashed lines are the respective exponential curve fittings. The standard deviation of the data points is ∼2%.

excited-state population decay measurement on Pr ions in the Pr:Ce:Y_2SiO_5 crystal as follows: (i) A zero absorption spectral window centered at frequency ν_0 was created using optical pumping.[29] (ii) A subset of Pr ions having their transition at frequency ν_0 is transferred to the $|\pm 5/2g\rangle$ state [the Pr ion level structure is shown in Fig. 2(b)]. (iii) A pulse with area of π excites these ions to their $|\pm 5/2e\rangle$ state with an efficiency of more than 85%. (iv) A Ce excitation pulse with duration time T was incident on the crystal. If there is Ce-Pr energy transfer or state changing interactions other than the frequency shifts due to the permanent dipole-dipole interaction, the Pr excited-state population should change. (v) After the time T the transmission of a pulse scanned in frequency around frequency ν_0 [see Fig. 2(b)] determines the population difference between the $|\pm 5/2g\rangle$ and $|\pm 5/2e\rangle$ state by measuring the absorption (this pulse is called the readout pulse in the following passage). Following the procedure above the Pr population difference (normalized to the initial population in $|\pm 5/2g\rangle$ state) between the excited and ground state, $N_e - N_g$, was recorded as a function of the separation time T between the π pulse and the readout pulse for the two cases where Ce ions were excited or not excited during the time T.

Figure 9 shows that the population differences of Pr ions when Ce ions are excited (online) and not excited (blocked) agree with each other within 3%. Similar measurements from the Ce offline excitation and Ce laser blocked cases also show the same result. Thus no effect of energy transfer between the Ce and Pr ions was observed. Based on the test on the pure Pr doped crystal (Fig. 8) and this excited-state population decay measurement of Pr ion (Fig. 9), to the best of our knowledge, the homogeneous broadening shown in Fig. 7 should be caused by the permanent dipole-dipole interaction between the Pr and Ce ions.

The homogeneous linewidth broadening induced by the permanent dipole-dipole interaction Γ_{br} relates to the $\Delta\mu$ of the interacting ions as[27]

$$\Gamma_{br} = \frac{1}{2\pi} C D_0 \langle W_{\mathrm{Ce}} \rangle, \tag{4}$$

where

$$C = \tfrac{2}{3}\pi^2 p \langle |\kappa| \rangle, \tag{5}$$

p represents the occupation probability of the Ce ions relative to the total number of ions in the crystal, and $\langle |\kappa| \rangle$ is in the order of 1,[25] representing the averaged value of κ [shown in Eq. (2)] over all angles defining the relative dipole orientations and the orientations between dipoles and the displacement.

D_0 describes the magnitude of the permanent dipole-dipole interaction with a unit distance of r_0,

$$D_0 = \eta(0) \frac{\Delta\mu_{\mathrm{Ce}} \Delta\mu_{\mathrm{Pr}}}{4\pi\epsilon_0 \hbar r_0^3}, \tag{6}$$

where $\Delta\mu_{\mathrm{Ce}}$ and $\Delta\mu_{\mathrm{Pr}}$ is the difference of the permanent dipole moment in the ground and excited state of Ce and Pr ions, respectively. $\eta(0) = 1.28$ represents the dielectric correction factor for long-range dipole-dipole interaction.[30] ϵ_0 is the vacuum permittivity. r_0 stands for the length of the cube which one ion occupies on average. $\langle W_{\mathrm{Ce}} \rangle$ represents the average excitation probability of the Ce ions contributing to the interaction during the dephasing time.

For the crystal used in this experiment, the occupation probability $p \simeq 1.92 \times 10^{-4}$ considering a 87% occupation on site 1.[31] $\langle W_{\mathrm{Ce}} \rangle \simeq 1.8(\pm 0.7) \times 10^{-7}$, which is estimated from the saturation intensity (shown in Sec. II B) and integrated over the inhomogeneous line as in Ref. 27. The excitation intensity used for the estimation is the average value over a volume with the beam diameter of ρ_{fwhm}, the full width at half maximum of the Pr excitation laser intensity, through the crystal thickness of 1 mm. $\Delta\mu_{\mathrm{Ce}}$ (site 1) is calculated as $9.6(\pm 5.3) \times 10^{-30}$ C m using Eqs. (3)–(5) with $r_0 = 0.237$ nm, $\langle |\kappa| \rangle_\Omega \simeq 0.7$, and $\Delta\mu_{\mathrm{Pr}} = 2.43 \times 10^{-31}$ C m.[27] We also calculated $\langle W_{\mathrm{Ce}} \rangle$ from the ratio of the number of absorbed photons (equivalently number of excited Ce ions) during 40 ns over the total number of Ce ions in site 1 for a certain volume (given by the laser

beam profile). The value is $1.8(\pm 0.4) \times 10^{-7}$, which agrees with the previous value very well.

The measured value of $\Delta\mu_{Ce}$ (site 1) is an encouraging result as it indicates that the transition line of a Ce ion will be shifted by more than 300 MHz on average due to the change of states of a nearby Pr ion in a Pr:Ce:Y_2SiO_5 crystal with a dopant concentration of 0.05% (the average ion-ion distance is ∼5 nm). This shift is clearly large enough to force the Ce ions in site 1 out of resonance with the readout laser which is initially on resonance. However, this shift does not prohibit the excitation of the Ce ions in site 2 since these ions are not excited at their zero-phonon line and the absorption spectrum is much broader than the permanent dipole-dipole interaction induced shift. This gives us a background fluorescence even if the single Ce ion in site 1 is shifted out of resonance. However, based on our preliminary investigation the fluorescence contrast within the range 380–420 nm (as shown in Fig. 4) is believed to be good enough for detecting a single Ce ion in site 1 with a reasonable signal-to-noise ratio. So the fluorescence emitted from the Ce ions in site 1 can still be used as an indicator to show which state ($|0\rangle$ or $|1\rangle$) the Pr ion occupies.

III. CONCLUSION

The spectroscopic properties of Ce^{3+} doped in an Y_2SiO_5 crystal were characterized for investigating the possibility to use it as a probe for detecting which hyperfine ground state a nearby ion (e.g., Pr) is occupying. Particularly (i) the ZPL of the $4f$-$5d$ transition of Ce^{3+} doped in Y_2SiO_5 was found around 370.83 nm with a linewidth of about 50 GHz. (ii) The homogeneous linewidth was measured by intensity modulated saturation spectroscopy to be ∼3 MHz. It is essentially limited by the excited-state lifetime of that transition, which is the optimal case for using Ce^{3+} as a readout ion. In this experiment we also have not observed any signs that there is a long-lived trapping state for Ce ions, which means that the fluorescence can be cycled as many times as needed. From the linewidth measurements the oscillator strength, absorption cross section, and saturation intensity were calculated to be $\sim 6.2(\pm 1.7)\times 10^{-7}$, $\sim 4.5(\pm 1.3)\times 10^{-19}$ m^2, and $\sim 1.4(\pm 0.4)\times 10^7$ W/m^2, respectively. (iii) The Ce-Pr interaction was demonstrated through a photon echo experiment and the difference in the permanent dipole moment ($\Delta\mu_{Ce}$, averaged value of all dipole orientations) for the $4f$ ($^2F_{5/2}$) and lowest $5d$ states was measured to be $\sim 9.6(\pm 5.3) \times 10^{-30}$ C m, which is sufficiently large to provide a frequency shift much larger than the Ce homogeneous linewidth for a suitable dopant concentration of qubit ions. The data obtained so far shows that the Ce ion is a very promising readout ion candidate and a setup for single Ce ion detection by observing the $5d$-$4f$ fluorescence is currently under construction. Single Ce ion detection in a YAG ($Y_2Al_5O_{12}$) crystal was recently demonstrated.[32] The ability of state selective readout of a single rare-earth ion in inorganic crystals would be a significant step forward for quantum computing in these materials where high fidelity gate operations on ensembles have already been carried out.[7,8] It also opens the possibility to use rare-earth ions as extraordinarily sensitive probes of the local environment in these types of crystals. The ability to carry out (and read out) operations on individual ions would strongly address the scalability problem and greatly reduce the qubit operation time since fewer and simpler pulses can be used when the dephasing caused by the inhomogeneous broadening is no longer a concern. It is also quite clear that rare-earth ion doped crystals generally have excellent properties for preserving quantum states seen from the impressive quantum memory development that is taking place in these materials.[33–35]

ACKNOWLEDGMENTS

We thank M. Bettinelli for the helpful discussion. This work was supported by the Swedish Research Council (VR), the Knut and Alice Wallenberg Foundation (KAW), the Maja och Erik Lindqvists forskningsstiftelse, the Crafoord Foundation and the EC FP7 Contract No. 247743 (QuRep), (Marie Curie Action) REA Grant Agreement No. 287252 (CIPRIS), Lund Laser Center (LLC), and the Nanometer Structure Consortium at Lund University (nmC@LU).

*Corresponding author: yan.ying@fyisk.lth.se

[1] T. D. Ladd, F. Jelezko, R. Laflamme, Y. Nakamura, C. Monroe, and J. L. Obrien, Nature (London) **464**, 08812 (2010).
[2] R. Blatt and D. Wineland, Nature (London) **453**, 1008 (2008).
[3] J. A. Jones, Prog. NMR Spectrosc. **59**, 91 (2011).
[4] J. H. Plantenberg, P. C. de Groot, C. J. P. M. Harmans, and J. E. Mooij, Nature (London) **447**, 836 (2007).
[5] A. P. Nizovtsev, S. Ya. Kilin, F. Jelezko, T. Gaebal, I. Popa, A. Gruber, and J. Wrachtrup, Opt. Spectrosc. **99**, 233 (2005).
[6] N. Ohlsson, R. K. Mohan, and S. Kröll, Opt. Commun. **201**, 71 (2002).
[7] J. J. Longdell and M. J. Sellars, Phys. Rev. A **69**, 032307 (2004).
[8] L. Rippe, B. Julsgaard, A. Walther, Y. Ying, and S. Kröll, Phys. Rev. A **77**, 022307 (2008).
[9] L. Rippe, M. Nilsson, S. Kröll, R. Klieber, and D. Suter, Phys. Rev. A **71**, 062328 (2005).
[10] J. H. Wesenberg, K. Mølmer, L. Rippe, and S. Kröll, Phys. Rev. A **75**, 012304 (2007).
[11] S. Bengtsson, Master thesis, Lund University, Sweden, 2012.
[12] A. Walther, B. Julsgaard, L. Rippe, Y. Ying, S. Kröll, R. Fisher, and S. Glaser, Phys. Scr. **T137**, 014009 (2009).
[13] Suggested by Olivier Guillot-Noël in the European Quantum Information Processing and Computing workshop, Rome, 2004.
[14] H. Suzuki, T. A. Tombrello, C. L. Melcher, and J. S. Schweitzer, Nucl. Instrum. Methods Phys. Res. A **320**, 263 (1992).
[15] T. Aitasalo, J. Hlsa, M. Lastusaari, J. Legendziewicz, J. Niittykoski, and F. Pell, Opt. Mater. **26**, 107 (2004).
[16] J. E. Hernandez, Master thesis, Lund University, Sweden, 2006.
[17] B. Henderson and G. F. Imbusch, *Optical Spectroscopy of Inorganic Solids* (Oxford University Press, New York, 1989), p. 262, Eq. (6.10a).
[18] A. Smakula, Z. Phys. **59**, 603 (1930).
[19] W. Drozdowski, A. J. Wojtowicz, D. Wisniewski, P. Szupryczynski, S. Janus, J. Lefaucheur, and Z. Gou, J. Alloy. Compd. **380**, 146 (2004).
[20] S. Völker, Annu. Rev. Phys. Chem. **40**, 499 (1989).

[21]R. C. Hilborn, Am. J. Phys. **50**, 982 (1982).
[22]D. G. Steel and S. C. Rand, Phys. Rev. Lett. **55**, 2285 (1985).
[23]M. Mitsunaga, N. Uesugi, and K. Sugiyama, Opt. Lett. **18**, 1256 (1993).
[24]R. Kolesov, Phys. Rev. A **76**, 043831 (2007).
[25]S. B. Altner, G. Zumofen, U. P. Wild, and M. Mitsunaga, Phys. Rev. B **54**, 17493 (1996).
[26]F. R. Graf, A. Renn, U. P. Wild, and M. Mitsunaga, Phys. Rev. B **55**, 11225 (1997).
[27]F. R. Graf, A. Renn, G. Zumofen, and U. P. Wild, Phys. Rev. B **58**, 5462 (1998).
[28]N. V. Kuleshov, V. G. Shcherbitsky, A. A. Lagatskya, V. P. Mikhailov, B. I. Minkov, T. Danger, T. Sandrock, and G. Huber, J. Lumin. **71**, 27 (1997).
[29]M. Nilsson, L. Rippe, S. Kröll, R. Klieber, and D. Suter, Phys. Rev. B **70**, 214116 (2004).
[30]G. D. Mahan, Phys. Rev. **153**, 983 (1967).
[31]Y. C. Sun, in *Spectroscopic Properties of Rare Earths in Optical Materials*, edited by G. Liu and B. Jacquier (Springer, Berlin, 2005), Chap. 7.
[32]R. Kolesov, K. Xia, R. Reuter, R. Stöhr, T. Inal, P. Siyushev, and J. Wrachtrup, arXiv:1301.5215.
[33]M. P. Hedges, J. J. Longdell, Y. M. Li, and M. J. Sellars, Nature (London) **465**, 1052 (2010).
[34]E. Saglamyurek, N. Sinclair, J. Jin, J. A. Slater, D. Oblak, F. Bussieres, M. George, R. Ricken, W. Sohler, and W. Tittel, Nature (London) **469**, 512 (2011).
[35]I. Usmani, Ch. Clasusen, F. Bussières, N. Sangouard, M. Afzelius, and N. Gisin, Nat. Photon. **6**, 234 (2012).

Paper IV

Satellite line mapping in Eu^{3+}-Ce^{3+} and Pr^{3+}-Ce^{3+} codoped Y_2SiO_5

D. Serrano, J. Karlsson, L. Zheng, Y. Dong, A. Ferrier, P. Goldner, A. Walther, L. Rippe, and S. Kröll.

Accepted for publication in J. of Lumin , (2015).

Satellite line mapping in Eu^{3+}-Ce^{3+} and Pr^{3+}-Ce^{3+} codoped Y_2SiO_5

D. Serrano[1]*, J. Karlsson[1], L. Zheng[2], Y.Dong[3], A. Ferrier[4,5], P. Goldner[4], A. Walther[1], L. Rippe[1], S. Kröll[1]

[1]Department of Physics, Lund University, P.O. Box 118, SE-22100 Lund, Sweden

[2]Shanghai Institute of Ceramics, Chinese Academy of Sciences, 588 Heshuo Road, Jiading District, 201899 Shanghai, China

[3]Shanghai Institute of Optics and Fine Mechanics, Chinese Academy of Sciences, 390 Qinghe Road, Jiading District, 201800 Shanghai , China

[4]PSL Research University, Chimie ParisTech-CNRS, Institut de Recherche de Chimie Paris, 75005 Paris, France

[5]Sorbonne Universités, UPMC Université Paris 06, 75005, Paris, France

Abstract

In this work we perform a high-resolution spectroscopic investigation of Eu^{3+}-Ce^{3+} and Pr^{3+}-Ce^{3+} codoped Y_2SiO_5 crystals. Satellite line spectra were recorded at low temperature around the Eu^{3+}:$^7F_0 \rightarrow {}^5D_0$ and the Pr^{3+}:$^3H_4 \rightarrow {}^1D_2$ transitions. It is observed that the incorporation of Ce^{3+} as a codopant notably changes the Eu^{3+} and Pr^{3+} satellite line patterns. Satellite lines measured in singly doped Eu^{3+}:Y_2SiO_5 were found at the same spectral positions in Eu^{3+}- Ce^{3+} codoped crystals. These coincident lines were concluded to be due to pairs of Eu^{3+} ions. Extra satellite lines appeared in the codoped crystals, which were assigned to Ce^{3+} related structures such as Ce^{3+}-Eu^{3+} pairs. The analysis of the Pr^{3+} satellite line spectra presents further challenges. Satellite lines associated to Pr^{3+} pairs show weaker intensity, presumably due to the efficient quenching of the Pr^{3+} $^1D_2$ emission through cross-relaxation paths ($^1D_2 \rightarrow {}^1G_4$; $^3H_4 \rightarrow {}^3F_4$). The investigation of the Eu^{3+} and Pr^{3+} satellite line patterns in Y_2SiO_5 is particularly interesting for their exploitation in rare-earth based quantum computation schemes.

Keywords: Y_2SiO_5, fluorescence microscopy, satellite lines, quantum computing.

* Current address: University of Zürich, Department of Chemistry, Winterthurerstrasse 190, CH-8057, Zürich, Switzerland. Email: diana.serrano@chem.uzh.ch.

1. Introduction

The quantum information processing field has seen promising developments in the last years. An interesting solid-state approach is based on the possibility to carry out controlled gate operations between rare-earth dopants in crystals, which are optically prepared as quantum information units or qubits [1-3]. A major challenge is still to implement scalable quantum computing designs involving a large number of interacting qubits [3]. In the case of rare-earth crystals, scalability can be attained by going down to the single-ion level. This implies the localization of chains of interacting dopants, each one representing a different qubit (Fig. 1a), and the development of techniques for the optical addressing of single ions in doped crystals. In this sense, important results have been recently reported about the detection [4] and optical manipulation [5] of single luminescent centers in solids. A further requirement for the implementation of quantum processors is also the development of methods to faithfully readout the qubit states. Here, the identification of the qubit states is planned through the interaction of the qubit ions with a so-called "readout ion" (Fig. 1a). The proposed readout mechanism exploits the fact that the excited state of the readout ion is shifted in energy when a neighbor qubit is promoted from the ground state to an excited state. This effect is attributed to the static electric dipole moment induced by the crystal field on the dopants, which actually changes when nearby ions become excited [6]. The qubit states are encoded in the hyperfine structure of the qubit ions. Thus, a pulse sequence can be designed so that the above mentioned energy shift occurs when the qubit ion is in one of the two possible qubit states (for example state 0) and does not occur when it is found in the other (state 1). [7]. Thus, in absence of line shift, it is possible to excite the readout ion. The detection of the subsequent fluorescence, referred to as readout emission, provides then direct information about the qubit quantum state.

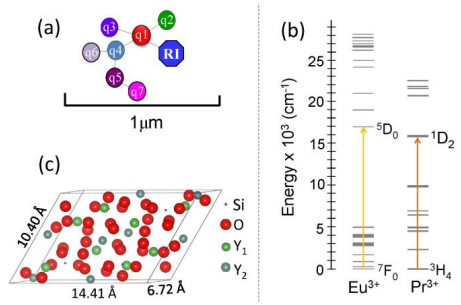

Figure 1. (a) Schematic local environment showing multiple qubits and a single readout ion (RI). (b) Energy level diagram for Pr^{3+} and Eu^{3+}. Arrows indicate the optical transitions targeted for quantum operations. (c) Y_2SiO_5 monoclinic unit cell. Yttrium ions occupy two different crystal sites referred to as Y_1 and Y_2.

The codoping of Ce^{3+} with either Eu^{3+} or Pr^{3+} in Y_2SiO_5 has been previously investigated for quantum computing purposes [7,8]. The interest in Eu^{3+} and Pr^{3+} ions comes from the particularly long optical coherence times observed for the Pr^{3+}:$^1D_2 \rightarrow {}^3H_4$ and Eu^{3+}:$^5D_0 \rightarrow {}^7F_0$ transitions (Fig. 1b), around 150 μs and 1.5 ms respectively [9]. Moreover, coherence times on the order of minutes [10] and up to hours [11] have been experimentally evidenced for the Pr^{3+} and Eu^{3+} ground state hyperfine transitions in Y_2SiO_5. Such results confirm the potential of these ions for their use as qubits in quantum computing schemes. Trivalent cerium, on the other hand, is being investigated as a possible readout ion for Eu^{3+} and Pr^{3+} qubit states [3]. Compared to the 4f→4f transitions, the high-emission rate of the Ce^{3+} 5d→4f transition, about 2.5×10^7 s^{-1} [12], is advantageous for the successful detection of fluorescence from a single Ce^{3+} ion. Among the latest results, evidence of permanent electric dipole-dipole interaction between Ce^{3+} and Pr^{3+} ions has been reported in Y_2SiO_5 [7] and critical ion-ion distances have been estimated for an efficient readout mechanism in this material [8].

An interesting approach to obtain information about the interaction between close lying dopants without actually detecting single ions is the

exploitation of the so-called satellite line structure [13]. Satellite lines appear in the optical spectra of doped crystals at frequencies around the main transition lines, typically associated to perturbed crystal sites. These minor sites are often related to dopant ions in the vicinity of point defects [14,15], including chemical impurities, vacancies and other dopants. The strain in the lattice created by a close-lying defect is enough to modify the crystal field seen by the optical center up to the point of shifting its transition frequency out of the main inhomogeneously broadened line. In the case of high quality doped crystals such as the ones investigated here, the density of defects is orders of magnitude lower than the doping density. Thus, satellite lines in rare-earth doped crystals are expected to result from aggregations of dopants, each spectral satellite line corresponding to a structurally different pair or aggregate [16-20]. Quantum computing targeting rare-earth ions in satellite lines has been proposed in Eu^{3+} stoichiometric crystals [13,21]. In the present work, we report the satellite line structure of Eu^{3+} and Pr^{3+} in Y_2SiO_5 with and without the presence of Ce^{3+} as a codopant. Consistent satellite lines resulting from Eu^{3+} and Pr^{3+} pairs are here identified for the first time in both singly doped and copoded Y_2SiO_5 crystals. The analysis also evidences the presence of satellite lines due to Eu^{3+}-Ce^{3+} and Pr^{3+}-Ce^{3+} pairs. These pairs are particularly interesting for further investigations in rare-earth based quantum computing as they provide optical access to Pr^{3+} and Eu^{3+} qubit ions which are located at a fixed short distance from a Ce^{3+} readout center.

2. Experimental

A series of Czochralski grown singly doped and codoped bulk Y_2SiO_5 were used in the spectroscopic studies (Table 1).

Table 1: Dopant concentration, dimensions and manufacturing origin of the investigated samples.

Dopant concentration	Dimensions (mm)	Manufacturing origin
0.1%Eu^{3+}	$3 \times 3 \times 8$	SMC [(1)]
0.1%Eu^{3+}-0.1%Ce^{3+}	$3 \times 3 \times 3$	SIC [(2)]
0.9%Eu^{3+}-0.1%Ce^{3+}	$3 \times 3 \times 3$	IRCP [(3)]
0.05%Pr^{3+}	$2 \times 1 \times 0.5$	SMC
0.03%Pr^{3+}-0.01%Ce^{3+}	$4 \times 5 \times 1$	SIC

[(1)] Scientific Materials Corporation
[(2)] Shanghai Institute of Ceramics
[(3)] Institut de Recherche de Chimie Paris

Low temperature excitation spectra were performed around the Eu^{3+} $^5D_0 \rightarrow {}^7F_0$ transition at 580 nm and the Pr^{3+}:$^1D_2 \rightarrow {}^3H_4$ transition at 606 nm (Fig. 1b). The excitation was performed by a tunable Coherent CR-699 dye laser with 1 MHz linewidth. The focusing of the excitation beam and the fluorescence collection was carried out by a 3 mm diameter Blu-ray lens with numerical aperture of 0.85 and estimated focal length of 1.2 mm. The position of the Blu-ray lens regarding the sample was optimized for maximum fluorescence collection with an Attocube positioning system. A special assembly was designed for low temperature spectroscopic measurements to contain the sample holder, the Blu-ray lens and the lens positioning system. The assembly was incorporated into a cold finger cryostat (Oxford Instruments Optistat CF-V) where the sample temperature was continuously monitored by a thermal sensor (Lakeshore DT-670-SD). Sharp filtering was performed to suppress the excitation wavelength while collecting the spectral emissions from the Eu^{3+} $^5D_0$ and Pr^{3+} $^1D_2$ energy levels (Fig 1b). The fluorescence intensity was detected by a photomultiplier tube (PMT) (Hamamatsu R943-02) and displayed as a function of the excitation wavelength by a LeCroy HRO 66Zi oscilloscope. Spectral analysis was performed with a Spectrometer from Oriel Instruments (MS125) with a 1200 l/mm grating blazed at 500 nm (model 77464). The detection was carried out by an intensified CCD-camera (Andor DH501-25U-01) with spectral response from 180 to 850 nm. The excitation wavelength was

calibrated within an estimated error of 5×10^{-3} nm using a HighFinesse WS-61R wavelength meter. The scheme of the experimental setup is displayed in Figure 2.

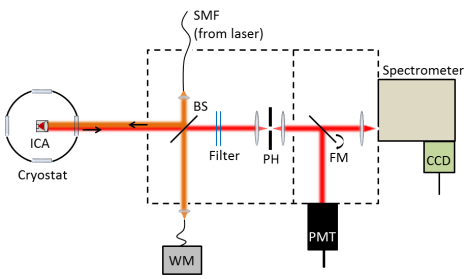

Figure 2: Experimental setup. Dashed lines represent shielding from room light and scattered laser light. Labels are defined as follows: ICA - Intracryostat Assembly containing the sample, the blue-ray lens and the lens positioning system, FM - Flip Mirror, BS - Beam Splitter, SMF - Single Mode Fiber, PH - Pinhole, PMT - Photomultiplier Tube, CCD – Charged Coupled Device (Camera) and WM – Wavelength meter.

3. Results and discussion

a. Main transitions

Two main absorption lines were found in Eu^{3+}:Y_2SiO_5 peaking at 580.040 nm and 580.208 nm for the $^7F_0 \rightarrow {}^5D_0$ transition in good agreement with previous spectroscopic studies [22]. Each line corresponds to an optically inequivalent crystallographic site characterized by its oxygen coordination (Fig. 1c). In addition, the $^3H_4 \rightarrow {}^1D_2$ transition at 605.978 nm (site 1) was recorded for both Pr^{3+} doped crystals (Table 1). Lorentzian line shapes provided the best fit to the experimental data from which the spectral widths were derived. A monotone increase of the inhomogeneous line width with the dopant concentration was reported in Eu^{3+} doped Y_2SiO_5 [23,24]. As shown in Table 2, the line width dependence on the overall dopant concentration is here not linear.

Table 2: Line width values obtained by Lorentzian fit.

Sample	Line width site 1 (GHz)	Line width site 2 (GHz)
0.1%Eu^{3+}	2.3	2.1
0.1%Eu^{3+}-0.1%Ce^{3+}	8.9	8.5
0.9%Eu^{3+}-0.1%Ce^{3+}	16	16
0.05%Pr^{3+}	6.9	-
0.03%Pr^{3+}-0.01%Ce^{3+}	8.5	-

The incorporation of Ce^{3+} induces a larger broadening than expected from an equivalent amount of Eu^{3+} content. In particular, line broadening from 2 to 4 GHz happens when increasing the Eu^{3+} content from 0.1% to 0.2% [23,24]. Instead, a line width of the order of 9 GHz is measured in Y_2SiO_5:0.1%Eu^{3+}-0.1%Ce^{3+} (Table 2). The radius mismatch between Ce^{3+} and Y^{3+}, much larger than that between Eu^{3+} and Y^{3+} [24], provides a good explanation for the observed broadening. Line broadening also appears in the Pr^{3+}-Ce^{3+} case compared to singly doped Pr^{3+}, although to a lesser extent. Indeed, the radius mismatch between Ce^{3+} and Y^{3+} is only slightly larger than the radius mismatch between Pr^{3+} and Y^{3+} [25]. Other than the strain in the lattice induced by the Ce^{3+} ions, the presence of some Ce^{4+} charged centers might also contribute to the spectral broadening in the codoped crystals [26]. In conclusion, the nonlinear line width increase observed for the Eu^{3+} and Pr^{3+} transitions in the codoped samples can be explained by the presence of cerium.

b. Eu^{3+} satellite line structure in Y_2SiO_5

Low temperature excitation spectra recorded for the singly doped 0.1%Eu^{3+}:Y_2SiO_5 and codoped 0.1%Eu^{3+}-0.1%Ce^{3+}:Y_2SiO_5 samples are displayed in Figure 3. For the singly doped Eu^{3+} sample (Fig. 3a), more than 30 satellite lines are resolved on the sides of the two main peaks at 580,040 nm and 580,208 nm. This result is consistent with previous investigations on the same material [24].

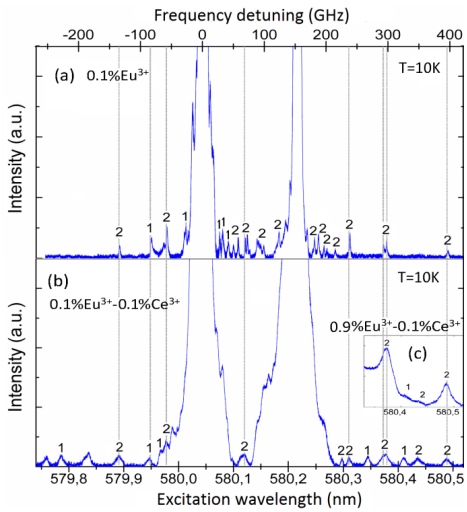

Figure 3: Low temperature excitation spectra recorded between 579,740 and 580,520 nm in (a) 0.1%Eu^{3+}:Y_2SiO_5 and (b) 0.1%Eu^{3+}-0.1%Ce^{3+}:Y_2SiO_5. The small numbers on top of the satellite lines indicate the dominating crystal site for the satellite lines. We label "1" the satellite lines presenting emission spectra similar to the Eu^{3+} main site at 580,040 nm, and "2" those presenting emission spectra similar to the Eu^{3+} main site at 580,208 nm. (c) Portion of the excitation spectra of the 0.9%Eu^{3+}-0.1%Ce^{3+} sample. Due to concentration related line broadening, only the outer satellite peaks can be resolved from the main lines in this crystal. Vertical lines connect the coincident satellite lines, associated to pairs of Eu^{3+} ions.

Well-resolved satellite lines present linewidth values between 2 and 3 GHz, therefore similar to the main lines (Table 2). The analysis of the emission spectra obtained after selective excitation of each satellite line demonstrates that the satellite structure is fully associated to Eu^{3+} centers and no other luminescent defects (Fig. 4). Vibronic nature of the Eu^{3+} satellite lines in Y_2SiO_5 was discarded in previous investigations by site-selective hole-burning measurements [27]. Thus, the satellite line structure is here due to minor crystal sites instead of phonon-coupled levels as reported in other hosts [28]. A similar analysis performed for the 0.1%Eu^{3+}-0.1%Ce^{3+} codoped sample evidences some interesting facts. First, the line broadening observed for the main lines appears also in the case of the satellite lines. Precisely due to the remarkable broadening of both main line and satellite lines, a lower number of peaks are resolved from the main lines in this case (Fig. 3b).

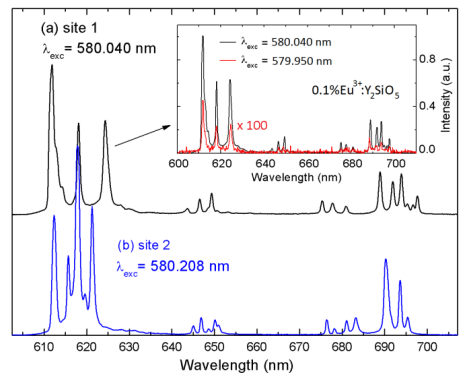

Figure 4: (a) Eu^{3+} site 1 and (b) Eu^{3+} site 2 emission spectra recorded at 4K in 0.1%Eu^{3+}:Y_2SiO_5. The different peaks correspond to transitions from the $^5D_0$ energy level to lower multiplets ($^7F_2$, $^7F_3$ and $^7F_4$). (c) Comparison of the emission spectra obtained after selective excitation of the main line and the satellite line at 579,950 nm, for the same sample. The dominating crystal site for the satellite line (1 in this case) can be easily identified.

Secondly, the comparison of the two spectra in Figure 3 evidences satellite peaks appearing at the same spectral positions, and assigned to the same crystal site in both samples. This result points to the conclusion that these coincident satellite lines are independent of the presence of Ce^{3+} and consequently associated to Eu^{3+} related structures, most likely Eu^{3+} pair sites [24]. Each peak must then be associated to a structurally different pair. Around 30 different combinations are possible within the Y_2SiO_5 lattice considering ion-ion distances up to 15 Å. Such pair distances are in principle short enough to give rise to satellite lines [21,24]. The assignment of each peak to a particular lattice distance is nevertheless non trivial. A simple approach would be to consider that the detuning of the satellite lines decreases with the increasing distance between the two ions following

multipolar interaction laws [29]. However, it has been recently shown that a simple distance dependence is insufficient to explain the spectral position of the satellite peaks, complex mechanisms being necessarily involved [21].

In addition to the peaks associated to Eu^{3+} pairs, extra satellite lines can be observed in the codoped case (Fig. 3b). Characteristic Eu^{3+} emission spectra were obtained under selective excitation of this new set of satellite lines, with the exception of two peaks, which could not be identified (at 579,759 nm and 579.836 nm). A reasonable explanation for the satellite peaks appearing exclusively in the codoped sample is that they are due to Eu^{3+} ions forming pairs with Ce^{3+} ions. We confirmed this hypothesis by the investigation of a different Ce^{3+}-Eu^{3+} codoped Y_2SiO_5 crystal with larger Eu^{3+} content (Table 1). In spite of the fact that only a few number of outer satellite peaks could be resolved from the broad main lines (Table 2), the results appeared conclusive. As displayed in Fig. 3c, the satellite lines previously associated to Eu^{3+} pairs appeared again in this sample, at the expected spectral positions. Besides, the peaks primarily associated to Eu^{3+}-Ce^{3+} pairs were also found, although presenting much weaker intensity than the Eu^{3+}-Eu^{3+} ones. Indeed, because of their weak intensity and broad line width, the analysis of the emission spectra was necessary for resolving the two weak peaks associated to Eu^{3+}-Ce^{3+} pairs between the high intensity Eu^{3+}-Eu^{3+} lines at 580.487 nm and 580.376 nm, as each one of them is assigned to a different Eu^{3+} site. The difference in intensity observed in Fig. 3c between the Eu^{3+} pair peaks and those assigned to Eu^{3+}-Ce^{3+} pairs (about a factor 8 for the two outer peaks at 580.487 nm and 580.437 nm respectively) can be explained from the distinct Eu^{3+} and Ce^{3+} concentrations in this sample. For a random distribution of dopants the intensity of the satellite lines should scale as the square of the Eu^{3+} concentration for Eu^{3+}-Eu^{3+} lines [24], while as the product of Ce^{3+} and Eu^{3+} concentrations for Eu^{3+}-Ce^{3+} lines. Thus, the intensity ratio between Eu^{3+}-Eu^{3+} peaks and Eu^{3+}-Ce^{3+} peaks is given by the concentration ratio between the two dopants, in this case Eu^{3+} and Ce^{3+}, as consistently shown by the experimental results in Figs. 3b and 3c. In conclusion, satellite line peaks associated to Eu^{3+}-Ce^{3+} pairs were recorded in two different codoped samples, where the line width and relative intensity of the peaks was found as expected, dependent on the ratio between the dopant concentrations.

c. Pr^{3+} satellite line structure in Y_2SiO_5

The excitation spectra of singly doped 0.05%Pr^{3+} and codoped 0.03%Pr^{3+}-0.01%Ce^{3+} were recorded at low temperature around the main line for the transition between the lowest stark levels of the $^3H_4$ and $^1D_2$ multiplets, peaking at 605.978 nm (Fig. 5) [30].

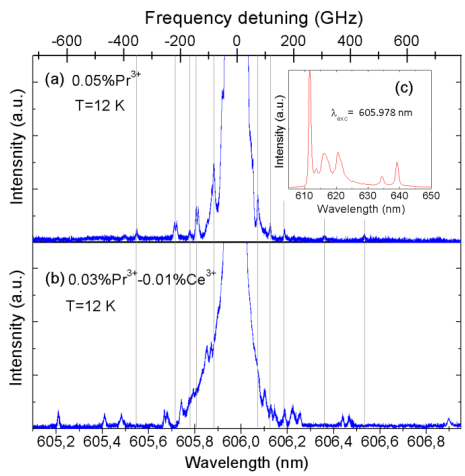

Figure 5: Low temperature excitation spectra recorded between 605.105 and 606.950 nm in (a) 0.05%Pr^{+}:Y_2SiO_5 and (b) 0.03%Pr^{3+}-0.01%Ce^{3+}:Y_2SiO_5. Vertical lines mark the spectral position of the satellite lines associated to pairs of Pr^{3+} ions (c) Characteristic Pr^{3+} $^1D_2 \rightarrow {}^3H_4$ site 1 emission spectrum obtained under 605,978 nm excitation.

Unlike the Eu^{3+} case, Pr^{3+} ions occupy in a large proportion the site 1 [31], which is the one investigated here. Around 12 and 17 satellite peaks were found at both sides of the 605.978 nm line in the

singly doped and Ce^{3+} codoped samples respectively, with line width values similar to that of the main lines in both cases. The detection of a smaller number of satellite lines compared to the Eu^{3+} case (about half) is not surprising as only one of the Pr^{3+} sites is here involved, or there is a lower number of possible combinations for the pairs. Selective excitation of the different peaks in Figures 5a and 5b gives rise to characteristic emission features for Pr^{3+} ions in site 1 (Fig. 5c) confirming also in this case that all satellite lines are associated to Pr^{3+} centers. No evident match was however found from the comparison of the two satellite line patterns in Figure 5. On the other hand, it was noticed that the outer satellite lines in the singly doped sample are particularly weak in terms of intensity (Fig. 5a). As an example, the intensity ratio between the satellite line at 606.535 nm and the main line is about 10^{-3}. Larger ratios, around 5×10^{-3}, were measured for the satellite peaks in the Eu^{3+} samples. This relative intensity difference cannot be explained by the fact that the Pr^{3+} samples present lower doping content, as due to site distribution, the effective Eu^{3+} concentration for each site is also 0.05%. The observed weak intensity can be actually due to fluorescence quenching by cross-relaxation in the satellite lines associated to Pr^{3+} pairs. Efficient cross-relaxation from the $^1D_2$ level ($^1D_2 \rightarrow {}^1G_4$; $^3H_4 \rightarrow {}^3F_4$) has been reported in Pr^{3+} doped materials, leading to a drastic decrease of the Pr^{3+} luminescence [32,33]. A further investigation of the codoped sample was performed with a modified experimental configuration for the excitation of a larger crystal volume: several mm^3 instead of the μm^3 resulting from the microscopy configuration described in section 2. The consequent increase in the collected fluorescence signal allowed evidencing that detuned satellite lines appearing in the singly doped sample (Fig. 5a) also exist in the codoped crystal. Their intensity is however between 5 and 10 times weaker than the peaks shown in Fig 5b, the accurate ratio being difficult to estimate due to the important background signal in this measurement. Thus, fluorescence quenching in the Pr^{3+}-Pr^{3+} pairs is the most likely explanation for the weak intensity of the satellite peaks in Fig. 5a and for their disappearance below the noise level in Fig. 5b. It is actually possible that there exist more satellite lines associated to Pr^{3+} pairs than those evidenced in Fig. 5a which have not been detected because of luminescence quenching. Indeed, the intensity of the lines decreases with the detuning from the main line in Fig 5a, which is consistent with a more efficient quenching for ion pairs characterized by a shorter ion-ion distance. We conclude from this analysis that the satellite peaks displayed in Fig. 5b, or at least the ones clearly detuned from the main line, must be related to quenching-free Pr^{3+}-Ce^{3+} pairs.

d. Discussion

In spite of the numerous reports of satellite lines in optical spectra [13-21], relatively little is known about the active mechanism responsible of these peaks in each particular system. In Pr^{3+} and Eu^{3+} doped Y_2SiO_5 vibronic nature is discarded for the satellite peaks from former investigations [27]. The spectroscopic analysis performed points out that the satellite line spectra are here associated to pairs of dopants and independent of other crystal defects. This is supported by the consistent satellite line patterns obtained from crystals provided by different manufacturers, therefore grown under slightly different conditions (Table 1). In Pr^{3+}:Y_2SiO_5, cooperative absorption in Pr^{3+} pairs has been previously suggested to give rise to satellite peaks [34]. This mechanism is however not considered here as it implies energy detunings of the order of the Stark splitting in the $^3H_4$ ground state (89 cm^{-1} or 2.6 THz [34]). The Pr^{3+} satellite lines reported in Fig. 5a are found at less than 25 cm^{-1} (750 GHz) from the main absorption peak. As previously mentioned, the measured satellite peaks (Figs. 3 and 5) are most likely due to the strain induced by the close-lying dopants and consequent modification of the local crystal field in the pair site. In this sense, the Eu^{3+} pairs are expected to appear at different spectral positions than the Eu^{3+}-Ce^{3+} pairs given by the difference in ionic radii between Eu^{3+} and Ce^{3+}, even for the same relative ion-ion distance. Same conclusion applies to Pr^{3+} pairs and

Pr^{3+}-Ce^{3+} pairs. This seems confirmed by the experimental results. In addition, direct interaction between the dopants such as permanent dipole-dipole coupling [24] and higher order multipolar interactions can also contribute to the spectral detuning of the satellite peaks, especially for the shortest pair distances available (Fig. 1b). A combination of mechanisms could actually explain the complexity of the satellite line spectra and the difficulty to properly assign each satellite peak to a particular pair structure. Regarding the line widths of the satellite peaks, spectral line widths of the same order are observed for the main lines and the satellite lines for a given dopant concentration. This suggests that the mechanism responsible for the inhomogeneous broadening of the satellite lines is not different from that of the main lines. Thus, it is not due to local effects but related to the average strain in the crystal lattice induced by the doping [34].

The spectroscopic method used for the detection of the satellite lines, described in section 2, allows the investigation of microscopic crystal volumes of around 1 μm^3. The efficient detection of a reduced number of ion pairs within a microscopic crystal environment is necessary for the long-term perspective of single-ion based quantum computing. In the Eu^{3+} crystals, judging from the intensities collected for the satellite lines, we are detecting less than 100 ion pairs per satellite line. With the exception of the previously discussed singly doped Pr^{3+} case, the signal to noise ratios are quite good (around 5:1). A decrease of the doping level and the use of suitable detectors should allow the detection of a still reduced number of ion pairs, in the limit a single ion-pair, by using the same experimental method.

Conclusion

Eu^{3+} and Pr^{3+} satellite line spectra were recorded in Y_2SiO_5 with and without the presence of Ce^{3+} as a codopant. The analysis of the satellite line patterns led to the identification of pair sites containing Ce^{3+} ions. These pairs are particularly interesting for further investigations in rare-earth based quantum computing as they provide optical access to Pr^{3+} and Eu^{3+} qubit ions which are located at a fixed short distance from a Ce^{3+} readout center.

Acknowledgements

This work was supported by the Lund Laser Center (LLC) Linnaeus Programme, the Swedish Research Council, the Knut & Alice Wallenberg Foundation, the Crafoord Foundation, the EC FP7 Contract no. 247743 (QuRep). The research leading to these results also received funding from the People Program (Marie Curie Actions) of the European Union's Seventh Framework Program FP7 (2007-2013) under REA grant agreement no. 287252(CIPRIS), and the Nanometer Structure Consortium at Lund University (nmC@LU). Thanks to Rose Ahlefeldt for useful discussions about the mechanisms behind the satellite line structure in rare-earth crystals.

References

[1] J. J. Longdell and M. J. Sellars, Phys. Rev. A 69 (2004), 032307
[2] L. Rippe, B. Julsgaard, A. Walther, Yan Ying, and S. Kröll, Phys. Rev. A 77 (2008), 022307
[3] J. H. Wesenberg , K. Mølmer, L. Rippe and S. Kröll, Phys. Rev. A 75 (2007), 012304
[4] R. Kolesov, K. Xia, R. Reuter, R. Stöhr, A. Zappe, J. Meijer, P.R. Hemmer and J. Wrachtrup, Nat. Commun. 3 (2012), 1029
[5] T. Utikal, E. Eichhammer, L. Petersen, A. Renn, S. Götzinger and V. Sandoghdar, Nat. Commun. 5 (2014), 3627
[6] F. R. Graf, A. Renn, G. Zumofen, and U. P. Wild, Phys. Rev. B 58 (1998), 5462
[7] Y. Yan, J. Karlsson, L. Rippe, A. Walther, D. Serrano, D. Lindgren, M.E. Pistol, S. Kröll, P. Goldner, L. Zheng and J. Xu, Phys. Rev. B 87 (2013), 184205
[8] D. Serrano, Y.Yan, J. Karlsson, L. Rippe, A. Walther, S. Kröll, A. Ferrier and P. Goldner. J. Lum. 151 (2014), 93
[9] R. Macfarlane, J. Lum. 100 (1-4) (2002), 1

[10] G. Heinze, C. Hubrich and T. Halfmann, Phys. Rev. Lett. 111 (2013), 033601
[11] M. Zhong, M. P. Hedges, R. L. Ahlefeldt, J. G. Bartholomew, S. E. Beavan, S. M. Wittig, J. J. Longdell and M. J. Sellars, Nature 517 (2015), 177
[12] H. Suzuki, T.A. Tombrello, C.L. Melcher and J.S. Schweitzer, Nucl. Instrum. Methods, Phys. Res. Sect. A 320 (1–2) (1992), 263
[13] R. L. Ahlefeldt, D. L. McAuslan, W. D. Hutchison, N. B. Manson and M. J. Sellars, Phys. Rev. Lett. 111 (2013), 240501
[14] M. Yamaguchi, P. K. Koyama, T. Suemoto and M. Mitsunaga, J. Lum. 76 & 77 (1998), 681
[15] R. L. Cone, R. T. Harley and M. J. M. Leask, J. Phys. C: Solid State Phys. 17 (1984), 3101
[16] H. Yamamoto, Y. Otomo and T. Kano, J. Phys. Soc. Jpn. 26 (1) (1969), 137
[17] W. Fricke, Z. Physik B 33 (1979), 255
[18] W. Fricke, Z. Physik B 33 (I979), 261
[19] R. Buisson and C.V. Vial, J. Phys 42 (1981), L115
[20] J.P. Chaminade, R.M. Macfarlane and F. Ramaz and J.C. Via, J. Lum. 48 & 49 (1991), 531
[21] R. L. Ahlefeldt, D. L. McAuslan, J. J. Longdell, N. B. Manson and M. J. Sellars, Phys. Rev. B 88 (18) (2013), 184424
[22] R. Yano, M. Mitsunaga, N. Uesugi J. Opt. Soc. Am. B 9 (6) (1992), 992
[23] F. Könz, Y. Sun, C. W. Thiel, R. L. Cone, R. W. Equall, R. L. Hutcheson and R. M. Macfarlane, Phys. Rev. B 68 (2003), 085109
[24] M.J. Sellars, E. Fraval and J.J. Longdell, J. Lum. 107 (2004), 150
[25] Y.Q. Jia, J. Sol. State. Chem. 95 (1) (1991), 148
[26] H. Goto, S. Nakamura, M. Kujiraoka and K. Ichimura, Opt. Exp. 21 (20) (2013), 24332
[27] R. S. Pandher, A. Jackson, A. Davis and B. R. Reddy, Appl. Opt. 38 (26) (1999), 5662
[28] H. Yamamoto, S. Makishima, and S. Shionoya, J. Phys. Soc. Jpn. 23 (1967), 1321
[29] W. P. Wolf and R. J. Birgeneau. Phys. Rev., 166 (2) (1968), 376
[30] R. W. Equall, R. L. Cone and R. M. Macfarlane, Phys. Rev. B 52 (6) (1995), 3963
[31] Y. V. Malyukin, P. N. Zhmurin, A. N. Lebedenko, M. A. Sholkina and B. V. Grinev, Low Temp. Phys. 28 (1) (2002), 54
[32] H. Chen, R. Lian, M. Yin, L. Lou, W. Zhang, S. Xia and J.C Krupa, J. Phys.: Condens. Matter 13 (5) (2001), 1151
[33] R.C. Naik, N.P. Karanjikar and M.A.N. Razvi, J. Lum. 54 (3) (1992), 139
[34] V.V. Seminko, A.A. Masalov, Y.I. Boyko, Y.V. Malyukin, J. Lum. 132 (2012), 2443
[35] A. M. Stoneham, Rev. Mod. Phys. 41 (1) (1969), 82

Paper V

Impact of ion-ion energy transfer on quantum computing schemes in rare-earth doped solids

D. Serrano, Y. Yan, J. Karlsson, L. Rippe, A. Walther, S. Kröll, A. Ferrier and P. Goldner.

J. of Lumin. **151**, 93-99 (2014).

Journal of Luminescence 151 (2014) 93–99

Contents lists available at ScienceDirect

Journal of Luminescence

journal homepage: www.elsevier.com/locate/jlumin

Impact of the ion–ion energy transfer on quantum computing schemes in rare-earth doped solids

D. Serrano [a,*], Y. Yan [a], J. Karlsson [a], L. Rippe [a], A. Walther [a], S. Kröll [a], A. Ferrier [b], P. Goldner [b]

[a] Department of Physics, Lund University, P.O. Box 118, SE-22100 Lund, Sweden
[b] Chimie ParisTech, Laboratoire de Chimie de la Matière Condensée de Paris, CNRS-UMR 7574, UPMC Univ. Paris VI, 11 rue Pierre et Marie Curie, 75005 Paris, France

ARTICLE INFO

Article history:
Received 1 November 2013
Received in revised form
23 January 2014
Accepted 31 January 2014
Available online 14 February 2014

ABSTRACT

We analyze the Ce^{3+}–Pr^{3+}:Y_2SiO_5 emission spectra obtained under selective excitation of the two Ce^{3+} sites in Y_2SiO_5 and we show clear evidence of direct energy transfer from Ce^{3+} to Pr^{3+}. Energy transfer microparameters were calculated from the experimental spectral overlap between the Ce^{3+} emission and the Pr^{3+} and Eu^{3+} absorptions from which, the transfer mechanisms $Ce^{3+}\rightarrow Pr^{3+}$ are concluded to be more efficient than the transfer mechanisms $Ce^{3+}\rightarrow Eu^{3+}$. The energy transfer processes demonstrated here are potentially detrimental for an efficient qubit readout, using Ce^{3+} as readout ion, as they lead to a quenching of the Ce^{3+} luminescence and can give rise to the unwanted change of Pr^{3+} and Eu^{3+} qubit states. The quantum computing readout scheme is based on permanent electric dipole interactions scaling as R^{-3}, where R is the distance between the Ce^{3+} and the qubit ion. The non-radiative energy transfer processes also depend on the ion–ion distances, however as R^{-6}. A discussion about the microscopic dopant distributions leading to an efficient single-ion readout quantum computing scheme is here presented. The likely existence of energy transfer paths between the qubits or, as in this case, between the readout ion and the qubit ions, has not been taken into account so far by the rare-earth based quantum computing approaches. The results of this study suggest the need to consider them in order to design realistic and efficient quantum computing schemes for rare-earth doped solids.

1. Introduction

The investigations pursuing the use of rare-earth doped crystals as hardware for quantum computers have led, in the last decade, to a number of achievements such as the possibility of qubit formation, control and the use of permanent electric dipole–dipole interactions for gate operations between qubits [1,2]. The detection of the qubit states is planned through a so-called readout ion sitting close enough to a qubit ion so that its excited state is shifted in energy when the qubit ion is promoted from the ground state to the excited state [3]. This approach is a single instance quantum computing implementation where each qubit consist of a single ion [3,4]. It is attractive since, in contrast to earlier work [1,2] based on qubit ensembles, it is scalable to many qubits which constitutes a fundamental requirement in terms of real quantum computation [5]. The long excited lifetime required for qubit operations makes difficult to use the qubit ions themselves to carry out the readout role as it implies the detection of a single emitter. A readout ion presenting a high emission rate is thus needed for this quantum computing approach [6]. Other approaches to build multiple qubit systems consist of rare-earth stoichiometric crystals lightly doped with another rare-earth ion [7,8]. In these materials, the different rare-earth ions surrounding the dopant ion are targeted as independent qubits. The advantage of this scheme is the short distance between the qubit ions, leading to a strong electric dipole–dipole coupling between them.

A number of rare-earth ions and host crystals have so far been studied for quantum information applications [9–11]. Y_2SiO_5 doped with Pr^{3+} and Eu^{3+} ions are among the most prominent. This is due to the long coherence times observed for the optical transitions at 606 nm (Pr^{3+}:$^3H_4\rightarrow{}^1D_2$) and 580 nm (Eu^{3+}:$^7F_0\rightarrow{}^5D_0$), as well as the long lifetimes and coherence times of the ground state hyperfine levels [12–14]. For instance, lifetimes of 100 s in the case of Pr^{3+} [15] and more than 20 days for Eu^{3+} [16] have been reported at zero magnetic field for the ground hyperfine levels. On the other hand, trivalent Cerium has been proposed to carry out the readout function [3] as its 5d→4f optical transition possesses a unity fluorescence quantum yield, no long-lived trapping states and excited state lifetime in the nanosecond scale. These features assure an emission rate high

* Corresponding author. Tel.: +46 462224877.
E-mail address: diana.serrano@fysik.lth.se (D. Serrano).

http://dx.doi.org/10.1016/j.jlumin.2014.01.072
0022-2313

enough to collect photons from a single emitter. In addition, Ce^{3+} can be introduced into the Y_2SiO_5 lattice as a codopant so that it can eventually be found in vicinity of an interacting qubit ion. Further evidence of permanent electric dipole–dipole interaction between Ce^{3+} and Pr^{3+} ions has recently been reported in Y_2SiO_5 [6] and the successful detection of the fluorescence of a single Ce^{3+} ion [17] has also been achieved in a YAG host. These results are very encouraging for the practical execution of the single ion quantum computing scheme.

A well-known phenomenon, often observed in rare-earth doped crystals and which has not been considered so far by the rare-earth based quantum computing approaches is the presence of energy transfer paths between the readout ion and the qubit ion. The energy transfer processes between trivalent rare-earth ions [18,19] have been actively investigated and exploited during the last decades for the development of rare-earth based phosphors [20,21], scintillators [22], luminescent solar converters [23], laser crystals [24] and in general, the study and application of upconversion phenomena [25]. Experimental evidences of efficient energy transfer mechanisms both from Ce^{3+} to Pr^{3+} and Ce^{3+} to Eu^{3+} have been shown in host materials such as $Lu_3Al_5O_{12}$, $Y_3Al_5O_{12}$ [26,27], YVO_4 [28] and $Y_2Zr_2O_7$ [29]. The existence of energy transfer from Ce^{3+} to Pr^{3+} has recently been reported in Ce^{3+}–Pr^{3+} codoped Y_2SiO_5 [30] and in the Ce^{3+}–Eu^{3+} case, it needs to be evaluated. The reason is that such processes can partially quench the Ce^{3+} luminescence, complicating the detection of the readout signal upcoming from a single Ce^{3+} emitter. At the same time, the qubit ion is promoted to an excited state as a consequence of the energy transfer and this would destroy the qubit state under readout.

A detailed description of the proposed readout scheme is displayed in Fig. 1 for the readout–qubit pairs Ce^{3+}–Pr^{3+} and Ce^{3+}–Eu^{3+}. The scheme is essentially the same independent of the qubit center. Pr^{3+} and the two Eu^{3+} isotopes, namely ^{151}Eu and ^{153}Eu, present 5/2 nuclear spin and so, the same number of hyperfine levels. The qubit is encoded in the hyperfine levels $|1/2g\rangle$ and $|3/2g\rangle$, and the objective of the readout is to determine wether the qubit is in state $|1/2g\rangle$ or $|3/2g\rangle$ after the computations are done. Thus, a first laser pulse resonant with the qubit optical transition from the hyperfine level $|3/2g\rangle$ to one of the hyperfine levels in the excited state is sent. The qubit ion does not interact with this pulse as it is in the state $|1/2g\rangle$ (Fig. 1a). Readout pulses, resonant with the Ce^{3+} 4f→5d zero-phonon transition are next sent in resulting in the excitation of the Ce^{3+} ion and subsequent radiative decay. In Fig. 1b, the qubit ion, whose initial state is $|3/2g\rangle$, becomes excited after interaction with the first pulse. The permanent dipole moment of the excited state of the qubit ion, being different from that of the ground state, changes the energy of the Ce^{3+} excited state so that, if the energy shift $|\Delta E|$ is large enough (Fig. 1b), the new transition is no longer resonant with the readout pulses and no excitation nor luminescence can be detected from the readout ion in this case. Therefore, the detection or absence of Ce^{3+} luminescence directly probes the qubit initial state.

In this paper, we estimate the efficiency of the energy transfer processes for pairs of Ce^{3+}–Pr^{3+} and Ce^{3+}–Eu^{3+} ions within Y_2SiO_5 as a function of the distance between the qubit and readout ions, and we discuss their impact on the single-ion based quantum computing readout scheme.

2. Optical measurements

Several Czochralski grown Y_2SiO_5 singly doped Pr^{3+} and Eu^{3+} crystals with final dopant concentrations of 0.05 at% and 0.1 at%, as well as a codoped 0.01 at% Ce^{3+} and 0.03 at% Pr^{3+} crystal were used in the study. Y_2SiO_5 is a biaxial monoclinic crystal with C2/c space group (number 15) and lattice parameters equal to $a=14.413$ Å, $b=6.7190$ Å, $c=10.4000$ Å, $\alpha=90$, $\beta=122.235$ and $\gamma=90$ [31,32].

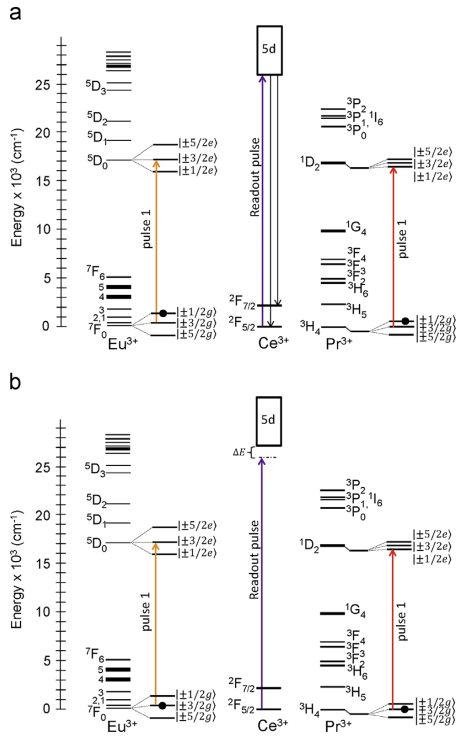

Fig. 1. Ce^{3+}–Pr^{3+}/Eu^{3+} readout scheme. Solid colored arrows represent the excitation pulses at approximately 370 nm, 606 nm and 580 nm for Ce^{3+}, Pr^{3+} and Eu^{3+} respectively. (a) Ce^{3+} emission should be detected when the qubit ion is initially found in the state $|1/2g\rangle$. (b) No emission is expected from the Ce^{3+} ion when the qubit is in the ground hyperfine state $|3/2g\rangle$. The hyperfine splitting of the $^7F_0$ and $^5D_0$ Eu^{3+} singlets and the lowest stark level of the $^3H_4$ and $^1D_1$ Pr^{3+} multiplets are not scaled in energy to the spin–orbit electronic levels as it is just several MHz (10^{-3} cm^{-1}) in the case of Pr^{3+} and hundreds of MHz for Eu^{3+} (10^{-2} cm^{-1}).

The Y^{3+} ions occupy two nonequivalent crystallographic sites within Y_2SiO_5, distinguished by their oxygen coordination (7 for site referred to as of type 1, and 6 for the site referred to as of type 2 [33]). The rare-earth dopants have been found to replace the Y^{3+} ions in both sites, with site occupancies which vary depending on the rare-earth ion considered. Thus, in the case of large ions such as Pr^{3+} and Ce^{3+}, most dopants occupy the site 1 [34]. The site occupation becomes much more equilibrated in the case of Eu^{3+} since this ion is similar in size to Y^{3+} [16].

Fig. 2 displays the emission spectra recorded at low temperature under two different laser excitation wavelengths for the Ce^{3+}–Pr^{3+} codoped Y_2SiO_5 sample. Laser excitation at 325 nm selectively excites the Ce^{3+} ions in site 2 (Ce2) [35] while the 370.83 nm diode laser excitation is centered on the zero-phonon absorption line (ZPL) of Ce^{3+} ions in site 1 (Ce1) [6]. The excitation of the Ce1 ZPL is actually the one aimed for the readout pulses (Fig. 1) since the transition must be narrow to be shifted off resonance by the dipole–dipole interaction. Broad emission bands are observed in the 370–500 nm (Fig. 2a) and 430–550 nm (Fig. 2c) spectral regions. Those are attributed to

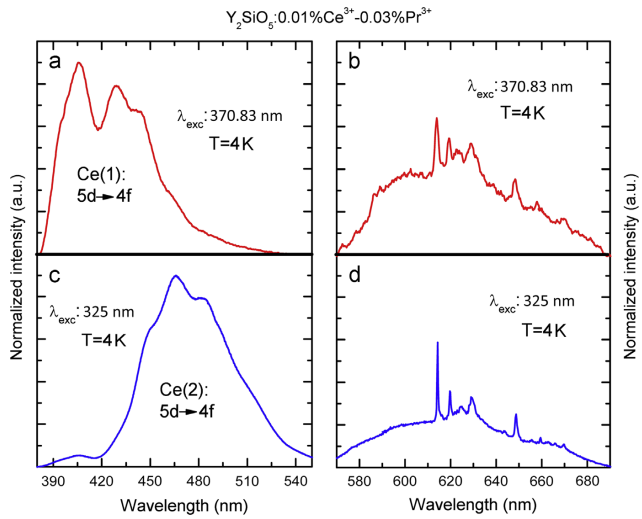

Fig. 2. (a) And (b) Emission spectrum obtained under Ce1 excitation at 370.83 nm. (c) And (d) Emission spectrum obtained under Ce2 excitation at 325 nm. The spectra were separated in two regions and normalized for the sake of clarity due to the intensity contrast between the strong Ce^{3+} bands (a) and (c), and the weak Pr^{3+} emissions (b) and (d).

the Ce^{3+} fluorescence in sites 1 and 2 respectively [35]. The band corresponding to Ce1 shows additional structure with a prominent peak at 400 nm and a second one around 425 nm, associated with the transitions $5d\rightarrow 4f$ ($^2F_{5/2}$) and $5d\rightarrow 4f$ ($^2F_{7/2}$). Besides the Ce^{3+} emissions, the appearance of a set of narrow emission peaks is observed in the 600–700 nm spectral region (Fig. 2b and d). These peaks actually correspond to Pr^{3+} emissions from the $^3P_0$ and $^1D_2$ energy levels and they are the result of an energy transfer from Ce^{3+} to Pr^{3+}. The energy transfer mechanism is therefore taking place from both Ce^{3+} sites as the Pr^{3+} emission lines are clearly observed when exciting at 370.83 nm (Fig. 2b) and 325 nm (Fig. 2d). A remarkably weak fluorescence signal was obtained for the Pr^{3+} emissions under 370.83 nm excitation. Nevertheless, lower energy transfer efficiency Ce1 to Pr^{3+} compared to the case Ce2 to Pr^{3+} cannot be derived from this result as the emission spectra were recorded under different experimental conditions for the two excitations. Thus, they cannot be directly compared. In the next section, we look at the energy transfer efficiencies from Ce^{3+} to Pr^{3+} in Y_2SiO_5, with an emphasis on the microscopic point of view of the mechanism, and we include in the study the investigation of the efficiency of the $Ce^{3+}\rightarrow Eu^{3+}$ energy transfer paths.

3. Microscopic energy transfer investigation

The energy transfer rate, A_{ET}, for a fluorescence resonant energy transfer (FRET) mechanism between two interacting ions, usually denoted as donor and acceptor, is given by

$$A_{ET} = \frac{C^{(k)}}{R^k} \tag{1}$$

where R is the distance between the two ions involved and $C^{(k)}$ is the so-called transfer microparameter, with $k = 6, 8, 10$ for dipole–dipole [18,36], dipole–quadrupole and quadrupole–quadrupole interactions respectively. For the dipole–dipole case, the transfer microparameter can be calculated as follows [37]:

$$C_{dd}^{(6)} = \frac{3c}{8\pi^4 n^2}\int \sigma_{Em,D}(\lambda)\sigma_{Abs,A}(\lambda)d\lambda \tag{2}$$

Thus, $C_{dd}^{(6)}$ depends on the integrated spectral overlap between the donor emission cross-section ($\sigma_{Em,D}$) and the acceptor absorption cross-section ($\sigma_{Abs,A}$), as well as the index of refraction of the host n, and vacuum light speed c. Expressions for the dipole–quadrupole and quadrupole–quadrupole mechanisms were derived by Kushida based on the tensor operator method [38]. Those are also demonstrated directly dependent on the spectral overlap between the donor emission and the acceptor absorption. The existence of energy transfer mechanisms from Ce^{3+} to Pr^{3+} in Y_2SiO_5 is not really surprising as the spectral region covered by the Ce^{3+} 5d emissions (Ce1 and Ce2) overlaps several Pr^{3+} absorption lines, in particular, the ^3P_J Pr^{3+} levels (Fig. 3a). The analysis of the Eu^{3+} energy level scheme, on the other hand, also points the more than likely existence of energy transfer paths from Ce^{3+} to Eu^{3+} as displayed in Fig. 3b. Establishing the efficiency of the energy transfer processes depicted in Fig. 3 and their eventual interference within the proposed single-instance quantum computing readout scheme appears necessary for the development of quantum information hardware. Experimental methods often used to investigate energy transfer efficiencies such as the study of the dynamics of the ion acting as donor, provide a general insight into the transfer efficiency for a given rare-earth doped crystal, or in other words, they offer some idea of the behavior of the majority of the ions in the crystal. These methods are however not really applicable to our case as they are unable to estimate the efficiency of the transfer mechanisms taking place between ions for a particular distribution of dopants within the crystal. The microscopic point of view of the transfer mechanisms has to be taken into account when discussing their influence on the single-ion based quantum computing readout scheme since this one is based on a single readout ion surrounded by qubits. In addtion, the qubit ions have to be close enough to the readout ion so that their dipolar fields

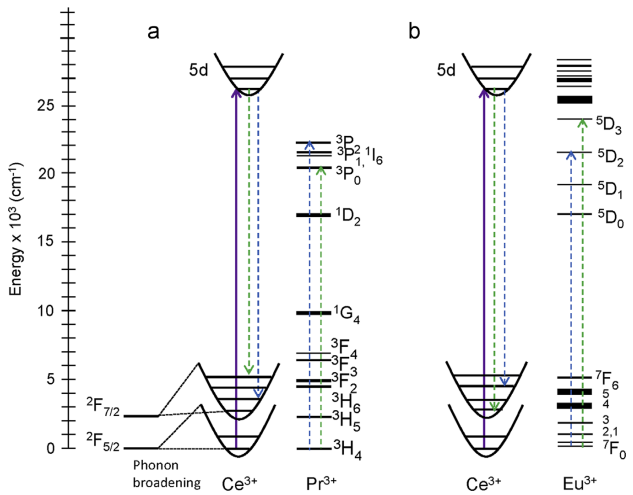

Fig. 3. (a) Ce^{3+}–Pr^{3+} and (b) Ce^{3+}–Eu^{3+} level schemes. Dashed arrows represent possible energy transfer paths after the excitation of Ce^{3+} into the 5d level. The Ce^{3+} levels are represented by a configurational coordinate diagram [38] in order to evidence the broadening of the 5d emission.

can interact (Fig. 1), the strength of interaction depending on the distance as R^{-3} [6]. The inter-ionic interaction distance is therefore a critical parameter which must be considered carefully as it is also going to determine the efficiency of the energy transfer processes (Eq. (1)).

The study of the energy transfer rates and efficiencies in Y_2SiO_5: Ce^{3+}–Pr^{3+} and Y_2SiO_5:Ce^{3+}–Eu^{3+} is here accomplished by the determination of transfer microparameters for resonant $Ce^{3+}\rightarrow Pr^{3+}$ and $Ce^{3+}\rightarrow Eu^{3+}$ energy transfers. Low temperature Pr^{3+} and Eu^{3+} absorption spectra were recorded in Y_2SiO_5, polarized along the principal axis, referred to as b, D_1 and D_2. The absorption of the $^3P_{0,1,2}$ and $^1I_6$ levels are observed in the Pr^{3+} absorption spectra within the 370–550 nm spectral region (Fig. 4). For Eu^{3+}, the absorption lines corresponding to the $^5D_1$, $^5D_2$, $^5D_3$ and $^5L_6$ transitions were identified (Fig. 5). The analysis of the Eu^{3+} and Pr^{3+} polarized absorption spectra reveals, as expected, the presence of peaks from both crystallographic sites, which could be assigned from previous spectroscopic studies [40–42]. The polarized absorption spectra for the Pr^{3+} ions in site 1 were distinguished and separated from the site 2, not considered in the study. Pr2 is in principle not aimed to create qubits due to its lower coherence times and low site occupancy compared to Pr1. Each one of the polarized Eu^{3+} absorption spectra, on the other hand, were split into the two Eu^{3+} sites as most of the peaks were unequivocally attributed to one site or the other. All the spectra were afterwards calibrated to absorption cross-section values as follows:

$$\sigma_i^{\phi}=\frac{\alpha_i^{\phi}}{N_i} \tag{3}$$

where α_i^{ϕ} and N_i are the absorption coefficient and the density of dopants respectively, with $i=1,2$ referring to the site and ϕ stating for the polarization orientation. N_i were determined by taking into account the Y^{3+} density in the host, the dopant concentration in the sample (0.05% and 0.1% for the Pr^{3+} and Eu^{3+} samples respectively), and the sites occupancies which were set to 4:1 for site 1 in Pr^{3+} and 1:1 in Eu^{3+}. Polarization averaged absorption spectra were finally calculated for the Pr^{3+} ions in site 1 (Pr1) and each one of the Eu^{3+} sites (Eu1 and Eu2). The Ce^{3+} emission spectra were calibrated in cross-section by using the Fluchtbauer–Ladenburg spectroscopic method [43]. Unlike the Eu^{3+} and Pr^{3+} absorptions, no significant differences are observed for the three polarized Ce^{3+} emissions in Y_2SiO_5 [30]. Thus, the emission spectra here presented were recorded under unpolarized light and arbitrary propagation direction. The cross-section calibrated polarization averaged absorption and emission spectra are displayed in Figs. 4 and 5. Spectral overlap is observed in all the cases investigated enabling resonant energy transfer paths.

Dipole–dipole energy transfer microparameters were derived from Eq. (2) for the $Ce^{3+}\rightarrow Pr^{3+}$ transfers. Any contribution of higher order energy transfer mechanisms to the total energy transfer rate is negligible in this case. The dipole–quadrupole energy transfer probability is proportional to the $U^{(2)}$ squared matrix element [39] and this one is 0 or very close to 0 for all the $^3H_4\rightarrow{}^3P_{0,1,2}$ transitions [44]. The Ce^{3+}–Eu^{3+} case is however more complex due to the nature of the Eu^{3+} transitions from the $^7F_0$ ground state. The transitions from $^7F_0$ to $^5D_{odd}$ are in principle dipole forbidden and typically assigned as magnetic dipole [45]. Two of these transitions, $^7F_0\rightarrow{}^5D_1$ (~526 nm) and $^7F_0\rightarrow{}^5D_3$ (~410 nm), appear within the Ce2 and Ce1 emission ranges respectively (Fig. 5). However, those are very weak transitions so that they hardly contribute to the transfer rate through the spectral overlap. The main contribution comes actually from the $^7F_0\rightarrow{}^5D_2$ transition for the overlap with Ce2 (Fig. 5b and d) and both from the $^7F_0\rightarrow{}^5D_2$ and $^7F_0\rightarrow{}^5L_6$ transitions for the overlap with Ce1 (Fig. 5a and c). The $^7F_0\rightarrow{}^5L_6$ presents induced dipole character. However, the $^7F_0\rightarrow{}^5D_2$ transition fulfils both induced electric-dipole and electric-quadrupole selection rules [45]. Besides, the $^7F_0\rightarrow{}^5D_2$ transition is dominated by the $U^{(2)}$ matrix element [46], which gives in principle a non-negligible dipole–quadrupole energy transfer probability. Dipole–dipole energy transfer microparameters were calculated for all the Eu^{3+} transitions included in the spectral overlap by Eq. (2), and electric–quadrupole transfer microparameters were calculated for the $^7F_0\rightarrow{}^5D_2$ using the expression given by Kushida [38]. The results obtained are summarized in Table 1.

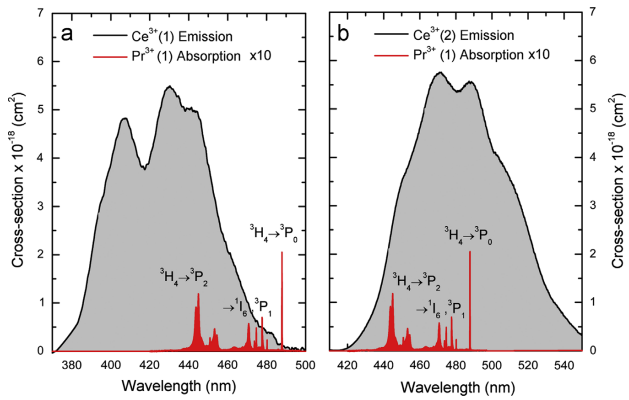

Fig. 4. Spectral overlap between the low temperature Ce^{3+} emissions (gray) and polarization averaged Pr^{3+} absorptions (red) for the cases (a) Ce1–Pr1 and (b) Ce2–Pr1 (color online).

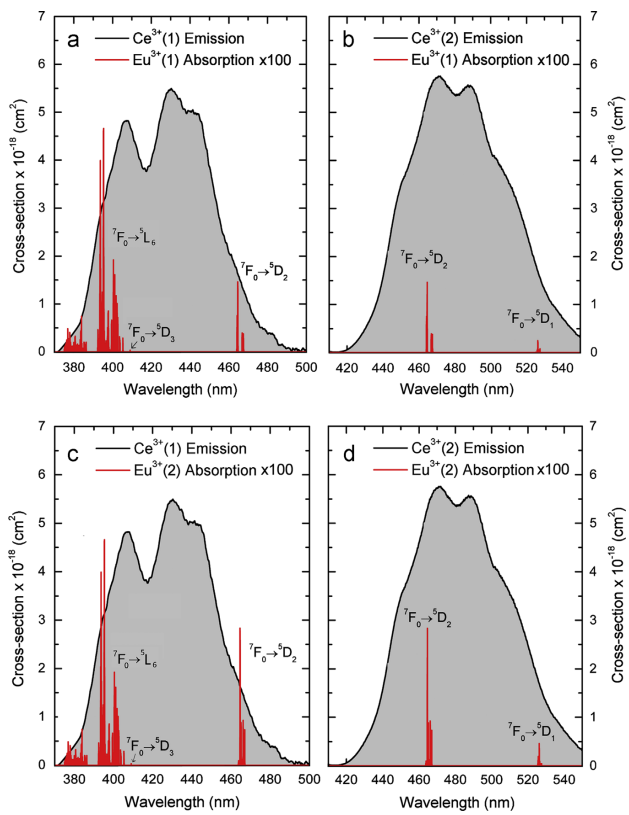

Fig. 5. Spectral overlap between the low temperature Ce^{3+} emissions (gray) and polarization averaged Eu^{3+} absorptions (red) for the cases: (a) Ce1–Eu1, (b) Ce2–Eu1, (c) Ce1–Eu2 and (d) Ce2–Eu2 (color online).

Table 1
Calculated energy transfer microparameters and critical distances. The results are displayed by decreasing critical distance.

Donor–acceptor	$C_{dd}^{(6)}$ ($\times 10^{11}$ Å^6 s^{-1})	$C_{dq}^{(8)}$ ($\times 10^{13}$ Å^8 s^{-1})	Distance (Å)
Ce2–Pr1	10.0	0	10.0
Ce1–Pr1	8.2	0	8.3
Ce2–Eu2	5.6	4.1	6.7
Ce2–Eu1	0.9	4.1	6.4
Ce1–Eu2	5.9	1.2	5.8
Ce1–Eu1	5.8	1.2	5.8

4. Consequences for the single-ion based quantum computing scheme

As shown in Table 1, higher values were found for the Ce^{3+}–Pr^{3+} dipole–dipole energy transfer microparameters. This is mainly due to the fact that the Pr^{3+} transitions involved present larger absorption cross-sections than the Eu^{3+} ones (almost one order of magnitude as shown by the scaling factor in Figs. 4 and 5). Thus, this leads to higher integrated spectral overlap values and consequently to higher energy transfer rates. Besides, a higher energy transfer microparameter is found for the case Ce2–Pr1 than Ce1–Pr1. The Ce2 emission spectrum, being red-shifted regarding the Ce1 emission, has a better overlap with the three ^3P_J transitions (Fig. 4). The analysis is less straightforward for the different Ce–Eu site combinations due to the two multipolar contributions. Critical energy transfer distances were calculated defined as the distance between donor and acceptor for which the total energy transfer rate (A_{ET}^{tot}) is identical to the radiative decay rate of the donor, where A_{ET}^{tot} is defined as

$$A_{ET}^{tot} = A_{ET}^{dd} + A_{ET}^{dq} \tag{4}$$

Larger critical distances were found for the $Ce^{3+} \rightarrow Pr^{3+}$ energy transfers in spite of the two energy transfer mechanism considered in the Ce^{3+}–Eu^{3+} case. Besides, all the critical distances found, including both codopings, are larger than the distance separating two dopants at nearest-neighbor positions within an yttrium orthosilicate crystal ($\sim$3.8 Å for two ions in site 1). Thus, the Ce^{3+} emission rate will be reduced by more than 50% for pairs of nearest-neighbors Ce^{3+} and Pr^{3+} or Eu^{3+} ions as a result of the energy transfers. A strong quenching of the readout ion fluorescence, symbolized by the critical distance, is not the only inconvenience which should be taken into account. Ideally, in order to avoid unwanted changes in the qubit state like its promotion to an excited state, the probability of energy transfer should be negligible during a full readout cycle. It has been estimated that the readout transition needs to be cycled a minimum of 2000 times to achieve enough photons emitted allowing to determine the qubit initial state [47]. This means that one has to find pairs of readout ions and qubit ions separated by distances so that the energy transfer probability is lower than 5×10^{-4}. The evolution of the energy transfer probability as a function of the inter-ionic distances was calculated from the ratio between the total energy transfer rate, A_{ET}^{tot}, given by Eq. (4), and the Ce^{3+} total desexcitation rate (A_{tot}):

$$A_{tot} = \tau_{rad}^{-1} + A_{ET}^{tot} \tag{5}$$

in which τ_{rad} is set to 39 ns for Ce1 and 59 ns for Ce2 [35]. The results are displayed in Fig. 6. In the Ce^{3+}–Pr^{3+} case, inter-ionic distances around 30 Å are needed to free the readout mechanism from energy transfer. This limit goes down to 20 Å for Ce^{3+}–Eu^{3+} due to the intrinsic lower efficiency of the energy transfer mechanisms in this codoping. The necessity to avoid distributions

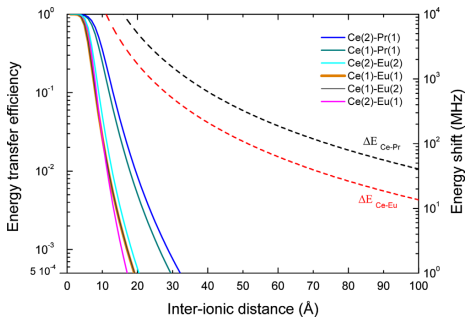

Fig. 6. Solid lines: Evolution of the energy transfer probability as a function of the inter-ionic distances for the different cases investigated (left axis). Dashed lines: Distance dependent evolution of the energy shift induced in the readout ion by a Pr^{3+} qubit ion (black) and Eu^{3+} qubit ion (red) (right axis) (color online).

of dopants were the ions are sitting at distances shorter than 30 Å may seem very problematic since, as it has been previously stated, the readout ion needs to interact with the qubit ion so that its excited state can be shifted (Fig. 1b). Shifts of several tens of MHz are however considered sufficient as the Ce^{3+} homogeneous line has been measured to 4 MHz [6]. The evolution of the energy shift as a function of the distance can be estimated as

$$\Delta E = \frac{1}{4\pi\varepsilon_0} \frac{(\epsilon(0)+2)^2}{9\epsilon(0)} \frac{\Delta\mu_{Ce}\Delta\mu_{qubit}}{R^3} \tag{6}$$

with $\Delta\mu_{Ce}$ and $\Delta\mu_{qubit}$ the difference between the electric dipole moment in the ground and excited state for Ce^{3+} and the qubit ion respectively, where the second factor is a local field correction. As displayed in Fig. 6, energy shifts of the order of tens of MHz can be in principle achieved for ions which are up to 100 Å away from each other. Thus, even avoiding pairs of readout and qubit ions separated by less than 30 Å for Pr^{3+} as qubit ion, and 20 Å for Eu^{3+}, any couple separated by distances between 30 and 100 Å could be eligible to carry out the readout mechanism successfully. A reduction of the doping concentration and consequent increase of the average distance between the ions is a straightforward way to limit the efficiency of the energy transfer processes. However, facing the eventual need of using relatively high doping concentrations in order to boost the qubit–qubit dipole–dipole coupling, the possibility of finding microscopic distributions of dopants fulfilling the distance criteria is small but not negligible. For instance, with a doping concentration of 2 at%, the probability of finding a readout ion separated by more than 2 nm from the closest qubit ion is about 0.04 in Y_2SiO_5 (4% of the cases). This value has been estimated by assuming a random replacement of the Y^{3+} sites by the dopant ions. It is important to note however that the detection of fluorescence arising from a single Ce^{3+} ion in such crystal would already indicate that this ion does not undergo a strong quenching by energy transfer. Thus, the single-ion detection required for the readout mechanism provides in addition a method to identify the microscopic dopant distributions free of energy transfer. This result, on the other hand, points at the difficulty of increasing the doping concentration beyond a certain amount. The use of stoichiometric crystals for quantum computing aims, and also, crystal hosts which tend to form pairs of dopants or any kind of clusters can be also problematic. The particular host and doping ions should however be discussed in order to state further conclusions.

5. Conclusion

The advances in the quantum computing field lead to an increasing complexity of the quantum computation schemes. In this context, the necessity to evaluate the existence of energy transfer mechanisms between the rare-earth dopants involved in the scheme has been demonstrated here. Resonant energy transfer paths have been demonstrated from Ce^{3+} to Eu^{3+} and Ce^{3+} to Pr^{3+} for the different crystallographic sites occupied by the dopants within yttrium orthosilicate. The evolution of the energy transfer probability with the distance between the ions considered indicates the need to avoid distances shorter than 3 nm in the case Ce^{3+}–Pr^{3+}, and 2 nm for Ce^{3+}–Eu^{3+} in order to successfully use Ce^{3+} as a probe to readout the Eu^{3+} and Pr^{3+} qubit states.

Acknowledgments

This work was supported by the Swedish Research Council, the Knut & Alice Wallenberg Foundation, the Crafoord Foundation, the EC FP7 Contract no. 247743 (QuRep). The research leading to these results also received funding from the People Program (Marie Curie Actions) of the European Union's Seventh Framework Program FP7 (2007–2013) under REA grant agreement no. 287252(CIPRIS), Lund Laser Center (LLC), and the Nanometer Structure Consortium at Lund University (nmC@LU). We also want to thank Lihe Zheng and Jun Xu for the Y_2SiO_5:Ce^{3+}–Pr^{3+} crystal, and David Lindgren and Mats-Erik Pistol for their experimental support.

Appendix A. Supplementary Information

Supplementary data associated with this article can be found in the online version at http://dx.doi.org/10.1016/j.jlumin.2014.01.072.

References

[1] J.J. Longdell, M.J. Sellars, Phys. Rev. A 69 (2004) 032307.
[2] L. Rippe, M. Nilsson, S. Kröll, R. Klieber, D. Suter, Phys. Rev. A 71 (2005) 062328.
[3] J.H. Wesenberg, K. Mølmer, L. Rippe, S. Kröll, Phys. Rev. A 75 (2007) 012304.
[4] A. Walther, B. Julsgaard, L. Rippe, Y. Ying, S. Kröll, R. Fisher, S. Glaser, Phys. Scr. T137 (2009) 014009.
[5] D.P. Di Vincenzo, Fortschr. Phys. 48 (9–11) (2000) 771.
[6] Y. Yan, J. Karlsson, L. Rippe, A. Walther, D. Serrano, D. Lindgren, M.E. Pistol, S. Kröll, P. Goldner, L. Zheng, J. Xu, Phys. Rev. B 87 (2013) 184205.
[7] J.J. Longdell, A.L. Alexander, M.J. Sellars, Phys. Rev. B 74 (2006) 195101.
[8] R.L. Ahlefeldt, W.D. Hutchison, M.J. Sellars, J. Lumin. 130 (9) (2010) 1594.
[9] I. Usmani, C. Clausen, F. Bussières, N. Sangouard, M. Afzelius, N. Gisin, Nat. Photonics 6 (2012) 234.
[10] E. Saglamyurek, N. Sinclair, J. Jin, J.A. Slater, D. Oblak, F. Bussières, M. George, R. Ricken, W. Sohler, W. Tittel, Nature 469 (2011) 512.
[11] M.P. Hedges, J.J. Longdell, Y. Li, M.J. Sellars, Nature 465 (2010) 1052.
[12] E. Fraval, M.J. Sellars, J.J. Longdell, Phys. Rev. Lett. 95 (3) (2005) 030506.
[13] M. Lovric, P. Glasenapp, D. Suter, B. Tumino, A. Ferrier, P. Goldner, M. Sabooni, L. Rippe, S. Kröll, Phys. Rev. B 84 (2011) 104417.
[14] G. Heinze, C. Hubrich, T. Halfmann, Phys. Rev. Lett. 111 (2013) 033601.
[15] M. Ohlsson, N. Nilsson, S. Kröll, Phys. Rev. A 68 (4–6) (2005) 393.
[16] F. Könz, Y. Sun, C.W. Thiel, R.L. Cone, R.W. Equall, R.L. Hutcheson, R.M. Macfarlane, Phys. Rev. B 67 (8) (2003) 085109.
[17] R. Kolesov, K. Xia, R. Reuter, R. Stöhr, T. Inal, P. Siyushev, J. Wrachtrup, Phys. Rev. Lett. 111 (2013) 120502.
[18] D.L. Dexter, J. Chem. Phys. 21 (5) (1953) 833.
[19] F. Auzel, C.R., Acad. Sci. (Paris) 262 (1966) 1016.
[20] R.T. Wegh, H. Donker, A. Meijerink, Phys. Rev. B 56 (21) (1997) 13841.
[21] V. Sivakumar, U.V. Varadaraju, J. Electrochem. Soc. 156 (7) (2009) J179.
[22] J.M. Ogieglo, A. Zych, T. Jüstel, A. Meijerink, C.R. Ronda, Opt. Mater. 35 (3) (2013) 322.
[23] B.M. van der Ende, L. Arts, A. Meijerink, Adv. Mater. 21 (30) (2009) 3073.
[24] H. Zellmer, P. Riedel, A. Tünnermann, Appl. Phys. B 69 (1999) 417.
[25] F. Wang, Y. Han, C.S. Lim, Y. Lu, J. Wang, J. Xu, H. Chen, C. Zhang, M. Hong et, X. Liu, Nature 463 (7284) (2010) 1061.
[26] X. Zhoua, K. Zhou, Y. Li, Z. Wang, Q. Feng, J. Lumin. 132 (11) (2012) 3004.
[27] J. Zhang, L. Wang, Y. Jin, X. Zhang, Z. Hao, X.J. Wang, J. Lumin. 131 (3) (2011) 429.
[28] Y. Wang, S. Wang, Z. Wu, W. Li, J. Alloys Compd. 551 (2013) 262.
[29] Q. Du, G. Zhou, H. Zhou, Z. Yang, Opt. Mater. 35 (12) (2012) 257.
[30] L. Zheng, R. Lisiecki, W. Ryba-Romanowski, G. Aka, J. Di, D. Li, X. Xu, J. Xu, J. Lumin. (2013), http://dx.doi.org/10.1016/j.jlumin.2013.08.003.
[31] B.A. Maksimov, V.V. Ilyukhin, Yu.A. Kharitonov, N.V. Belov, Kristallografiya 15 (5) (1970) 926.
[32] C. Cannas, A. Musinu, G. Piccaluga, C. Deidda, F. Serra, M. Bazzoni, S. Enzo, J. Solid State Chem. 178 (2005) 1526.
[33] T. Aitsalo, J. Hölsä, M. Lastusaari, J. Niittykoski, F. Pellé, Opt. Mater. 27 (2005) 1551.
[34] Y.V. Malyukin, P.N. Zhmurin, A.N. Lebedenko, M.A. Sholkina, B.V. Grinev, N. V. Znamenskii, E.A. Manykin, Y.V. Orlov, E.A. Petrenko, T.G. Yukina, Low. Temp. Phys. 28 (1) (2002) 54.
[35] H. Suzuki, T.A. Tombrello, C.L. Melcher, J.S. Schweitzer, Nucl. Instrum. Methods Phys. Res. Sect. A 320 (1–2) (1992) 263.
[36] T. Förster, Ann. Phys. 437 (1–2) (1948) 55.
[37] J.A. Caird, A.J. Ramponi, P.R. Staver, J. Opt. Soc. Am. B 8 (7) (1991) 1391.
[38] T. Kushida, J. Phys. Soc. Jpn. 34 (5) (1973) 1318.
[39] R.T. Wegh, A. Meijerink, Phys. Rev. B 60 (15) (1999) 10820.
[40] R. Yano, M. Mitsunaga, N. Uesugi, J. Opt. Soc. Am. B 9 (6) (1992) 992.
[41] N.V. Kuleshov, V.G. Shcherbitsky, A.A. Lagatsky, V.P. Mikhailov, B.I. Minkov, T. Danger, T. Sandrock, G. Huber, J. Lumin. 71 (1) (1997) 27.
[42] R.W. Equall, R.L. Cone, R.M. Macfarlane, Phys. Rev. 52 (6) (1995) 3963.
[43] P.L. Pernas, E. Cantelar, Phys. Scr. T118 (2005) 93.
[44] W.T Carnall, P.R. Fields, K. Rajnak, J. Chem. Phys. 49 (1968) 4424.
[45] M.J. Weber, Phys. Rev. 157 (2) (1967).
[46] W.T Carnall, P.R. Fields, K. Rajnak, J. Chem. Phys. 49 (1968) 4450.
[47] A. Walther, L. Rippe, Y. Yan, J. Karlsson, D. Serrano, S. Bengtsson, S. Kröll (2014) (in preparation).

Paper VI

High-fidelity readout scheme for rare-earth solid-state quantum computing

A. Walther, L. Rippe, Y. Yan, J. Karlsson, D. Serrano, A. N. Nilsson, S. Bengtsson and S. Kröll.

Phys. Rev. A **92**, 022319 (2015).

PHYSICAL REVIEW A **92**, 022319 (2015)

High-fidelity readout scheme for rare-earth solid-state quantum computing

A. Walther,* L. Rippe, Y. Yan,† J. Karlsson, D. Serrano, A. N. Nilsson, S. Bengtsson, and S. Kröll
Department of Physics, Lund University, 221 00 Lund, Sweden
(Received 31 March 2015; published 10 August 2015)

We propose and analyze a high-fidelity readout scheme for a single-instance approach to quantum computing in rare-earth-ion-doped crystals. The scheme is based on using different elements as qubit and readout ions, where the readout ions are doped into the material at a much lower concentration than the qubit ions. It is shown that by allowing the qubit ion sitting closest to a readout ion to act as a readout buffer, the readout error can be reduced by more than an order of magnitude. The scheme is shown to be robust against certain experimental variations, such as varying detection efficiencies, and we use the scheme to predict the attainable quantum fidelity of a controlled NOT (CNOT) gate in these solid-state systems. In addition, we discuss the potential scalability of the protocol to larger qubit systems. The results are based on parameters which we believe are experimentally feasible with current technology and which can be simultaneously realized.

DOI: 10.1103/PhysRevA.92.022319 PACS number(s): 03.67.Lx, 03.65.Wj, 42.50.Dv

I. INTRODUCTION

The possibility of realizing a quantum computer is being investigated using a large variety of different experimental implementations. Currently, the largest entangled qubit systems have been realized in ion traps [1,2] and using linear optics with single photons [3]. There is, however, intrinsic value in investigating solid-state systems, as they are generally regarded as having a higher potential for future scalability to larger systems. For solid-state systems, the best progress has been achieved with superconducting circuits [4] and impurity-doped solids, such as nitrogen-vacancy (NV) centers in diamond [5]. Another impurity-doped system, rare-earth ions in crystals, has demonstrated very good performance in terms of quantum memories [6–8] but has yet to demonstrate reliable two-qubit gates between spin qubits or a realistic route towards larger qubit systems. A major obstacle has been that, so far, only large ensembles of rare-earth ions have been used for gate operations [9,10], and this has been shown to scale poorly [11]. A promising approach to scalability in rare-earth quantum computing (REQC) is to move into the single-instance regime, although this requires detecting single rare-earth ions inside their crystal hosts. Bare detection of single ions was just recently realized [12,13] with certainty, but there has been no clear description of how these detection schemes can be directly used in quantum information processing.

In this paper, we present a readout scheme that, in principle, allows for an arbitrarily high readout fidelity of the quantum state of a single ion inside a macroscopic host. The readout scheme is based on using a special buffer step (indicated in Fig. 1) that can by cycled repeatedly, a scheme that is similar in nature to what has been done previously for multispecies atomic clocks [14]. We show that with such a readout, a full controlled-NOT (CNOT) gate can be performed in these systems with fidelity of about 99% based on simulations that are supported by what is currently experimentally achievable. We also discuss further scaling towards larger multiqubit systems by showing how chains of single ions can be mapped out, and we find that, including most known error sources as discussed in Sec. IV, entangled states of 10 qubits remaining above 92% fidelity appear feasible, as long as all ions can control each other.

It is interesting to note that at the single-ion level, these impurity-doped systems resembles the trapped-ion systems but with two major differences. The first is the advantage that the ions are trapped by the comparatively large trapping potentials of the crystal bindings. This enables the ions to sit much closer to each other than in ion traps (nanometers instead of microns), which in turns allows the direct electrical dipole interactions between ions to be used as an entangling mechanism. The second difference is the disadvantage that the surrounding environment is not vacuum but a crystal host that can cause additional decoherence effects as well as worsen the single-ion detection possibilities through, e.g., scattering. While the disadvantages may at first appear daunting, it is important to note that one of the main limitations to scalability in ion traps is that the entangling mechanism, the common motional modes, becomes increasingly more complex the more ions that are involved [15]. The direct dipole interactions that can be used in REQC, however, do not suffer from this problem, and we thus expect that once the initial hurdle of establishing single-ion readout is overcome, the scaling to a larger number of qubits will be much more manageable.

This paper is organized as follows: In Sec. II the basic single-instance quantum computing scheme is described together with a discussion of reasonable material parameters. Section III details the readout scheme, and in Sec. IV we go through a full CNOT gate from initialization to readout. Further scalability to larger qubit systems is discussed in Sec. V, followed by a summary of our findings in Sec. VI.

II. OVERVIEW AND PARAMETER CONSIDERATIONS

The single-instance scheme is based on using single rare-earth qubit ions, where the qubit levels are suitable

*andreas.walther@fysik.lth.se
†Present address: College of Physics, Optoelectronics and Energy and Collaborative Innovation Center of Suzhou Nano Science and Technology, Soochow University, Suzhou 215006, China, and Key Lab of Advanced Optical Manufacturing Technologies of Jiangsu Province and Key Lab of Modern Optical Technologies of Education Ministry of China, Soochow University, Suzhou 215006, China.

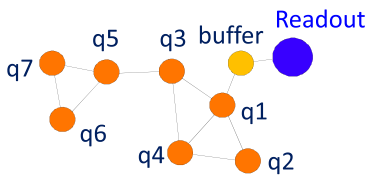

FIG. 1. (Color online) A chain consisting of one readout ion in the vicinity of several qubit ions (e.g., Eu), where the closest qubit ion is being used as a buffer stage (the bright one); see the text for more details. The lines between the ions show which of them can interact directly via frequency shifts caused by changes to the permanent dipole moments. With a 4% doping concentration, it is expected that each Eu ion can, on average, interact with about five other Eu ions surrounding it.

ground-state nuclear-spin states (hyperfine states) with long coherence times and where a long-lived optically excited state can be used for ion-ion interactions. europium has generally demonstrated impressive coherence properties [16], and throughout the paper we will assume Eu as a qubit ion. It is very difficult to detect single ions with long excited-state lifetimes, however, and to circumvent this, several schemes could be considered such as those where a readout ion of a different species is used. Coupling between ions, both between two qubit ions for gates and between a qubit ion and a readout ion for detection, will be mediated via permanent dipole-dipole interactions (dipole blockade effect). In either case, when two ions are sufficiently close, the change in the static dipole moment as one ion is excited is enough to shift the energy level of the neighboring ion out of resonance with a driving laser, thus providing a control mechanism.

Previously, considerable attention has been given to using the short-lived $5d$ transition in Ce as a potential readout ion [17–19]. However, recent measurements have revealed that Eu absorbs at the same wavelength as the cycling transition in Ce (at least in the favored host material, Y_2SiO_5), which makes it necessary to find an alternative readout ion. A very promising scheme for detecting single rare-earth ions is via Purcell enhancement of fluorescence due to coupling of the ion to a high-finesse cavity with a very small mode volume. A fiber-based cavity setup [20] is a suitable candidate and would allow single-ion detection of, in principle, any rare-earth $4f$ transitions. As an example we will here use Nd, which has a relatively high oscillator strength, but in the case of unexpected energy transfers or overlapping absorption lines, any other rare-earth ion could be used with the same readout scheme with no significant changes.

It will be assumed that we are working with a Eu^{3+}:Y_2SiO_5 crystal, where 4% of the yttrium ions in the crystal host have been replaced with europium, distributed roughly equally in each of two different sites (although with only one isotope). This is a relatively high doping concentration, and simulations have shown that, given the difference between the dipole moment of the ground and excited states, any ion will, on average, have more than five other ions sufficiently close to be controlled by it. It is worth pointing out that it has been shown that the coherence time for Eu is independent of the doping concentration [21]. For the readout ion, on the other hand, background trace elements of Nd are expected to be enough; no special doping is required since one readout ion is enough for an entire chain of qubits. Eu has an excited-state transition frequency of about 517 THz (580 nm), whereas the qubit nuclear spin levels have splittings on the order of tens of MHz. Also note that while the inhomogeneous width of the ensemble is increased at higher concentrations, the energy splittings of individual ions remain largely unaffected.

Any state-to-state transfer will be done with complex hyperbolic secant (sech) pulses. These chirped pulses have the advantage over simple square pulses that they are robust against certain errors, such as amplitude and frequency fluctuations; see Ref. [22] for more details. Bloch simulations suggest that the Eu ions can be transferred to and from the excited state by such pulses of 400-ns duration with an efficiency of 99.96% (i.e., an error of 4×10^{-4}), which will be used for the following calculations. The transfer efficiency is limited almost entirely by the duration of the pulse relative to the excited-state lifetime, where the lower limit of the duration is set by the inverse of the qubit nuclear-spin-level separations. It should be noted that the transfer efficiency for Eu has not been fully verified by experiments and does not include effects such as instantaneous spectral diffusion (see, e.g., [23]). It is believed, however, that the effects from spectral diffusion can be strongly mitigated by hole-burning sequences that aim at keeping the total number of ions in the qubit frequency channels very low. The high transfer efficiency can be compared with experiments performed with the similar element praseodymium, where the experimental transfer efficiency matches simulations rather well. For praseodymium, the measured and calculated efficiency is about 96% [10], and the main limitations are the short excited-state lifetime and the limited Rabi frequency available, as well as the fact that an ensemble was used as a qubit. Such an ensemble not only has an inhomogeneous frequency spread but also sits in different spatial parts of the beam profile, making different ions experience different Rabi frequencies. For single-ion Eu transfers inside a cavity, both of those limitations are strongly reduced, and preliminary measurements on Eu ensembles also supports that higher fidelities can be obtained in Eu systems [24].

III. READOUT SCHEME

The state of the qubit ions can be read out with a readout ion using a permanent dipole blockade mechanism, which is also used for the quantum gates [11,25]. The dipole blockade mechanism is demonstrated in Fig. 2, although for now we will study only a single transfer step, i.e., from the buffer ion (which is a type of qubit ion) to the readout ion. The full scheme of Fig. 2 will be explained later. In order to determine whether one ion is in state $|0\rangle$ or $|1\rangle$, it should be selectively excited to state $|e\rangle$ with a pulse resonant with the $|0\rangle \rightarrow |e\rangle$ transition. If the ion is excited, the readout ion's transition frequency is Stark shifted by the dc electric dipole field of the excited state of the qubit ion. This means that a readout laser tuned to the readout ion's unshifted resonant frequency will not excite it.

The readout ion, in our example Nd, has a lifetime of 100 μs. With a reasonable cavity finesse of 10^4–10^5 and

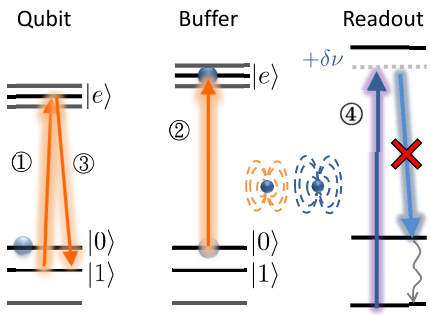

FIG. 2. (Color online) Pulse sequence for reading out the state of one qubit via one buffer ion and the readout ion (note that the buffer is just the closest qubit ion). In the instance shown the qubit is in the $|0\rangle$ state, and the first pulse, (1), resonant with the $|1\rangle \rightarrow |e\rangle$ qubit transition, does not excite it. The buffer ion is now unshifted, and a pulse, (2), resonant with the $|0\rangle \rightarrow |e\rangle$ buffer transition will cause an excitation of the buffer ion. At this stage, the qubit ion is coherently returned to the ground state by pulse (3), such that it spends a minimum amount of time in the excited state. Finally, the readout ion is continuously excited and light is detected, (4). In the current example, the readout ion was shifted due to an excited buffer ion, and there is no fluorescence. However, if the qubit were originally in the $|1\rangle$ state, pulse (2) would be off resonant, and the buffer would not get excited, and thus the readout ion would instead fluoresce.

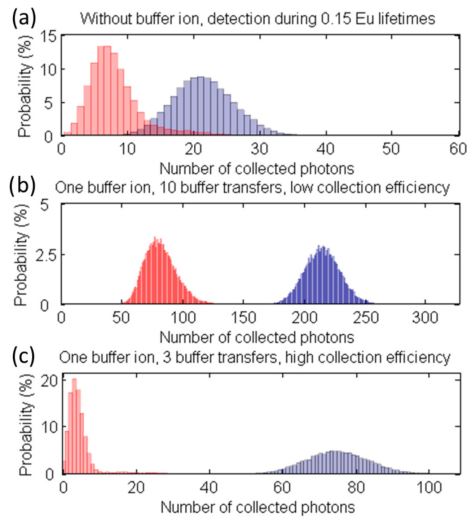

FIG. 3. (Color online) Histograms of simulated photon statistics for detection of a single Nd ion in a cavity. In (a), the readout ion Nd is directly controlled by the qubit ion. In (b) and (c) the cumulative statistics is shown from 10 and 3 repeated readouts, respectively, using one buffer step. The vertical axis shows the probability of receiving n photons during the optimal photon collection time, and the corresponding probabilities of correctly distinguishing the states are (a) 93%, (b) 99.7%, and (c) 99.85%. For (b) and (c), detection efficiencies of 1% and 10%, respectively, have been used, which also makes it possible to obtain good distinguishability with fewer buffer transfers in (c).

a mode volume of a few wavelengths cubed [20], a Purcell factor higher than 10^4 can be achieved. Taking into account the decay branching ratios, we then obtain an effective readout ion lifetime of about 200 ns, which can thus be cycled many times during the duration of the qubit excitation, as $T_{1,\mathrm{Eu}} = 1.9$ ms. The collection efficiency of a typical fluorescence detection setup may be about 1%. However, in a cavity with a high Purcell factor, almost all light will be spontaneously emitted into the same spatial mode. This can yield collections efficiencies in excess of 90%, and including other factors like detector quantum efficiency can allow a total detection efficiency to go up to 10%. Scenarios with different collection efficiencies have been simulated using a Monte Carlo method for both qubit starting states, $|0\rangle$ and $|1\rangle$, as shown in Fig. 3. The simulations are purely statistical in nature; that is, they do not account for any coherent dynamics, only state occupations, updated at short time steps based on decay probabilities. The blue histograms show the number of collected photons when the readout ion is unshifted (qubit in state $|1\rangle$ before the excitation pulse), and the red ones show the number of collected photons when it is shifted (qubit in state $|0\rangle$ before the excitation pulse). The best discrimination between the two states is achieved for different photon collection times depending on the total collection efficiency and background light level. For instance, for 1% collection efficiency, a photon collection time of $0.15T_{1,\mathrm{Eu}}$ was found to be optimal, with the probability to determine the correct state reaching approximately 93%. The largest source of error here is spontaneous decay of the qubit ion due to the finite lifetime of Eu. For a 10% collection efficiency, the optimal collection time was instead $0.025T_{1,\mathrm{Eu}}$.

The readout protocol can be improved significantly by introducing a buffer ion between the qubit ion and the readout ion, as shown in Fig. 2. For the discussion we use the same ion species for the buffer as for the qubit, but another species could potentially be used with some advantages. Now, two mutually interacting qubit ions are used, where one of them, the buffer ion, can control the readout ion. Selective excitation of different qubit ions and the buffer ion can generally be carried out as different ions have different resonance frequencies; that is, they sit on different parts of the inhomogeneous profile. First, one pulse is used to state selectively excite the qubit ion; then a second pulse is used to selectively excite the buffer ion, conditioned on the qubit ion not being excited. A third pulse then coherently deexcites the qubit ion back to the ground state if it was excited during the earlier stage (i.e., the third pulse is effectively the inverse of the first pulse). After this selective excitation the buffer ion state is read out as described above, and the number of photons from the readout ion during the $0.15T_{1,\mathrm{Eu}}$ detection time is counted. This pulse sequence is illustrated in Fig. 2.

After one detection event, the buffer ion can be reinitialized through optical pumping. The qubit ion is still in its original state, and the same pulse sequence can be applied again to make another fluorescence measurement, yielding further information about the same qubit ion state. This process can be repeated several times, such that the total effective number of detected photons that depends on the qubit state can be increased substantially. The optimal number of times to repeat this buffering sequence depends on the detection efficiency and the background light level of the particular setup. Figures 3(b) and 3(c) show two different setups with 1% and 10% detection efficiency, respectively, that both can reach a probability of readout of the correct qubit state of about 99.7%–99.9%. For the gate fidelity simulations described in the next section we will assume a representative readout error of 2×10^{-3}. We note that roughly the same state distinguishability can be reached for both cases, showing that the scheme is robust against such experimental parameters but that a larger number of buffer transfers is needed for lower detection efficiency. The final error is given mostly by the amount of time the qubit ion spends in the excited state, which cannot be reduced lower than the time it takes to do a state transfer on the buffer ion (see Sec. IV for more details). In principle, further buffer stages could be concatenated for an exponentially decreasing error probability; however, the buffer state transfer time of 400 ns relative to the Eu excited state lifetime makes protocols with more than one buffer stage unrewarding for Eu in particular (but could still be useful for other setups).

IV. CNOT GATE FIDELITY

A full CNOT gate experiment will include the following steps:

(1) Initialization
(2) $\pi/2$ pulse, between $|0\rangle$ and $|1\rangle$, on the control qubit
(3) π pulse, $|0\rangle \rightarrow |e\rangle$, on the control qubit
(4) NOT on the target qubit
(5) π pulse reversing the excitation in step 3
(6) Readout

The different steps in the list above will now be described in detail, including assumptions and expected errors for each step. The total CNOT error obtained in the end will include the error from all steps, with care taken to model the different nature of the errors. We use a discrete time model in which each step is represented using operator sum notation (for details see, e.g., Nielsen and Chuang [26]). For example, any transfer pulse will cause both bit- and phase-flip errors, represented by bit- and phase-flip channels, respectively, while any time spent in the excited state will be subject to lifetime decay, modeled as an amplitude-damping channel.

(1) Initialization. The initialization step starts with finding a suitable chain of ions that can function as buffer and qubits and can be described in four main steps (for an overview picture of the different parts of the chain, also see Fig. 1): (i) A readout ion is found by scanning a laser tuned to the readout ion transition in frequency until fluorescence is observed. (ii) The readout laser is kept on, and another laser is now tuned to the qubit ion transition in a similar way. The qubit ions are then excited using π pulses to invert the population, and each frequency channel in the inhomogeneous width of the qubit ions is consecutively scanned through until the fluorescence from the readout stops. This means that an ion sufficiently close to the readout ion to shift it in frequency has now been excited. This will be the buffer ion (compare with Fig. 2). (iii) Still keeping the readout laser on, the inhomogeneous width of the qubit ions is scanned from the start again, repeating the excitation procedure described in the previous step. For each frequency channel throughout the new scan, a π pulse is applied on that frequency but is now followed by a π pulse also exciting the buffer ion, while we monitor when the readout ion resumes fluorescing. This indicates that the frequency of an ion that can control the buffer ion, shifting it out of resonance, has been identified. This will be the first qubit ion. (iv) Repeat the previous step one more time, such that two qubit ions that are both in the vicinity of the buffer ion are found. They will most likely also be sufficiently close to each other, but if they are not and longer chains of ions are desired, the step is instead extended to find ions that shift the previous qubit ion, thus stopping it from controlling the buffer ion. This process can be nested as many layers away from the readout ion as it takes, with the overhead cost of only one extra pulse per layer away.

After a sufficient chain of controlling ions has been established, the qubit ions should be initialized to the $|0\rangle$ state, which can be done by means of optical pumping to an auxiliary state followed by a frequency-selective state transfer back in a manner similar to that of protocols used previously in the ensemble approach [10]. The error during the initialization step is therefore assumed to be equal to the error of the final transfer pulse (a sech; see Sec. II for details); that is, the starting state is considered to be a mixed state with a probability of being in the wrong level of 4×10^{-4} for each qubit.

(2) $\pi/2$ pulse between $|0\rangle$ and $|1\rangle$ on the control qubit. Transitions between the nuclear-spin states cannot be directly driven by a single optical laser field. However, two simultaneous laser fields, where the difference frequency matches the nuclear-spin levels, can accomplish arbitrary single-qubit gates using a dark-state technique, as demonstrated in Ref. [10]. These pulses have the same duration as the transfer pulses (defined in Sec. II) and thus essentially have the same error. For an arbitrary gate two successive such bi-chromatic pulses are needed, which will yield phase- and bit-flip errors twice as large as those of a transfer pulse, i.e., 8×10^{-4} on the control qubit.

(3) π pulse, $|0\rangle \rightarrow |e\rangle$, on control qubit. This step is a straightforward sech pulse, with phase- and bit-flip errors both considered to be 4×10^{-4} for the control qubit.

(4) NOT on target qubit. Although the target qubit operation is conditioned on the control ion not causing a frequency shift, this step is essentially just a π pulse on the nuclear-spin levels, i.e., a single-qubit gate, making an error on the target qubit equal to 8×10^{-4}. In addition, while waiting for the gate to be performed, the control qubit spends two pulse durations in the excited state, which gives a decay probability due to limited lifetime of $1 - e^{-0.8\mu s/1.9\text{ms}} \approx 4 \times 10^{-4}$.

(5) π pulse reversing the excitation in step 3. This step has the same operation and errors as the step 3 excitation.

(6) Readout. For the purpose of finding the achievable CNOT fidelity we use the scheme with one buffer ion, as described above, using a readout error of 2×10^{-3} that we obtained

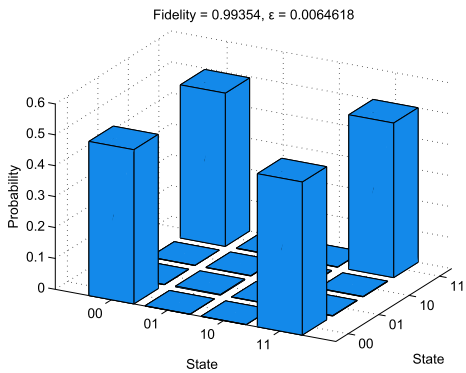

FIG. 4. (Color online) The (real) elements of the density matrix of a prepared Bell state, including all error sources as described in the text. The total fidelity is 99.4% without readout and 99.1% with readout.

earlier (Sec. III). Note that this error is asymmetrical; that is, it represents the probability that a $|0\rangle$ is counted as a $|1\rangle$. The reverse error is usually much smaller because the main error decays from the excited state, and state $|1\rangle$ is never excited.

Final experiment fidelity. The effects of all operations described above are calculated from actions applied to a starting density matrix. In the end when all steps have been taken into account, but before the readout, the system will be in a final density matrix ρ_f. We can then compute the fidelity of the state as $F = \langle\psi_{\max}|\rho_f|\psi_{\max}\rangle$, where $\psi_{\max}$ is the state we aim to create, such as a maximally entangled Bell state. Without the readout step, the total error $\varepsilon = 1 - F$ is found to be $\sim 6 \times 10^{-3}$. The readout is included by allowing the calculated density matrix to be sampled as it would during a real readout sequence, with projections to the four possible two-qubit states. A quantum-state-tomography sequence was then simulated using 15 different observables in 9 different measurement settings (see, e.g., [27]). This gives a recreated density matrix (shown in Fig. 4) that can be used to obtain the fidelity, including the readout stage, and we find the total error to be $\sim 9 \times 10^{-3}$. This means that both the coherent operations and the readout process contribute significantly to the overall fidelity, which emphasizes the need for using the proposed readout buffer stage.

Note that while an effort has been made to include most systematic error sources, a real experiment will also include random projection noise caused by a limited number of experimental count cycles, but that has not been included here. In practice, this error will be limited by the total duration of the full protocol, and since gate operations can be made in submicroseconds, the largest time is consumed by the readout stage. However, the fluorescence detection itself is not the main culprit, as a buffer stage with 10 repetitions, each one with a photon collection time of $0.15T_{1,\mathrm{Eu}}$ or better, will last a maximum of 3 ms, which is comparable to other single-ion detection rates. Instead, the main time consumption arises from the reinitialization of the buffer step that has to be done between each repetition cycle. If simple optical pumping via the long-lived excited state is used to reset the buffer state, then several lifetimes of Eu has to be used to reset it with good fidelity, which is a few tens of milliseconds per repetition. To circumvent this, a quenching mechanism can be used by means of stimulating the transition from the excited state down to another Stark level, which then decays very fast to the ground state by nonradiative processes.

V. SCALABILITY

The previous section detailed the specific case of a two-qubit gate, where the errors were included in a careful manner in the total density matrix describing the system. This approach is difficult to extend to larger qubit systems, as the size of the Hilbert space scales exponentially with the number of qubits. In this section, we will attempt to give some figures for the scaling of larger qubit states by simpler considerations based on the values of the CNOT gate obtained in the previous section. We will focus on the expected fidelity of an n-qubit Greenberger-Horne-Zeilinger (GHZ) state of the form $|\Psi\rangle = |0\cdots0\rangle + |1\cdots1\rangle$, which is a simple yet useful type of entangled state. The expected fidelity of this state can be fairly straightforwardly calculated by realizing that it is created by $n-1$ successive CNOT gates. Moreover, this fidelity will be the same both for the case of only nearest-neighbor interactions and for the case where each ion can control each of the other ions. This result is shown in Fig. 5, both with and without readout. One limitation of the prediction is that while the creation of the GHZ state allows situations where only nearest-neighbor interactions are possible, the readout step is calculated with the assumption that each ion can control a buffer ion directly without additional swap operations. As discussed earlier in Sec. II, this is expected to be a reasonable case for at least up to five qubits for a doping concentration of 4%. The obtained fidelities indicate that the single-instance

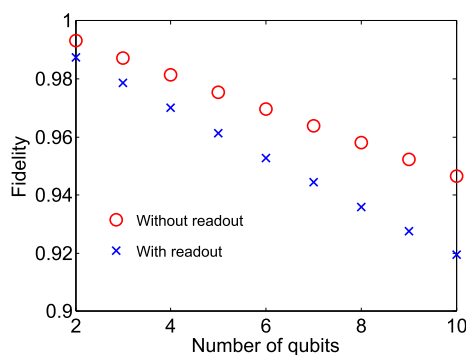

FIG. 5. (Color online) Predicted fidelity of n-qubit GHZ states with and without readout. The fidelity includes pulses for tomography but assumes that all ions can interact with each other, which is reasonable at least up to five qubits with 4% doping concentration.

rare-earth quantum computer schemes can be comparable to those of other multiqubit schemes, such as trapped ions [2] or superconducting qubits [28].

VI. CONCLUSIONS

We have presented and described how to realize a readout scheme for detecting quantum states of single ions inside a crystal host. The scheme is based on having a buffer ion, onto which the state of the qubit ions can be repeatedly mapped. This buffer ion is within dipole-dipole interaction range of a readout ion, and the state of the buffer ion can control the excitation frequency of the readout ion. This will enable or disable excitation of the readout ion, and the state can thus be detected by cavity-enhanced fluorescence. Several buffer stages can, in principle, be concatenated to yield very long effective detection times, such that readout errors can be reduced by more than one order of magnitude and reach $\varepsilon = 10^{-3}$ for a wide variety of collection efficiencies and background levels. We then used this result together with known error sources to obtain expected fidelities for a CNOT gate of above 99% and for larger GHZ states remaining above 92% for up to ten qubits. One of the limitations of our assumptions is presently that the expected increase in performance for qubit rotations when switching from Pr to Eu has not been fully experimentally verified as of yet. Our results indicate that rare-earth quantum computing can be feasible in the single-instance regime.

ACKNOWLEDGMENTS

The authors acknowledge useful discussions with D. Hunger. This work was supported by the Swedish Research Council, the Knut and Alice Wallenberg Foundation, and the Crafoord Foundation. The research leading to these results also received funding from the People Programme (Marie Curie Actions) of the European Union's Seventh Framework Programme FP7 (2007-2013) under REA Grant Agreement No. 287252 (CIPRIS), Lund Laser Center (LLC), and the Nanometer Structure Consortium at Lund University (nmC@LU).

[1] H. Häffner, W. Hänsel, C. F. Roos, J. Benhelm, D. Chek-al-kar, M. Chwalla, T. Körber, U. D. Rapol, M. Riebe, P. O. Schmidt, C. Becher, O. Gühne, W. Dür, and R. Blatt, Nature (London) **438**, 643 (2005).

[2] T. Monz, P. Schindler, J. T. Barreiro, M. Chwalla, D. Nigg, W. A. Coish, M. Harlander, W. Hänsel, M. Hennrich, and R. Blatt, Phys. Rev. Lett. **106**, 130506 (2011).

[3] X. -C. Yao, T. -X. Wang, P. Xu, H. Lu, G. -S. Pan, X. -H. Bao, C. -Z. Peng, C. -Y. Lu, Y. -A. Chen, and J. -W. Pan, Nat. Photonics **6**, 225 (2012).

[4] M. H. Devoret and R. J. Schoelkopf, Science **339**, 1169 (2013).

[5] J. Wrachtrup and F. Jelezko, J. Phys. Condens. Matter **18**, S807 (2006).

[6] H. Riedmatten, M. Afzelius, M. U. Staudt, C. Simon, and N. Gisin, Nature (London) **456**, 773 (2008).

[7] M. Afzelius, I. Usmani, A. Amari, B. Lauritzen, A. Walther, C. Simon, N. Sangouard, J. Minár, H. de Riedmatten, N. Gisin, and S. Kröll, Phys. Rev. Lett. **104**, 040503 (2010).

[8] M. P. Hedges, J. J. Longdell, Y. Li, and M. J. Sellars, Nature (London) **465**, 1052 (2010).

[9] E. Fraval, M. J. Sellars, and J. J. Longdell, Phys. Rev. Lett. **95**, 030506 (2005).

[10] L. Rippe, B. Julsgaard, A. Walther, Y. Ying, and S. Kröll, Phys. Rev. A **77**, 022307 (2008).

[11] J. H. Wesenberg, K. Mølmer, L. Rippe, and S. Kröll, Phys. Rev. A **75**, 012304 (2007).

[12] R. Kolesov, K. Xia, R. Reuter, R. Stöhr, A. Zappe, J. Meijer, P. Hemmer, and J. Wrachtrup, Nat. Commun. **3**, 1029 (2012).

[13] T. Utikal, E. Eichhammer, L. Petersen, A. Renn, S. Götzinger, and V. Sandoghdar, Nat. Commun. **5**, 3627 (2014).

[14] D. B. Hume, T. Rosenband, and D. J. Wineland, Phys. Rev. Lett. **99**, 120502 (2007).

[15] D. Kielpinski, C. Monroe, and D. Wineland, Nature (London) **417**, 709 (2002).

[16] M. Zhong, M. P. Hedges, R. L. Ahlefeldt, J. G. Bartholomew, S. E. Beavan, S. M. Wittig, J. J. Longdell, and M. J. Sellars, Nature (London) **517**, 177 (2015).

[17] A. Walther, B. Julsgaard, L. Rippe, Y. Ying, S. Kröll, R. Fisher, and S. Glaser, Phys. Scr. T **137**, 014009 (2009).

[18] Y. Yan, J. Karlsson, L. Rippe, A. Walther, D. Serrano, D. Lindgren, M. -E. Pistol, S. Kröll, P. Goldner, L. Zheng, and J. Xu, Phys. Rev. B **87**, 184205 (2013).

[19] R. Kolesov, K. Xia, R. Reuter, M. Jamali, R. Stöhr, T. Inal, P. Siyushev, and J. Wrachtrup, Phys. Rev. Lett. **111**, 120502 (2013).

[20] H. Kaupp, C. Deutsch, H. -C. Chang, J. Reichel, T. W. Hänsch, and D. Hunger, Phys. Rev. A **88**, 053812 (2013).

[21] F. Könz, Y. Sun, C. W. Thiel, R. L. Cone, R. W. Equall, R. L. Hutcheson, and R. M. Macfarlane, Phys. Rev. B **68**, 085109 (2003).

[22] I. Roos and K. Mølmer, Phys. Rev. A **69**, 022321 (2004).

[23] R. W. Equall, Y. Sun, R. L. Cone, and R. M. Macfarlane, Phys. Rev. Lett. **72**, 2179 (1994).

[24] A. N. Nilsson, L. Rippe, A. Walther, and S. Kröll (unpublished).

[25] N. Ohlsson, R. K. Mohan, and S. Kröll, Opt. Commun. **201**, 71 (2002).

[26] M. A. Nielsen and I. L. Chuang, *Quantum Computation and Quantum Information* (Cambridge University Press, Cambridge, UK, 2000), Chap. 8.

[27] C. F. Roos, G. P. T. Lancaster, M. Riebe, H. Haeffner, W. Haensel, S. Gulde, C. Becher, J. Eschner, F. Schmidt-Kaler, and R. Blatt, Phys. Rev. Lett. **92**, 220402 (2004); arXiv:quant-ph/0307210.

[28] R. Barends *et al.*, Nature (London) **508**, 500 (2014).